



PhD-FSTC-2019-68  
The Faculty of Sciences, Technology and Communication

## DISSERTATION

Defence held on 11/10/2019 in Luxembourg  
to obtain the degree of

## DOCTEUR DE L'UNIVERSITÉ DU LUXEMBOURG EN PHYSIQUE

by

**Lawrence William HONAKER**  
Born on 8 June 1990 in Honolulu, Hawaii (USA)

## LIQUID METALS AND LIQUID CRYSTALS SUBJECT TO FLOW: FROM FUNDAMENTAL FLUID PHYSICS TO FUNCTIONAL FIBERS

### Dissertation defence committee

Dr. Jan P.F. Lagerwall, dissertation supervisor  
*Professor of Physics, Université du Luxembourg*

Dr. Elizabeth K. Mann  
*Professor of Physics, Kent State University*

Dr. Phillip J. Dale, Chairman  
*Associate Professor of Physics, Université du Luxembourg*

Dr. Maria-Helena Godinho  
*Associate Professor of Materials Science, Universidade Nova de Lisboa*

Dr. Helen F. Gleeson  
*Professor of Physics, University of Leeds*





# **LIQUID METALS AND LIQUID CRYSTALS SUBJECT TO FLOW: FROM FUNDAMENTAL FLUID PHYSICS TO FUNCTIONAL FIBERS**

A thesis submitted in partial fulfillment of the requirements  
for the conferral of the degree of  
*Docteur de l'Université du Luxembourg en Physique*

by Lawrence W. Honaker  
all rights reserved  
except for previously published material

ISBN: 978-99959-0-527-9

Electronic version is permanently available at <http://hdl.handle.net/10993/41196>.

© 2019-2020 Lawrence W. Honaker

All rights reserved except for previously published material

Cover images:

Front: a collage of experimentally-obtained fibers and jetting co-flows arranged in a spiderweb.

Back: a stylized representation of co-flowing jets of galinstan within sheaths of aqueous PVA solution, with varying galinstan flow rates producing different degrees of core continuity.

Printed by Gildeprint – Enschede (NL)

Typeset in PT Serif

# TABLE OF CONTENTS

ACKNOWLEDGEMENT OF FUNDING .....	viii
LIST OF PUBLICATIONS, PRESENTATIONS, AND SUPERVISION .....	ix
LIST OF FIGURES.....	xi
LIST OF TABLES .....	xvi
TABLE OF CHEMICALS .....	xvii
TABLE OF ABBREVIATIONS, SYMBOLS, AND VARIABLES .....	xx
ABSTRACT .....	xxi
SOMMAIRE (EN FRANÇAIS) .....	xxii
 CHAPTER 1: MOTIVATION .....	 1
 CHAPTER 2: BACKGROUND .....	 5
2.1 Liquid Crystals .....	5
2.1.1 Liquid Crystal Classes and Varieties .....	6
2.1.2 Liquid Crystalline Phases.....	6
2.1.3 Alignment and Anisotropy of Liquid Crystals.....	7
2.1.4 Liquid Crystal Optics .....	11
2.2 Polymers .....	16
2.2.1 Polymer Structure and Function.....	16
2.2.2 Polymers in Solution: The Good, the Bad, and Theta .....	19
2.2.3 Polymer Flow and Viscoelasticity .....	20
2.3 Liquid Metals .....	22
2.4 Interfacial Tension and Surfactants .....	24
2.5 Jetting and Plateau–Rayleigh Instability .....	27
2.6 Diffusion and Osmotic Pressure .....	29
2.7 Solubility and Miscibility .....	31
2.8 Microfluidics.....	33
 CHAPTER 3: MICROFLUIDIC INTERFACIAL TENSIOLOGY: DEVELOPMENT, MEASUREMENT, AND OPTIMIZATION.....	 35
3.1 State-of-the-Art of Interfacial Tensiometry .....	36
3.1.1 Pendant Drop.....	36
3.1.2 Ring and Plate Methods .....	38
3.1.3 Sessile Drops.....	39
3.1.4 Bubble Deformation Method .....	40
3.1.5 Droplet Deformation and Relaxation Methods .....	41
3.2 Technique Basics.....	42

3.2.1 Principle of Micropipette Aspiration .....	42
3.2.2 Flow-Focusing and Droplet Generation Chips .....	43
3.3 Technique Development and Optimization .....	44
3.3.1 First Generation Tensiometer: Immediate Aspiration .....	44
3.3.2 Second Generation Tensiometer: Aspiration into a Constricted Capillary .....	48
3.4 Equilibrium Surface and Interfacial Tensions .....	53
3.4.1 Calibration with Surfactant Solutions .....	53
3.4.2 Interfacial Tension of Nematic Liquid Crystals against Aqueous Surfactant Solutions .....	54
3.4.3 Interfacial Tension of Nematic Liquid Crystals against Aqueous Polymer Solutions .....	58
3.4.4 Surface Tension of Air against Surfactant Solution .....	60
3.4.5 Interfacial Tensions of Liquid Metals .....	61
3.4.6 Attempted Measurements between CNC Dispersion Phases .....	63
3.5 Dynamic Interfacial Tension .....	64
3.6 Conclusions and Outlook .....	66
CHAPTER 4: MICROFLUIDIC WET SPINNING OF PURE POLYMER FIBERS AND FIBERS CONTAINING LIQUID CRYSTAL CORES .....	
4.1 Why Wet Spinning? .....	70
4.2 Materials, Methods, and Equipment .....	71
4.2.1 Microfluidic Spinneret Device: Production .....	71
4.2.2 Polymer Dopes .....	73
4.2.3 Coagulation Baths .....	75
4.2.4 Flow Rates and Ratios .....	76
4.2.5 Fiber Collection .....	77
4.3 Wet Spinning of Pure Polymer Fibers .....	78
4.3.1 Spinning of Polyisoprene Fibers .....	78
4.3.2 Spinning of Pure PVA Fibers .....	83
4.4 Wet Spinning of Fibers with a Liquid Crystal Core .....	85
4.4.1 Achiral Nematic Liquid Crystal Core Elastomer Fibers .....	86
4.4.2 Cholesteric Liquid Crystal Core Elastomer Fibers .....	89
4.5 PVA Fibers with Cholesteric Liquid Crystal Cores .....	97
4.6 Numerical Analysis of the Spinning Parameters .....	99
4.7 Conclusions .....	101
CHAPTER 5: LIQUID METAL JETTING IN CO-FLOWING SYSTEMS: TOWARDS PRODUCING CORE-SHEATH FIBERS WITH LIQUID METAL CORES .....	
5.1 Motivation and Background: Co-Flowing of Galinstan .....	105
5.2 Theoretical Framework .....	107
5.2.1 Recap: Numerically Predicting Flow and Jetting Stability .....	107
5.2.2 Oxidation of Galinstan and the Péclet Number .....	108
5.3 Experimental Set-Ups for Co-Flowing and Jetting .....	109

5.3.1 Two-Flow: Materials and Configuration .....	110
5.3.2 Three Flow Set-Ups for Jetting towards Fiber Production .....	111
5.4 Experimental Results .....	112
5.4.1 Two-Flows and the Galinstan Flow State Diagram.....	112
5.4.2 Three-Flow Results for Jetting of Galinstan in PETA .....	115
5.4.3 Three-Flow Results for the Jetting of Galinstan in Polymer Solutions.....	117
5.5 Conclusions .....	123
CHAPTER 6: CONCLUSIONS AND OUTLOOK.....	125
REFERENCES .....	129
ACKNOWLEDGEMENTS.....	141

## ACKNOWLEDGEMENT OF FUNDING

The work in this thesis was funded primarily by an *Aide à la formation–recherche* (AFR-PhD) grant awarded by the Luxembourg National Research Fund (FNR) (grant n°. 9784104; project code LIMEFLOW) from October 2015 to October 2019. Some of the equipment and materials used during this thesis are part of a project that has received funding from the European Research Council (ERC) under the European Union’s Horizon 2020 research and innovation programme (Grant agreement No. 210174891, project code INTERACT), and some of the travel expenses covered during this work were funded by the Doctoral Program in Physics and Materials Science of the University of Luxembourg.



## LIST OF PUBLICATIONS, PRESENTATIONS, AND SUPERVISION

The following publications comprise the work on which this thesis is based:

### Peer-Reviewed Journal Articles

- (1) L.W. Honaker, J.P.F. Lagerwall, and V.S.R. Jampani, "Microfluidic Tensiometry Technique for the Characterization of the Interfacial Tension between Immiscible Liquids", Langmuir **34**, 2403-2409 (2018), DOI: 10.1021/acs.langmuir.7b03494.
- (2) L.W. Honaker, S. Vats, M. Anyfantakis, and J.P.F. Lagerwall, "Elastic Sheath-Liquid Crystal Core Fibres Achieved by Microfluidic Wet Spinning", Journal of Materials Chemistry C **7**, 11588 (2019), DOI: 10.1039/C9TC03836A.

### Contributed Oral Presentations

- (1) L.W. Honaker, S. Vats, M. Anyfantakis, J.P.F. Lagerwall, "Wet Spinning of Coaxial Liquid Crystal-Filled Elastomer Fibers with Microfluidics". Presented at the 15<sup>th</sup> European Conference on Liquid Crystals, Wrocław, Poland, 4 July 2019.
- (2) L.W. Honaker, S. Vats, M. Anyfantakis, J.P.F. Lagerwall, "Microfluidic Wet-Spinning of Core-Sheath Elastomer-Liquid Crystal Fibers". Presented at the 46<sup>th</sup> German Liquid Crystal Conference, Paderborn, Germany, 29 March 2018.
- (3) L.W. Honaker, J.P.F. Lagerwall, V.S.R. Jampani, "Microfluidics for Measuring Equilibrium and Dynamic Interfacial Tensions of Liquid Crystals". Presented at the 45<sup>th</sup> German Liquid Crystal Conference, Luxembourg, Luxembourg, 22 March 2018.
- (4) L.W. Honaker, J.P.F. Lagerwall, V.S.R. Jampani, "Microfluidic Interfacial Tensiometry of Liquid Crystals". Presented at the 14<sup>th</sup> European Conference on Liquid Crystals, Moscow, Russian Federation, 28 June 2017.

### Poster Presentations

- (1) L.W. Honaker, S. Vats, C.G. Reyes, A. Sharma, M. Anyfantakis, J.P.F. Lagerwall, "Jetting in Polymer-Liquid Crystal Co-Flows for Wet-Spinning of Composite Fibers". Presented at the 27<sup>th</sup> International Liquid Crystal Conference, Kyoto, Japan, 26 July 2018.
- (2) L.W. Honaker, V.S.R. Jampani, J.P.F. Lagerwall, "Microfluidics for Measuring Equilibrium and Dynamic Interfacial Tensions of Liquid Crystals". Presented at the 27<sup>th</sup> International Liquid Crystal Conference, Kyoto, Japan, 24 July 2018.
- (3) L.W. Honaker, J.P.F. Lagerwall, V.S.R. Jampani, "Microfluidics for Surface and Interfacial Tensiometry". Presented at the University of Luxembourg DPPM

Kick-Off Event, Esch-sur-Alzette, Luxembourg, 23 February 2018.  
DOI: 10.5281/zenodo.1250321.

- (4) L.W. Honaker, J.P.F. Lagerwall, V.S.R. Jampani, "Pressure-Based Microfluidic Interfacial Tensiometry". Presented at the 26<sup>th</sup> International Liquid Crystal Conference, Kent, OH, USA, 3 August 2016.

The following additional publications and presentations were published during the course of the preparation of this thesis, but are not directly a part of the material presented herein.

- (1) L.W. Honaker, "Conference report on the 45th German Liquid Crystal Conference", Liquid Crystals Today **27** (2018), 3, 77-79, DOI: 10.1080/1358314X.2018.1525056.
- (2) L.W. Honaker, "Conference report on the 45th German Liquid Crystal Conference and GLCC Research Synopsis – 'Microfluidics for Interfacial Tensiometry of Liquid Crystals'", Bunsenmagazin **20** (2018), 4, 143-145.
- (3) N. Popov, L.W. Honaker, M. Popova, N.V. Usol'tseva, E.K. Mann, A.I. Jákli, P. Popov, "Thermotropic Liquid Crystal-Assisted Chemical and Biological Sensors", MDPI Materials **11** (2018), 14-17, DOI: 10.3390/ma11010020.
- (4) P. Popov, L.W. Honaker, M.S. Mirheydari, E.K. Mann, A.I. Jákli, "Chiral Nematic Liquid Crystal Microlenses", Scientific Reports **7** (2017), DOI: 10.1038/s41598-017-01595-6.
- (5) P. Popov, L.W. Honaker, E.E. Kooijman, E.K. Mann, A.I. Jákli, "A Liquid Crystal Biosensor for Specific Sensing of Antigens", Sensing and Bio-Sensing Research **8** (2016), 31-35, DOI: 10.1088/1367-2630/11/7/075021.
- (6) L.W. Honaker, P. Popov, E.E. Kooijman, E.K. Mann, A.I. Jákli, "Specific Sensing of Biological Materials with Liquid Crystals". Poster Presentation. Presented at the 26<sup>th</sup> International Liquid Crystal Conference, Kent, OH, USA, 3 August 2016.

The projects underlying the following theses were performed partially under my supervision during the course of the work presented in this thesis and comprise some of the material, in whole or in part, presented herein:

- (1) Andy Schanen, "Microfluidics for measuring the interfacial tension of liquid crystals". Master's of Science (M.Sc.) Thesis, Condensed Matter Physics, University of Luxembourg, September 2018–June 2019. Co-supervised with Prof. Jan Lagerwall and Dr. V.S.R. Jampani.
- (2) Hala Alami-Laroussi Akhriff, "Rheology of Simple and Complex Elastomer Solutions". Bachelor's of Science (B.Sc.) Thesis, Physics, University of Luxembourg, March 2019–June 2019. Co-supervised with Prof. Jan Lagerwall, Dr. Jörg Baller, and Dr. Alex Gansen.



## LIST OF FIGURES

<i>Figure 1. A diagram of the mesophases of common thermotropic liquid crystal phases consisting of rod-shaped molecules, with the two "melting points" (the solid-liquid melting point and the nematic-isotropic "clearing point") indicated.....</i>	<i>7</i>
<i>Figure 2. Schematic of the three common bulk deformations of the liquid crystal director: (a) splay, (b) twist, and (c) bend. ....</i>	<i>9</i>
<i>Figure 3. A selection of surface liquid crystal defects with topological charges of (a) <math>+\frac{1}{2}</math>; (b) and (c) <math>+1</math>; (d) <math>-\frac{1}{2}</math>; and (e) <math>-1</math>. ....</i>	<i>10</i>
<i>Figure 4. Schematic representation of birefringence through a sample, where components polarized perpendicularly and parallel to the optic axis are refracted differently. ....</i>	<i>11</i>
<i>Figure 5. A modernized version of the Michel-Lévy birefringent color chart. This chart relates color to the optical path difference, which is in turn a function of the product of sample thickness and birefringence <math>\Delta n</math>. ....</i>	<i>12</i>
<i>Figure 6. Illustration of the transmission of light through crossed polarizers and a liquid crystal element with an optical path difference <math>\Delta\Lambda</math>. ....</i>	<i>14</i>
<i>Figure 7. Cholesteric liquid crystal phase prepared from the nematic liquid crystal mixture RO-TN 615 (Hoffmann-La Roche) with 25% w/w chiral dopant ZLI-3786. ....</i>	<i>15</i>
<i>Figure 8. Schematic of Bragg reflection from an aligned cholesteric liquid crystal. ....</i>	<i>16</i>
<i>Figure 9. Example of the hydrogen bonding between the amide groups of nylon chains, which promote semicrystallinity and improve the tensile strength of nylon. ....</i>	<i>18</i>
<i>Figure 10. The two isomers of 1,4-polyisoprene. ....</i>	<i>19</i>
<i>Figure 11. Curves relating polymer strain (<math>\epsilon</math>) to stress (<math>\sigma</math>) applied for a variety of different kinds of fluids (shear-thinning, shear-thickening, and Newtonian fluids and Bingham plastics). ....</i>	<i>20</i>
<i>Figure 12. Examples of the three-dimensional structures that can be printed with gallium-based liquid metals (here, eutectic gallium-indium alloy). ....</i>	<i>23</i>
<i>Figure 13. A diagram of a typical definition of surface tension. ....</i>	<i>25</i>
<i>Figure 14. Simplified diagrams of the flow parameters and how they interact with each other. ....</i>	<i>29</i>
<i>Figure 15. Schematic of the pendant drop technique. ....</i>	<i>37</i>

Figure 16. Examples of the (a) Wilhelmy plate and (b) du Noüy ring for measuring interfacial tension. ....	39
Figure 17. Demonstration of the sessile drop technique. ....	40
Figure 18. Illustration of the bubble deformation technique. ....	41
Figure 19. The deformation and relaxation of the droplets in the vicinity of the constriction. ....	41
Figure 20. A schematic of a droplet being aspirated into a capillary ....	43
Figure 21. A schematic of the assembly of the injection and collection capillary, where the injection capillary is placed somewhat inside the collection capillary. ....	45
Figure 22. The assembled microfluidic device used for interfacial tension measurements. ....	46
Figure 23. First-generation microfluidic set-up for droplet generation and interfacial tension measurement. ....	47
Figure 24. Demonstration of the aspiration technique on a droplet of 5CB in a 1.0 mM CTAB solution. ....	48
Figure 25. Production and aspiration process of a drop of 5CB in 1.0 mM CTAB solution using the constricted capillary geometry. ....	50
Figure 26. Schematic of a droplet held in the constriction without distortion. ....	50
Figure 27. Schematic of the aspiration of the droplet upon application of a pressure $\Delta P$ . ....	51
Figure 28. Aspiration of a droplet of 5CB in a solution of 10 mM SDS (aq). ....	52
Figure 29. Image of the pressure graph obtained during the experiment with images corresponding to the droplet states. ....	53
Figure 30. Interfacial tension of 5CB against aqueous SDS solutions of various concentrations. ....	57
Figure 31. Aspiration process of 5CB in a 1% w/w PVA (aq) solution at (a) an initial pressure and (b) at an increased pressure. ....	58
Figure 32. A two-dimensional projection of the liquid crystal alignment in a droplet. ....	59
Figure 33. Measurement of the surface tension of a 6.0 mM SDS (aq) solution using the aspiration technique. ....	60
Figure 34. Image from the measurement of the interfacial tension of galinstan in PETA. ....	62
Figure 35. Attempted droplet production of the anisotropic phase of a CNC dispersion. ....	63
Figure 36. A schematic of the progression of the aspirated edge of droplet into the constriction with time. ....	64

Figure 37. Measurement curve of the dynamic interfacial tension of 5CB against a 6.0 mM SDS (aq) solution. ....	66
Figure 38. A schematic of the spinneret device for producing droplets and shells that was initially used for fiber production. ....	72
Figure 39. Snaking of a co-flowing jet of 5CB in a 30% w/w SBS in toluene solution, contained in a bath of 10% w/w PVP in ethanol. ....	72
Figure 40. A schematic of the modified spinneret device for producing fibers. ....	73
Figure 41. Different flow rate combinations of 14% PB dope in n-hexane in a co-flowing system with 7% LiBr and 10% PVP in ethanol as the outer phase and the resulting effects on jet continuity. ....	77
Figure 42. A wire frame onto which polybutadiene fibers spun from n-hexane were collected and stored overnight. ....	78
Figure 43. Spinning process of pure polyisoprene fibers. ....	80
Figure 44. A PI fiber spun from 14% w/w PI in n-hexane dope. ....	81
Figure 45. Birefringence of a PI fiber and the correlation of the birefringent color to the numerical value. ....	82
Figure 46. A sample of polybutadiene kept at ~5°C for a period of six months. ....	83
Figure 47. A PVA fiber spun from 20% w/w PVA (aq) dope. ....	84
Figure 48. A PVA fiber spun from 25% w/w PVA (aq) dope. ....	85
Figure 49. Jetting of a core of RO-TN 651 within a sheath of 12.5% PI in n-hexane and a coagulation bath of 7% LiBr and 10% PVP in ethanol. ....	86
Figure 50. Micrographs taken during the spinning process of a core of RO-TN 615 flowing within a polyisoprene sheath (14% w/w in n-hexane), as viewed between crossed linear polarizers, at different flow rate combinations. ....	87
Figure 51. A PI fiber spun from a 14% w/w PI in n-hexane dope with a core consisting of the liquid crystal mixture RO-TN 615. Scale bars indicate 100 $\mu\text{m}$ with an approximate fiber diameter of ~30 $\mu\text{m}$ , of which 10-15 $\mu\text{m}$ is the core. ....	88
Figure 52. A PI fiber spun from a 14% w/w PI in n-hexane dope with a core consisting of the liquid crystal mixture RO-TN 615. Scale bars indicate 100 $\mu\text{m}$ with an approximate fiber diameter of ~80 $\mu\text{m}$ , of which of which ~50 $\mu\text{m}$ is the core. ....	88
Figure 53. Two configurations of planar alignment of a liquid crystal confined within a core. ....	89
Figure 54. A long (~20 cm) sample of a PI fiber filled with a mixture of 25% w/w ZLI-3786 in RO-TN 651, viewed under ambient room lighting. ....	90
Figure 55. A PI fiber filled with a mixture of 25% w/w ZLI-3786 in RO-TN 615. ....	91
Figure 56. An idealized schematic of the proposed liquid crystal structure of a spun PI fiber filled with a cholesteric, using a typical unstretched fiber. ....	92

Figure 57. A PI fiber filled with a mixture of 25% w/w ZLI-3786 in RO-TN 615, mounted on a glass slide and viewed in reflection mode between crossed polarizers with an inserted quarter wave plate.....	92
Figure 58. Schematic representation of the pitch within a confined cholesteric between two parallel glass substrates with a sample thickness $d$ .....	94
Figure 59. A PI fiber filled with 25% w/w ZLI-3786 in RO-TN 615 mixture, as viewed in reflection mode between crossed polarizers. The difference between (a), (b), and (c) is stretching the fiber to thin it progressively. ....	95
Figure 60. Jetting observed in a tri-flowing system consisting of an outer bath phase of 8% $\text{CaCl}_2$ and 10% PVP in anhydrous ethanol, an aqueous polymer dope prepared with 20% PVA as a middle phase, and a core of 25% ZLI-3786 in E55 mixed with 5% w/w anhydrous ethanol. ....	98
Figure 61. Beading shown in a fiber spun from 20% PVA (aq) with a core of 25% ZLI-3786 in RO-TN 615, as viewed in reflection mode between crossed polarizers, shown in two different sections of fiber. ....	98
Figure 62. Alternate proposed spinneret geometry to minimize clogging issues.....	103
Figure 63. Jetting of galinstan in a viscous medium.....	106
Figure 64. Co-flowing device used to observe the flow behavior of galinstan in contact with another solution.....	110
Figure 65. Filling procedure for loading the syringes with galinstan.....	111
Figure 66. State diagram constructed from a two-flow system of galinstan in a polymer solution.....	113
Figure 67. Two-flow jetting of galinstan in 15% w/w PVA solution with different flow rate combinations and corresponding different combinations of outer phase capillary number and inner phase Weber number. ....	114
Figure 68. Jetting of galinstan in a flow of degassed PETA (sheath) and 7.5% w/w PVP in 25% v/v ethanol in water (outer). ....	115
Figure 69. (a) Galinstan flow in PETA (middle) and PVP in 25% ethanol (outer), as in Figure 68, accompanied by (b) the estimated Weber number at different points in the channel indicated.....	116
Figure 70. Jetting of galinstan in a co-flow of 20% w/w PVA (aq) (middle) as a dope and 15% w/w $\text{CaCl}_2$ and 10% w/w PVP in ethanol (outer) as the bath.....	118
Figure 71. Jetting of galinstan in a co-flow of 25% w/w PVA (aq) (middle) as a dope and 15% w/w $\text{CaCl}_2$ and 10% w/w PVP in ethanol (outer) as the bath.....	118
Figure 72. (a) A still frame of the galinstan jetting seen in Figure 70(d) with (b) the corresponding estimated Weber numbers relative to the position from the spinneret..	119
Figure 73. Calculated threshold flow rates for galinstan jetting as a function of initial jet diameter. ....	120

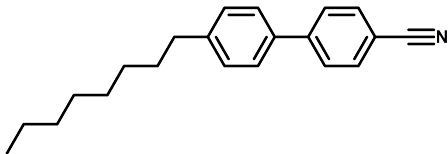
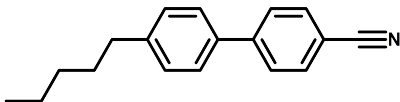
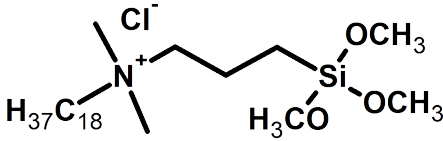
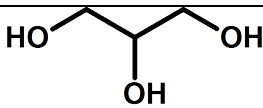
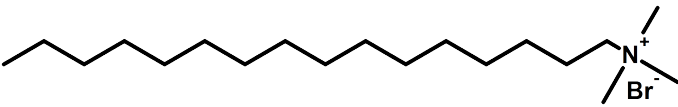
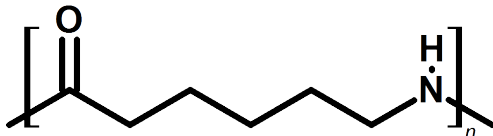
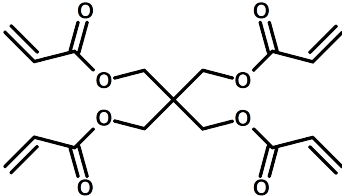
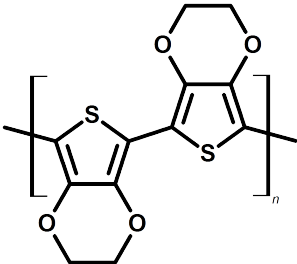
<i>Figure 74. Jetting of galinstan in a co-flow of 25% w/w PVA (aq) (middle) as a dope and 15% w/w CaCl<sub>2</sub> and 10% w/w PVP in ethanol (outer) as the bath.....</i>	<i>121</i>
<i>Figure 75. Jetting of galinstan in a co-flow of 25% w/w PVA (aq) (middle) as a dope and 15% w/w CaCl<sub>2</sub> and 10% w/w PVP in ethanol (outer) as the bath.....</i>	<i>122</i>
<i>Figure 76. Sample of a PVA fiber spun from 20% w/w PVA dope with galinstan as the core.....</i>	<i>123</i>

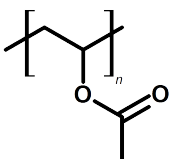
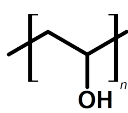
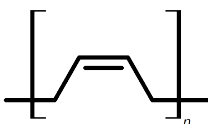
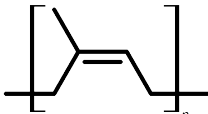
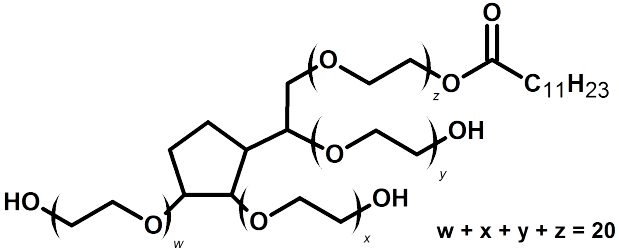
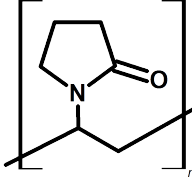
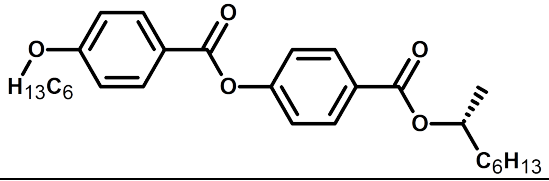
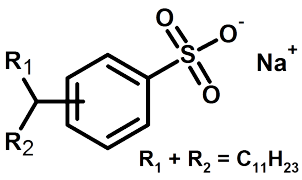
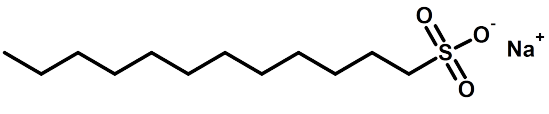
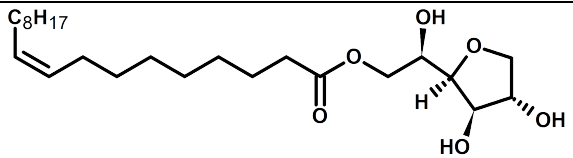
## LIST OF TABLES

<i>Table 1. Molar attraction constant contributions of polyisoprene functional groups.....</i>	<i>32</i>
<i>Table 2. Group contributions to the calculated Hansen parameters of 5CB. ....</i>	<i>33</i>
<i>Table 3. Interfacial tensions of TWEEN 20 (aq) solutions against SPAN 80 in hexadecane solutions. ....</i>	<i>54</i>
<i>Table 4. Interfacial tension values of 5CB against aqueous solutions of SDS of various concentrations. ....</i>	<i>56</i>
<i>Table 5. Interfacial tensions of galinstan against sodium hydroxide solutions of various concentrations. ....</i>	<i>61</i>

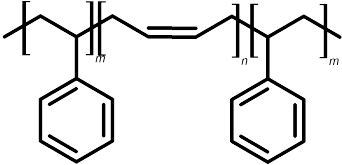
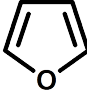
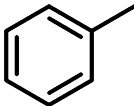
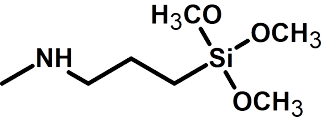
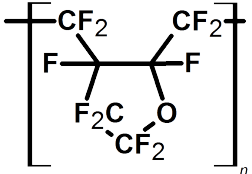
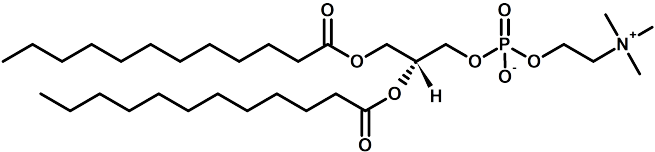
## TABLE OF CHEMICALS

The following chemicals are referenced in this dissertation.

Name(s)	Structure
4-cyano-4'-octylbiphenyl, 8CB	
4-cyano-4'-pentylbiphenyl, 5CB	
dimethyloctadecyl [3(trimethoxy-silyl)propyl] ammonium chloride, DMOAP	
glycerol; glycerine	
hexadecyltrimethyl-ammonium bromide; cetrimonium bromide; CTAB	
nylon-6, polycaprolactam	
pentaerythritol tetraacrylate; PETA	
poly(3,4-ethylene-dioxythiophene); poly(2,3-dihydrothieno[3,4- <i>b</i> ][1,4]dioxane-5,7-diyl); PEDOT	

poly(vinyl acetate); PVAc	
poly(vinyl alcohol); PVA	
polybutadiene, <i>cis</i> -1,4-polybutadiene, poly(1,4-butadiene); PB	
polyisoprene, <i>cis</i> -1,4-polyisoprene, poly(1,4-isoprene); PI	
polysorbate 20; TWEEN 20	
polyvinylpyrrolidone; PVP	
<i>R</i> -2-octyl 4-[4-(hexyloxy) benzoyloxy] benzoate; ZLI-3786; R811	
sodium dodecyl benzenesulfonate; SDBS	
sodium dodecyl sulfate; SDS	
sorbitan oleate; SPAN 80; E495	



styrene-butadiene-styrene co-block polymer; SBS	
tetrahydrofuran; THF	
toluene	
trimethoxy[3-(methylamino)propyl]silane; MAP	
CYTOP	
1,2-didodecyl- <i>sn</i> -glycero-3-phosphocholine; DLPC	

## TABLE OF ABBREVIATIONS, SYMBOLS, AND VARIABLES

$\vec{\nabla}$	gradient operator ( $\vec{\nabla} = \frac{\partial}{\partial x} \hat{i} + \frac{\partial}{\partial y} \hat{j} + \frac{\partial}{\partial z} \hat{k}$ in $xyz$ space)	Da	dalton, a unit of molar mass (1 Da = 1 g · mol <sup>-1</sup> )
$a_g$	gravitational acceleration (typically 9.8 m · s <sup>-2</sup> )	$l$	monomer length
$f_d$	elastic energy density	$n$	refractive index
$k_B$	Boltzmann's constant $k_B = 1.38 \cdot 10^{-23}$ J · K <sup>-1</sup>	$N$	number of monomers (aka degree of polymerization)
$k_{ii}$	Frank elastic deformation constant ( $i = 1$ for splay; $i = 2$ for twist; $i = 3$ for bend)	$p$	cholesteric pitch
$\hat{n}$	liquid crystal director	$Pe$	Péclet number; $Pe = \frac{vl}{D}$
$R_G$	molar ideal gas constant $R_G = 8.314$ J · K <sup>-1</sup> · mol <sup>-1</sup>	$Q$	flow rate
$S_N$	nematic liquid crystal order parameter	$Re$	Reynolds number; $Re = \frac{\rho vl}{\eta}$
$\mathbb{Z}^+$	the set of all positive integers	$S$	entropy
$\delta_{\alpha\beta}$	Kronecker delta tensor $\delta_{\alpha\beta} = \begin{cases} 1, \alpha = \beta \\ 0, \alpha \neq \beta \end{cases}$	$T$	temperature
$\mu^o$	chemical potential	$v$	flow velocity
$\Delta n$	birefringence	$We$	Weber number; $We = \frac{\rho v^2 l}{\gamma}$
$Ca$	Capillary number; $Ca = \frac{\eta v}{\gamma}$	$\gamma$	interfacial tension
$D$	diffusivity, diffusion coefficient	$\Gamma$	surface coverage
		$\delta$	solubility parameter
		$\eta$	dynamic viscosity
		$\vartheta$	polar orientation angle
		$\theta$	angle of incidence
		$\lambda$	wavelength
		$\rho$	mass density
		$\sigma$	surface tension
		$\varphi$	azimuthal orientation angle

## ABSTRACT

Technology over the past few decades has pushed strongly towards wearable technology, one such form being textiles which incorporate a functional component. There are several ways to produce polymer fibers on both laboratory and industrial scales, but the implementation of these techniques to spin fibers incorporating a functional heterocore has proven challenging for certain combinations of materials. In general, fiber spinning from polymer solutions, regardless of the method, is a multifaceted process with concerns in chemistry, materials science, and physics, both from fundamental and applied standpoints, requiring balancing of flow parameters (interfacial tension, viscosity, and inertial forces) against solvent extraction. This becomes considerably more complicated when multiple interfaces are present.

This thesis explores the concerns involved in the spinning of fibers incorporating functional materials from several standpoints. Firstly, due to the importance of interfacial forces in jet stability, I present a microfluidic interfacial tensiometry technique for measuring the interfacial tension between two immiscible fluids, assembled using glass capillary microfluidics techniques. The advantage of this technique is that it can measure the interfacial tension without reliance on sometimes imprecise external parameters and data, obtaining interfacial tension measurements solely from experimental observations of the deformation of a droplet into a channel and the pressure needed to induce the same.

Using the knowledge gained from both microfluidic device assembly and the interfacial tension, I then present the wet spinning of polymer fibers using a glass capillary spinneret. This technique uses a polymer dope flowed along with a coagulation bath tooled to extract solvent, leaving behind a continuous polymer fiber. We were able to spin both pure polymer fibers and elastomer microscale fibers containing a continuous heterocore of a liquid crystal, with the optical properties of the liquid crystal maintained within the fiber. While we were not able to spin fibers of a harder polymer containing a continuous core, either liquid crystalline or of a liquid metal, I present analysis of why the spinning was unsuccessful and analysis that will lead us towards the eventual spinning of such fibers.

## SOMMAIRE (EN FRANÇAIS)

La recherche en technologie se tourne actuellement vers la technologie portable, qui inclut les fibres des textiles incorporant des matériaux qui répondent aux stimuli. Que l'on produise ces fibres synthétiques en laboratoire ou de façon industrielle, le processus de fabrication engage à la fois la chimie, la physique, et les sciences des matériaux, et se complexifie quand on veut réaliser des fibres coaxiales avec des noyaux fonctionnels.

Cette thèse se penche de plusieurs façons sur les aspects de la production des fibres dotées d'un noyau de matériaux fonctionnels. Dans un premier temps, en raison de l'importance de la tension superficielle pour la stabilisation des jets liquides, on présente une technique pour mesurer la tension superficielle entre deux fluides immiscibles. Cette technique utilise des capillaires en verre dans une géométrie microfluidique. L'avantage de cette technique est de permettre de mesurer la tension superficielle uniquement sur la base des observations de la déformation des gouttelettes et de la pression nécessaire pour réaliser cette déformation dans le capillaire, sans avoir à compter sur les valeurs externes, comme la densité et la viscosité. Les valeurs obtenues sont similaires à celles disponibles dans la littérature.

En exploitant les informations obtenues lors des premières expériences, on présente le filage au mouillé, qui produit des fibres en polymère avec une filière construite des capillaires en verre. On a réussi à produire des fibres de polymère pur ainsi que des fibres incorporant un noyau de cristal liquide nématique ou cholestérique, et les fibres obtenues avec les cristaux liquides conservent les propriétés optiques caractéristiques. Il n'a en revanche pas été possible d'obtenir des fibres avec des noyaux continus de métal liquide ; on présente une analyse des causes de cet échec et on suggère une autre méthode pour parvenir à réaliser éventuellement des microfibres avec un noyau continu de métal liquide.

# CHAPTER 1

## MOTIVATION

Liquid crystals and liquid metals are, in their own rights, fascinating materials with unique properties. Just as their names alone suggest, these are novel phases that combine two seemingly contradictory properties into a single material. Merely being an interesting material, though, is rarely a suitable reason for research to focus on them, let alone money be granted by a funding agency for investigating the material. Therefore, research is driven primarily on *what* can we do with these materials and *how* can we do so rather than merely what they can do.

In the case of liquid crystals, it turns out that their high degree of sensitivity to their surrounding environment, in combination with the striking visual responses they exhibit, allows for their use in many applications. These range from the liquid crystal displays that can be found everywhere in day-to-day life and at many size scales, from millimeters to meters [1,2], to thermometers that quickly produce feedback through striking color changes [3] and ultimately, and more recently, to sensing platforms that show fast, clear responses to external stimuli, whether generalized (such as to temperature, exposure to volatile organic compounds, or the presence of surface-active compounds) [4–8] or specific (such as to proteins or antigens) [9–11].

Gallium-based liquid metal alloys such as EGaIn (eutectic gallium-indium alloy) and galinstan (eutectic gallium-indium-tin alloy) are quite interesting partly due to their property of oxidizing on air contact to form a nanometer-thick, rigid oxide "skin" [12]. This skin can be used in applications such as building circuits [13] and for three-dimensional printing of millimeter-scale liquid metal structures [14,15]. Galinstan additionally possesses a very good thermal conductivity, which lends itself to use in thermometers [16] in much the same way mercury is traditionally used (though without the risk of toxicity).

Being liquids, though, both liquid crystals and liquid metals usually need to be confined in some manner for their use in applications. For liquid crystals, we often do so by sandwiching the liquid crystal between two glass substrates [7,17–20] or occasionally containing the liquid crystal within the form of a free-standing structure, such as a supported film [9,21], droplet [7,22,23], or shell [24,25], but each of these approaches has drawbacks: glass cells are rigid and not suitable for sensing that requires contact, and the free-standing structures are difficult to handle in the liquid state. While gallium-based alloys are protected by their oxide skin, this oxide

skin is still fragile [26] and easily breakable, rendering the resultant structures difficult to handle.

One such way to incorporate these materials into an easily handleable platform is in the form of a wire or fiber, like a textile. This can be achieved through processes such as electrospinning, which can incorporate liquid crystals [4,7,27–33] and, in one case, a liquid metal [34], into either the bulk or the core of a polymer micro- or nanofiber. There have been successes with electrospinning liquid crystal-filled fibers, but the range of polymers that have been reported as being spinnable is comparatively limited [33], and spinning a fiber with a liquid crystal core is far from straightforward [4,7,27,31,32]. While liquid metals have been shown to be fillable into structures with sub-millimeter diameters through capillary action, the size of these structures is also quite large [15], and proceeding to smaller structures is difficult due to oxidation issues. A single report on the electrospinning of liquid metal-filled fibers exists, but reproducing these results has been elusive. [34]

The focus of this dissertation is on the characterization of interfaces between polymer solutions and liquid heterocore materials with a view to incorporating them into the form of fibers. This is largely driven by the following questions:

- (1) What parameters govern jetting, and how can we use them to predict jet stability in a co-flow? (And, if possible, how can we measure these parameters?)
- (2) How can we make polymer fibers, apart from electrospinning, that we can fill with a heterocore?

First, in Chapter 2, the relevant concepts and parameters for the production of fibers containing heterocores are reviewed. These include the properties of the materials with which fibers will be produced (polymer dopes with heterocores from either liquid crystals or liquid metals) in addition to the physics concepts that can be employed for successful fiber production, from interfacial tension to dimensionless flow numbers that can help us predict whether jetting is attainable and fibers are obtainable.

From Chapter 2, we establish, in part, that knowing the interfacial tension between two liquids that will co-flow with each other is important to being able to understand and predict how they will flow [35–37]. To measure interfacial tension, in Chapter 3, we present the development of a microfluidic technique for the characterization of interfacial tension and apply it to a wide variety of immiscible fluids along with the characterization of the interfacial tensions of a variety of systems consisting of anisotropic and isotropic fluids. Our technique works over a wide range of interfacial tensions, from sub-mN/m to the order of N/m, requiring only small amounts of fluid and not requiring outside knowledge of the material properties of the system that other interfacial tensiometry techniques need [38–43] and obtaining results [44] that generally agree with literature data where such exist [21,45,46]. We measure the interfacial tensions between polymer solutions and liquid crystals and between viscous polymer precursors and liquid metals, as these are materials we will ultimately be spinning into fibers, obtaining reproducible data. As a point of curiosity, since the interfacial tension between the liquid crystal 5CB

and water is not well-established and is difficult to measure [21,46,47], we checked to see if our technique was able to measure the 5CB-water interfacial tension, both with and without surfactant: in addition to values with surfactant present, which corresponds to the values with homeotropic liquid crystal alignment, we were able to directly measure the 5CB-water interfacial tension, the results in reasonable agreement with literature values where such exist. We found that the use of a non-surface-active stabilizer, such as the polymer poly(vinyl alcohol) (PVA), does not affect the liquid crystal interfacial tension. While we found that there is a difference between the zero-surfactant interfacial tension in the planar case versus the homeotropic case for nematic phase 5CB, the difference is quite small.

Using the microfluidic fabrication techniques needed to characterize interfacial tension, in Chapter 4, the spinning of polymer fibers using a microfluidic wet spinning technique is achieved. By constructing a spinneret device and through adjustment of flow rates, we are readily able to spin pure poly(vinyl alcohol) and elastomer fibers into a co-flowing coagulation bath [48]. The elastomer fibers are additionally able to have both achiral nematic and cholesteric liquid crystals incorporated as continuous cores in the fibers. This is a consequence of the miscibility between the liquid crystal and the polymer dope: such miscibility produces an extremely low interfacial tension between the two phases [49], leading to more ready jetting and the suppression of the onset of Rayleigh instability. On the other hand, without the presence of miscibility between core and sheath, core continuity cannot be readily obtained, as we see with attempting to spin PVA fibers from an aqueous dope containing a liquid crystal core, and only when we add ethanol to the liquid crystal (to create some miscibility with the polymer dope solvent) do we get core incorporation into PVA fibers (albeit a discontinuous core). This can be attributed to a much higher interfacial tension between the polymer solution and the liquid crystal compared to the case where we spin with organic solvents for the polymer. We find that the fibers, both spun from PVA and elastomers, with a cholesteric liquid crystal core show Bragg reflection due to the spontaneously developed helical periodic modulation of the liquid crystal core. The observed optics are somewhat consistent with those seen with the reflection from liquid crystal shells [25,50], though with the addition of Bragg reflection from a multidomain "powder" structure. We find, however, that the elastomers are swelled by liquid crystals, negatively affecting their longevity and durability.

In Chapter 5, with a view to incorporating liquid metals into fibers in a manner similar to the incorporation of liquid crystals, we characterize the jetting behavior of a liquid metal, galinstan, in a co-flowing system. The aim is to see, with a liquid metal as an inner phase and a polymer solution as the outer phase, under what flow conditions can instability be suppressed and jetting obtained and if the data match expectations for the jetting of immiscible fluids in a more classical system [35–37]. We ultimately find that jetting can be achieved with co-flows of liquid metals, but that the flow rate of the liquid metal phase within the co-flow has to be considerable, much higher than the flow rates needed for flowing liquid crystals, for jetting to persist over a substantial length. The data we acquired about jetting

stability were then used to develop the wet spinning of fibers containing a liquid metal core in a fashion similar to the production of liquid crystal-filled fibers presented in Chapter 4. We present data on attempts to jet liquid metals in a co-flowing outer phase to produce fibers: while we are able to create a co-flowing jet with the three phases (coagulation bath outer phase, polymer dope as the sheath, and a galinstan core), and while we are able to encapsulate galinstan within a PVA sheath, the resultant fiber core is discontinuous. There still exist numerous issues to be resolved in order to eventually incorporate the liquid metal into a continuous core.



## **CHAPTER 2**

### **BACKGROUND**

The process of spinning fibers, both pure and multi-component, is a complex, multifaceted endeavor that requires consideration of a plethora of material properties and factors: we need to create a jet that remains intact long enough for solvent to be extracted, producing a solidified fiber. When a heterocore is introduced, an additional interface is present with its own characteristics and another jet needs to be stabilized to obtain a continuous core. In order to optimize a system to obtain fibers, we need to consider a number of parameters, both related to the physical phenomena we see and are aiming to achieve and the chemical and physical processes behind successful fiber production.

In this chapter, we review the materials and some of the fundamental concepts behind the work presented in future chapters. The materials and techniques used for the work are varied and often require special care and consideration in order to achieve our goals.

#### **2.1 Liquid Crystals**

The term "liquid crystal", much like the name suggests, refers to the phase of a material which is capable of displaying both properties of crystals and liquids; more specifically, in certain mesophases, or intermediate phases between the crystalline and liquid states, they exhibit orientational and/or positional ordering characteristic of crystals combined with the flow behavior of liquids [51,52]. Since their initial discovery in the 1880's by the Austrian botanist Friedrich Reinitzer, who noticed that a cholesterol derivative unusually showed two "melting points" upon heating (the first to a turbid liquid phase; the second to a clear, oil-like liquid) and particularly with the development of what would become one of the most studied synthetic liquid crystal materials (5CB) by George Gray in the 1960's [1], liquid crystals have become ubiquitous in our daily lives. The most prominent uses of liquid crystals are in display applications [1,53,54], but they have also been known for their use in thermometers for several decades. More recently, explorations of their capabilities of biological and chemical sensing due to their high degree of sensitivity, the rapid responses to the environment around them, and their anisotropic properties which lead to striking visual textures have become increasingly common [4,5,8–11,55–58].

### 2.1.1 Liquid Crystal Classes and Varieties

The two broadest groupings of liquid crystal materials are *thermotropic* liquid crystals, where the occurrence of mesophases is temperature-dependent, and *lyotropic* liquid crystals, where the presence of mesophases is additionally concentration-dependent [59]. Lyotropic phases are typically formed from amphiphilic molecules, such as surfactants, where the molecule itself does not form a liquid crystal phase, but instead assembles into aggregates from which the liquid crystal phase is formed. *Chromonic* liquid crystals, while functionally a subset of lyotropics, form another category of liquid crystal, where the aggregates are formed from assemblies of molecules (such as the stacking of discs into rods) [60,61]. Liquid crystalline phases can also be formed from colloidal assemblies of particles with significant shape anisotropy, often called *colloidal liquid crystals* [62]. While similar in principle to the idea of lyotropics, where the formation of a liquid crystal phase is concentration-dependent, colloidal liquid crystal phases are purely concentration-dependent and are not formed from amphiphiles, with common model phase generators including the tobacco mosaic virus [51] and cellulose nanocrystals [63].

While the realm of liquid crystals is broad and diverse, the liquid crystals used in this work are mostly thermotropic rod-shaped (or calamitic) materials, either pure components or a mixture of components.

### 2.1.2 Liquid Crystalline Phases

Liquid crystal mesogens, or the molecules that can form liquid crystal phases, are characterized by the kinds of mesophases they exhibit and under what conditions these mesophases arise [52,64]. Within the grouping of thermotropic rod-shaped liquid crystals, the most commonly-encountered mesophases are the *nematic* phase (from Greek *nýma*, or "thread", referring to the thread-like disclination lines visible in polarizing optical microscopy), where the molecules align with long-range orientational order without a corresponding positional order, and the *smectic* phase (from Latin *smecticus*, or "soap", referring to the structures being similar to those found in soap films), where the molecules additionally align in layers, producing a two-dimensional fluid where molecules can flow freely within the layers, but not across them. These mesophases are represented graphically in Figure 1, but they are far from the full spectrum of the possible liquid crystal mesophases [52].

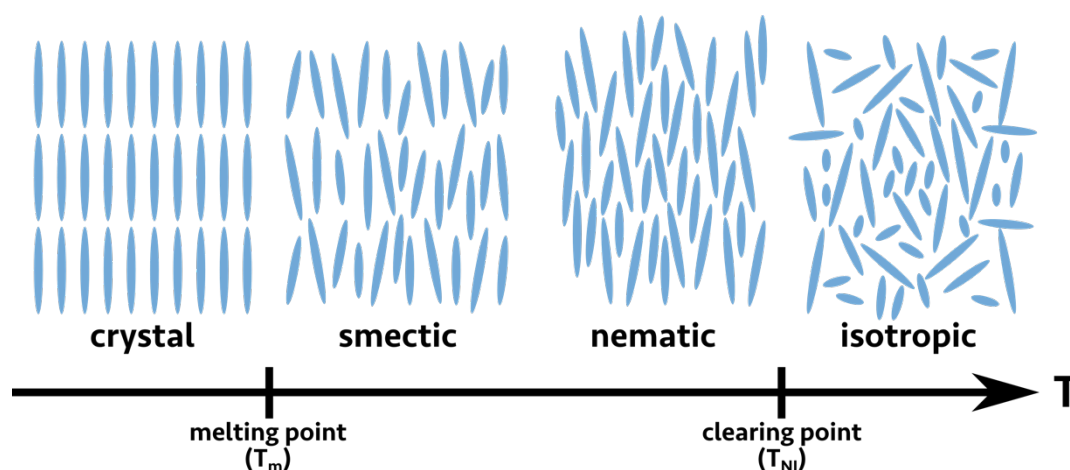


Figure 1. A diagram of the mesophases of common thermotropic liquid crystal phases consisting of rod-shaped molecules, with the two "melting points" (the solid-liquid melting point and the nematic-isotropic "clearing point") indicated. Nematic phases show a long-range orientational order of the molecules, while smectic phases additionally show positional ordering by their arrangement into layers.

Not all molecules are capable of forming liquid crystal mesophases: as previously mentioned, a molecule needs to possess a significant shape anisotropy, such as that of a rod [52], disc [65], banana [66,67], or pear [68], in order to show liquid crystalline phase behavior, and that anisotropy has to be considerable. For example, out of the cyanobiphenyl series of molecules, 5CB (4-cyano-4'-pentylbiphenyl), with a five-carbon aliphatic tail, is the shortest capable of producing a liquid crystal phase alone. Additionally, not all molecules that can display a liquid crystal phase display all possible liquid crystal phases: for example, in the cyanobiphenyls, 8CB (4-cyano-4'-octylbiphenyl), with an eight-carbon tail, is the shortest for which a smectic phase is attainable [69].

*Cholesteric*, or chiral nematic, phases, are formed from either an inherently chiral molecule or by doping an achiral liquid crystal "host" with a chiral dopant [23,70], often with a structure very similar to the host liquid crystal it is dissolved into. When well aligned, the helical structure that self-organizes in a cholesteric liquid crystal, with adequate helix pitch, gives rise to striking reflected colors that are not purely a function of birefringence, but additionally due to Bragg reflection of light from the helical structure. The wavelength of light reflected from a cholesteric is a function of the helical pitch of the structure [50,71].

### 2.1.3 Alignment and Anisotropy of Liquid Crystals

In nematic and smectic phases, the average direction along which the mesogens are oriented is described by a unit pseudovector called the *director*, typically denoted by  $\hat{n}$ . The director points along the principal axis of symmetry of the phase. For rod-shaped mesogens, the molecular long axis aims to orient along the director; in the case of a disc-shaped mesogen, though, the short axis of the molecule will strive to align with the director. To quantify how well ordered a liquid crystal material is (that is, how well the axes of symmetry of the liquid crystal molecules themselves

are aligned with the director), there are several different order parameters that can be used. The most often used for simple uniaxial systems is the scalar order parameter, commonly represented by  $S$  (but denoted in this work by  $S_N$  to avoid confusion with entropy, which is often noted as  $S$ ), which defines an order parameter based on the average orientation of all polar angles  $\vartheta$  with respect to  $\hat{n}$  [51,69,72]:

$$S_N = \frac{1}{2} \langle 3 \cos^2 \vartheta - 1 \rangle \quad (2.1)$$

The interval of this parameter is  $S_N \in \left[-\frac{1}{2}, 1\right]$ , with  $S_N = 0$  indicating a complete lack of orientational order;  $S_N = 1$  indicating that all of the molecules are perfectly aligned in a single direction, most likely in a crystal; and  $S_N = -\frac{1}{2}$  a case where *none* of the long axes of the liquid crystal molecules are pointing in the director direction [51,72,73]<sup>a</sup>. Typically, for a nematic liquid crystal such as the materials used here, the value of the scalar order parameter is between 0.4 and 0.7 [51].

Depending on how the director of the liquid crystal is arranged, the overall material may have substantially different properties. In general, we can distinguish between two principal anchoring configurations: *homeotropic*, where the director orients normally to an interface, and *planar*, where the director is instead parallel to the same. Air, for example, will generally produce homeotropic anchoring for most common liquid crystal materials, while water and untreated borosilicate glass will both induce planar anchoring [5,8,9]. Similarly, the presence of an amphiphile, such as a surfactant, will force a liquid crystal to adopt a homeotropic alignment [8,74,75]. The condition for planar anchoring, absent treatment or a stimulus, however, is degenerate [76], with the liquid crystal alignment not favoring a particular direction or orientation. Thus, in order to force an alignment of a liquid crystal into a specific direction, the substrate can be treated either by rubbing an alignment layer, commonly of a polymer such as a polyimide, or by another means of inducing uniform alignment such as the use of carbon nanotube sheets [20,77].

These are, of course, the ideal cases of liquid crystal alignment, but these are not always present for a number of reasons: topological constraints and uneven anchoring conditions can both distort the liquid crystal director field. There is a cost to this inhomogeneity in the director configuration, as described by the Oseen-Frank elastic deformation energy equation [78,79]. This equation links the free energy density in the bulk of a liquid crystal sample,  $f_d$ , with elastic deformations, which can be described with three fundamental types of bulk director distortions:

$$f_d = \frac{1}{2} \left[ k_{11} (\vec{\nabla} \cdot \hat{n})^2 + k_{22} (\hat{n} \cdot (\vec{\nabla} \times \hat{n}) - q_0)^2 + k_{33} (\hat{n} \times (\vec{\nabla} \times \hat{n}))^2 \right] \quad (2.2)$$

These three distortions are *splay* (given by  $k_{11} (\vec{\nabla} \cdot \hat{n})^2$ ), *twist* ( $k_{22} (\hat{n} \cdot (\vec{\nabla} \times \hat{n}) - q_0)^2$ ), and *bend* ( $k_{33} (\hat{n} \times (\vec{\nabla} \times \hat{n}))^2$ ), with  $k_{11}$ ,  $k_{22}$ , and  $k_{33}$  being the respective elastic deformation constants corresponding to each of these distortions and  $q_0$  in the twist

---

<sup>a</sup>While long treated as a curiosity [51], some recent work on making elastomeric materials from liquid crystals has produced materials displaying a negative order parameter. [72,73]

term corresponding to the pitch wavenumber ( $q_0 = 2\pi/p_0$ , where  $p_0$  is the equilibrium pitch of the structure; for an achiral nematic,  $q_0 = 0$  as  $p_0 = \infty$ ). Schematics of these director configurations are presented in Figure 2.

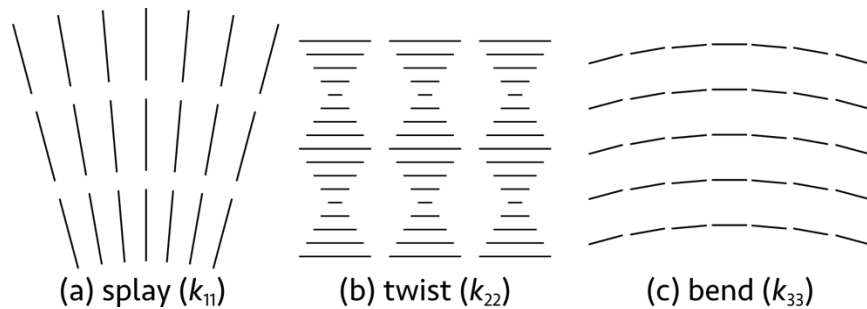


Figure 2. Schematic of the three common bulk deformations of the liquid crystal director: (a) splay, (b) twist, and (c) bend. As the director is a pseudovector, we can denote the director field with lines.

A proper treatment of the elastic energy density includes consideration of an additional *saddle-splay* deformation constant ( $k_{24}$ ), which describes the case when the director field has both positive and negative principal curvatures, but this term is often negligible in large samples where surface effects are minimal compared to the bulk [69,78,80].

For most calamitic liquid crystals, the bend deformation elastic constant ( $k_{33}$ ) is the highest, followed by the splay constant ( $k_{11}$ ) and lastly the twist elastic constant ( $k_{22}$ ), which is often much smaller than the splay constant [78,81,82].<sup>b</sup>

In not all geometries, however, can the alignment of liquid crystals be defined in all positions, and the points where the director is undefined (and the order parameter is zero) are called *defects* [51,69]. Defects are topological features that arise from constraints either imposed by a surface or by the bulk geometry and can manifest themselves in a number of ways, such as in point defects and line defects [51,69,83,84]. In many cases, defects are not desirable, as they can negatively affect the performance of devices where alignment is critical, but they have shown uses in some applications, such as in directing the self-assembly of structures [85], and are the backbone behind the structures of blue phases [55,86], which are optically-anisotropic liquid crystal phases that form from a "lattice" of defects.

Defects are characterized by their "strength", sometimes also called "topological charge", a quantity that describes how deformed the director is about the defect core. The charge is defined as how many times the director rotates within a  $360^\circ$  segment running counterclockwise around the defect: if the director rotates counterclockwise by  $+360^\circ$ , such a defect has a strength of  $+1$ . A selection of some defect configurations is presented in Figure 3. Since the director is a pseudovector,

---

<sup>b</sup>In discotic liquid crystals, on the other hand, the splay elastic energy is normally higher than the bend elastic energy, as this is due to how the deformations are defined with respect to the deformation of the director and not simply from the molecular orientation.

the admissible defect strengths are all integer multiples of  $\frac{1}{2}$ ; were it to be a proper vector, then only integer defect strengths could be present. [51]

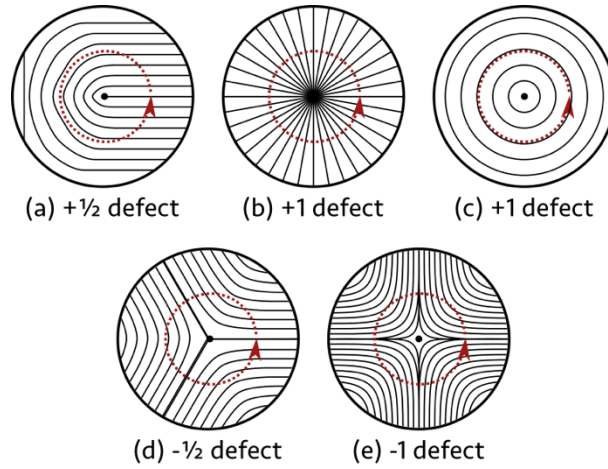


Figure 3. A selection of surface liquid crystal defects with topological charges of (a)  $+\frac{1}{2}$ ; (b) and (c)  $+1$ ; (d)  $-\frac{1}{2}$ ; and (e)  $-1$ . This list is far from exhaustive.

The configuration of defects present on a self-closing, continuous surface with planar orientation is dictated by the Poincaré-Hopf theorem, which provides that the total topological charge of defects in a vector (or pseudovector) field on a closed surface is equal to that surface's Euler characteristic [51,87]: for a sphere, this means that the total charge should equal  $+2$ , normally in the form of two  $+1$  defects or four  $+\frac{1}{2}$  defects. Defects show interactions with each other similar to the behavior of electrical charges, where two defects of the same magnitude of charge will repel each other and two defects of opposite charge will attract and eventually annihilate.

Compared to the case of defects on a surface, within the bulk of a liquid crystal, the picture looks different. While the description of the surface charge is applicable for the case of a boundary with planar alignment, where the Poincaré-Hopf theorem applies to the liquid crystal orientation on the surface, the director orientation at a homeotropic boundary is different. Gauss' theorem says that, with purely homeotropic alignment around a sample with spherical topology, there should be a defect at the core of a three-dimensional object (called a "hedgehog") [87].

While cholesteric liquid crystals also are aligned by surfaces and the differing anchoring conditions, the resultant textures are very different. In the presence of a planar-aligning substrate, the result, provided the pitch of the cholesteric is in an appropriate range, is a uniformly colored reflection; with homeotropic alignment, however, what arises is instead a "fingerprint" texture (visible assuming that the helical pitch is not shorter than the visible light spectrum) that comes from the presence of helical modulation where the helix axis lies parallel to the surface rather than normal to it [21,76].

There exists a wide array of properties of liquid crystals that show orientation dependence. These include the viscosity [64,88], where the viscosity is lower for flows along the director (as detailed by Mięsowicz [89]); the interfacial tension [46], which results in specific configurations of alignment of the liquid crystal at an

interface; and the magnetic and dielectric susceptibilities, which, in turn, additionally give rise to anisotropic refractive indices [64,90]. The anisotropic refractive indices give rise to many of the optical properties of liquid crystals.

#### 2.1.4 Liquid Crystal Optics

One of the most notable properties of liquid crystal phases that lends itself to their use in display applications is their birefringence, or double refraction. Birefringence arises any time there are multiple refractive indices in a sample that arises from molecular anisotropy, whether as a result of a crystal lattice structure or from the molecule structure itself in combination with the long-range orientational ordering of the molecules. Using Snell's Law for refraction at an interface ( $\frac{n_1}{n_2} = \frac{\sin \theta_1}{\sin \theta_2}$ , where  $n_1$  is the refractive index and  $\theta_1$  the angle of incidence with respect to the normal from one side of the interface and  $n_2$  and  $\theta_2$  the refractive index and angle of incidence on the other side of the interface), if there are two different refractive indices for a material, each will correspond to a different angle of refraction and, thus, a different optical path taken through the sample. With a given incident wave, light with incident polarization perpendicular to the optical axis is refracted differently to the light with incident polarization parallel to the same. Figure 4 shows a schematic representation of birefringence for incident light containing both polarizations.

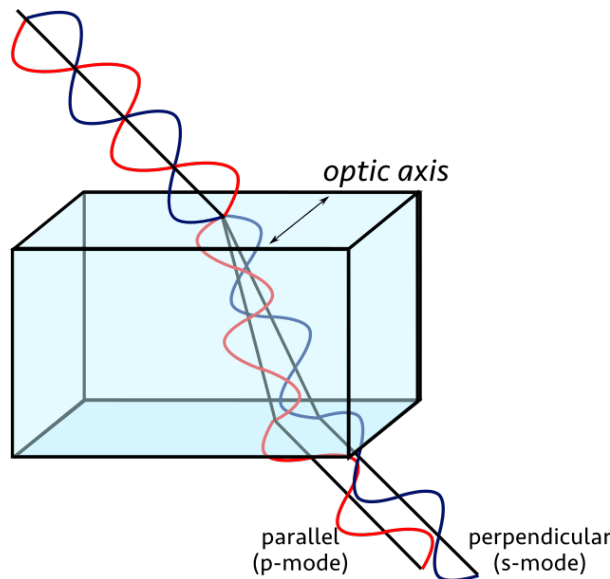


*Figure 4. Schematic representation of birefringence through a sample, where components polarized perpendicularly and parallel to the optic axis are refracted differently. The difference between the two refractive indices will dictate which component of light is refracted more.*

Taking a uniaxial liquid crystal phase from rod-shaped molecules as an example, this asymmetry causes light to propagate differently along the director as opposed to across it. Macroscopically, this then translates into two distinct indices of refraction, each corresponding to the different modes of propagation [91]. While birefringence was initially observed for solid crystal samples [92], anything with an



axial or crystal group anisotropy, such as well-aligned polymer films [93,94] and liquid crystals [53,69,90], is capable of exhibiting birefringence.

Numerically, birefringence (denoted by  $\Delta n$ ) is simply defined as the difference between the two indices of refraction. For a uniaxial liquid crystal substance, these two indices are  $n_{\perp}$ , the refractive index for polarizations of light perpendicular to the director, and,  $n_{\parallel}$ , which is for light polarized along the director (which is equivalent to the optic axis of the liquid crystal). This means we then define the birefringence as simply the difference between the two refractive indices:

$$\Delta n = n_{\parallel} - n_{\perp} \quad (2.3)$$

While observed in different forms by earlier scientists, the relationship of birefringence to observed color was shown for the first time in a consolidated form by the French geologist Auguste Michel-Lévy in 1888 [92]. In this work, he presented the first version of the interference color chart, commonly called the Michel-Lévy diagram and presented in Figure 5, relating birefringence and sample thickness, thus the optical path difference, to the colors of light seen between crossed polarizers.

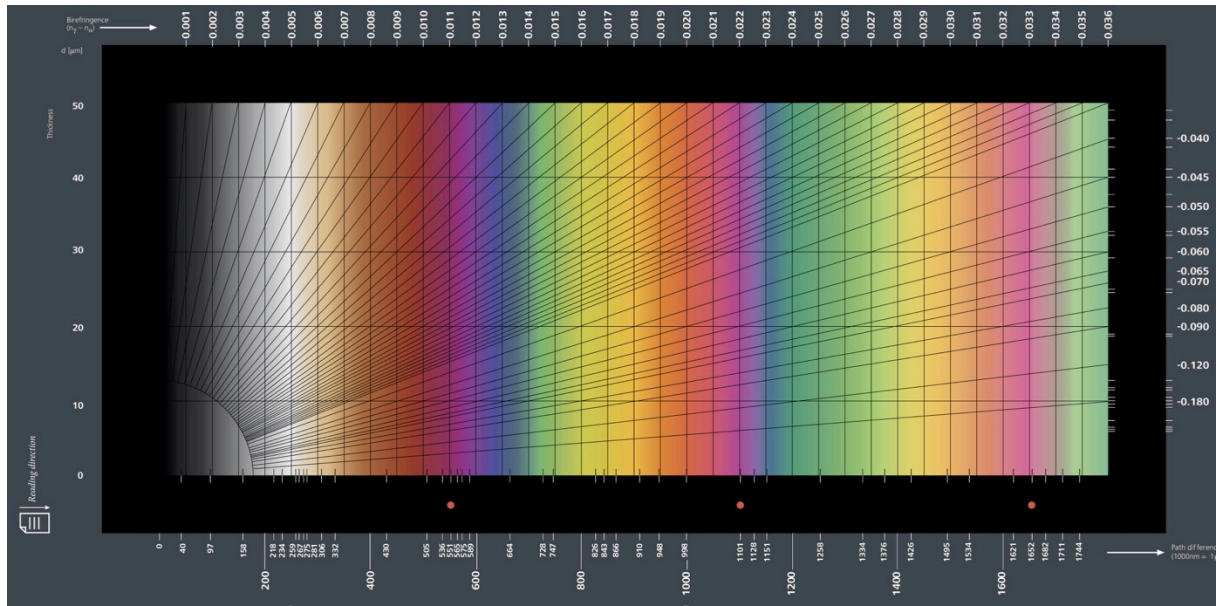


Figure 5. A modernized version of the Michel-Lévy birefringent color chart. This chart relates color to the optical path difference, which is in turn a function of the product of sample thickness and birefringence  $\Delta n$ . Adapted from an image by Carl Zeiss GmbH (<https://www.flickr.com/photos/zeissmicro/21257606712/>) and used under a Creative Commons License.

Because the effective indices of refraction of a liquid crystal are orientation-dependent [64], we can visualize the orientation and arrangement of the liquid crystal director based on the presence (or absence) of birefringence between crossed linear polarizers. If, for example, light propagates along the director, then there is no resulting birefringence and, consequently, the liquid crystal would appear uniformly dark. If the liquid crystal is not uniformly homeotropic (either with planar alignment, a hybrid alignment with planar at one interface and homeotropic at the



other, or with an intermediate orientation), then the liquid crystal molecules will affect the polarization of light, thus leading to the sample appearing bright when the liquid crystal is viewed between crossed linear polarizers or circular polarizers of opposite handedness [21,75,95].

When polarized light is transmitted along a direction orthogonal to the optic axis through a birefringent medium of thickness  $d$ , light with wavelength  $\lambda$  will undergo a phase shift ( $\Delta\psi$ ), which we can define as [69]:

$$\Delta\psi = \frac{2\pi d \cdot \Delta n}{\lambda} \quad (2.4)$$

This phase shift then corresponds to an optical path difference,  $\Delta\Lambda$ , between the two refracted polarization modes.

$$\Delta\Lambda = \Delta\psi \cdot \frac{\lambda}{2\pi} = d\Delta n \quad (2.5)$$

The phase shift leads to an output of elliptically-polarized light from the birefringent material, where the output ellipticity is dependent on the magnitude of this optical path difference [96]. (Both linearly- and circularly-polarized light are special cases of elliptical polarization: in the former, with linearly-polarized incident light, this happens where  $\Delta\Lambda$  is an integer multiple of  $\lambda/2$ , and in the latter, when  $\Delta\Lambda$  is an odd integer multiple of  $\lambda/4$ , eg.  $\Delta\Lambda = \lambda/4, 3\lambda/4, 5\lambda/4 \dots$ )

An achiral planarly-aligned liquid crystal sample viewed between crossed linear polarizers (where the polarizer axes of the two elements are orthogonal to each other) will show brightness dependent on the orientation of the liquid crystal with respect to the polarizer axis: if the liquid crystal director lies parallel to either of the polarizer axes, no light is transmitted through the sample, as incoming light only encounters a single refractive index. The light intensity  $I$  transmitted by a liquid crystal sample between two polarizers, oriented such that its director is at an angle  $\phi$  with respect to the analyzer (second polarizer for outbound light), is described by [69]:

$$I = \frac{1}{2} \sin^2 2\phi \sin^2 \frac{\pi \cdot \Delta n \cdot d}{2\lambda} \quad (2.6)$$

As seen by this equation, transmittance is at a maximum when the director is at  $45^\circ$  with respect to both the polarizer and analyzer and when the phase shift term is  $90^\circ$  (or, equivalently,  $\Delta\Lambda = \lambda/2$ ). This is schematically represented in Figure 6.

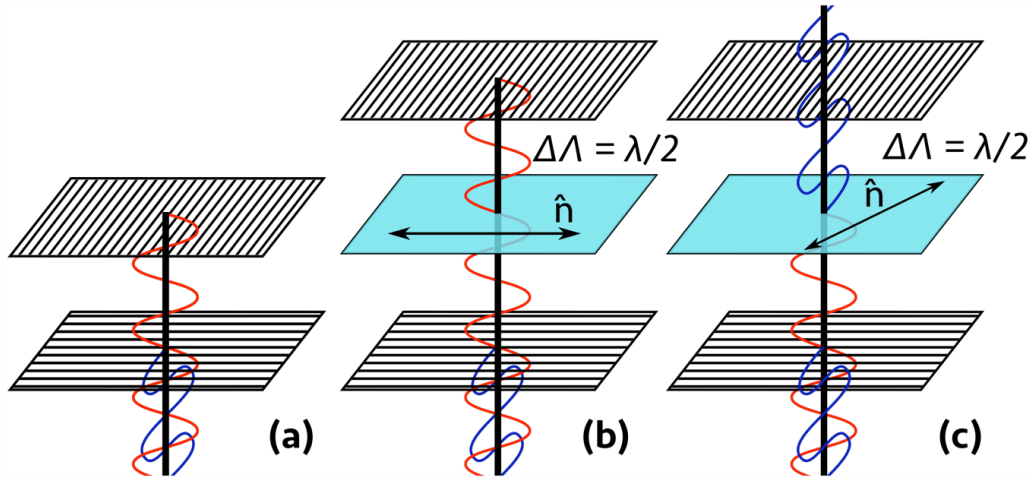


Figure 6. Illustration of the transmission of light through crossed polarizers and a liquid crystal element with an optical path difference  $\Delta\Lambda$ . (a) Without a liquid crystal element to modulate the linearly-polarized light after the first polarizer, no light is permitted through the second polarizer (analyzer). (b) When a liquid crystal element is present, but whose director lies along either the polarizer or analyzer axis, the polarization is unaffected; thus, no light is allowed through the analyzer. (c) If the liquid crystal is oriented at  $45^\circ$  with respect to the analyzer (and the polarizer) and the sample thickness is sufficient, then this is the maximum brightness condition: the incoming light has components both parallel and perpendicular to the optic axis of the liquid crystal, allowing its birefringence to change the polarization state such that, unless the optical path difference happens to be a multiple of the wavelength, at least some light passes through the analyzer. If the optical path difference is exactly  $\lambda/2$ , then the polarization is mirrored in the optic axis and the full light intensity after the first polarizer is also able to exit through the analyzer. The wave and the liquid crystal element are not to scale.

An achiral nematic liquid crystal will allow all wavelengths of light to pass through, albeit with different degrees of phase shift for each component wavelength. Cholesteric liquid crystals, however, exhibit a band gap for the circular polarization with the same handedness as the helix, an interval where incident light of the correct handedness between two specific wavelengths is reflected rather than transmitted through the material [69] due to the refractive index being imaginary and transmission of light being forbidden, while light of the other handedness is transmitted unobstructed. This interval is described by

$$\lambda \in (n_{\perp}p, n_{\parallel}p) \quad (2.7)$$

where  $p$  is the cholesteric pitch. As pitch is sensitive to both temperature and chiral dopant concentration, this allows the bandgap, in turn, to be shifted and for the cholesteric to be tunable by either of these parameters. Unlike the eigenmodes of an achiral nematic, which are linearly polarized, the eigenmodes corresponding to both transmission through and reflection from a cholesteric (or from any helical structure) are instead circularly-polarized [53,69,97].

For a given cholesteric material, the reflected color is tunable by adjusting the concentration of chiral dopant present, with higher concentrations of dopant decreasing the helical pitch, thus blueshifting the reflected light. An example of

such colors obtained from a prepared mixture of a cholesteric liquid crystal is presented in Figure 7.

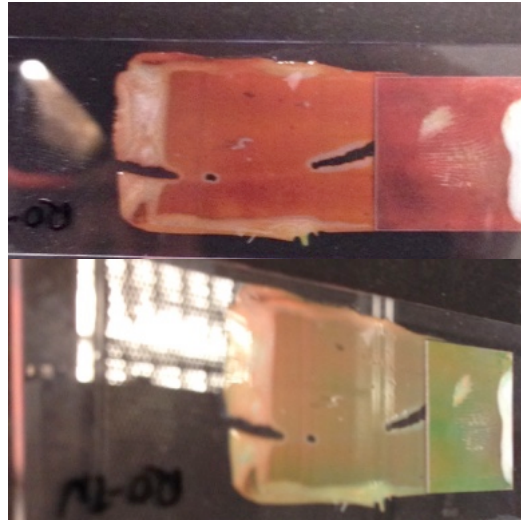


*Figure 7. Cholesteric liquid crystal phase prepared from the nematic liquid crystal mixture RO-TN 615 (Hoffmann-La Roche) with 25% w/w chiral dopant ZLI-3786. If viewed with normal incidence, as seen in the top image, the sample reflects strongly in the red region; with an oblique viewing angle, the color is blueshifted.*

This blueshifting of observed reflected color by changing the angle of viewing, as mentioned, is due to Bragg reflection, which describes the reflection of light from a periodic structure. Light reflected from the periodic structure is either constructively or destructively interfered, but we consider the case of constructive interference. Constructive interference conditions are met for all wavelengths of light which satisfy the Bragg reflection condition:

$$\lambda = 2p \cos \vartheta \quad (2.8)$$

where  $\vartheta$  is the angle of incidence of light with respect to the helix axis (the sample normal in a flat film) [71]. This results in an angle-dependent shift of the reflected color, as schematically presented in Figure 8 and as demonstrated in Figure 7.

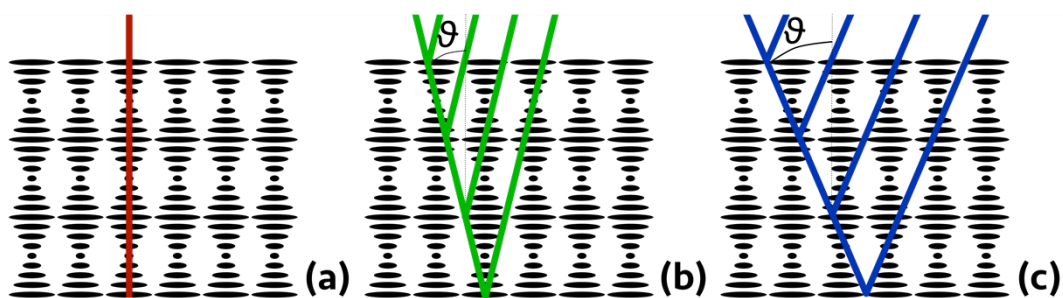


Figure 8. Schematic of Bragg reflection from an aligned cholesteric liquid crystal. When light is incident normal to the surface, the light reflected has a wavelength equal to the cholesteric pitch. As the angle of incidence  $\theta$  with respect to the surface normal increases, the wavelengths of light that satisfy the Bragg condition decrease, thus blueshifting the reflected light.

## 2.2 Polymers

As suggested by its name, a polymer is a material consisting of a repeated functional unit, termed a *monomer*. To be classified as a polymer as opposed to an oligomer, the number of repeating units should be substantial, with the smallest chains termed "polymer" starting from chains on the order of  $10^2$  repeating units (with smaller chains being termed *oligomers*), though there is no clear demarcation between an oligomer and a polymer. While it is commonplace to use "polymer" as shorthand for certain kinds of plastic materials, such as when describing banknotes, polymers are actually much broader in scope and appear all throughout nature, from the basic foundation of genetics and life (deoxyribonucleic acid, ribonucleic acid, and proteins) to what we wear and use on a daily basis (such as cellulose, polyacrylamides, nylons, and rubbers) going up to materials that save lives (such as Kevlar and nylon).

### 2.2.1 Polymer Structure and Function

Unless a specific material has a trade name (such as nylon or Kevlar), polymer nomenclature classically refers to the repeating monomer unit (and not the simplest repeating unit). For example, polybutadiene, one of the elastomers used in this work, is a polymer of buta-1,3-diene; despite what the name suggests, however, the polymer does not have two double bonds remaining in the repeating unit as one of them was reacted during the polymerization reaction. The repeating monomer unit is usually a clue as to how a polymer is synthesized (using the example of polybutadiene, it is, indeed, synthesized from butadiene monomers), but there are notable exceptions, such as poly(vinyl alcohol), which is normally fabricated through hydrolysis of poly(vinyl acetate) rather than direct synthesis from vinyl alcohol monomers. Polymers are synthesized either through addition reactions, which build a molecule linearly, or condensation reactions, which react two units (either monomers or oligomers) into a single product.

How the resultant polymer is arranged can be modeled in a number of ways, with one of the simplest models being the ideal chain (sometimes also called a random

walk distribution) [51,98]. In this description, a polymer is described as a long chain of segments, each of which is oriented randomly without interacting with or being affected by any of its neighbors. While there are many possible polymer configurations for a given chain, the radius of the most probable configuration of a polymer chain, and thus its effective size, is normally defined by the *radius of gyration*,  $r_G$ :

$$r_G = l \cdot \sqrt{\frac{N}{6}} \quad (2.9)$$

where  $N$  is the number of monomers and  $l$  the effective monomer size. Due to entropy, conformations corresponding to the radius of gyration are among the most probable states for the polymer to be in absent external stimuli (due to the probability distribution of microstates).

The total mass of a polymer is termed its *molecular mass* or *molecular weight*, but, since polymerization is rarely uniform, it is common to report the weight-averaged molecular weight ( $M_W$ ) and the number-averaged molecular weight ( $M_N$ ). These are defined as

$$M_N = \frac{\sum N_i M_i}{\sum N_i} \quad (2.10)$$

$$M_W = \frac{\sum N_i M_i^2}{\sum N_i M_i} \quad (2.11)$$

where  $M_i$  is a given molecular weight and  $N_i$  is the number of molecules corresponding to that weight. The ratio of the two is the *dispersity*, sometimes called *polydispersity* ( $\mathfrak{D} = M_W/M_N$ ), which tells how uniformly distributed the molar mass is between the polymer chains present: a dispersity close to unity says that the polymer chains are all fairly uniform, while values much larger than unity say that there is considerable variance in polymer chain size. (Because the weight-averaged molecular weight is always larger, the minimum value of dispersity is 1.)

The longer the chain, the more likely a polymer is to not behave like an ideal coil and, instead, to form *entanglements*. The ideal chain assumes that a polymer is free to move in all dimensions and directions, but entanglements from other chains are an impediment to this [99]. Entanglements will be present in a concentrated solution or polymer melt provided that the constituent polymer is larger than the entanglement weight  $M_e$ . One of the outcomes of this is that an entangled polymer, whether in solution or a melt, can only flow out of the entangled state in a process known as *reptation*, where the polymer is limited to motion along its length (much how a snake slithers). The time for reptation to fully occur and the polymer to flow relates to the weight of the polymer [99]: if the polymer weight is low compared to the entanglement weight ( $M_w < M_e$ ), the relaxation time scale is on the order of  $\tau \sim M_w$ . Highly entangled polymers, however, relax on timescales  $\tau \sim M_w^{3.4}$  (which, in turn, scales the viscosity with a similar relationship). The main effect of this is

that, for highly entangled polymers, over "short" time scales, we can treat the material as though it were solid-like<sup>c</sup>.

The structure of a polymer in terms of the repeating units has a drastic impact on its physical properties. The main properties that affect function are related to packing, or how ordered the polymer chains are with respect to each other. For example, when a polymer has a propensity for hydrogen bonding or other dipole-dipole interactions, a structure results that shows high resistance to stress and strain. An example of this can be found in polyacrylamides (nylons), a class of polymers formed either by a condensation reaction of a dicarboxylic acid or acid dihalide with a diamine [100] or by a ring-opening polymerization of a cyclic amide. A representative polymer, nylon-6 (polycaprolactam), is formed from a ring-opening polymerization of caprolactam induced by high temperatures and an inert atmosphere. The strong intermolecular interactions (in the case of nylon-6, arising from hydrogen bonds with the amide groups) between the polymer chains help to promote ordered packing, which results in crystallinity from the dipole-dipole interactions and high tensile strength.

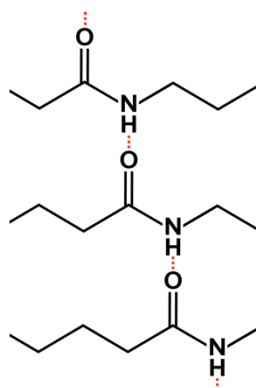


Figure 9. Example of the hydrogen bonding between the amide groups of nylon chains, which promote semicrystallinity and improve the tensile strength of nylon.

Another example of structure being related to function is the case of polyisoprene. This polymer has four isomers, of which the two isomers of 1,4-polyisoprene are of interest for this work. These isomers are presented in Figure 10.

---

<sup>c</sup>One way to characterize how a polymer flows over the timescale of an experiment is the dimensionless *Deborah number* ( $De$ ), which relates relaxation time to observation time  $t_{exp}$  ( $De = \tau/t_{exp}$ ). If  $De > 1$ , then we can assume the material to be solid-like over the duration of the experiment; for  $De < 1$ , the material is liquid-like over the observation timescale. We assume here that, due to the scaling of the relaxation time by  $M_w^{3.4}$ , our observation times fall under high  $De$  number regimes and that we can assume our polymer to remain solid-like throughout the experiment and subsequent observation.

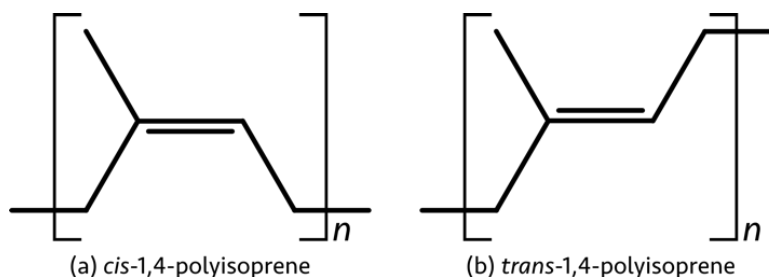


Figure 10. The two isomers of 1,4-polyisoprene: (a) the *cis* isomer, which is a component of natural rubber; and (b) the *trans* isomer, which instead is a component of the rigid thermoplastic gutta-percha.

The *cis* isomer is a component of natural and synthetic rubbers, with the formation of a lattice structure impeded by the hindrance of chain packing. The absence of close packing reduces the crystallinity of the resulting polymer, which results in a considerable increase in stretchability and deformability. On the other hand, the *trans* isomer of 1,4-polyisoprene readily crystallizes, as its structure allows for close and regular packing of the polymer chains in a regular lattice. The most common application of the *trans* isomer of polyisoprene is in gutta-percha, a latex used as a thermoplastic.

### 2.2.2 Polymers in Solution: The Good, the Bad, and Theta

The presence of any interface has an energy cost associated with it, and polymers in solution are no exception. Because we are preparing fibers from polymer solutions, the interactions of a polymer with solvent are essential. For a given polymer in solvent, we can distinguish between three cases:

- In the case of a *good solvent*, interactions between the solvent molecules and the polymer chain are favorable, more than interactions of the polymer chain with itself are. These interactions cause the polymer chain to swell, increasing its effective size with a shell of solvent molecules due to excluded volume interactions (space where other polymer chains are not permitted to enter).
- For a *poor solvent*, the interactions between solvent and polymer are much less energetically favorable than polymer-polymer interactions. This results in the polymer contracting into globules rather than evenly dispersing and often resulting in sedimentation and creaming. A poor solvent is often also referred to as a nonsolvent.
- The case of a *theta solvent* is where a polymer displays ideal chain behavior, with both solvent-polymer and polymer-polymer interactions being equally favorable. Theta conditions for a polymer-solvent system are very narrow, requiring both a specific solvent and a very specific temperature under which theta conditions are present: for example, PVP has a theta temperature in water of 130.5°C [101].

Concentration additionally plays an important role in the behavior of a polymer in solution: the higher the concentration of polymer and the higher the polymer molecular weight, if the weight is above a critical entanglement mass, the greater the number of entanglements of the polymer chains with each other. As a polymer chain is constrained from crossing or overlapping with other chains, the polymer

can only become disentangled through reptation [102,103]. The practical effect of this is that, if either the concentration and/or the polymer mass is high with respect to the entanglement weight, the time necessary to fully dissolve the polymer greatly increases and the viscosity of the resultant solution is quite high, often increasing nonlinearly with polymer concentration [104], and even in a "good" solvent.

Polymer solutions show particular flow behavior under shearing, where a typical behavior is for the polymer solution viscosity to decrease under shearing. This is called *shear-thinning* behavior and results from the polymer chains becoming more readily disentangled under shearing. Shear-thinning fluids are part of the broader category of *non-Newtonian fluids*, which refer to fluids with a shear-dependent viscosity, either increasing (shear-thickening), decreasing (shear-thinning), or with a high initial shear needed to begin to induce a deformation (Bingham plastics) with an otherwise linear viscosity. The strain-stress curves for representative fluids are shown in Figure 11.

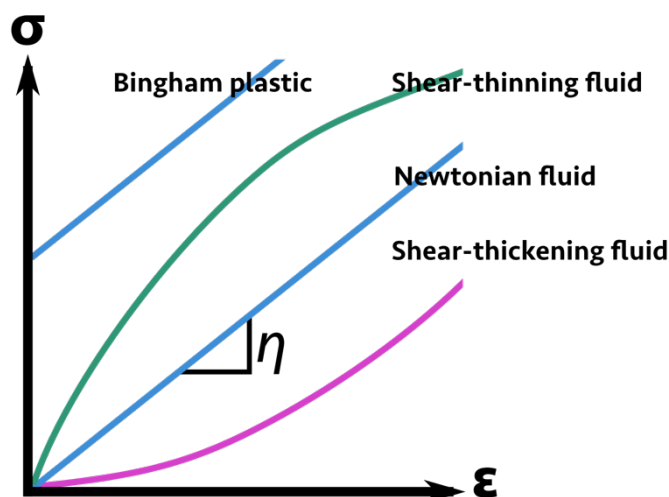


Figure 11. Curves relating polymer strain ( $\epsilon$ ) to stress ( $\sigma$ ) applied for a variety of different kinds of fluids (shear-thinning, shear-thickening, and Newtonian fluids and Bingham plastics). The derivative of the curve is the viscosity,  $\eta$ : this is constant for a Newtonian fluid, but increasing with an increasing strain for a shear-thickening fluid and decreasing with increasing strain for a shear-thinning fluid.

### 2.2.3 Polymer Flow and Viscoelasticity

In the "solid state", below the melting temperature  $T_m$ , high-weight, entangled polymers can either be hard and brittle or soft and rubbery. The boundary between these two is the *glass transition temperature*,  $T_g$ . Below the glass transition temperature, a polymer will be in a glassy state, a kinetically-arrested amorphous solid which is hard and brittle.

For temperatures between  $T_g$  and  $T_m$ , if the polymer is of a sufficient weight, the polymer is instead rubbery, showing a viscoelastic response to stress [51]. This manifests itself as a combination of viscous behavior, where the polymer "flows" under the applied stress and the work applied to the system is dissipated (either through stress relaxation or creep), and an elastic response, where, upon release of



the stress, the polymer will revert to its original configuration (much like a spring) and the work performed is not dissipated in the material [51]. In the polymers that will be used in Chapters 4 and 5, PVA typically has a glass transition temperature of 85°C [105], meaning we will deal with it in a glassy form; both polybutadiene and polyisoprene, however, have glass transition temperatures of -70°C or below [106,107], meaning that they are viscoelastic at room temperature.

Over short time scales, a polymer can be treated like an elastic material, with its response modeled like an elastic spring with spring constant  $k = \frac{3k_B T}{Nl^2}$ . [98] When we stretch a polymer, we necessarily need to apply work to disturb it from its equilibrium configuration; this will be further expounded on in Chapter 4 for the stretching of elastomers. For a polymer molecule in a given configuration (with a radius  $r$ ), we can describe the polymer chain entropy as [98]:

$$S = -\frac{3}{2}k_B \frac{r^2}{Nl^2} + S_0 \quad (2.12)$$

with  $k_B$  being Boltzmann's constant<sup>d</sup>. The change in entropy upon stretching a polymer between two lengths, from  $r_1$  to  $r_2$ , is thus:

$$\Delta S = -\frac{3}{2} \frac{k_B}{Nl^2} (r_2^2 - r_1^2) \quad (2.13)$$

Knowing that heat is defined as  $q = T\Delta S$ , if we stretch the polymer, we can assume that work is the only energy source; thus, upon stretching from two states, we find

$$\begin{aligned} W &= \int_{r_i}^{r_2} \vec{F} \cdot d\vec{r} = - \int_{r_i}^{r_2} k\vec{r} \cdot d\vec{r} = -k(r_2^2 - r_1^2) \\ &= -\frac{3}{2} \frac{k_B}{Nl^2} (r_2^2 - r_1^2) \end{aligned} \quad (2.14)$$

which means that our polymer can be modeled as an entropic spring, meaning the energy put into the system will be translated into heat (as can be seen when a rubber band heats upon stretching).

To improve the resilience and strength of polymers (and especially elastomers) and to prevent them from flowing over time, permanent cross-links between the polymer chains can be created through a number of processes, such as light-induced crosslinking [108,109], with or without an initiator, or other chemical reactions (such as oxidation). For rubbers in particular, the primary process used is vulcanization [110], where the elastomer is heated in the presence of sulfur or a sulfurous compound, either with or without an accelerant. This creates sulfur "bridges" of varying lengths between the polymer chains. Regardless of the crosslinking method, however, the properties of the resultant rubber are dependent on the density of crosslinks: if the crosslink density is high, then the polymer becomes stiff and rigid, while a low density of cross-links helps to maintain elasticity.

---

<sup>d</sup>This expression comes from the classical description of entropy for a given number of microstates  $\Omega$ ,  $S = k_B \ln \Omega$ , applied to the Gaussian distribution of polymer configurations for a given size  $r$  ( $\Omega \propto e^{-\frac{3}{2} \frac{r^2}{Nl^2}}$ ) [241].

## 2.3 Liquid Metals

Liquid metals have been known to man for many millennia, the most well-known and abundant being mercury. The main attractiveness and novelty of liquid metals is that they are highly conductive liquids (much more than water), both thermally and electrically. The high thermal conductivity of mercury, for example, facilitates its use in thermometers. However, its high vapor pressure in combination with its high toxicity make it unsuitable for use in day-to-day life, especially in any application where there exists a risk of exposure to humans or animals, such as with commodity fibers. Another liquid metal, sodium-potassium alloy (NaK), while less toxic, is extremely violently reactive, especially with water, which makes it equally problematic. Other candidates for liquid metals also include alloys of other alkali metals (such as cesium and rubidium, each having melting points very close to room temperature), but alkali metals as a whole are violently reactive with water and atmospheric oxygen.

Gallium-based alloys, on the other hand, have none of the drawbacks of mercury and alkali metals. Elemental gallium has a melting point of roughly 30°C, but alloying gallium with other metals will drive its melting point down: for example, galinstan has a melting point of -19°C [12,26]. Gallium alloys are largely non-toxic [12,26] and do not violently react with water or oxygen, and display a high degree of conductivity, making them suitable for use in wires, antennae, and other electrically-conducting applications [13,26,111,112]. The two most common liquid metal alloys are eutectic gallium-indium alloy (EGaIn; 75% gallium and 25% indium by weight) and galinstan (a proprietary alloy consisting of ~68% gallium, ~22% indium, and ~10% tin by weight with trace amounts of bismuth and antimony<sup>e</sup>).

A remarkable property of gallium-based alloys is the rapid oxidation of the gallium component of the alloy upon oxygen contact, forming a nanometer-thick solid "skin" of gallium (III) oxide ( $\text{Ga}_2\text{O}_3$ ) [12,26,113]. This gallium skin forms readily, with very low concentrations of oxygen being sufficient to induce oxidation [26]. The solid behavior of this skin facilitates the creation of a versatile array of free-standing structures through processes such as three-dimensional printing [14,15]. Examples of such structures are shown in Figure 12.

---

<sup>e</sup>Galinstan is a proprietary material patented by Geratherm GmbH [16]. While the composition of the Geratherm version of Galinstan is not well-known, other companies sell eutectic gallium-indium-tin alloys branded as "galinstan"; one such product, and the one used throughout this dissertation, was sourced from Smart Elements GmbH, Vienna (Austria), and is labeled as being a mixture of 69% Ga, 22% In, and 9% Sn by weight.

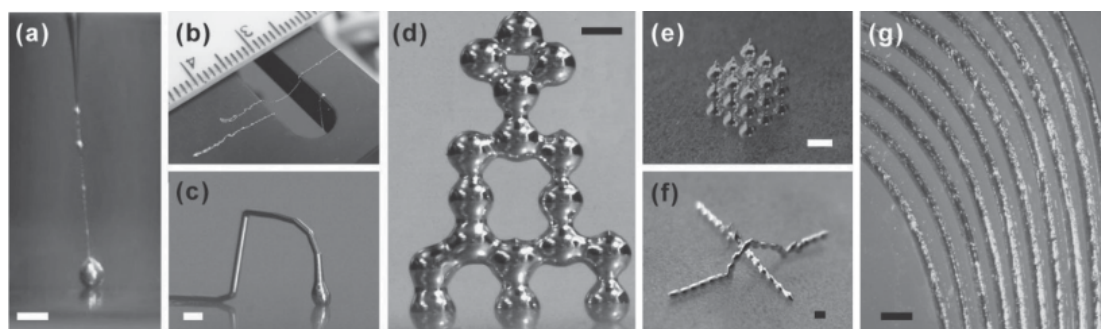
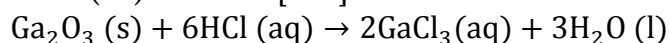


Figure 12. Examples of the three-dimensional structures that can be printed with gallium-based liquid metals (here, eutectic gallium-indium alloy), ranging from (a-c) filaments and wires to (d-f) freely standing beaded structures and (g) large-scale microchannels. Scale bars 500  $\mu\text{m}$ . Image reproduced from Ladd et al [14] and used under license from Wiley-VCH.

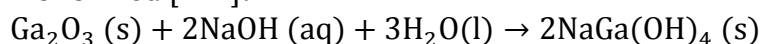
Despite its thinness, though, the skin is impregnable to oxidation, keeping the interior liquid metal fluid and protected from oxygen. An attractive application of this is the potential incorporation of galinstan into flexible electronics [111], combining the conductivity of the metal and the solid-like behavior of the skin to stabilize a nonspherical structure while still maintaining the fluidity of the core. Even when removed, whether chemically or by breaking, if oxygen still is present, the galinstan rapidly re-oxidizes, forming a skin anew [26].

This gallium oxide skin can be removed (or be prevented from forming entirely) in either a strongly acidic ( $\text{pH} < 3$ ) or strongly basic ( $\text{pH} > 10$ ) environment [111]. The mechanism of removal of the oxide skin proceeds differently, however, in each case: in an acid such as hydrochloric acid,  $\text{Ga}_2\text{O}_3$  reacts to produce a gallium halide salt, in this case gallium (III) chloride [112]:



Gallium (III) chloride is readily soluble in water, leading to a dissolution of the salt into its constituent ions [112]<sup>f</sup>. This process is slow, however, requiring reaction times of upwards of two hours.

An alkaline environment will also produce a salt, but of a very different character: for hydroxide bases, such as sodium hydroxide, a salt formed from a gallate ( $\text{Ga}(\text{OH})_4^-$  anion is formed [114]:



The marked difference here is that gallates are insoluble in water, leading to the formation of a white precipitate (and consequent loss of material). On the other hand, though, this procedure is rapid, with skin removal occurring within seconds [112]. Once the skin is removed, if the metal remains in the acidic or basic environment, the interface will remain stable, with no further oxidation occurring.

<sup>f</sup>Similar reactions can be observed with other strong acids, such as nitric and sulfuric acid, which will react with the oxide to produce gallium salts with the corresponding anion (either nitrate or sulfate, respectively).

Liquid metals of all kinds have very high interfacial and surface tensions [112,115,116], as defined and presented in section 2.4. The gallium oxide skin, on the other hand, has a very high propensity to adhere to surfaces [111,113,117]. Despite the formation of an oxide skin, though, like most metals, galinstan is extremely conductive [26], which makes it of interest to incorporate as the core of fibers. While gallium alloys have been incorporated into channels through capillary filling [13], the limitation here is the size, usually being on the order of millimeters.

A downside to the use of these gallium alloys, however, is that EGaIn and galinstan both are made with indium, a byproduct of ore mining with traditionally inefficient extraction processes [118]<sup>§</sup>. Indium is already used in many applications, one of the most popular being the optically transparent electrode material indium tin oxide (ITO), used as the electrode in many liquid crystal optical devices (such as liquid crystal displays) to apply the voltage that drives liquid crystal switching, and with increasing use in photovoltaic and solar cell applications. Supply for indium is still quite low, with a much lower estimated supply potential compared to other metals such as gallium [118]. Though some demand for ITO is slightly decreased due to the introduction and progress towards optical devices that do not use ITO, particularly by using an entirely different material as the electrode [20,77], the supply of indium is still not sufficient to facilitate commercialization of any applications. This means that, under the present circumstances, any applications using galinstan or EGaIn would likely either be niche products, used to serve a specific, narrow market, or need to use very small quantities of the liquid metal. Alternatively, since gallium itself melts at a low temperature, it is possible that there could be other eutectic liquid metal alloys that can be developed, using gallium as the "solvent" while still preserving some of the unique characteristics of gallium in alloys, in particular its oxidation.

## 2.4 Interfacial Tension and Surfactants

As mentioned above for the case of polymers in solution, in general, the presence of an interface between two phases has an energy cost associated with it. This is known as the *interfacial tension*, which is the energy cost of having an interface of a given surface area against another substance, and arises from the cohesive forces that "pull" molecules from the surface towards the center in order to minimize the energy from the surface. The terms *surface tension* (usually denoted by  $\sigma$ ) and *interfacial tension* (usually written as  $\gamma$ ) are often used interchangeably, but surface tension generally refers to the interfacial tension with a gaseous phase on one side of the interface, while interfacial tension generally describes the case of any two interfaces, particularly liquid-liquid interfaces.

---

<sup>§</sup>In terms of price, the price of the galinstan used during the work in this thesis ranged anywhere from €1-€3/gram (€7-€20/mL), while EGaIn was observed to be significantly more expensive (on the order of at least €30/gram).

The energy cost with the presence of an interface means that an interface will seek to minimize its surface area, with a higher interfacial/surface tension indicative of a greater tendency to do so. A definition of interfacial/surface tension can also be considered in terms of energy. First, we consider a frame with a fixed side  $L$  and a movable side, also of length  $L$ , in which a soap film with surface tension  $\gamma$  is drawn, as shown in Figure 13.

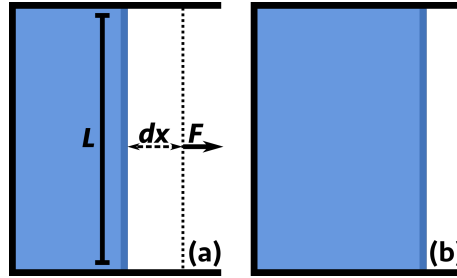


Figure 13. A diagram of a typical definition of surface tension, deriving from the expansion of a thin film between (a) and (b) by the displacement of a side of the barrier of length  $L$ .

The force the soap film exerts on the movable side is counterbalanced, to maintain a relatively stable state, by an externally applied force. As there are two sides to the film, the force needed to maintain the surface area on one side is half the total force; thus, we define the interfacial tension as:

$$\gamma = \frac{1}{2} \frac{F}{L} \quad (2.15)$$

If the movable side is displaced by a distance  $dx$ , this corresponds to a change in the surface area of  $dA = 2L \cdot dx$ , since the soap film has two interfaces (one on each side), which leads to the factor of  $\frac{1}{2}$  in the definition of interfacial tension.

Another consequence of surface tension is the Laplace pressure, which relates the pressure difference across a curved surface (such as a bubble) with its interfacial tension and its principal radii of curvature,  $R_1$  and  $R_2$  [42,119]:

$$\Delta P = \gamma \left( \frac{1}{R_1} + \frac{1}{R_2} \right) \quad (2.16)$$

This equation reduces to  $\Delta P = \frac{2\gamma}{R}$  in the case of a spherical droplet (where  $R_1 = R_2$ ). For a convex interface, the pressure is always higher; i.e. the pressure inside the droplet is higher than the pressure outside it.

The most common method to reduce interfacial tension is through the use of a surfactant, or surface-active material. A surfactant is an amphiphilic molecule, commonly containing a nonpolar (frequently organic) tail and a polar, usually ionic, head group, which adsorbs at the interface between a polar (ex. water) and a nonpolar (ex. oil) phase, thus driving down the interfacial tension between them [120]. Surfactants can be found in many places, ranging from detergents for cleaning to natural surfactants such as lipids and the surfactants found in the lungs to enable us to breathe [121]. We commonly categorize surfactants by their head group: *anionic* surfactants, such as sodium dodecyl sulfate (SDS), have negatively charged head groups with cations (here,  $\text{Na}^+$ ) as their counterions. *Cationic*

surfactants, such as hexadecyltrimethylammonium bromide (CTAB), instead have a positively-charged head group and an anion as the counterion (such as Br<sup>-</sup>). Alternatively, *zwitterionic* surfactants, such as phospholipids, have both charges in the head group and lack a dissociable counterion; these include phospholipids, such as DLPC, but such materials will not be looked at in the work within this thesis.

The excluded volume of the surfactant molecule with respect to its geometry (the *packing parameter*) governs how the surfactants pack and arrange and the resultant shapes of the micellar assemblies. This packing parameter,  $N_p$ , is defined as:

$$N_p = \frac{V}{a_0 l_0} \quad (2.17)$$

where  $V$  is the excluded volume of the surfactant molecule,  $a_0$  the projected surface area of the surfactant molecule head, and  $l_0$  the length of the tail [122]. The packing parameter describes what structures will be formed by the surfactant: generally, lower packing parameters favor convex arrangements, such as micelles while a packing parameter of  $N_p \sim 1$  (corresponding to more cylindrical structures) favors the formation of bilayers and vesicles. Eventually, with sufficiently large tail-to-head ratios, yielding packing parameters greater than one, inverse phases, where the micelles encapsulate the surrounding aqueous phase, develop [9,76,123]. The surfactants we work with in this work, however, fall more into the situations with low packing parameters and the resultant formation of spherical micelles.

There are two important parameters that dictate how a surfactant system behaves when in solution. The first is the *critical micelle concentration* (often abbreviated as CMC), which is the threshold concentration above which complete interfacial coverage is achieved and the excess surfactant will go into micellar assemblies. The interfacial tension against surfactant solutions *below* the critical micelle concentration will show a concentration-dependent behavior, where the interfacial tension decreases with increasing surfactant concentration [40,124], usually following a logarithmic dependence on surfactant concentration. This dependence is described by a form of the Szyszkowski equation, which describes the relationship of interfacial tension to surfactant concentration  $c$  [125,126]:

$$\gamma(c) = \gamma_0 - R_G T \Gamma_\infty \ln(1 + K_L c) \quad (2.18)$$

where  $\gamma_0$  is the interfacial tension at zero surfactant concentration;  $R_G$  the ideal gas constant;  $\Gamma_\infty$  the monolayer surface coverage capacity, given in units of m<sup>-2</sup>; and  $K_L$  an equilibrium constant related to the chemical potential of the solute<sup>h</sup>. The outcome of this is that we should expect, until full surface coverage is reached, the interfacial tension to decrease, with  $\Delta\gamma \propto -\ln(c)$ . Once full surface coverage is achieved at the CMC, the interfacial tension should plateau and remain largely constant, as  $\Gamma_m$  will not increase further. Above the critical micelle concentration, however, since the maximum surface coverage has been achieved, addition of

---

<sup>h</sup>This constant is defined as  $K_L = e^{\frac{\mu_b^0 - \mu_s^0}{RT}}$ , where  $\mu_b^0$  and  $\mu_s^0$  are the respective chemical potentials of the surfactant in the bulk and at the surface, respectively [175]. Generally, however, both  $K_L$  and  $\Gamma_\infty$  need to be determined experimentally [125].

further surfactant will not affect the interfacial tension as strongly and the excess surfactant can form micelles.

The second is the *critical micelle temperature*, or *Krafft temperature*, a temperature below which micelle formation will not occur. Even with a surfactant concentration above the CMC, no micelles will form because the maximum solubility of the surfactant is below the CMC (with the excess often visibly crystallizing out). Keeping this temperature in mind when working with surfactants is thus important, since the surfactant being used needs to be appropriate for the application and remain in solution throughout the course of an experiment.

## 2.5 Jetting and Plateau–Rayleigh Instability

When a thin column or stream of a liquid is poured from a height, such as water flowing from a faucet, we can see the columnar shape is lost and the stream breaks apart into droplets. This arises from the Plateau–Rayleigh instability<sup>i</sup>, a description of how the surface tension of a jet drives its break-up [127]. Over the length of a stream, small instabilities and wavelike perturbations in the surface of the column will develop, which then propagate over the length of the column/jet and lead to breaking, also known as dripping. The development of the Rayleigh instability in an inviscid liquid will occur when the ratio between the perturbation wavelength within the jet and the jet diameter is approximately equal to pi [128].

More recently, and more relevant to the work in this thesis, the transition from jetting regimes to dripping regimes has been theoretically and experimentally described as a balance between the interfacial tension forces, which aim to break the jet apart into droplets, and the forces within the jet that counter this break-up, either through viscous forces or momentum [35–37,129,130]. To describe the balance of these forces and which forces govern the dynamics at the interface, we can look at a system of four dimensionless fluid dynamics numbers: the capillary number of the outer (continuous) phase, the Reynolds number of the inner (dispersed) phase, and the Weber and capillary numbers of the inner phase.

The *capillary number* ( $Ca$ ) is a measure of the importance of viscous forces against interfacial forces in a flow. For our system, we first look at the capillary number of the outer phase,  $Ca_{out}$ , which is defined as:

$$Ca_{out} = \frac{\eta_{out} v_{out}}{\gamma} \quad (2.19)$$

where  $\eta_{out}$  is the dynamic viscosity of the outer phase (noted in Pa·s in SI units),  $v_{out}$  the outer fluid flow speed<sup>j</sup>, and  $\gamma$  the interfacial tension between the materials.

---

<sup>i</sup>The Plateau–Rayleigh instability is often referred to as "Rayleigh instability", particularly among Anglophone audiences: while it was initially discovered/proven experimentally by Joseph Plateau, the principle was theoretically proven by J.W. Strutt III, Lord Rayleigh. In an attempt to reduce verbosity in this work, this work will largely refer to "Rayleigh instability" as a shorthand.

<sup>j</sup>Flow rate is converted into flow speed by dividing the volumetric flow rate ( $Q$ ) by the cross-sectional area of the jet, which is estimated from the jet radius  $r$ :  $v = \frac{Q}{\pi \cdot r^2}$ .

Physically, we can conceptualize this as how resistant the outer phase is to filling in the "gaps" that would be created from the break-up of the inner flow through interfacial forces: a more viscous material flows less readily. When  $Ca_{out} \geq O(1)$ , these viscous forces are large enough to counteract the interfacial forces that would drive jet break-up [35–37,130]. A low capillary number, however, indicates the dominance of the interfacial forces over the viscous forces and the consequent jet breaking.

The inner phase has three fluid dynamics numbers that describe its situation, however. The first, the inner phase *Reynolds number*, quantifies the importance inertial forces (kinetic energy) with respect to the viscous forces:

$$Re_{in} = \frac{\rho_{in} v_{in} l_{in}}{\eta_{in}} \quad (2.20)$$

Reynolds numbers are very commonly used in aerodynamics and flow to discuss the transition between turbulent and laminar flow, with  $Re > O(2)$  indicative of the onset of turbulence [131,132] and numbers below that predicting laminar flow. In microfluidics set-ups, however, the Reynolds numbers are considerably lower than this. Instead, Castro-Hernández et al used the inner flow Reynolds number to determine which was more important: inertial forces, represented by the inner flow Weber number ( $We_{in}$ ), or viscous forces, represented by the inner flow capillary number ( $Ca_{in}$ ) [35,36]. If  $Re_{in} > 1$ , then the inertial forces are dominant, which means that we can consider  $We_{in}$  to predict the inner flow; for  $Re_{in} < 1$ , the viscous forces dominate, which means  $Ca_{in}$  is the more appropriate predictor.

In the  $Re_{in} < 1$  case,  $Ca_{in}$  is the more important flow indicator [35,36], which we define much in the same way as the outer flow capillary number:

$$Ca_{in} = \frac{\eta_{in} v_{in}}{\gamma} \quad (2.21)$$

This is, again, a balance of interfacial forces which are opposed by viscous forces that resist the flow to fill in the gaps in the jet, but this time these are the viscous forces from the inner fluid.

For cases where  $Re_{in} > 1$ , we look at the inner flow *Weber number* ( $We_{in}$ ), which characterizes the balance of inertial forces which would oppose jet break-up against interfacial forces which would drive the breaking apart of the jet:

$$We_{in} = \frac{\rho_{in} v_{in}^2 l_{in}}{\gamma} \quad (2.22)$$

where  $\rho_{in}$  is the density of the inner fluid;  $v_{in}$  the flow velocity of the inner fluid; and  $l_{in}$  a characteristic length of the jet, typically on the order of the jet diameter [35–37].<sup>k</sup> While Weber number is classically treated as a force balance, it can also be thought of as an energy balance between the areal kinetic energy density (the  $\rho_{in} v_{in}^2 l_{in}$  term), which favors jet continuity, and the areal interfacial energy

---

<sup>k</sup>The preference of Weber number for higher Reynolds number cases can also be seen in that  $Re = \frac{We}{Ca}$ . A high Reynolds number would indicate a relative dominance of the Weber number, and vice-versa for a low Reynolds number and the capillary number.



density (which is represented by the term  $\gamma$ , by definition the interfacial energy per unit area), which favors the jet breaking into droplets. If  $We_{in} > 1$ , kinetic energy dominates interfacial energy and jetting results; if  $We_{in} < 1$ , interfacial forces drive jet break-up and dripping ensues. A graphical summary of what these flow numbers describe a given jetting system is presented in Figure 14.

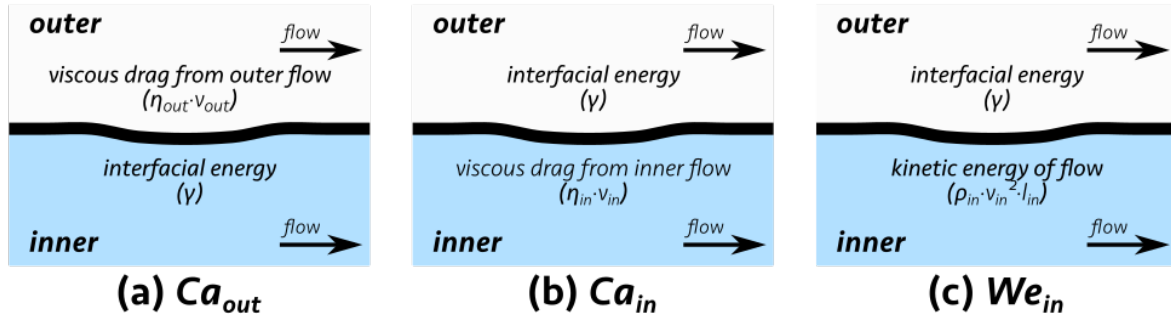


Figure 14. Simplified diagrams of the flow parameters and how they interact with each other. (a) The outer phase capillary number describes how viscous drag from the outer flow opposes the breaking of the continuous inner fluid jet that would be created by interfacial tension. (b and c) The interfacial tension-driven break-up of the inner flow is opposed either by (b) the viscous drag forces of the inner flow, which resist jet breaking, or (c) by the kinetic energy, which represents an inertial term that can be thought to oppose the propagation of perturbations in the jet.

As can be seen in all of the capillary and Weber numbers considered, a key term in both of the denominators is the interfacial tension between the two liquids. Having an accurate idea of what the interfacial tension is will provide a sense of what parameters need to be tuned and to what range in order to obtain stable jetting conditions: over the course of an experiment, the only parameters that can be readily tunable without either changing the materials entirely or introducing an additional interface are the flow velocity and the characteristic length, both via the flow rates (and, in the case of a multiple-flow system, additionally by the flow rate of the surrounding medium). This demonstrates a clear need for knowing the interfacial tension between two fluids in order to understand and predict how stable a jet will be.

## 2.6 Diffusion and Osmotic Pressure

Material will diffuse from a region of higher concentration to a region of lower concentration to attempt to equalize the concentration of material throughout a system. When two reservoirs are separated by a semi-permeable membrane that only admits the passage of certain materials through it, this is instead an osmosis process, where, for example, only solvent molecules are able to cross the membrane. One of the most common examples of this is the flow of water into living cells across a cell membrane, leading to either dehydration in a hypertonic or turgor in a hypotonic environment (such as deionized water).

When considering the wet spinning processes to be presented in Chapter 4, we can think of the solvent extraction process as a kind of osmosis: since we have a polymer that is miscible in one solvent but immiscible in the corresponding bath solvent, the only material that can migrate across the interface between the polymer dope and the coagulation bath is the polymer solvent (such as toluene, hexane, or THF). If we add a solute, often a salt, on the bath side of this semi-permeable interface, there exists an osmotic pressure, noted as  $\Pi$ , that then drives the movement of solvent from the dope to the bath.

Osmotic pressure ( $\Pi$ ) can be quantified by the van 't Hoff equation, which relates the osmotic pressure against a gradient to the molar concentration of solute  $C$ , the ideal gas constant  $R_G$ , temperature  $T$ , and the "van 't Hoff index"  $i$ , which measures the dissociation of a molecule/component into its constituent ions/parts [133]:

$$\Pi = iCR_GT \quad (2.23)$$

The combination of both  $i$  and  $C$  in the equation shows that, being a colligative property, diffusion/osmosis is driven solely by the concentration of ions or solute rather than by *what* those ions are. Therefore, to increase the osmotic pressure (and thus flow) across a gradient, one would increase the concentration of solute on one side of the membrane. In the systems we use, where we prepare a coagulation bath containing a polymer and a salt, we use a salt to drive this osmotic gradient to extract solvent; thus, the  $C$  term in the van 't Hoff equation is based on the ion concentration.

To quantify the rate of flux/flow of a material within a system, one can use Fick's laws of diffusion. Fick's first law relates the molar flux,  $\vec{J}$ , or the rate of flow of a solute, to the gradient in solute concentration  $\vec{\nabla}\phi$  and a diffusion coefficient  $D$ :

$$\vec{J} = D\vec{\nabla}\phi \quad (2.24)$$

The change in concentration of a solute,  $\phi$ , over time due to diffusion is given by

$$\frac{\partial}{\partial t}\phi = D\nabla^2\phi \quad (2.25)$$

The diffusion coefficient in both of the above equations,  $D$ , is given in units of area per unit time (often written as  $\text{mm}^2/\text{s}$  due to the very low diffusivities of most materials) and represents the mobility of the solute within the solvent. In a co-flowing system, particularly in the wet spinning systems presented in future chapters, the importance of diffusion with respect to inertial forces and flow velocity is stated by the *Péclet number*, a dimensionless number that relates advection, which is responsible for mass transport by flowing (often given by the flow speed,  $v$ ), to the diffusivity of the solute in the solvent ( $D$ , the same quantity as used in Fick's law) divided by a characteristic length scale  $L$  [69]:

$$Pe = \frac{v}{(D/L)} \quad (2.26)$$

A low  $Pe$  means that diffusion is more important for mass transport, while a high  $Pe$  means that diffusion is less important compared to advection. In a co-flowing system, a high  $Pe$  means that mixing from diffusion of the components is less likely to occur.

## 2.7 Solubility and Miscibility

A general maxim in chemistry and physics, when seeing whether two materials are miscible in each other, is "like dissolves like": a polar solvent will dissolve a polar solute and a nonpolar solvent will dissolve a nonpolar solute. A question arises, though, in *how* exactly this likeness can be measured and what parameters are needed to quantify this. For example, while PVA, a somewhat polar polymer molecule, dissolves readily in water, it does not dissolve in ethanol, which is a polar solvent (albeit less so than water).

To quantify how similar two materials are, Hildebrand [133] introduced the concept of a solubility parameter ( $\delta$ ), a value that expresses how a molecule interacts with its surroundings [134,135]. The idea with Hildebrand parameters is that the components are soluble/miscible if the parameters are similar to each other, as these parameters suggest how materials will interact with each other. Hildebrand parameters, however, neglect to account for intermolecular forces such as hydrogen bonding and polarity. For example, polyisoprene has a Hildebrand parameter of  $8.2 \text{ (cal/cm}^3)^{1/2}$  [136]. The organic solvent *n*-hexane, which dissolves PI, has a solubility parameter  $\delta = 7.3 \text{ (cal/cm}^3)^{1/2}$ . In the case of ethyl acetate,  $\delta = 9.1 \text{ (cal/cm}^3)^{1/2}$ ; despite the fact that  $|\delta_{PI} - \delta_{hexane}| = |\delta_{PI} - \delta_{ethyl\ acetate}|$ , ethyl acetate is not a solvent for PI. Hildebrand parameters are thus adequate to determine whether or not two compounds are miscible with each other only if the polarity and hydrogen bonding capabilities of the two components are similar to each other [134,137].

The concept of solubility parameters was further developed by Charles Hansen in the 1960's. He decomposed the single-component Hildebrand parameter into a system of three solubility parameters [137,138]: one to quantify the dispersion energy contributions of the molecule ( $\delta_D$ ), one for the polar interactions ( $\delta_P$ ), and one for the hydrogen bonding ( $\delta_H$ ). These three terms can be combined into a total solubility parameter,  $\delta$ :

$$\delta^2 = \delta_D^2 + \delta_H^2 + \delta_P^2 \quad (2.27)$$

Both Hildebrand and Hansen solubility parameters are experimentally calculable and a wealth of references exist to give data for the solubility parameters of a wide number of common materials, but a method of approximating these parameters to a reasonable degree to lesser-known materials, such as liquid crystals, is the tabular calculation method. Introduced by Fedors for Hildebrand parameters [134], this method assigns values for an interaction parameter ( $\Delta e_i$ ) and a molar volume ( $\Delta v_i$ ) to each of the functional groups in a molecule, with the solubility parameter ultimately defined as:

$$\delta = \sqrt{\frac{\sum \Delta e_i}{\sum \Delta v_i}} \quad (2.28)$$

For a long-chain, high-weight polymer, the Hildebrand parameter  $\delta$  can be approximated instead as:

$$\delta = \rho \frac{\Delta f_i}{M_i} \quad (2.29)$$

where  $\rho$  is the mass density of the polymer,  $\Delta f_i$  the sum of the "molar attraction constant" contributions of the constituent functional groups of the monomer, and  $M_i$  the molar mass of the repeating unit. Using the Fedors method, for example, we can determine the Hildebrand solubility parameter of polyisoprene by using a tabular method, using the "molar attraction" constants detailed in Table 1:

*Table 1. Molar attraction constant contributions of polyisoprene functional groups. Molar attraction constants are reproduced from Fedors [134].*

Functional Group	$\Delta f_i$ [ $\text{cal}^{1/2} \text{cm}^{3/2} \text{mol}^{-1}$ ]
vinyl, monosubstituted	111
vinyl, disubstituted	19
methylene	133
methyl	214

With two methylene groups, we can then calculate the Hildebrand parameter as follows, using  $\rho_{PI} = 0.91 \frac{\text{g}}{\text{cm}^3}$  as the density of polyisoprene [106]:

$$\delta = \rho_{PI} \frac{(\Delta f_{\text{methyl}} + 2 \cdot \Delta f_{\text{methylene}} + \Delta f_{\text{vinyl}})}{(12 \cdot 5 + 8 \cdot 1)}$$

$$\delta = \left(0.91 \frac{\text{g}}{\text{cm}^3}\right) \frac{(214 + 2 \cdot 133 + (111 + 19)) \frac{\text{cal}^{1/2} \text{cm}^{3/2}}{\text{mol}}}{(12 \cdot 5 + 8 \cdot 1) \frac{\text{g}}{\text{mol}}}$$

$$\delta = 8.2 \text{ cal}^{1/2} \text{cm}^{-3/2} = 16.7 \text{ MPa}^{1/2}$$

This compares well to literature values. [106,138] Tabular methods can additionally be used for Hansen parameters in the same way, by summing together the components for a compound or polymer, the difference for Hansen parameters being that each of the equations needs to be separately applied to the three components ( $\delta_D$ ,  $\delta_H$ , and  $\delta_P$ ) [138]; however, instead of individual calculations for a given polymer, many of the Hansen parameters for commonly-used polymers can be readily obtained from databases.

For smaller molecules, such as a liquid crystal, the three components to the Hansen parameter can be found, again, using a tabular method by summing the contributions of each of the functional groups of the molecule [134,138]. The three of these, using equation (2.27), can then be summed together to calculate the final overall solubility parameter. For example, using the Hansen tabulation method for a small molecule, we can calculate the Hansen solubility parameters of the commonly used liquid crystal 5CB as follows:

- First, in the case of 5CB, we identify the functional groups: these are a cyano (CN) group, two phenyl rings, four methylene units (single-bonded  $\text{CH}_2$ ), and one terminal methyl ( $\text{CH}_3$ ) group. This means that the corresponding overall solubility parameter equation would look like:

$$\delta = \left( \frac{1 \cdot \Delta e_{\text{CN}} + 2 \cdot \Delta e_{\text{phenyl}} + 4 \cdot \Delta e_{\text{methylene}} + 1 \cdot \Delta e_{\text{methyl}}}{1 \cdot \Delta v_{\text{CN}} + 2 \cdot \Delta v_{\text{phenyl}} + 4 \cdot \Delta v_{\text{methylene}} + 1 \cdot \Delta v_{\text{methyl}}} \right)^{1/2} \quad (2.30)$$

- Next, we identify the contributions for each of the groups to the three components of the solubility parameter. These values can be found in literature [134,135,138,139] and are summarized below in Table 2.

*Table 2. Group contributions to the calculated Hansen parameters of 5CB. Reference values obtained from Hansen [138].*

Functional Group	$\Delta v$ [cm <sup>3</sup> /mol]	$\Delta e_D$ [cal/mol]	$\Delta e_H$ [cal/mol]	$\Delta e_P$ [cal/mol]
cyano	32.0	0	3750	400
phenyl	52.4	7530	50	50
methylene	16.1	1180	0	0
methyl	33.5	1125	0	0

- Finally, for each of the individual components to the solubility parameter, we input the values into equation (2.17):

$$\begin{aligned}
\delta_D &= \left( \frac{(0) + (2 \cdot 7530) + (4 \cdot 1180) + (1125)}{(32.0) + (2 \cdot 52.4) + (4 \cdot 16.1) + (33.5)} \right)^{1/2} \\
&= 9.4 \text{ cal}^{1/2}\text{cm}^{-3/2} = 19.3 \text{ MPa}^{1/2} \\
\delta_P &= \left( \frac{(3750) + (2 \cdot 50) + (4 \cdot 0) + (0)}{(32.0) + (2 \cdot 52.4) + (4 \cdot 16.1) + (33.5)} \right)^{1/2} \\
&= 4.1 \text{ cal}^{1/2}\text{cm}^{-3/2} = 8.3 \text{ MPa}^{1/2} \\
\delta_H &= \left( \frac{(400) + (2 \cdot 50) + (4 \cdot 0) + (0)}{(32.0) + (2 \cdot 52.4) + (4 \cdot 16.1) + (33.5)} \right)^{1/2} \\
&= 1.5 \text{ cal}^{1/2}\text{cm}^{-3/2} = 3.0 \text{ MPa}^{1/2} \\
\delta^2 &= (19.3)^2 + (8.3)^2 + (3.0)^2 = 450 \text{ MPa} \\
\delta &= 21.2 \text{ MPa}^{1/2}
\end{aligned}$$

The Hansen parameters of commonly used polymers, such as polyisoprene, are often obtainable from reference literature [138]. These parameters alone, however, especially in a system of a polymer in solvent, do not determine whether a system is miscible: instead, the concept of a "relative energy distance" is used to determine miscibility, calculated as the ratio of a "solubility radius",  $R_a$ , to an "interaction radius" of the polymer.

$$R_a^2 = 4 \cdot (\Delta\delta_D)^2 + (\Delta\delta_H)^2 + (\Delta\delta_P)^2 \quad (2.31)$$

Interaction radii ( $R_o$ ) for a given polymer are obtainable from databases and references [138]. If the ratio between the two,  $R_a/R_o$ , is less than unity, the solvent is contained within the solvent's "miscibility sphere" and, consequently, the polymer and solvent are miscible. In contrast, if the ratio between the two is greater than unity, then the polymer and solvent do not have overlapping miscibility spheres and, consequently, the two are immiscible. [138]

## 2.8 Microfluidics

In the modern world, producing technology capable of operating at smaller scales is a tantalizing prospect from the standpoints of cost, environmental footprint, and

efficiency in fields such as diagnostics [140,141]. One such way to achieve this miniaturization is through the use of microfluidic techniques. The term *microfluidics* refers to an array of techniques which function with small quantities of liquid and materials [132].

Normally, the achievement of these techniques first involves the fabrication of devices, either through soft lithography techniques (using materials such as PDMS or polycarbonate) [142–145] or glass capillary assemblies [24,146–148], designed to work with quantities of as low as nanoliters or picoliters. Because of the small dimensions of these set-ups, the physics becomes quite different from the macroscale. For example, one consequence is that the flow of fluids through a microfluidic device occurs under non-turbulent conditions [132] with a low Reynolds number. There are several outcomes of this, one being that the mixing between fluids is diffusion-driven (and governed by the Péclet number) rather than turbulence-driven. Another consequence is that the interfacial forces play a key role at this scale, particularly in the development of menisci, and gravitational forces diminish in importance: in our case, this becomes important because we work with materials which can have a considerable mismatch in densities, which enables us to neglect gravitational forces in our devices.

## CHAPTER 3

### MICROFLUIDIC INTERFACIAL TENSIONOMETRY: DEVELOPMENT, MEASUREMENT, AND OPTIMIZATION

As described in Section 2.5, the jetting of liquids in a co-flow is a delicate balance of a number of material parameters. In all flow regimes, however, a key quantity is the interfacial tension between the two fluids in the flow: very high interfacial tensions will favor the breaking of a jet even if the flow rates are high. In order to better predict whether jetting will result in a system, we need to have an idea of the interfacial tension; however, its characterization is not a trivial process. A variety of techniques exist for the measurement of interfacial tension between immiscible fluids, but, when it comes to the interfacial tensions of liquid crystals, many of these methods have proven unsuitable. This demonstrates a need for a more universal technique capable of working with a wide variety of fluids and rapidly and repeatably producing trustworthy results.

This chapter, therefore, details the development of a technique for the measurement of the interfacial tension between immiscible fluids in a microfluidic set-up. After first presenting an overview of other techniques and the issues they encounter when used with the systems we are interested in, particularly with liquid crystals, we then present the technique of micropipette aspiration of cells to measure cortical interfacial tensions [119,149–153] and how we adapted it for use with immiscible fluids without membranes [154]. Our technique has shown itself to be effective for a variety of combinations of fluids, ranging from surface tension measurements between air and an aqueous surfactant solution to systems of two isotropic fluids (oil and water mixed with surfactants with very well-characterized interfacial tensions [155]), systems of liquid metal and alkaline solutions, and, most interestingly, liquid crystals against aqueous surfactant and polymer solutions. When compared to previously obtained values, these measurements show a reasonable degree of concordance with literature values and agree well with predictions of interfacial tension behaviors of liquid crystals and liquid metals. We can also use this technique for dynamic measurements, where we measure the time-dependent interfacial tension decrease due to the adsorption of surfactant at the interface.

The work presented in this chapter is largely based on the publication *Microfluidic Tensiometry Technique for the Characterization of the Interfacial Tension between Immiscible Liquids*, published in Langmuir in 2018 [154]. I would like to particularly thank Dr. V.S.R. Jampani for developing the basic idea for the experiments and his help in designing the experimental protocols and executing the initial work in this

chapter. I would additionally like to thank Mr. Andy Schanen, a M.Sc. student working in the ESMP group under my supervision from September 2018 through June 2019, for further carrying out experiments and working to further automate and improve the tensiometry technique, and Dr. Christina Schütz for providing the cellulose nanocrystal dispersions that were used in the experiments in Section 3.4.6.

### 3.1 State-of-the-Art of Interfacial Tensiometry

A number of techniques have been developed to characterize the interfacial tension between two fluids. Most of these utilize shape analysis techniques that seek to fit a shape of a given interface of a material, often in the form of a droplet surrounded by another target fluid, to the interfacial tension between phases. In this section, a selection of commonly used techniques for interfacial tension characterization, along with their drawbacks when applied to the fluids under study in this chapter, will be presented.

#### 3.1.1 Pendant Drop

The pendant drop technique is a well-established technique for interfacial tensiometry, both for surface tensions with air [47,156] and interfacial tension between fluids [21,26,42,43,157,158]. The pendant drop technique has been extensively characterized and employed, with full descriptions presented by Neumann et al [42,43]. Pendant drops were not employed here, so a complete treatment of the technique is beyond the scope of this work, but, for completeness, a short summary of the technique is presented here.

A droplet of one of the materials is produced within a bath of the other liquid, its final shape being a function of the interfacial tension between the materials, which aim to minimize the droplet shape, balanced against the gravitational force acting upon the droplet, which acts on the droplet to cause the spherical shape to be lost. Pendant drops are formed vertically, either top-down by producing a drop of a more dense liquid in a less dense fluid or bottom-up when the material being observed is less dense than the bath. By tracing contours of the shape of the produced droplet, the interfacial tension can be extracted as a function of the pressure of the droplet as a function of both height ( $\Delta P(z)$ ) and the curvature-induced Laplace pressure; the density difference between the phases ( $\Delta\rho$ ); and the radii of curvature ( $R_1$  and  $R_2$ ) of the produced droplet [21,42,43,157], as described in equations (3.1a) and (3.1b):

$$\Delta P = \gamma \left( \frac{1}{R_1} + \frac{1}{R_2} \right) \quad (3.1a)$$

$$\Delta P(z) = \Delta P_0 \pm \Delta\rho a_g z \quad (3.1b)$$



where  $a_g$  is acceleration due to gravity<sup>a</sup>. Equation (3.1a) is simply the Laplace pressure equation, so the point of the pendant drop technique is to fit how the shape of the droplet deviates from what would be expected from the Laplace equation due to the weight of the droplet. A schematic of a typical pendant drop technique is presented in Figure 15.

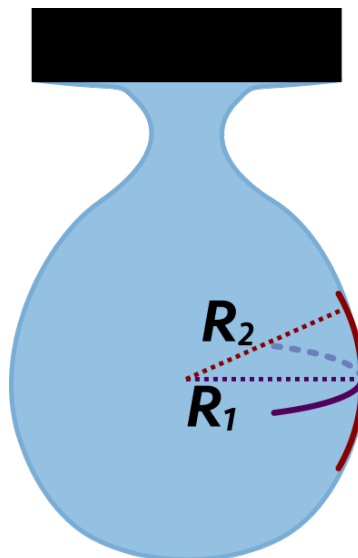


Figure 15. Schematic of the pendant drop technique, indicating the radii of curvature used in equation (3.1(a)).

The fitting of the contours of the droplet surface to the interfacial tension between the phases is normally performed by *axisymmetric drop shape analysis* (ADSA), a technique developed by the Neumann group [42,43] which uses an iterative method to solve the Laplace pressure equation, fitting the resultant interface to a corresponding interfacial tension. Pendant drops fitted using ADSA are most suitable for systems with intermediate Bond number<sup>b</sup> regimes [42] ( $Bo \in \sim[0.1,10]$ ), where neither gravitational nor interfacial tension forces strongly dominate. More recently, contour-fitting methods developed by Peters et al [158], rather than using the ADSA method, instead fit the data to a different force balance equation, based in part on the Young force balance equation, centered at the apex of the droplet and accounting for gravitation, buoyancy, and droplet curvature. When summed together, the components of the force balance for the contour fitting give an

---

<sup>a</sup>I use the terminology  $a_g$  instead of  $g$  because acceleration due to gravity is not constant and instead is dependent on factors such as altitude, latitude, and influence of neighboring objects. The choice of  $a_g$  is made to emphasize that this is a variable acceleration term as opposed to a constant.

<sup>b</sup>The Bond number ( $Bo$ ), also generally known in non-Anglophone Europe as the Eötvös number ( $Eu$ ), is a dimensionless quantity that measures the relative importance of gravitational forces against interfacial tension forces. It is given by  $Bo = \frac{\Delta\rho a_g l^2}{\gamma}$ , where  $l$  is a characteristic length scale for the system (ex. the radius of curvature of a droplet): for high  $Bo$ , the gravitational forces will dominate the interfacial tension forces.

equation dependent on contact angle, the densities of each of the phases, and parameters of the shape of the droplet (such as its height and width).

While powerful for many materials, the reliance of both methods of pendant drop fitting on the difference in density between the two phases is problematic when the densities of the two phases are very close to each other, such as is the case for liquid crystals against water. For example, Kim et al reported a significant range in interfacial tensions when measuring 5CB against a 1.0 mM (above CMC) aqueous solution of CTAB [46]: the uncertainty arises from the wide array of values reported for the density of 5CB, ranging from 1.008 g/ml [159,160] to 1.035 g/ml [161]. This raises concerns in being able to obtain precise values for interfacial tension using density-dependent measurements when the densities of the two phases are similar [46,162]. Additional concerns arise in systems where equilibration of the droplet is a slow process, particularly when a dynamic interfacial tension process develops where being able to measure the interfacial tension immediately upon droplet production is necessary.

### 3.1.2 Ring and Plate Methods

Another type of interfacial tension measurement is often performed with ring and plate methods. These include the du Noüy ring [163] and the Wilhelmy plate [159,164] techniques, but these both operate under a similar principle. In short, either a plate or a ring, commonly made out of platinum, is immersed in the fluid of interest and then gradually lifted from the surface with a given force. The interfacial tension is extracted from a force balance relationship (eq. (3.2a) for the Wilhelmy plate and (3.2b) for the du Noüy ring):

$$F = \gamma \cdot l \cos \theta \quad (3.2a)$$

$$F = w_{ring} + 2\pi \cdot \gamma(r_1 + r_2) \quad (3.2b)$$

where  $F$  is the force used to lift the part of the apparatus, either the ring or the plate, from the surface/interface of the fluid, and the other parameters as defined by the apparatus (for the plate,  $\theta$  being the contact angle of the liquid with the plate and  $l = 2w + 2d$  being the perimeter of the plate cross section; for the ring,  $w_{ring}$  being the weight of the ring (defined as  $w_{ring} = m_{ring} \cdot a_g$ ) and  $r_1$  and  $r_2$  the outer and inner radii of the ring, respectively). The apparatuses are presented in Figure 16.

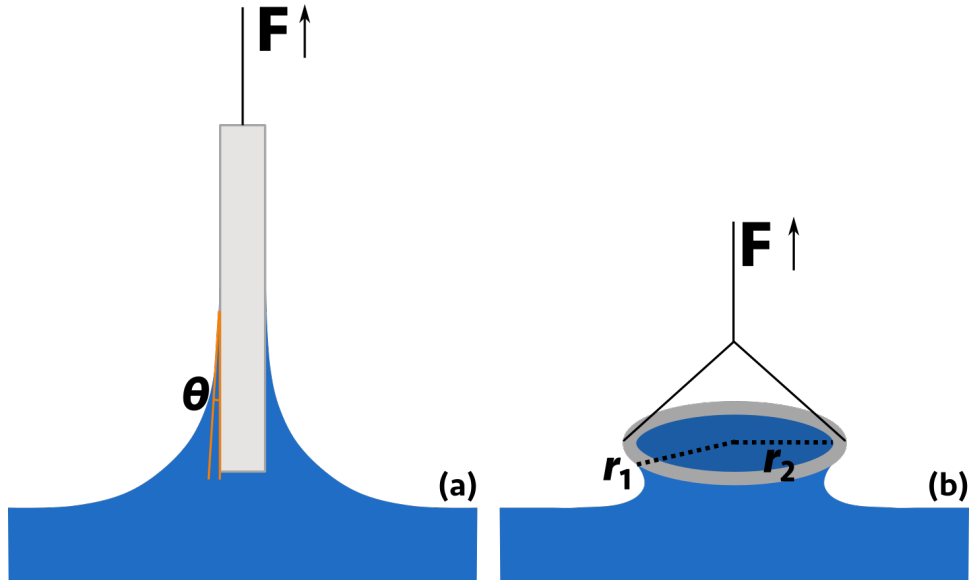


Figure 16. Examples of the (a) Wilhelmy plate and (b) du Noüy ring for measuring interfacial tension. The required parameters for using equation (3.2a) for the Wilhelmy plate are the wetting parameter ( $l$ , defined as the perimeter of the plate cross-section), the contact angle between the fluid and plate ( $\theta$ , typically assumed to be  $0^\circ$ ), and the force  $F$  with which the plate is raised from the interface, while the parameters necessary from the du Noüy ring are the inner and outer radii of the ring and the force applied to lift the ring from the surface.

Plate and ring methods are quite common to measure surface tensions of surfactant systems, but they operate under an assumption, especially with the du Noüy ring, of complete wetting of the measurement plate. Additionally, these methods are most suitable for surface tension measurements, as the immersion of the measurement tool in a bath to begin the measurement is necessary: liquid-liquid interfacial tensions are very rarely, if ever, measured with either of these techniques. Lastly, both the plate and ring must be cleaned extremely well before any measurements, with the initial surface free of any surfactants or contaminants, in order to obtain good data. The process of cleaning can be time-consuming, sometimes requiring specialized equipment and careful handling to avoid contamination before the commencement of an experiment.

### 3.1.3 Sessile Drops

The sessile drop method is a simple method that uses the Young force balance equation to obtain interfacial tension [26,155], most commonly between air and the liquid of interest. A single droplet of fluid is placed on a solid surface and the contact angle between the droplet and the solid substrate is optically measured. The contact angle of the droplet with the substrate,  $\theta$ , relates to a balance of the horizontal components of three interfacial tensions (between the liquid and solid surface,  $\gamma_{LS}$ ; between the liquid and vapor phases,  $\gamma_{LV}$ ; and between the solid and vapor,  $\gamma_{SV}$ ):

$$\gamma_{LS} + \gamma_{LV} \cos \theta = \gamma_{SV} \quad (3.3)$$

A demonstration of a set-up for sessile drop measurements is presented in Figure 17.

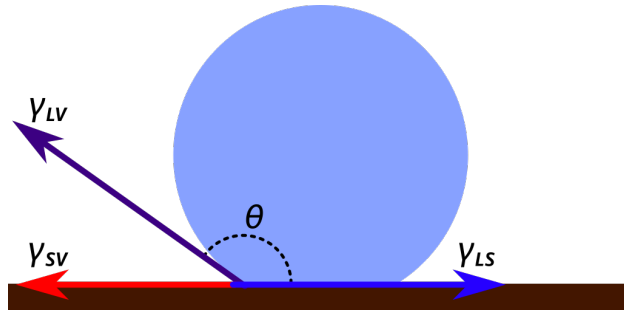


Figure 17. Demonstration of the sessile drop technique. The target interfacial tension ( $\gamma_{LV}$ ) is determined as a function of contact angle with the substrate.

This technique is a fairly standard technique for measuring interfacial tensions and can cover a wide variety of systems, but it requires an assumption of a completely smooth surface (lacking any roughness) and knowledge of the other two interfacial tensions (liquid-solid and vapor-solid). This is a non-trivial matter when it comes to novel or unusual systems of materials, such as liquid crystals and liquid metals.

### 3.1.4 Bubble Deformation Method

The bubble method developed by Harth et al measures interfacial tension by creating a bubble of material, usually a smectic liquid crystal bounded on both sides by an aqueous solution [40,41]. A small air bubble is then floated to the top of the smectic bubble. The buoyant force of the air bubble deforms the liquid crystal bubble, and this deformation of the liquid crystal bubble is then related to the interfacial tension, the material density  $\rho$  and the density of air  $\rho_{air}$ , gravitational acceleration  $a_g$ , and other parameters acquirable from the images taken during the measurement:

$$\gamma = \frac{V_{air}(\rho - \rho_{air})a_g}{2\pi d_{ring} \left( \cos \theta - \frac{d_{ring}}{4} \left( \frac{1}{R_2} + \frac{1}{R_1} \right) \right)} \quad (3.4)$$

A schematic of the set-up for measurement with this technique is presented in Figure 18.

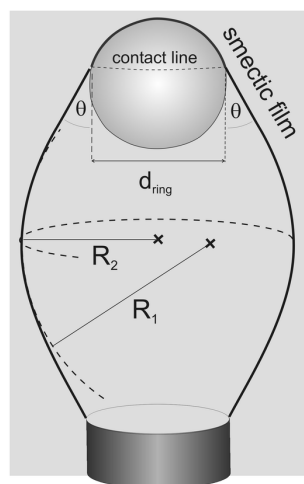


Figure 18. Illustration of the bubble deformation technique, with the relevant parameters for equation (2.6) indicated in the image. Figure reproduced from Harth et al [41]–Published by the PCCP Owner Societies and re-used under a Creative Commons Attribution-Non-Commercial 3.0 License.

One of the advantages of this technique, especially over pendant drops, is that it does not rely on the miniscule difference in densities between water and most liquid crystals and it enables the observations of dynamic interfacial tension (the decrease of the interfacial tension of an interface with respect to time). This technique, however, has only been successfully employed for smectic liquid crystals such as 8CB [40,41]. For nematic liquid crystals, the fluid nature of the phase means that isolating and maintaining a bubble of the nematic liquid crystal during the measurement is extremely difficult, if not impossible, as also seen by issues with equilibration of pendant drops of nematic liquid crystals.

### 3.1.5 Droplet Deformation and Relaxation Methods

Another method for interfacial tension measurement, developed by Hudson et al [165,166] and further expanded on by Brosseau et al [39] for use with dynamic interfacial tension measurements, generates droplets of a fluid in a co-flowing system that are then forced through a microchannel, thus causing them to become elongated and deformed. When the droplets exit the constriction, they then relax back to their undistorted state.

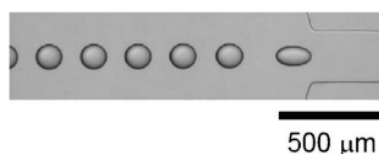


Figure 19. The deformation and relaxation of the droplets in the vicinity of the constriction. The time for the droplets to relax from the deformed state to their initial state is related to the viscosity of the droplet medium, the matrix in which the droplets are formed, and the interfacial tension between the two phases. Figure adapted from Cabral et al [166] and used under license from the Royal Society of Chemistry.

The time required for such relaxation,  $\tau$ , is inversely related to the interfacial tension and described by [166]

$$\tau = \frac{\eta_c r_0}{\gamma} \left[ \frac{(2\hat{\eta} + 3)(19\hat{\eta} + 16)}{40(\hat{\eta} + 1)} \right] \quad (3.5)$$

where  $r_0$  is the radius of the droplets,  $\eta_c$  the viscosity of the surrounding fluid, and  $\hat{\eta} = \frac{\eta_d}{\eta_c}$  being a ratio between the viscosity of the droplet fluid  $\eta_d$  and the surrounding fluid. Notably, the use of this technique is predicated on knowing the viscosities of the fluids being studied, which works well in the case of liquids with Newtonian behavior. For polymer solutions and liquid crystals, the viscosities are not a straightforward matter, however: liquid crystals exhibit orientation-dependent viscosity [69,88] and concentrated polymer solutions often show shear thinning behavior [103], both of which are obstacles to ascertaining with certainty the viscosity to be used in the equation.

## 3.2 Technique Basics

### 3.2.1 Principle of Micropipette Aspiration

The idea behind the microfluidic technique developed is based on the micropipette aspiration techniques used to measure the cortical tension of cells (the interfacial tension of the cell membrane) developed by Hochmuth [119]. This technique aspirates a cell into a microcapillary of radius  $r_d$ , relating the interfacial tension to the initial cell radius  $r_i$  and the pressure difference produced from the aspiration  $\Delta P$  through a modified Young–Laplace equation:

$$\Delta P = 2\gamma \left( \frac{1}{r_d} - \frac{1}{r_i} \right) \quad (3.6)$$

The derivation of this equation proceeds from first considering the canonical Laplace equation for the pressure difference created from a curved interface,  $P_L$ , of radius of curvature  $R$  [119,150,151,167]:

$$P_L = \frac{2\gamma}{R} \quad (3.7)$$

When a droplet or a cell is stable, the pressure on both sides of the interface is equal: the external ambient pressure  $P_1$  and Laplace pressure  $P_L$  sum to the droplet internal pressure  $P_i$ .

$$P_i = P_1 + P_L = P_1 + \frac{2\gamma}{R} \quad (3.8)$$

We then consider the case of a droplet aspirated into a microcapillary with radius  $r_d$  by a pressure  $P_1 + \Delta P$ . As the droplet remains intact, the pressure on both interfaces should be maintained, and the greater pressure from the one side is counterbalanced by the increase in Laplace pressure from the other side, as shown in Figure 20.

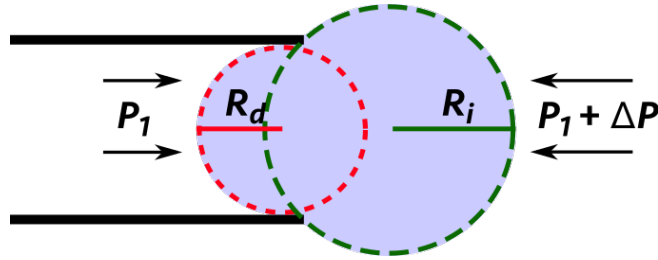


Figure 20. A schematic of a droplet being aspirated into a capillary, indicating the initial, unaspirated radius ( $r_i$ ), the distorted radius ( $r_d$ ), and the pressure difference ( $\Delta P$ ) needed to produce the aspiration. Figure reproduced with permission from Honaker et al, "Microfluidic Tensiometry Technique for the Characterization of the Interfacial Tension between Immiscible Liquids". Copyright 2018 American Chemical Society. [44]

This transforms the pressure balance equation into:

$$P_1 + \Delta P + \frac{2\gamma}{r_i} = P_1 + \frac{2\gamma}{r_d} \quad (3.9)$$

Simple rearrangement of (3.9) gives equation (3.6):

$$\Delta P = \frac{2\gamma}{r_d} - \frac{2\gamma}{r_i} = 2\gamma \left( \frac{1}{r_d} - \frac{1}{r_i} \right)$$

which can also be expressed, by simple rearrangement in terms of the interfacial tension  $\gamma$ :

$$\gamma = \frac{\Delta P}{2 \left( \frac{1}{r_d} - \frac{1}{r_i} \right)} \quad (3.10)$$

Remarkably, equation (3.10) relates the interfacial tension to values that can be obtained simply from an experimental set-up: the initial radius  $r_i$ , the distorted radius  $r_d$ , and the pressure difference  $\Delta P$  needed to produce such a change in radius. Hochmuth, however, employed micropipette aspiration on mammalian cells, and cells have fixed, flexible lipid membranes allowing the aspiration of single cells from a dish or other vessel [119,149,152,153]; most systems of fluids do not have membranes separating the two components from each other, so droplets will coalesce when in contact with each other.

### 3.2.2 Flow-Focusing and Droplet Generation Chips

An obvious solution to the problem of droplet coalescence detailed in section 3.2.1 is to utilize a system where single drops and droplets can be produced and subsequently measured. For this, we can use microfluidic droplet generation devices: whether fabricated from glass or from polydimethylsiloxane (PDMS), these devices are capable of producing monodisperse, uniform droplets of a given diameter by simply tuning the ratio of the flow rate of the continuous phase to that of the dispersed phase [7,24,147,168,169].

We have chosen to use glass capillary microfluidic chips for several reasons. First, the ease of their construction and fabrication allows for rapid changes and adaptations to the geometry of the device whereas, by using a PDMS-based system, a new master mold would have to be created any time changes were needed with the device. Additionally, the glass capillaries themselves are relatively inexpensive and

do not require expensive micro- or nanofabrication suites to process. Finally, the use of PDMS can produce surface-active contaminants in the form of oligomers and residues, which can contaminate our system: in contrast, if properly treated, such a worry is not present with the use of glass.

### 3.3 Technique Development and Optimization

Harnessing both the micropipette aspiration technique and the droplet generation method in a microfluidic chip, the principle of our interfacial tensiometer is to produce a droplet, then immediately measure its interfacial tension soon after production, without the need to collect the droplets in a vial and aspirate them later. We constructed a glass capillary microfluidic device designed to achieve these two aims, thus allowing us to apply the micropipette aspiration technique to fluids.

#### 3.3.1 First Generation Tensiometer: Immediate Aspiration

Round, cylindrical capillaries (Drummond Microcaps, 30  $\mu$ L capacity) were first pulled using a Sutter P-100 pipette puller to create long, tapered points. These points were then cut using either a Narishige Microforge or manually with a diamond cutter blade to create injection capillaries with the desired opening orifice diameter. Once cut, both cut and uncut capillaries were first cleaned by oxygen plasma, which both removes any contaminants adhering to the glass and allows better bonding of any silanes used, before surface treatment to produce glass with the desired anti-wetting properties. Surface treatment was either direct exposure to a silane-based surfactant (here, MAP), immersion of the capillary in a silane-based surfactant solution (prepared from DMOAP), or coating the surface of the glass with a fluoropolymer (CYTOP).<sup>c</sup>

While cleaned, untreated glass is itself hydrophilic, for the hydrophilic substrates used in this work, we sought to improve the hydrophilicity of the glass. To do so, we first cleaned the glass with an oxygen plasma to remove any residues and to make the glass more receptive to silanization treatment. The plasma-treated substrates were then flushed with MAP through capillary filling, ensuring that the surface of the capillary was uniformly coated with surfactant. After allowing these capillaries to stand for at least 10 min, the capillaries were rinsed at least twice with ultrapure deionized water, flushed with air, and dried under vacuum at 120°C for at least 30 min.

To produce hydrophobic glass surfaces, a dilute solution of ~2% w/w DMOAP (42% in methanol, Sigma Aldrich) was prepared in deionized water [170]; the glass capillaries, after plasma treatment, were then immersed in this solution for at least 30 min, changing the solution after 15 min, before rinsing with deionized water and drying under vacuum, similarly to how the MAP-treated capillaries were produced. Alternatively, the superhydrophobic fluoropolymer CYTOP can be used to coat the

---

<sup>c</sup>The names and structures of the materials corresponding to these abbreviations can be found in the "Table of Chemicals" on page xvii.



glass for a hydrophobic coating; however, due to how CYTOP bonds to glass (it merely physisorbs to the glass, as opposed to the chemisorption resulting from DMOAP and MAP treatment), careful handling is needed to both achieve a uniform coating layer and to avoid the polymer layer from detaching from the glass. In contrast, the silanes (such as DMOAP and MAP) chemically bond to the surface in a manner that does not affect the diameter of the capillary.

The ideal capillary treatment is such that the dispersed phase from which the droplets are made does not wet the glass surface, while the continuous phase does. Micropipette aspiration on cells works in part because the plasma membrane of the cell helps to maintain its shape [119], but droplets are not surrounded by membranes and are thus susceptible to coalescing and wetting to surfaces. We aim to treat the glass such that the continuous phase wets to its surface, creating a "slip layer" between the droplet and the glass, which helps to keep the droplet from wetting to the glass [171]. If the droplet wets, the equilibrium shape of the droplet is lost and measurement of the droplet radii becomes difficult, if not impossible.

Once dried, the devices were assembled on clean glass microscopy slides. At its simplest, a device requires an injection port for each of the continuous and dispersed phases and a collection capillary to act as an outlet. Both the injection and collection capillaries were inserted into a square enclosing capillary and adjusted while viewing under a microscope: the injection capillary was placed slightly inside the collection capillary. A schematic of this is presented in Figure 21.

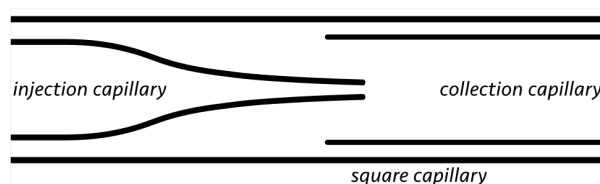


*Figure 21. A schematic of the assembly of the injection and collection capillary, where the injection capillary is placed somewhat inside the collection capillary and the whole set-up is encased by the square capillary. This ensures that, when a significant mismatch in density is present, the droplet is still pushed into the channel rather than into the surrounding square capillary.*

Once the capillaries were arranged, a 21-gauge cannula, with its plastic base notched to straddle the collection and to sit directly above the opening of the square capillary, was placed. Two-part epoxy (Pattex) was used to fix the capillaries and the cannula in place, while UV-curable optical adhesive (Norland 81) was capillary filled into the space between the square capillary and the injection capillary before curing with a UV lamp (330 nm) for 10 min to cure the adhesive and create an airtight seal out of which none of the material could flow, producing a device with only three inlets/outlets. The assembled device was then allowed to stand overnight to allow all epoxies to dry before use. An example of an assembled device is presented in Figure 22.

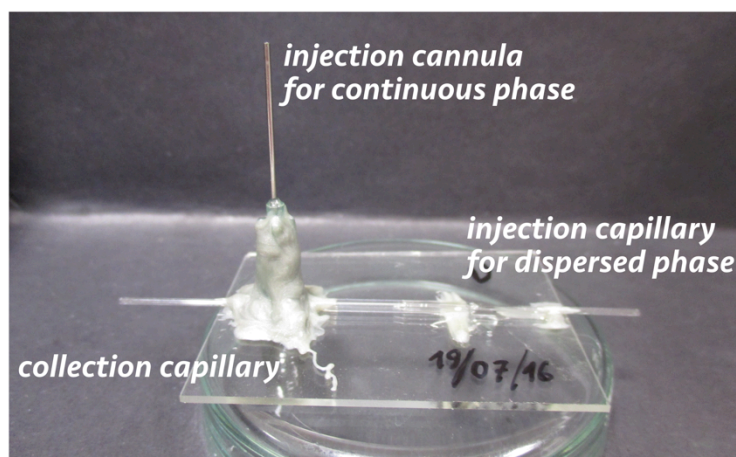


Figure 22. The assembled microfluidic device used for interfacial tension measurements, consisting of two injection points (one for the continuous phase and the other for the dispersed phase) and a collection capillary into which the droplets are produced.

Materials were then flowed using a microfluidic flow control unit (Fluigent MFCS-EZ) consisting of an air compressor, a pressure regulator combined with a manometer to adjust and continuously monitor the pressure supplied to the system, and septa used to pressurize and seal the vials. Fresh septa and fresh small diameter, sharp-tipped needles to pierce the septa (normally 23 gauge, but with 18 gauge needles used for more viscous materials) were used in every experiment: piercing the septa repeatedly with needles creates holes that can cause pressure to leak. Airtight tubing was used to seal the system, ensuring that the pressure readings obtained were precise and accurate; the pressure used to flow the liquids,  $\Delta P$ , is directly related to the flow rate by the Hagen–Poiseuille equation:

$$\Delta P = \frac{8\eta L Q}{\pi R^4} \quad (3.11)$$

where  $Q$  is the volumetric flow rate,  $L$  the length of the tube/pipe,  $\eta$  the dynamic viscosity of the material being flowed through the tube, and  $R$  the radius of the tube. The Hagen–Poiseuille equation is not straightforward to apply to our system due to the changing radii of the tube (we go from the needle to the needle connector, then to the tubing, and finally into the capillary, each of which is of different lengths and, in the case of the capillary, additionally changing radii), but shows that we can, by adjusting the pressure supplied from the pressure regulator, directly increase or decrease the flow rates of materials. All three vials need to be pressurized throughout the experiment, since we will be eventually applying a pressure to push the droplet back towards the injection capillary. A schematic of the full experimental set-up, with the device connected to the inputs and outputs, is shown in Figure 23.

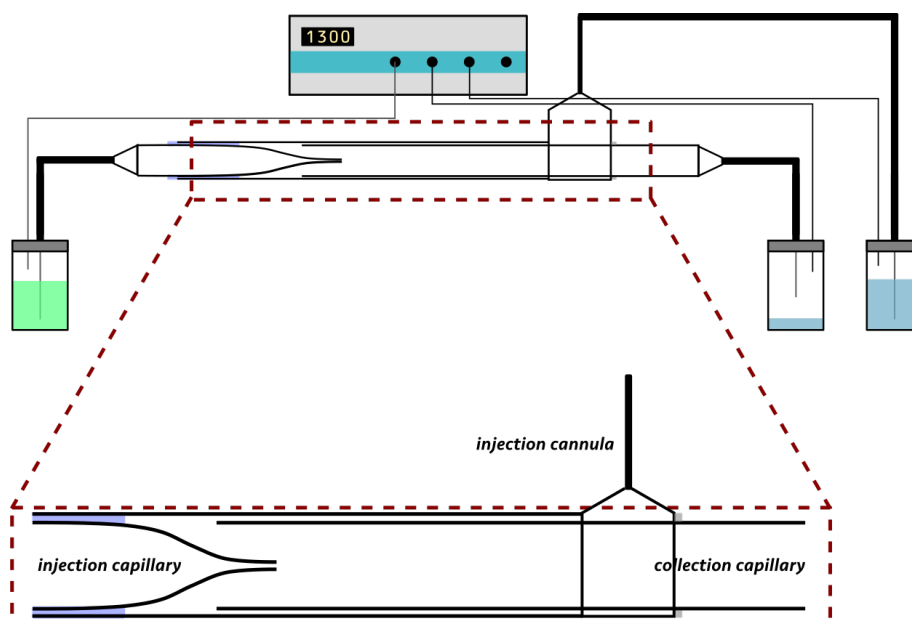


Figure 23. First-generation microfluidic set-up for droplet generation and interfacial tension measurement. The microfluidic device, as shown in the inset, is connected with tubing to vials sealed with septa. A pressure regulation system then supplies a well-controlled pressure to each of the vials, producing a flow as described by the Hagen–Poiseuille equation. The collection vial is sealed additionally with a septum to create the backwards pressure necessary to measure the interfacial tension.

After producing droplets with the device, the droplet can be immediately aspirated back into the capillary from which it was produced, with the interfacial tension being related to the pressure necessary for aspiration, the initial radius of the droplet produced, and the orifice diameter of the injection capillary. To do so, once an appropriate droplet is first identified and isolated, all of the pressures supplied to the device are reduced to a point where the droplet is held steady against the injection capillary without aspiration occurring. From that point, pressure from the outlet is increased until aspiration takes place; the difference in pressures between these states is defined as  $\Delta P$ , the quantity needed in equation (3.6). The process of aspiration of the droplet is detailed in Figure 24.

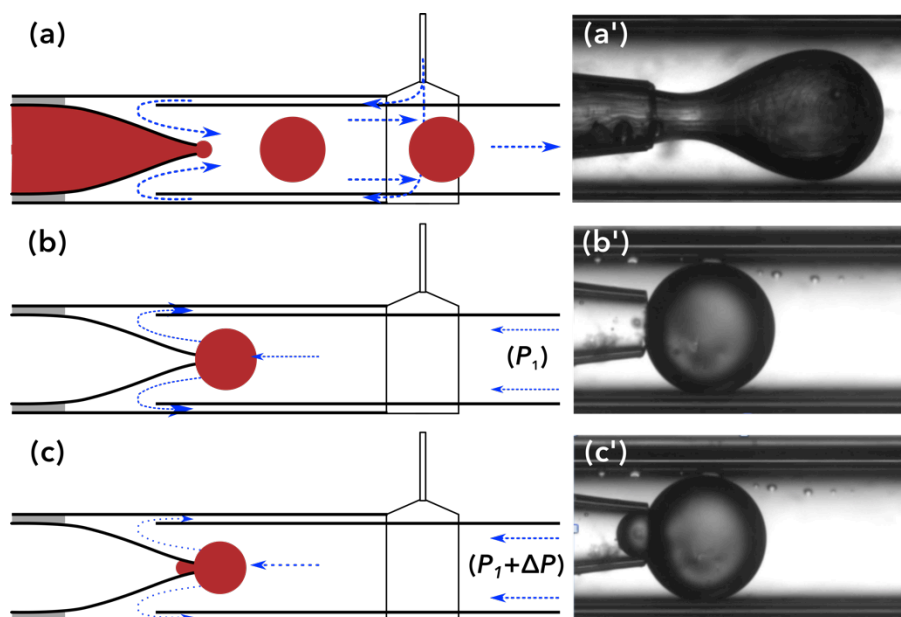


Figure 24. Demonstration of the aspiration technique on a droplet of 5CB in a 1.0 mM CTAB solution. (a) A schematic of the droplet production process in a flow-focusing device. (a') A picture of the process depicted in (a). (b) and (b'): The aspiration process, demonstrating when the droplet is held steady in the channel against the injection capillary. The radius of the droplet at this point corresponds to  $r_i$  in equation (3.5). (c) and (c'): When the pressure necessary for aspiration is applied, the droplet then begins to retract into the injection capillary; the left-hand droplet radius here corresponds to  $r_d$ . Figure reproduced with permission from Honaker et al, "Microfluidic Tensiometry Technique for the Characterization of the Interfacial Tension between Immiscible Liquids". Copyright 2018 American Chemical Society. [44]

Once the pressure difference ( $\Delta P$ ) necessary to induce aspiration is identified, the equilibrium droplet radius before aspiration ( $r_i$ ) and left-hand droplet radius upon aspiration into the injection capillary ( $r_d$ ; in the latter case, this is normally the orifice diameter of the injection capillary) are both measured. These can be manually measured using an image processing software, such as ImageJ or even MSPaint, obtaining the radii in pixels, or measured using an automatic droplet detection algorithm [172]. The measured radii are then converted into SI units and input into equation (3.6) to finally obtain the interfacial tension.

To avoid any contamination that could result from residues adhering to any of the epoxies used, a given device would be used only for a single combination of fluids and surfactant solutions, with thorough cleaning with at least two cycles of alternating rinses of isopropanol and ultrapure deionized water if a device were to be reused. Generally, however, devices would typically be used for one set of experiments before being discarded.

### 3.3.2 Second Generation Tensiometer: Aspiration into a Constricted Capillary

While the first generation tensiometer has the advantage of a simple construction, during the initial measurements, several issues became obvious. One of these issues was that it was quite difficult to pinpoint the exact pressure necessary for the

aspiration: as soon as aspiration begins, the droplet continuously retracts into the injection capillary. Depending on the size of the injection capillary relative to the size of the droplet produced, there was also the issue that, rather than being aspirated into the injection capillary, the droplet could frequently become aspirated into the space around the injection capillary. This often happened with very heavy materials such as liquid metals. If such an aspiration happened, this would result in no obtainable measurement and wasted material.

To solve these issues, the device was adjusted to, rather than aspirating droplets into the injection capillary, aspirate the droplets into a constricted capillary; that is, a capillary where, somewhere along its length, the capillary tapers into a constriction before widening again. Such capillaries are produced by programming the pipette puller to heat the glass to soften it while very gently and slowly pulling from both ends, creating a narrowing of as small as 150  $\mu\text{m}$ .<sup>d</sup> Silanization and preparation of the glass proceed as for the first generation tensiometer, with particular care needed to avoid breakage at the constriction, before assembly on a glass slide following the same procedure as before. Keeping the constriction within the length of the enclosing square capillary, such that the constriction was immersed in the continuous phase, was found to be necessary in order to minimize lensing effects from the curvature of the cylindrical capillary. This allowed for a more accurate measurement of the radii of curvature.

The aspiration procedure proceeded similarly to the technique where the droplet was measured at the injection capillary orifice, with the produced droplet being first immobilized in the channel before proceeding with the measurement. Unlike the case of the first-generation tensiometer, the application of different aspiration pressures can produce different distortions of the droplet within the constriction, allowing for multiple measurements with different pressure differences to be obtained on the same droplet, thus improving the overall accuracy of the technique. The process of both droplet generation and aspiration in this geometry is depicted in Figure 25.

---

<sup>d</sup>Constriction diameters of as low as 60  $\mu\text{m}$  were obtainable, and it is conceivable that such capillaries can be useful when measuring extremely low interfacial tensions (on the order of  $\mu\text{N/m}$ ). However, because capillaries pulled to that diameter have extremely thin glass walls, they easily break. The smallest feasible constriction diameter was found to be about 150  $\mu\text{m}$ : with this diameter, it was considerably more resilient during the treatment process and while assembling the device.

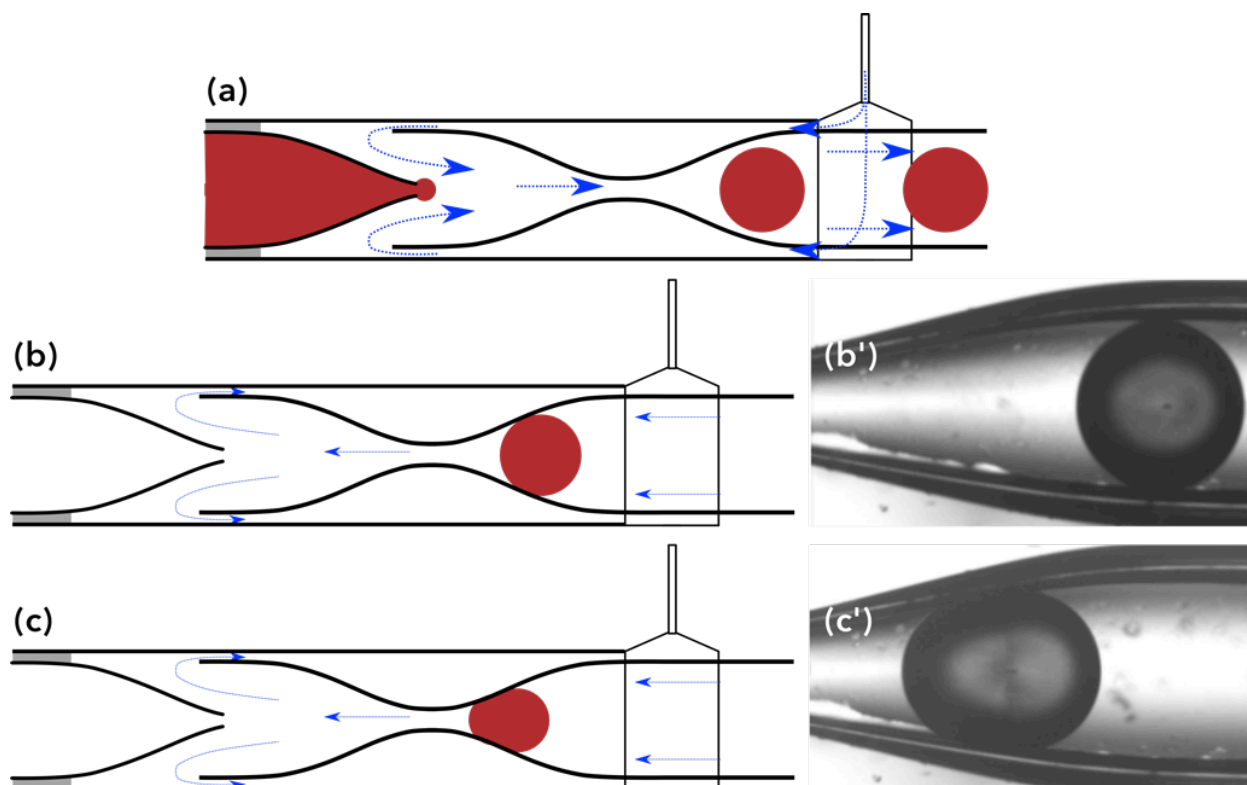


Figure 25. Production and aspiration process of a drop of 5CB in 1.0 mM CTAB solution using the constricted capillary geometry, showing (a) the droplet production process; (b) and (b') the initial state of the droplet before aspiration into the channel; (c) and (c') the aspirated droplet. Figure reproduced with permission from Honaker et al, "Microfluidic Tensiometry Technique for the Characterization of the Interfacial Tension between Immiscible Liquids". Copyright 2018 American Chemical Society. [44]

While the measurement technique is similar to that of the first-generation interfacial tensiometer, where the aspirated radius (often denoted in these images as the left-hand radius) is the one that becomes deformed, this is not immediately apparent. To show that the left-hand radius alone is sufficient to measure the interfacial tension, we first consider the case when the droplet is held stationary in or very near the entrance of the constriction, as shown in Figure 26.

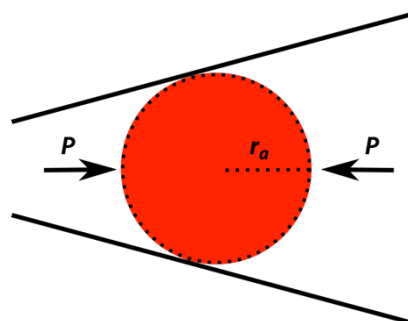


Figure 26. Schematic of a droplet held in the constriction without distortion. The pressure on each side is  $P$ , keeping the droplet in place, with the radius of the droplet  $r_a$ .

In this case, the droplet is held fixed by a pressure  $P$  applied from both sides, resulting in the droplet with radius  $r_a$  maintaining its shape without deformation. This means that the droplet internal pressure  $P_i$  is balanced at each interface with the ambient and Laplace pressure:

$$P_i = P + \frac{2\gamma}{r_a} \quad (3.12)$$

Once the droplet proceeds into the constriction upon applying a pressure difference  $\Delta P$  from the side outside the constriction, Figure 27, there are then two different interfaces: the interface inside the constriction, which has a smaller radius of curvature ( $r_{b1}$ ), and the interface outside the constriction with a larger radius of curvature ( $r_{b2}$ ) against which the increased pressure  $P + \Delta P$  is applied. We assume here that the liquid does not wet the surface of the capillary, a necessary condition to ensure that the pressure changes we apply to the droplet only result in a deformation of the droplet: large contact areas were not seen to negatively affect the results obtained provided wetting did not occur.<sup>e</sup>

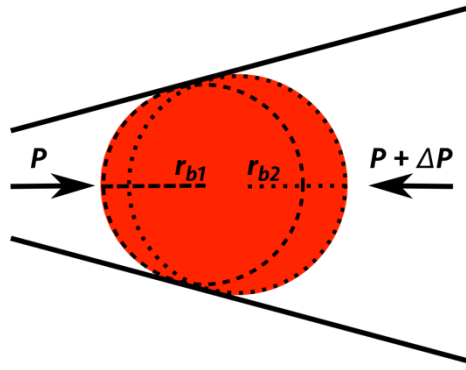


Figure 27. Schematic of the aspiration of the droplet upon application of a pressure  $\Delta P$ , now with two different radii: one on the left-hand side,  $r_{b1}$ ; the other on the right-hand side,  $r_{b2}$ .

Assuming a uniform interfacial tension, the pressure balance on the left-hand side thus becomes:

$$P + \frac{2\gamma}{r_{b1}} = P_i \quad (3.13a)$$

while the pressure balance on the right-hand side is:

$$P + \Delta P + \frac{2\gamma}{r_{b2}} = P_i \quad (3.13b)$$

Setting these two equations equal to each other, we then get:

$$\begin{aligned} P + \frac{2\gamma}{r_{b1}} &= P + \Delta P + \frac{2\gamma}{r_{b2}} \\ \Delta P &= \frac{2\gamma}{r_{b1}} - \frac{2\gamma}{r_{b2}} = 2\gamma \left( \frac{1}{r_{b1}} - \frac{1}{r_{b2}} \right) \end{aligned} \quad (3.14)$$

---

<sup>e</sup>Wetting issues were found to typically occur within the narrowest parts of the constriction, where the surface was often not sufficiently non-wetting due to the difficulty of plasma treatment in narrow areas.



Equation (3.14) is very similar to (3.6), the difference being that it references the left- and right-hand radii of the droplet rather than initial and final states. Experimentally, however, we see that the initial and final right-hand radii of curvature *are* often equal to each other, as indicated in Figure 28.

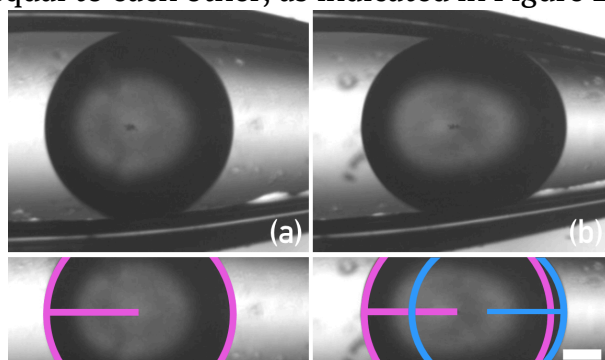


Figure 28. Aspiration of a droplet of 5CB in a solution of 10 mM SDS (aq), (a) before and (b) after the application of aspiration pressure. The droplet is aspirated to the right, mirrored to the cases shown in Figure 26 and Figure 27; while an appreciable difference in the radius on the right-hand side, indicated in blue (exposed to lower pressure), is observed between (a) and (b), there is no change in the radius on the left-hand side, as indicated by the pink circle drawn in the lower images.

Because of lensing and distortion, the radii of curvature of the droplet are not the same as the apparent radii one would measure. This means the radii of curvature need to be measured, as much as possible, *without* including the portion of the capillary close to the wall: despite the immersion of the constriction in a liquid, whether water or another material, the cylindrical structure of the capillary can lead to prominent distortion of the droplet close to the wall. Therefore, while it appears that the left-hand radius of the droplet (the side not under aspiration) decreases as the droplet is pushed into the constriction, when the region close to the capillary wall is cropped out, it becomes clear that the radius of curvature does not change between the initial and aspirated states. The outcome of this is that equation (3.6), for many deformations, becomes applicable to our system. This means that, in Figure 25, the interfacial tension can be determined by measuring the radius of curvature nearest to the constriction both before and after aspiration.

The determination of the interfacial tension proceeded similarly to measurements with the first-generation tensiometer, using the difference in readings from the pressure regulator before and after the aspiration process. Often with this tensiometer, we would begin with the droplet slightly "pre-aspirated" into the channel before applying small changes in the pressure to ensure that the pressure differences applied were "true" pressure differences that produced the change in the droplet radii. The process of pressure determination is illustrated in Figure 29.



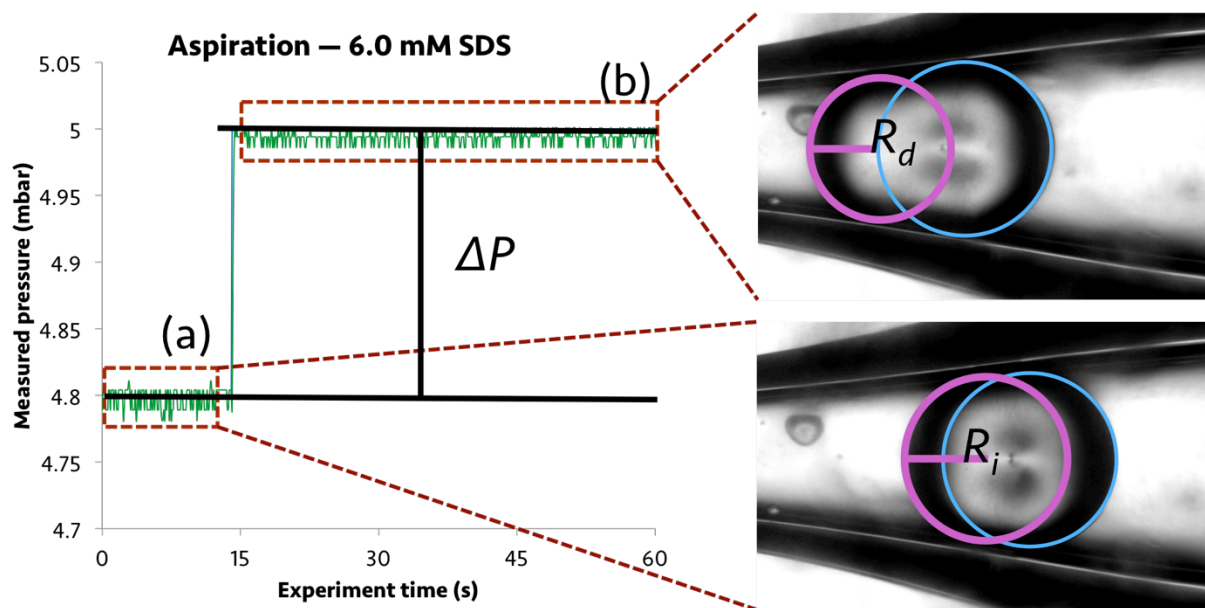


Figure 29. Image of the pressure graph obtained during the experiment with images corresponding to the droplet states. (a) indicates the pressure before applying the aspiration pressure and the corresponding initial radius; (b) the pressure and corresponding droplet state upon applying the pressure. The difference in pressure between these two states is the  $\Delta P$  needed in equation (3.6) to determine interfacial tension, with the radii of curvature used in the equation measured by the left-hand (aspirated) side. The blue circle on the right-hand side of the droplet indicates the radius of curvature on the right-hand side, which remains unchanged, allowing us to use the technique as described. The nonzero initial pressure from the pressure graph is a product of hydrostatic pressure from the columns of fluids produced by the tubing.

### 3.4 Equilibrium Surface and Interfacial Tensions

#### 3.4.1 Calibration with Surfactant Solutions

We began the process of testing the interfacial tensiometer by using it to measure the interfacial tensions between a series of aqueous solutions of the surfactant TWEEN 20 (polysorbate 20) and of the surfactant SPAN 80 (sorbitan oleate) in hexadecane. These systems were chosen due to their extensive previous characterization by Hashimoto et al using sessile drop methods [155]; therefore, being able to reproducibly replicate their results shows the utility of our system and our technique. These solutions also have the advantages of being straightforward to prepare and store and us being able to easily treat the glass substrates to prevent undesired wetting of the dispersed phase: since we are producing water droplets in the oil phase, we can use hydrophobized glass in both the injection and collection capillaries to prevent wetting of the water droplets.

We prepared a series of five solutions (0.02% w/w, 0.2% w/w, and 2.0% w/w TWEEN 20 in water and 0.03% w/w and 0.3% w/w SPAN 80 in hexadecane). This enabled us to measure a total of six systems of liquid-liquid interfacial tensions, obtaining the values for the interfacial tensions between the phases given in Table 3.

Table 3. Interfacial tensions of TWEEN 20 (aq) solutions against SPAN 80 in hexadecane solutions. Reference values from Hashimoto et al [155] are indicated in parentheses. Data reproduced with permission from Honaker et al, "Microfluidic Tensiometry Technique for the Characterization of the Interfacial Tension between Immiscible Liquids". Copyright 2018 American Chemical Society. [44]

concentration TWEEN 20 (aq), w/w	concentration SPAN 80 in hexadecane (w/w)	
	0.03%	0.3%
0.02%	4.4 ± 0.5 mN/m (4.4 ± 0.2 mN/m)	1.7 ± 0.2 mN/m (1.4 ± 0.2 mN/m)
0.2%	2.3 ± 0.3 mN/m (2.5 ± 0.2 mN/m)	0.8 ± 0.3 mN/m (0.7 ± 0.1 mN/m)
2.0%	2.7 ± 0.4 mN/m (2.4 ± 0.4 mN/m)	0.4 ± 0.2 mN/m (0.2 ± 0.0 mN/m) <sup>f</sup>

While the uncertainty values in our measurements are considerably higher than those reported by Hashimoto et al [155], the results fall within the interfacial tension values reported. The uncertainties arise from uncertainties of the determination of the droplet radius optically and the uncertainties in the pressure pump and regulator themselves: the pressures used to induce aspiration had a precision of as little as 0.01 mbar, which corresponded to the uncertainty supplied by the pressure regulator.

### 3.4.2 Interfacial Tension of Nematic Liquid Crystals against Aqueous Surfactant Solutions

To date, the interfacial tension of the nematic liquid crystal 5CB has been difficult to measure, primarily because of the inadequacies of the pendant drop technique and the sensitivity of most other interfacial tensiometry techniques to data that are not well characterized for 5CB [39,46,162,173]. We thus sought to measure the interfacial tension of 5CB against aqueous solutions of surfactants. The plan was to first measure the interfacial tension of 5CB against a solution of 1.0 mM CTAB in water, a system that was characterized by Kim et al using the pendant drop technique [46], before reducing the surfactant concentration and extrapolating to a zero surfactant concentration (by fitting to a Szyszkowski equation).

Prior to commencing any measurement, an important parameter to consider is the surface treatment. Typically, the optimal measurement method is to treat the glass so that the continuous phase readily wets or that the dispersed phase does not wet: this is why we used hydrophobic glass for measuring the interfacial tension of the water solutions against hexadecane, as hexadecane wets readily to DMOAP-treated glass while water will not wet. The situation with 5CB is more complicated: 5CB wets very readily to untreated and hydrophilically treated glass. However, 5CB

<sup>f</sup>The error value of ±0.0 mN/m here, as reported by Hashimoto et al, likely represents an error that, when significant digits are accounted for, is then approximated below 0.05 mN/m rather than a complete absence of uncertainty.

wets *less* to glass treated with DMOAP (a hydrophobizing agent) compared to hydrophilic glass. DMOAP-treated substrates are hydrophobic [170] to the extent that 5CB will not readily wet the surface; since the condition we need is that the dispersed phase should not wet the glass substrates, DMOAP treatment is the best choice. The use of CYTOP is problematic because of the treatment process, requiring a uniform coating of polymer (which can be very difficult to achieve absent spin coating). An alternative approach to avoid wetting issues would be to produce water droplets in 5CB, using a hydrophobic coating to prevent the water droplets from wetting the glass, but there are two main obstacles to this. First, compared to the surfactant solutions, 5CB is a relatively expensive compound: at the time of preparing this thesis, the cheapest source of 5CB we found with reasonable purity was for €0.70/gram. In contrast, the materials for preparing a 1.0 mM aqueous CTAB solution would cost less than €0.001/mL. Additionally, 5CB in the nematic phase is optically scattering (it appears opaque), which would make measurements difficult to accomplish since the constriction would be immersed in a scattering medium.

With 1.0 mM CTAB in water (above CTAB's critical micelle concentration, CMC, of 0.9 mM), we obtained an interfacial tension value of  $3.2 \pm 0.8$  mN/m at room temperature [154], which corresponds to the range reported by Kim et al [46] taking into account the uncertainty in the density values reported for 5CB. Measurements of lower concentrations of CTAB in water, however, were difficult to perform due to CTAB's particularly high Krafft temperature: below  $\sim 25^\circ\text{C}$  [174], CTAB crystallizes out of solution, making it difficult to maintain a constant surfactant concentration. To overcome this, we instead switched to using SDS, which, in addition to having a lower Krafft temperature ( $\sim 15^\circ\text{C}$  [174]), has a higher CMC (8.2 mM). We thus performed measurements on a series of SDS solutions of different concentrations, ranging from 0.010 mM to 20 mM (both above and below the critical micelle concentration), obtaining the values for interfacial tensions presented in Table 4. Working with lower concentrations of surfactant, however, had issues in terms of avoiding wetting, which was problematic if the surfaces were not adequately treated, but some data were still obtainable.

*Table 4. Interfacial tension values of 5CB against aqueous solutions of SDS of various concentrations. Each measurement between 0.10 mM and 20.0 mM represents an average of a minimum of four data points for each concentration, while only one data point was possible for 0.010 mM due to wetting issues.*

<b>Concentration SDS</b>	<b>Interfacial Tension</b>
20.0 mM	$3.8 \pm 1.0$ mN/m
10.0 mM	$3.7 \pm 0.3$ mN/m
6.0 mM	$10.4 \pm 0.8$ mN/m
5.0 mM	$11.4 \pm 0.8$ mN/m
2.0 mM	$13.9 \pm 0.9$ mN/m
1.0 mM	$17.0 \pm 0.3$ mN/m
0.10 mM	$28.3 \pm 0.7$ mN/m
0.010 mM	$30.5 \pm 0.6$ mN/m

Above the CMC of SDS, the interfacial tension is very similar to that of the case of CTAB above its critical micelle concentration. The results for interfacial tensions below the critical micelle concentration show a logarithmic dependence on surfactant concentration, corresponding to an increase in the total surface coverage of the interface with surfactant molecules. This logarithmic dependence is expected by the Szyszkowski equation (as described by equation (2.18) [175]), and also as we expect due to the surfactant covering the surface of the liquid crystal droplet to form a monolayer. We are able to fit below-CMC data to equation (2.18), obtaining the fitting equation as  $\gamma = 31.8 - 4.65 \cdot \ln(1 + 18.2 \cdot c)$ , with  $\gamma_0 = 31.8$  mN/m,  $\Gamma_\infty = 1.9 \cdot 10^{-3}$  m<sup>-2</sup> (assuming room temperature), and  $K_L = 18.2$ . With this, overall, these data agree with the behavior of the surface tension of surfactants in aqueous solutions [120] and observations of the interfacial tension of a smectic liquid crystal as a function of surfactant concentration [40,41]: a greater coverage of the interface with surfactant will correspond to a decrease in the interfacial tension.

For the two points above the critical micelle concentration, no significant change in interfacial tension is observed with increasing concentration: as the surfactant coverage at the interface is complete, no further molecules should adsorb to the interface, which means the interfacial tension should plateau and remain constant. The only known data to report on the interfacial tension above the critical micelle concentration, by Guo et al, reports a value of  $\sim 5$  mN/m for 17.5 mM SDS solution [176]; within the margin of error, this does agree with the results for 20.0 mM SDS solution, and all of these data match well to the values obtained for using above-CMC solutions of CTAB. At the same time, the discontinuity between the sub-CMC and above-CMC values is disconcerting, since the two curves should not be discontinuous. It may be that the surfactant "emulsifies" the liquid crystal droplets once complete surface coverage is achieved, creating some degree of miscibility to drive the interfacial tension downwards [49]. Further work would be needed, in particular by measuring the interfacial tension at additional points closer

to the CMC on both sides, to better fit the Szyszkowski equation curve and to determine whether the discontinuity we see is real.

The results obtained by our technique are additionally summarized in graphic form in Figure 30.

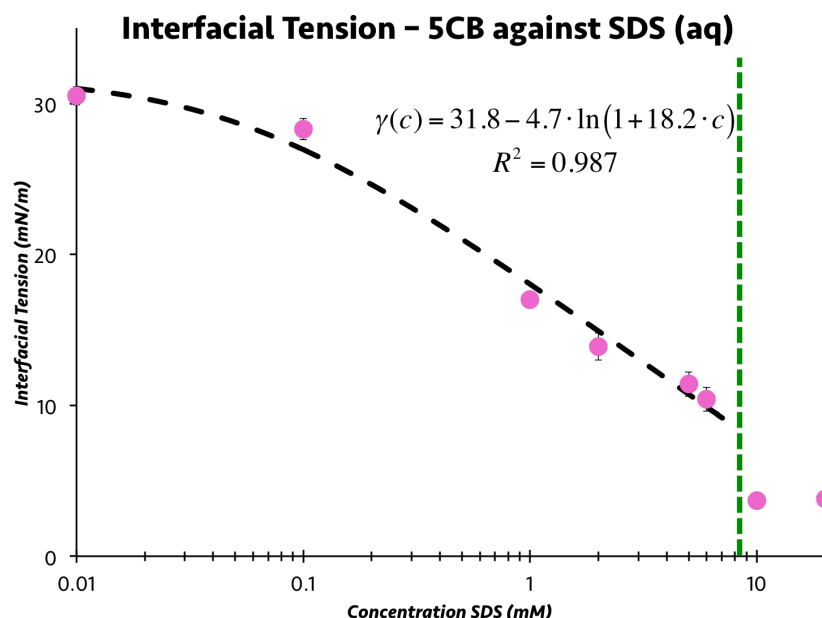
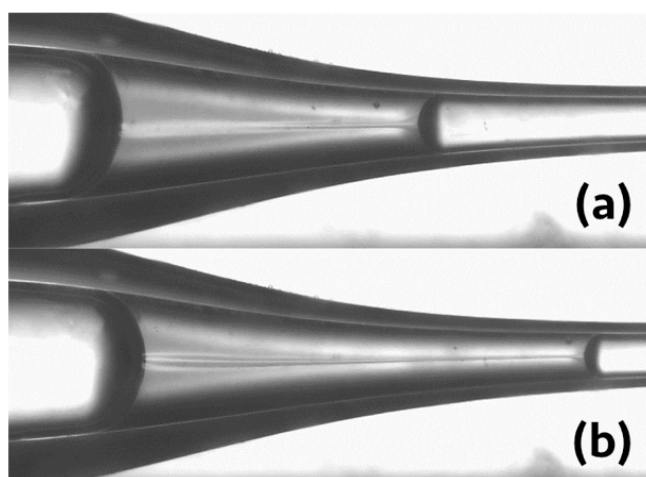


Figure 30. Interfacial tension of 5CB against aqueous SDS solutions of various concentrations. The error bars indicate the uncertainties indicated in the measurements presented in Table 4, while the line is drawn through the data points below the CMC. The green dotted line indicates the CMC. Figure adapted with permission from Honaker et al, "Microfluidic Tensiometry Technique for the Characterization of the Interfacial Tension between Immiscible Liquids". Copyright 2018 American Chemical Society. [44]

Normally, the measurement of the interfacial tension of 5CB in pure water without surfactant is difficult to achieve [46,162]; we were able to, however, obtain a value of  $30.8 \pm 7.5$  mN/m [44], reasonably in agreement with literature values [45,177]. We find that this number is lower than the Szyszkowski extrapolation value of 31.8 mN/m, which is due to the anchoring condition of the liquid crystal: in the absence of surfactant, the liquid crystal will adopt a planar configuration, while a homeotropic anchoring condition exists in the presence of surfactant, the threshold condition for homeotropic anchoring occurring at a low surfactant concentration [178]. In the absence of surfactant, the liquid crystal droplets very readily wet the glass capillary surfaces, regardless of surface treatment, which is a part of the reason for the high uncertainty in this value: while DMOAP treatment helps the issue, some problems with wetting, especially in the narrowest parts of the capillary, still exist.

### 3.4.3 Interfacial Tension of Nematic Liquid Crystals against Aqueous Polymer Solutions

We additionally obtained measurements of 5CB against aqueous solutions of PVA, commonly used as a continuous or internal phase in the production of stabilized droplets and shells [24,169,179]. Because PVA is a non-surfactant stabilizer, similar to the case of 5CB in pure water, wetting issues were particularly observable, as depicted in Figure 31.



*Figure 31. Aspiration process of 5CB in a 1% w/w PVA (aq) solution at (a) an initial pressure and (b) at an increased pressure. Despite wetting issues which produce negative curvature, the radii of curvature can be defined in both (a) and (b), allowing interfacial tension to be calculated by instead using the absolute value of the curvature.*

Despite these, radii of curvature of both undistorted and distorted droplets remained identifiable, and we were able to obtain a value for the interfacial tension of 5CB against 1% w/w PVA solution of  $30.3 \pm 6.0$  mN/m. While no literature data for this system was found, Andy Schanen, during his Master's thesis in the ESMP group, found that the interfacial tension of 5CB against a 5% w/w solution of the same PVA was  $29.7 \pm 1.5$  mN/m [172], which reasonably confirm these values. In the experiments by Mr. Schanen, no wetting issues were observed (and a spherical droplet shape obtained, more akin to the cases in Figure 28), the reason most likely being the increased concentration of PVA which forms a better protective "shell" around the droplet, preventing wetting more effectively akin to the case of the higher concentrations of surfactant.

The similarity of both of these values (at 1% and 5% w/w PVA) to the 5CB-pure water interfacial tension [44,45] suggests that PVA, while a stabilizer during droplet and shell production, employs a different mechanism of stabilization compared to a surfactant. The PVA does not act as a surfactant, where it would partially embed within the liquid crystal at the interface like an amphiphile would [8,76,178,180], but instead most likely forms a protective "shell" around the liquid crystal droplet to stabilize it. This has a consequence on the liquid crystal alignment: water alone induces planar alignment of 5CB [46,74,75], and the lack of surfactant behavior of PVA means that the liquid crystal alignment remains planar. In comparison, most

surfactants, particularly those with long alkyl tails, adsorbed to the surface produce homeotropic alignment [8,75,180,181]. A schematic of the alignment of a liquid crystal in these three situations (planar alignment in pure water; planar alignment in the presence of PVA; and homeotropic alignment with an adsorbed surfactant) is presented in Figure 32.

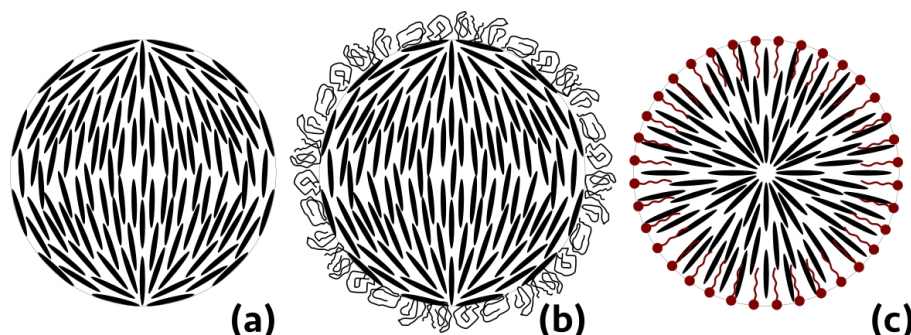


Figure 32. A two-dimensional projection of the liquid crystal alignment in a droplet with (a) planar aligning conditions induced by pure water; (b) planar aligning conditions in the presence of an aqueous solution of PVA, which does not embed itself into the liquid crystal droplet; and (c) homeotropic alignment created by a surfactant, where the surfactant molecules adsorb to the interface between the liquid crystal and water. The structures presented in both (a) and (b) are each one possible configuration of the director orientation in the case of planar alignment: as shown by the Poincaré-Hopf theorem, the sum of the strengths of the defects present on a spherical surface must equal  $+2$  [51]. Additional equilibrium configurations would include two  $+1$  defects arranged such that the director forms concentric rings around the defect rather than radiating radially from the defect. This drawing is not to scale.

As liquid crystals are anisotropic materials with alignment-dependent properties, it stands to reason that the interfacial/surface tension of a liquid crystal is correspondingly alignment-dependent. Work by both Proust et al and Gannon et al, however, suggested that there was no significant difference in the interfacial tension of 5CB based on alignment [45,159]. We found that, by extrapolating the Szyszkowski equation to zero surfactant concentration, the interfacial tension difference between the two alignments was about  $1.0 \text{ mN/m}$  ( $31.8 \text{ mN/m}$  for homeotropic alignment compared to  $30.8 \text{ mN/m}$  for planar alignment), which is on the same order as previously described. Additionally, while there was a surface tension change upon the phase transition from nematic to isotropic (as is the case with many anisotropic liquid crystal properties, such as the refractive indices [90], where there is discontinuity upon phase transition), the discontinuity was small ( $\sim 0.4 \text{ mN/m}$ ). Further work will aim to establish the exact magnitude of this difference.

In the absence of surfactants, aside from the extrapolation technique, the difference between interfacial tensions could be measurable by the use of a magnetic field to align the liquid crystal into either its homeotropic or planar configuration. This would not be readily achieved by using droplets, however, due to topological concerns: achieving a pure radial configuration in the droplet is not



possible with magnetic field alignment. We would thus be more readily able to achieve uniform homeotropic alignment under a field either by using flat films or menisci. As the equipment for this creates added complexity, however, the use of the extrapolation method is most likely the simplest technique to measure the interfacial tension in the radial configuration.

### 3.4.4 Surface Tension of Air against Surfactant Solution

Since the system can measure between immiscible fluids, as air is largely immiscible with water, an interest is whether or not the system can measure surface tension. To do so, we first produced air bubbles in a 6.0 mM sodium dodecyl sulfate (SDS) solution<sup>§</sup>; then we measured them in the same manner as the oil–water system in Section 3.4.1. The image is easily resolvable to determine the surface tension: as seen in Figure 33, the air bubble inside the surfactant solution provides a very clear interface that neither wets the glass surface nor collapses during the measurement. Hydrophilic treatment, nevertheless, is preferable for the glass to ensure better wetting of the surfactant solution.

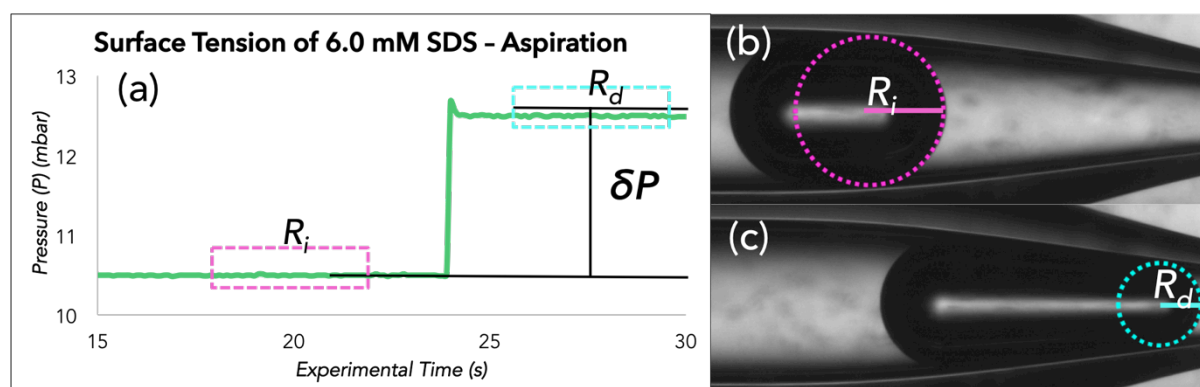


Figure 33. Measurement of the surface tension of a 6.0 mM SDS (aq) solution using the aspiration technique, with the relevant parameters as indicated in (a) the pressure graph during the measurement; (b) before aspiration, with the initial radius of curvature as indicated; and (c) after aspiration, which reduces the radius of curvature. The measurement of the surface tension is similar to the interfacial tension measurements described in this chapter, with the difference being the use of an air bubble as opposed to another liquid. Figure reproduced with permission from Honaker et al, "Microfluidic Tensiometry Technique for the Characterization of the Interfacial Tension between Immiscible Liquids". Copyright 2018 American Chemical Society. [44]

Using our constricted capillary technique, the surface tension of the solution was found to be  $35 \pm 4$  mN/m, which is consistent with literature measurements [182].

<sup>§</sup>A 6.0 mM SDS solution was chosen for the continuous phase, as opposed to pure water, primarily because solution was prepared and this measurement could be done either before or after a measurement with liquid crystals in Section 3.4.2.



### 3.4.5 Interfacial Tensions of Liquid Metals

With one of the goals of the thesis being to incorporate gallium alloys into fibers, being able to characterize the interfacial tension of galinstan, the intended alloy to be used, is of interest. Since pH does not normally have an appreciable effect on surface/interfacial tension, and since we need to avoid oxidation of the galinstan surface (which can be accomplished either by using acidic or basic conditions [12,112]) in order to measure the interfacial tension of galinstan against water (and not of gallium oxide), we sought to characterize the interfacial tension of the liquid metal galinstan against water by using solutions of the strong base sodium hydroxide (NaOH). A difference in the protocol when using galinstan as opposed to another material is that a syringe pump was used to flow the galinstan to avoid any unintentional introduction of oxygen and premature oxidation of the material, as the pressure regulators operate by blowing air onto the solutions to induce pressure.

Measurements were performed using aqueous 0.01 M, 0.1 M, and 1.0 M NaOH (aq) solutions, corresponding to pH values of 12, 13, and 14, respectively, the results of which are presented in Table 5 [154].

*Table 5. Interfacial tensions of galinstan against sodium hydroxide solutions of various concentrations. Each point represents a minimum of three measurements for each value. Table reproduced with permission from Honaker et al, "Microfluidic Tensiometry Technique for the Characterization of the Interfacial Tension between Immiscible Liquids". Copyright 2018 American Chemical Society. [44]*

Concentration NaOH (aq)	Interfacial Tension
0.010 M	442 ± 18 mN/m
0.10 M	446 ± 18 mN/m
1.0 M	462 ± 32 mN/m

These measurements are largely in concordance with literature values [183] and, within the measurement uncertainties, do not show a dependence of interfacial tension on system pH, as all of the values fall within the same range. While a high precision can be measured, in principle, using this technique, the high degree of uncertainty in the pressure measurement means that we should consider fewer digits of certainty in the measurement (giving  $440 \pm 20$ ,  $450 \pm 20$ , and  $460 \pm 30$  mN/m for concentrations of 0.010, 0.10, and 1.0 M, respectively), which shows a much cleaner concordance with each other and that the interfacial tension does not appreciably differ, if at all, with a change in pH.

As outlined in Chapter 2, due to the different chemistry of removing the oxide skin by an acid as opposed to a base, measurements of the interfacial tension against aqueous HCl solutions were not achievable. From a practical standpoint, the amount of time needed to produce a stable measurement with hydrochloric acid is quite considerable: Bilodeau et al, for example found the equilibration time needed for pendant drop measurements of galinstan against 1.0 M HCl (aq) solution was up

to 90 min due to the slow etching of the gallium oxide by the acid, compared to almost immediate equilibration against a 0.1 M NaOH (aq) solution [112]. The source of this is most likely because gallate salts (here,  $\text{NaGa}(\text{OH})_4$ ) precipitate out of aqueous solution, which drives the reaction to consume more gallium oxide (if present). In contrast, gallium halide salts (such as  $\text{GaCl}_3$ ) are soluble in water, suggesting a tendency for the system to reach an equilibrium ion concentration and, as this concentration is reached, the conversion of gallium oxide into gallium halide salts is greatly slowed.

Another measurement of interest to us is the interfacial tension of galinstan against a polymer or polymer precursor, such as the monomer pentaerythritol tetraacrylate (PETA), a highly viscous ( $>1300$  mPa·s) tetra-functional monomer that can be polymerized into a hard plastic. This measurement is interesting to us for two reasons: first, this is an unknown system for which no literature data exists. Secondly, as will be presented in Chapter 5, PETA is one of the materials with which we look to co-flow with galinstan with a view to producing a fiber containing a continuous liquid metal core. When degassed before use, we observed by the lack of development of a solid interface<sup>h</sup> that PETA does not hold enough dissolved oxygen to induce the oxidation process, allowing us to measure interfacial tension at the liquid-liquid interface. A challenge in this measurement, however, is the refractive index of PETA being almost perfectly matched to that of borosilicate glass, as seen in Figure 34, making identifying the contours of the droplet with relation to its position in the constriction difficult.

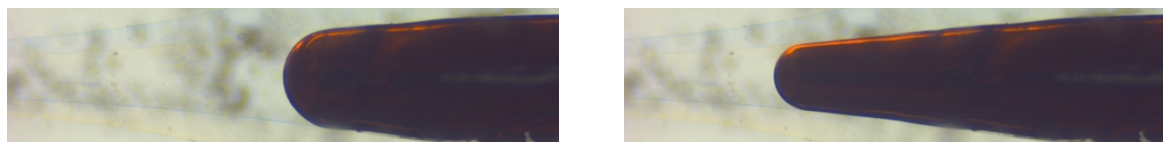


Figure 34. Image from the measurement of the interfacial tension of galinstan in PETA, showing the elongated droplet (left) before and (right) after the application of aspiration pressure.

Despite the imaging difficulty, we obtained a value for the interfacial tension between the materials of  $569 \pm 15$  mN/m, showing that reasonably precise measurements are possible even with extremely viscous materials. While no known literature data on this system exist, the order of magnitude of the value is close to that of the measurements of galinstan against NaOH solutions, suggesting a reasonable degree of accuracy in the measurement. The higher interfacial tension between galinstan and PETA arises probably from a lower affinity of galinstan for PETA compared to water due to dipole-dipole interactions (water, and especially with the presence of dissolved NaOH, is more polar than PETA), which reduce the energy cost associated with the interface: since interfacial tension arises from the

---

<sup>h</sup>In addition to the solid-like behavior of gallium oxide, the presence or absence of oxidation is easily verified by appearance: galinstan is a brilliant, highly-reflective silver color, while gallium oxide is a dull, less-reflective gray.

favorability or unfavorability of the presence of an interface, having an interface that is less polarizable likely contributes to the increased interfacial tension.

### 3.4.6 Attempted Measurements between CNC Dispersion Phases

As a colloidal liquid crystal, a dispersion of cellulose nanocrystals (CNCs), at the right concentration, will phase separate over time into an isotropic phase with a lower concentration of CNC rods and a more highly-concentrated anisotropic phase [184,185]. To our knowledge, there has only been a single successful measurement reported on the interfacial tension between the two phases of such a material, giving an interfacial tension on the order of  $10^{-4}$  mN/m [63].

Attempting to measure the interfacial tension between the phases with our technique, however, provided an insurmountable challenge with either the injection capillary or constriction measurement technique protocols, as shown in Figure 35. While we could see that the two phases were distinct before coming into contact with each other, no distinct droplet or jet shapes could be seen after contact, either with or without crossed polarizers.

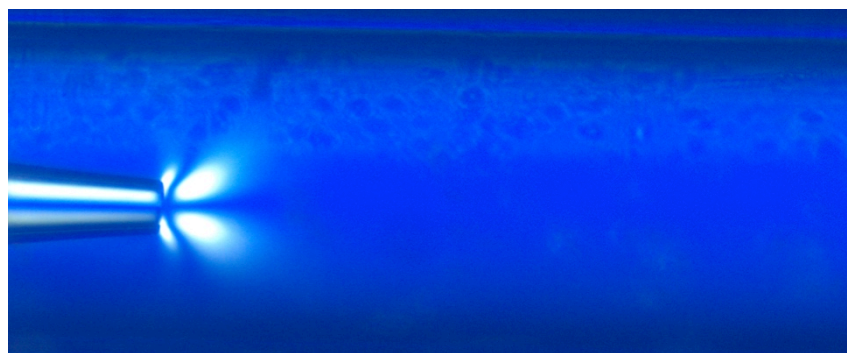


*Figure 35. Attempted droplet production of the anisotropic phase of a CNC dispersion, prepared from a CNC dispersion with an overall concentration of 7% w/w in the coexistence regime, within its isotropic counterpart, as viewed between crossed polarizers. No shapes are clearly distinguishable, nor is any birefringence from an anisotropic phase alignment visible away from the injection capillary tip.*

The redispersion of the anisotropic phase in the isotropic, as can be seen by the jetting in Figure 35 where the high birefringence from the anisotropic phase flow is immediately lost, appears to happen almost instantaneously. The flow-induced mixing between the two phases causes the equilibrium phase separation to become lost. The measurements reported by Chen et al were obtained through goniometry techniques, though additionally requiring long equilibration times to allow for proper phase separation [63]; thus, the most likely means to be able to measure the interfacial tension would be to set the device up for vertical measurement, allowing a phase separation to develop within the measurement capillary and to which a pressure difference would be applied to induce a change in curvature of the interface between the two phases as opposed to a droplet [151].

### 3.5 Dynamic Interfacial Tension

When an interface is produced to which surfactant molecules can adsorb, the rate at which the interface becomes covered by surfactant molecules is finite. The increasing surface coverage with time leads to a subsequent decrease in interfacial tension until saturation occurs, representing equilibrium surface coverage of the interface by the surfactant. The development of this phenomenon is particularly noticeable at surfactant concentrations below the critical micelle concentration [41]. Thus, it becomes interesting to measure how the interfacial tension decays with time as surfactant adsorbs to the interface between the continuous phase and the droplet (here, of our liquid crystal). Bubble deformation techniques are able to measure this for smectic liquid crystals [41], but we wanted to see if our droplet aspiration technique would work for measuring dynamic interfacial tensions of other materials, such as in the case of 5CB against a surfactant solution (like SDS in water).

In order to measure the dynamic interfacial tension, a fixed pressure difference can be applied to a droplet to slowly push it into the constriction of the collection capillary. Over time, as represented in Figure 36, we observe that the droplet continues further and further into the channel, eventually stopping at a point representing equilibrium surfactant coverage of the droplet interface. Since  $r_d$  from equation (3.6) and (3.13) change, but  $r_i$  and  $\Delta P$  do not, the motion of the droplet into the channel and the corresponding decrease in radius of curvature of one side is due to a decrease in the interfacial tension rather than, for example, a change in initial radius or a change in the pressure applied.

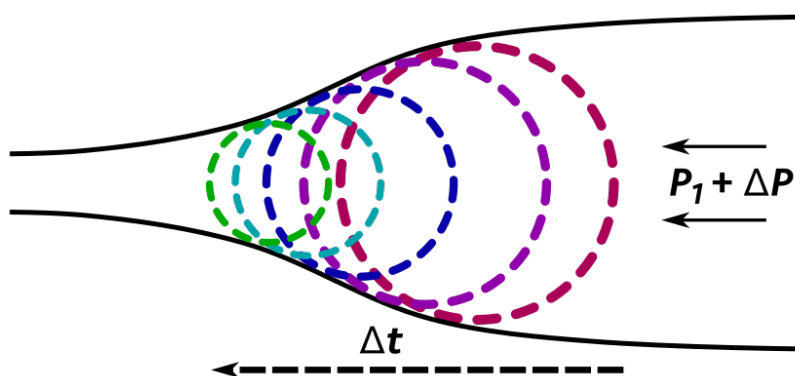


Figure 36. A schematic of the progression of the aspirated edge of droplet into the constriction with time. Figure reproduced with permission from Honaker et al, "Microfluidic Tensiometry Technique for the Characterization of the Interfacial Tension between Immiscible Liquids". Copyright 2018 American Chemical Society. [44]

We performed dynamic interfacial tension measurements on 5CB in a 6.0 mM SDS solution<sup>i</sup>. An advantage to using 5CB as the material to be studied was that, in addition to seeing the motion of the droplet into the capillary cease, visual cues in the form of the texture of 5CB viewed under the microscope with one polarizer inserted would help to confirm the point when equilibrium coverage and, thus, interfacial tension was achieved. During the adsorption process, both the liquid crystal configuration, which transitions from poorly aligned (ideally planar) to homeotropic, and the surfactant coverage reach their equilibrium states. These transition times are not necessarily identical, since the former depends on anchoring strength and liquid crystal elastic deformation energy [78] and the latter on thermodynamics of surfactant adsorption, but they can experimentally be seen to be similar to each other [186]. In the experiments performed here, we noticed that, once the liquid crystal structure stabilized into a radial configuration as evidenced by a single point defect at the center of the droplet, this corresponded to the droplet ceasing to be aspirated further and an equilibrium interfacial tension being achieved.

As a surfactant such as SDS promotes homeotropic liquid crystal alignment, when adsorbed at the interface at above a given threshold concentration (found by Popov et al to be ~0.9 mM at neutral pH [187]), in the presence of such, a liquid crystal droplet adopts a radial configuration. A demonstration of this measurement technique is presented in Figure 37.

---

<sup>i</sup>We chose to use this concentration for the proof of concept dynamic interfacial tension measurements for three reasons: first, a concentration below the CMC of SDS (8.2 mM) is ideal for dynamic measurements, since this ensures that the equilibrium coverage is not in the plateau region. Secondly, we observed comparatively fewer wetting issues during the equilibrium interfacial tension measurements at this concentration compared to at lower concentrations (such as at 2.0 mM). Finally, 6.0 mM is above the threshold concentration at which a homeotropic structure is achieved at equilibrium (which is normally below 1.0 mM) [187].

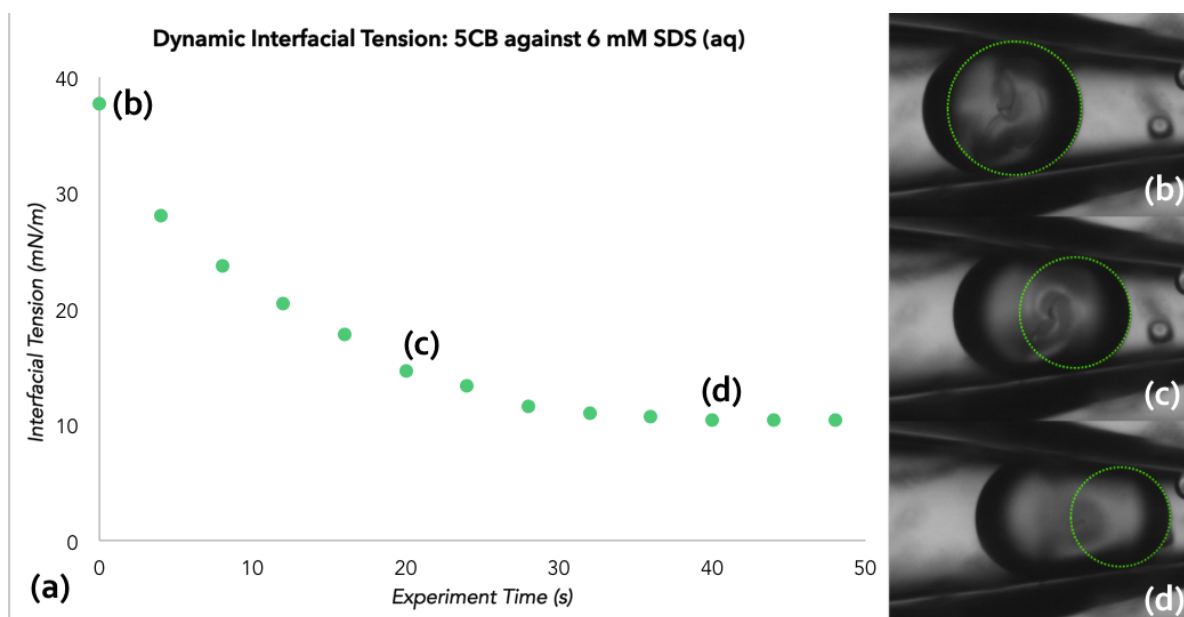


Figure 37. Measurement curve of the dynamic interfacial tension of 5CB against a 6.0 mM SDS (aq) solution. The points (b), (c), and (d) indicate measurements taken immediately upon starting the measurement, at 20 s, and at 40 s, once the interfacial tension plateaus. In (d), a final stable configuration is present and evidenced by the presence of a single point defect towards the center of the liquid crystal droplet, while both (b) and (c) show a more turbulent, dynamic liquid crystal alignment configuration. Figure reproduced with permission from Honaker et al, "Microfluidic Tensiometry Technique for the Characterization of the Interfacial Tension between Immiscible Liquids". Copyright 2018 American Chemical Society. [44]

The shape of the curve and the plateauing behavior are similar to those observed with a smectic liquid crystal against a solution of sodium dodecylbenzene sulfonate (SDBS) [41]. The decay in the curve corresponds to increasing surface coverage of the interface, with the equilibration time reached extremely quickly due to the high surfactant concentration present and the surfactant adsorbing quickly to the liquid crystal interface. The plateau corresponds to the equilibrium surface coverage for the given concentration of surfactant. However, because the measurement of the droplet is not immediately accessible once we create the droplet, we cannot measure the full extent of the decay of interfacial tension with time. At the concentration of surfactant we used, we found that equilibrium is reached within two minutes of droplet production. To better be able to measure the full behavior of interfacial tension with time, we would need to reduce the time from droplet production to measurement. This is achievable by reducing the distance from the injection capillary to the constriction and by being able to induce aspiration immediately upon the droplet clearing the constriction.

### 3.6 Conclusions and Outlook

The interfacial tensiometry technique presented here is robust, capable of measuring the interfacial tensions of many immiscible fluid combinations. Like

many other interfacial tensiometry techniques, though, there are several shortcomings and limitations of this technique. Most are largely equipment-related, with some issues related to materials:

- Since the pressure difference required for aspiration can be as little as 0.05 mbar, with the uncertainty supplied by the pressure regulator being 0.01 mbar, non-negligible uncertainty results from here. This uncertainty can lead to fairly high error bars. Similarly, the camera resolution greatly affects the resolution of the data: for example, a camera with a high pixel value (length per pixel) produces data with a much higher uncertainty compared to a when a low pixel value is present.
- Wetting issues can be considerable, especially when amphiphiles (such as liquid crystals) are used as dispersed phases: droplets that wet the surface of the capillary are largely unmeasurable. Adequate surface treatment, if available, can help to mitigate these issues, but a treatment protocol optimized for liquid crystals remains elusive. While inverting the system to avoid the wetting behavior (for example, using a liquid crystal as the continuous phase with water as the dispersed phase), other issues will then be present, such as the cost and optical transparency (or lack thereof) of the continuous phase.
- The fluids need to be immiscible over the experimental time scales<sup>1</sup>. Lacaze et al indicate that, even between miscible fluids, there exists an interfacial tension between the two phases that rapidly decays [49], but miscibility of the droplet with the outer phase, combined with the time needed to isolate and measure a droplet makes such a measurement extremely difficult, if not impossible, to carry out. We saw this in our attempts to measure the interfacial tension between phases of a CNC suspension [63], where the two phases are close enough to being miscible that we lose the distinction between the two. There could be possibilities to measure the interfacial tension by preparing a vertically oriented device, where the phases are moved upwards and downwards with a manostat, but the equipment for such would be challenging to produce and long time scales would be needed to measure such a system.
- The implementation of the interfacial tensiometry technique described here uses manual determination of droplet radii, a laborious and time-consuming process. The system can be made much more efficient through the implementation of an automated image analysis algorithm to be able to filter through the large number of images collected, allowing for the determination of droplet radii much more quickly; this can then be integrated into a more automated process with further integration of the pressure measurements. Work has been performed in the Master's thesis of Andy Schanen towards the implementation of an automated system [172], but further work is needed to both make the technique user-friendly and accessible and, as a further step, to integrate both the camera and pressure

---

<sup>1</sup>Hexadecane, for example, is labeled by the manufacturer as being hygroscopic, but we did not see any miscibility with water over the course of an experiment.

regulator into the software, which would allow for live measurements of interfacial tension without the need for post-processing.

If these issues can be overcome, with exceptionally small constriction diameters, better pressure regulator resolution, and high camera pixel resolution, we predict that this technique will be able to readily measure interfacial tensions on the order of  $\mu\text{N/m}$ .

The primary use of interfacial tensiometry here was to be able to characterize the interfacial tension between a polymer solution ("dope") from which we spin fibers and a core material of interest, such as a liquid crystal. The data we obtained, in particular from the measurements in Sections 3.4.3 and 3.4.5, will then be used to help predict the jetting stability needed to produce fibers in the following chapters.



## CHAPTER 4

### MICROFLUIDIC WET SPINNING OF PURE POLYMER FIBERS AND FIBERS CONTAINING LIQUID CRYSTAL CORES

Both the production of microfluidic devices for interfacial tensiometry and the characterization of interfacial tension, a key parameter in understanding the transition between jetting and dripping, helped to lay the groundwork for the development of wet spinning of glassy polymer and elastomer fibers containing heterocores, such as liquid crystals and liquid metals. Regardless of the technique employed, the process of producing polymer fibers from solution is a delicate balance of a number of flow parameters against the rate of solvent removal: enough solvent needs to be removed from the fiber to "solidify" the system before the onset of Rayleigh instability in the sheath and the resultant loss of the jet and fiber. Incorporating a core presents an extra challenge, since the system then has two jets in which contiguity needs to be maintained [4,7,29,31,188]. At the same time, options for processing highly stretchable polymers are rather limited, with electrospinning not a viable option for the volatile solvents and compounds used [27,33], and very little work has been done on the production of liquid crystal-core fibers with elastomer sheaths.

In this chapter, work is presented on the production of fibers using a microfluidic wet spinning technique. First, the considerations for both device fabrication and material selection are presented, with suitable candidates for systems of polymer "dopes" (solutions) and their respective coagulation baths identified. Results are then presented on the spinning of pure polymer fibers, both of a glassy polymer (PVA) and of an elastomer (*cis*-1,4-polyisoprene, or PI), with attention paid to the storage methods and how the fibers can be kept for both long-term storage and later characterization. Finally, we incorporate a liquid crystal, both an achiral and a chiral nematic, into the core of the fibers. We additionally present the characterization of these fibers, both optically and mechanically. Lastly, we present the interpretation of these results and the further steps to be taken to improve the system.

The content of this chapter is largely based on the paper "Elastic sheath–liquid crystal core fibres achieved by microfluidic wet spinning", published in the *Journal of Materials Chemistry C* in 2019 [48]. I would like to especially thank Dr. Manos Anyfantakis for both the support in selecting and preparing the polymer dopes used for spinning and for help during the optical characterization process and both Shameek Vats and Dr. MD Asiqur Rahman for assisting me during the initial stages of fiber production and characterization.

## 4.1 Why Wet Spinning?

Most industrial or research techniques for fiber production focus on post-processing: rather than producing fibers *in situ* via a chemical reaction (such as the condensation reaction behind the nylon rope), they use an already-formed polymer from which fibers are spun. These techniques range from electrospinning, which produces fibers by using an electric field [4,33,189–191], to dry spinning, which evaporates solvent from a polymer solution by using hot air, and to extrusion processes, such as melt [192,193] or gel spinning [194], which force a molten polymer through a die head to "squeeze" out fibers before quenching to cool and solidify them. On an industrial scale, extrusion is one of the most widely used methods, having a very high throughput, but it has the distinct disadvantage of not being able to easily integrate a core into the produced fibers. Electrospinning can produce core-sheath fibers quite readily, either via a phase separation [27] or simultaneously during spinning [7,34,84,189,195], but there are some limitations in what polymers can be readily electrospun [33] and in the conditions that are required for the spinning of fibers, with a high sensitivity to ambient conditions [4,28,33]: in particular, very few elastomers are readily electrospinnable [196] due, in part, to the solvents needed to dissolve such materials. We also note that there are no reported studies of coaxial electrospinning with an elastomer as the sheath, and production of coaxial fibers with an elastomer sheath is one of our aims. The electrospinning of liquid metals into cores is also elusive, with only a single known paper discussing the topic [34].

Wet spinning refers to a technique where a fiber is spun from a solution (often called a "dope") by pumping the material into a coagulation bath. This coagulation bath is designed to extract the dope solvent by being miscible with and engineered to remove it as quickly as possible, leaving behind only a solidified polymer [197–199]. The aim is similar to that in electrospinning: in order to produce a single, continuous fiber that can be used in applications, solvent has to be removed from the fiber before instability kicks in and the jetting regime transitions to the dripping regime. Most wet spinning work done to date has not focused on coaxial wet spinning with a functional core, however, instead aiming to produce either pure fibers [198,200] or composite fibers from a single dope, incorporating the functional material within the fiber bulk [199,201,202].

Wet spinning was chosen over electrospinning in this thesis for several reasons. First, wet spinning is relatively easy to implement in a microfluidic set up on laboratory scales; because it is also used fairly extensively on an industrial scale, the wet spinning process we develop is amenable to being scaled up to an industrial level readily. We also can use wet spinning to incorporate other materials of interest as both core and sheaths that ordinary electrospinning processes are not able to easily work with, such as elastomers dissolved in volatile organic solvents (such as THF and linear alkanes) for sheath phases and conductive materials, such as the conductive polymer PEDOT [190,203–205] and liquid metals [15], the latter being a goal at the forefront of the aims of this thesis. Finally, with a capillary-based microfluidic approach, we can more easily visualize all stages of the spinning process, from fiber spinning to eventual coagulation and drying, with the use of a

microscope. We can see whether or not the core is being incorporated and whether its continuity is being maintained throughout the spinning process, from the initial jetting to the final encapsulation of the fiber.

## **4.2 Materials, Methods, and Equipment**

With the goal being to incorporate a core into a polymer fiber, the initial aim was to begin with the production of pure polymer fibers without cores: once a system that consistently produces solidified polymer fibers is found, heterocores can then be introduced into the fiber. This procedure required first developing a spinneret device for fiber production, then identifying a suitable candidate system to produce fibers (both the fiber dope and the coagulation bath), tuning the flow parameters to yield continuous fibers, and finally collecting the produced fibers.

### **4.2.1 Microfluidic Spinneret Device: Production**

The starting point for the microfluidic device used to make fibers is the glass-capillary flow focusing chip that has been consistently used for the production of liquid crystal shells [7,22,25,169] and for the initial version of interfacial tensiometry experiments described in Chapter 3. The main feature of this device is the flow-focusing junction where the three inputs meet: the outer phase, the middle phase, and the inner phase.

Initially, we used a flow-focusing device identical to those used for shell and droplet production, which use a tapered collection capillary to collect the shells and droplets. Such a device is presented in Figure 38. Capillaries were treated with silanization before being assembled into the device, using device assembly techniques presented in Chapter 3. Since three inputs are necessary rather than two, however, we used three cannulas, one each to introduce the component fluids from each of the points.

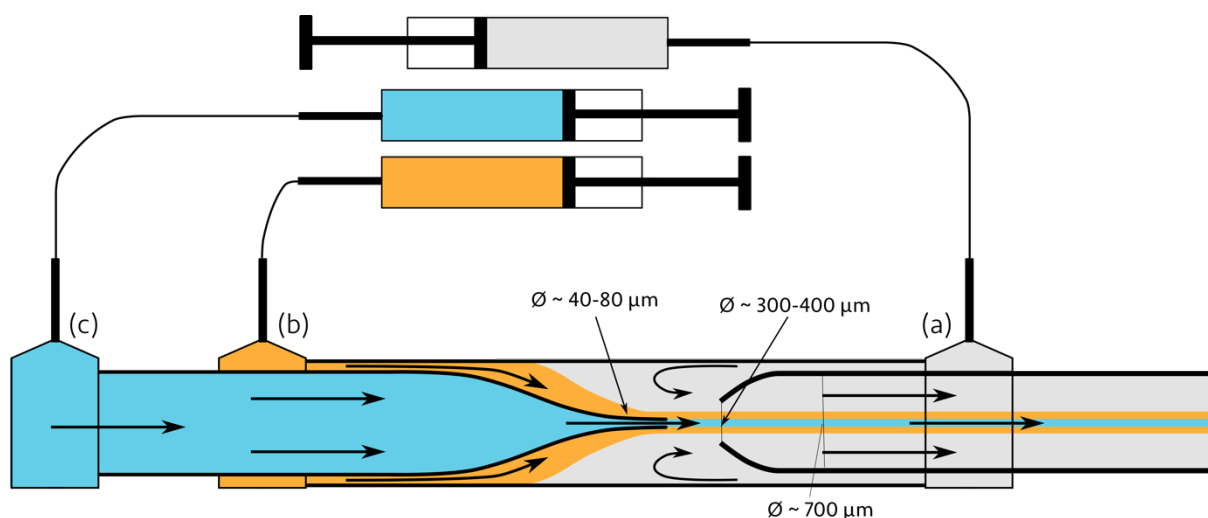


Figure 38. A schematic of the spinneret device for producing droplets and shells that was initially used for fiber production, with inputs for (a) the coagulation bath or flow stabilizer bath, (b) the fiber dope, and (c) the core, such as a liquid crystal. Capillary and orifice diameters are as indicated.

Preliminary experiments in producing both galinstan-filled and liquid crystal-filled fibers using this geometry, however, showed issues in stabilizing the flow: in particular, the flow sometimes showed snake-like motion, as shown in Figure 39.

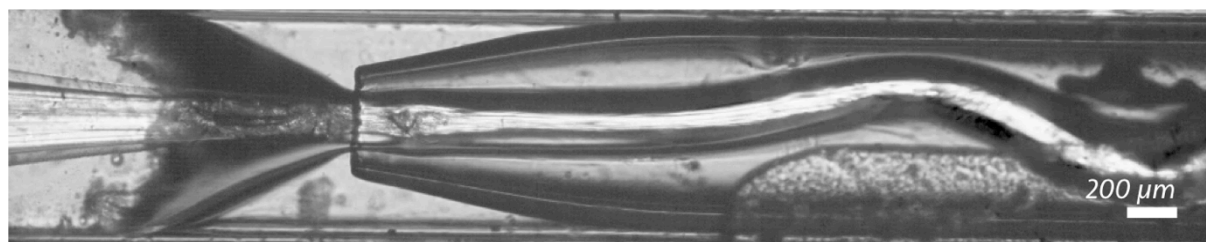


Figure 39. Snaking of a co-flowing jet of 5CB in a 30% w/w SBS in toluene solution, contained in a bath of 10% w/w PVP in ethanol. Scale bar as indicated.

Both preliminary experiments and numerical analyses suggest that, when the fiber exits into a tapered collection tube, the conditions under which stable jetting is obtained (in particular, the flow speed of the outermost phase) [36] can quickly disappear over the length of a tapered collection capillary. As the fluid flows through the tapered capillary, the flow rate remains constant, but the flow speed decreases rapidly due to the increase in cross section, thus potentially contributing to the loss of stability.

Jet breaking is desirable for the production of shells and droplets, but it is not desirable for maintaining a continuous jet to achieve a fiber [24,169]. Therefore, we changed the device used for fiber spinning to one that uses a treated (silanized) but untapered capillary to reduce the effects from a drop in flow velocity from the widening of the channel. The untapered collection capillary can further be extended by a length of tubing attached over its end, allowing, if needed, for more time for a fiber to solidify in the coagulation bath before exiting the spinneret and being collected. A schematic of the spinneret device used is presented in Figure 40.

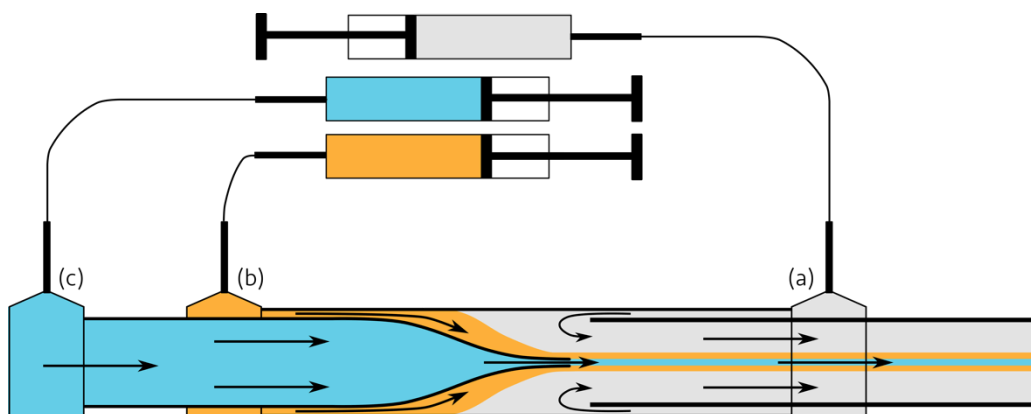


Figure 40. A schematic of the modified spinneret device for producing fibers, with inputs for (a) the coagulation bath, (b) the fiber dope, and (c) the core, such as a liquid crystal.

Three inputs are used here, with no sealing of the device outlet in order to be able to collect fibers. Flexible tubing, normally made of polyethylene, is used to connect the fluid containers, either syringes or vials equipped with septa, to the spinneret device, ensuring a tight seal with no leakage of material. Fibers can be directly drawn from the spinneret itself as they are produced; more commonly, however, a length of tubing attached to the end of the collection capillary ejects the produced fiber into a reservoir of coagulation bath solvent to wash the fiber and promote further coagulation before the fiber is ultimately collected for storage.

The fluids are flowed through the spinneret device using syringe pumps (NEMESYS, 3 bar units, interfaced with software provided by the manufacturer). These were chosen over pressure regulator systems (such as the Fluigent MFCS) because of the high viscosity of the materials being flowed, especially the polymer dopes, and the air-sensitivity of some of the eventual materials to be used. Syringe pumps also give a more straightforward reading of flow rates: the pressure regulators only directly give readings of the pressures used to flow the materials. These would then have to be converted to flow rates via the Hagen-Poiseuille equation (equation 3.6), and the conversion process requires knowing a number of parameters (tubing length, tube diameter, and viscosity). By establishing the conditions directly with flow rates, we can both directly convert the flow rates into flow velocity, one of the quantities necessary in the Weber and capillary number analyses of the jetting system, and additionally better reproduce the jetting conditions in future experiments.

#### 4.2.2 Polymer Dopes

In order to produce fibers from a polymer dope, the wet spinning approach requires the dissolution of a polymer in a solvent before pumping it into a coagulation bath. Fiber spinning, regardless of the technique, is often best achieved by using a polymer with a high molecular weight [4].

In order to spin fibers of poly(vinyl alcohol), we spun from an aqueous dope containing 15% w/w to 20% w/w PVA ( $M_w \sim 85\text{--}93$  kDa;  $M_e \sim 5.3$  kDa [105]; 87–89% hydrolyzed, Sigma Aldrich). PVA powder was added under constant stirring to hot

(~80°C) ultrapure deionized water. The mixture was allowed to stir at least overnight, obtaining a viscous, optically homogeneous solution. This solution was then cooled to room temperature before use in experiments. Fibers were spinnable from 15%, 20%, and 25% w/w PVA solutions, but more concentrated solutions were often too viscous to work with.

When choosing an elastomer to use as the polymer sheath, there is a paucity of high molecular-weight elastomers available commercially, the most readily available being block copolymers of styrene and butadiene (SBS). SBS is soluble in many organic solvents, including toluene and THF, at weight concentrations of around 30% before forming a highly viscoelastic solution, but is not miscible with linear alkanes and short-chain alcohols. The rheological behavior of SBS, however, is rather complicated due to its co-block nature, showing possible microscale phase segregation when in solution: the styrene and the butadiene blocks are very likely not equally soluble in a given solvent. Additionally, most grades of commercially available SBS are not of high weight suitable for spinning, requiring very high concentrations before a substantially thick solution for spinning is obtainable. For example, the most commonly available grade from Sigma Aldrich at the time of the experiments had a molecular weight of 130 kDa: this compares quite unfavorably to the entanglement weight of polystyrene alone, which is 16.5 kDa, and we need a high entanglement weight to molecular weight ratio to get proper entanglement for fiber spinning. Further motivation for avoiding the use of SBS arose during the initial co-flowing experiments of SBS with a liquid crystal core to attempt to obtain fibers filled either with a liquid crystal or a liquid metal: SBS jets often "snaked" and final coagulation of the jet was almost impossible to achieve, with most results of the spinning process being a gooey mass without distinct fibers. We additionally found that the rheological behavior of SBS showed some anomalies, in part due to the phase separation and different miscibilities of the blocks of the polymer in a given solvent, which further motivated the decision to find a polymer that was less problematic to work with.

Instead of using SBS, we were able to obtain high mass *cis*-1,4-polyisoprene ( $M_w \sim 1$  MDa;  $M_e \sim 4.8$  kDa [106]; PI) and *cis*-1,4-polybutadiene ( $M_w \sim 0.5$  MDa;  $M_e \sim 3$  kDa [107]; PB) from Goodyear Innovation Center Luxembourg, both of which are rubbery materials. These materials are soluble in many of the same solvents that SBS is, but with much lower maximum concentrations: as an example, one can achieve concentrations of 14% w/w PI in *n*-hexane (99%, VWR) and 12.5% w/w PB and/or PI in toluene (99%, Roth) before the solution becomes difficult to flow. By contrast, the SBS used does not reach this point even at 30% w/w in toluene. We can simply prepare these solutions by adding the desired mass of polymer to the solvent, normally *n*-hexane or toluene, and stirring for at least two to three days at room temperature (~22-25°C) and with a stir speed of 200-300 rpm. In the work presented in this chapter, because of the higher molecular weight of PI and with a view to focus on optimizing a single system, we spun primarily from PI dope, both in toluene and in *n*-hexane.

### 4.2.3 Coagulation Baths

For wet-spinning, we need a bath miscible with the dope solvent but not with the polymer itself (or, rather, a bath solvent in which the polymer is not soluble) [201,206]. For example, when THF is used as the dope solvent, it is possible to use water as the bath solvent, but experiments performed with THF/water systems were unsuccessful: the water dried the polymer solution extremely quickly, causing the spinneret device to become quickly clogged with no fibers obtainable from the same. With a linear alkane or toluene as the dope solvent, however, ethanol instead needs to be used. We can additionally use ethanol as the coagulation bath solvent when water is the polymer dope solvent, such as for PVA (since PVA is insoluble in ethanol).

Two additional components are usually employed in the coagulation bath: a nonionic polymer stabilizer/thickener, similar to that used in work on shell and droplet production [24,72,169,179], and a salt, which is used to drive a diffusion/osmotic gradient to more quickly extract the dope solvent [207,208]. Previous work on coagulating polymer latexes used salts like magnesium sulfate [208] in water; however, very few salts are more than sparingly soluble in ethanol ( $\text{MgSO}_4$ , for example, will dissolve, at most, at a concentration of 0.1% w/w). Some of the few salts soluble in ethanol at substantial concentrations are lithium bromide ( $\text{LiBr}$ ) and calcium chloride ( $\text{CaCl}_2$ ), both of which are readily soluble in ethanol at concentrations of up to and including 15% w/w. Similarly, while the polymer PVA is commonly used as a stabilizer for shell production [22], it is not soluble in ethanol; PVP, however, is readily soluble in high concentrations, 15% w/w included, which makes up the other component of the coagulation bath.

For this work, with both PVA and the elastomer fibers, the most commonly used coagulation bath consisted of 10% w/w PVP ( $M_w \sim 1.3$  MDa, Sigma Aldrich) and 7% w/w  $\text{LiBr}$  (99.995%, Sigma Aldrich) dissolved in ethanol (99%+, Acros Organics). For both spinning PVA and PB/PI fibers, we found that this ratio can produce continuous fibers within the length of the spinneret. This coagulation bath is prepared through simple dissolution of the PVP and  $\text{LiBr}$  powders in an appropriate quantity of ethanol at room temperature and under constant stirring, obtaining a solution that is optically clear, yet somewhat viscous.  $\text{CaCl}_2$  (96%, Merck) was also found to be a suitable coagulant to be added to an ethanol bath, with its primary advantage over  $\text{LiBr}$  being its cost.<sup>a</sup>

Work was also performed exploring the use of a coagulation bath consisting of an aqueous solution of  $\text{MgSO}_4$  (anhydrous, Sigma-Aldrich) at varying concentrations, from 1% w/w up to 30% w/w, as well as a solution of sodium sulfate for the production of PVA fibers. However, attempting to add  $\text{Na}_2\text{SO}_4$  to a coagulation bath prepared in water with PVP was not successful: the resulting coagulation bath was inhomogeneous and not uniformly dissolved, with blobs of PVP dispersed in the mixture. The culprit is likely the change in the lower critical solution temperature

---

<sup>a</sup>As a point of comparison, at the time of preparing this thesis, the price per gram of high-purity  $\text{LiBr}$  from Sigma-Aldrich was €6/g, while the price for  $\text{CaCl}_2$  from the same source was €1.08/g.

induced by the presence of a salt. While PVP is quite soluble in water alone [209], the addition of a salt, especially in the concentrations used in a coagulation bath, creates a competition for water molecules between the constituent ions in the bath and the PVP molecules. The salt ions are much more hydrophilic compared to PVP, which draws water away from the PVP molecules and reduces its effective solubility [210]. Sulfate ions are very strong at inducing this effect; thus, the sodium sulfate drives the solubility of the PVP down.

#### **4.2.4 Flow Rates and Ratios**

Rayleigh instability propagates more readily through thin jets [127,211,212]. This, however, interferes with our aim of producing very thin, continuous fibers, which requires the flow rates, in addition to the compositions of the materials, to be tuned to optimize this process.

To produce thin, continuous fibers, we need the length of the jet to be such that it does not break up before the solvent extraction at least begins to dry the sheath exterior. Once the onset of coagulation begins, the viscosity of the middle phase will increase substantially, resulting in the suppression of Rayleigh instability development. Using the spinneret geometry, regardless of the combination of dope and coagulation bath we used, flow rate ratios that achieved continuous fibers were typically between 3 : 1 and 4 : 1 of bath to polymer, with a minimum dope flow rate typically of 0.15 mL/h (below this threshold, continuous fibers were not readily obtainable). While it was possible to obtain jets even with flow rate ratios of 20 : 1 of bath to dope in some cases, especially for PI dope, the resulting fibers were extremely thin: because of the volume decrease from the swollen polymer to the dried state, which proceeds from outside inwards, thinner jets are much more prone to breaking compared to thicker jets. Since keeping the polymer flow rate low helps to both produce thinner fibers and to achieve dried fibers faster, the coagulation bath flow rate needs to be kept relatively low in order to prevent the outer phase from pinching off droplets of the polymer sheath dope [7,147]. An example of some outcomes of varying flow rate combinations for a sample system is presented in Figure 41.



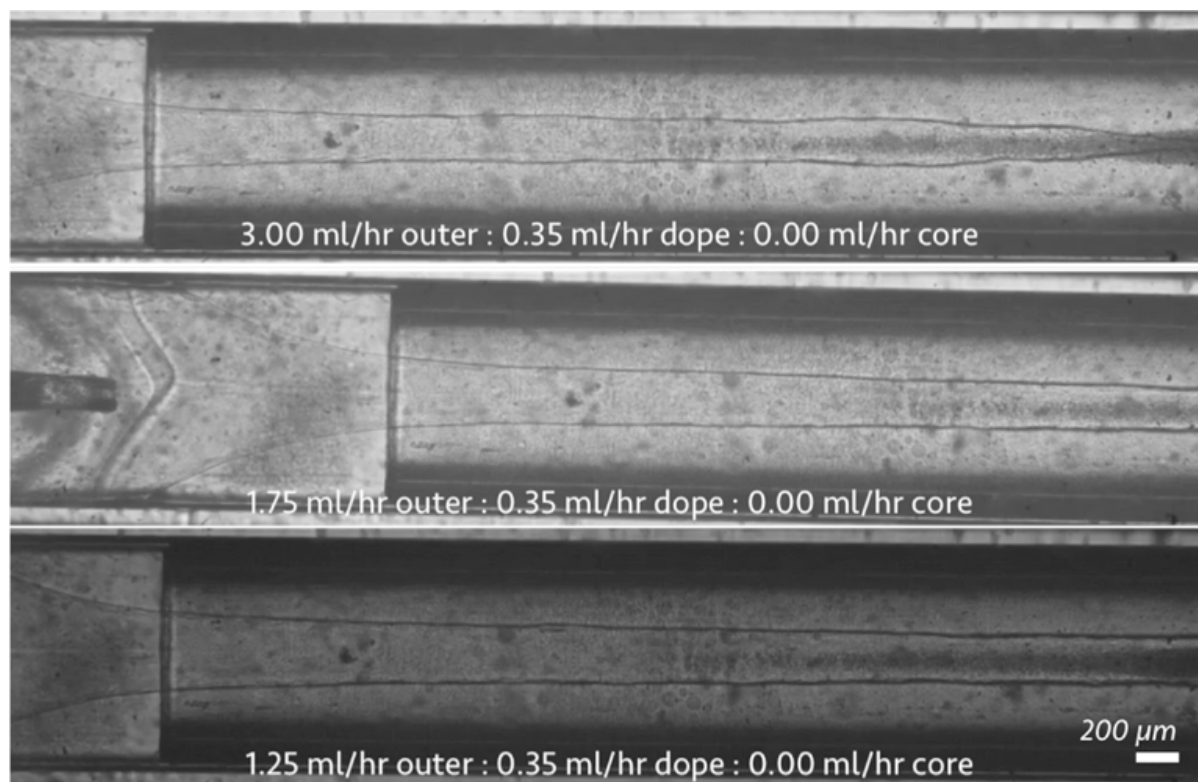
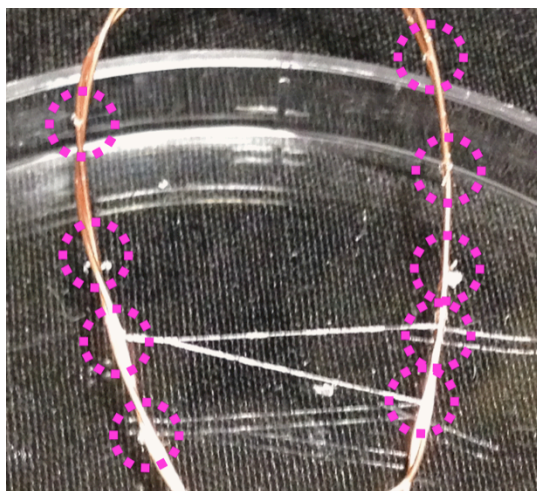


Figure 41. Different flow rate combinations of 14% PB dope in *n*-hexane in a co-flowing system with 7% LiBr and 10% PVP in ethanol as the outer phase and the resulting effects on jet continuity. Higher flow rates of the coagulation bath relative to the polymer can lead to instability and breaking apart of the jet. The onset of coagulation is visible within the length of the channel, as seen by the darkening of the edges of the polymer jet. Adapted and reproduced from Honaker et al (2019) with permission from the Royal Society of Chemistry [48].

#### 4.2.5 Fiber Collection

Once fibers are collected, we need to store them, both for additional drying of solvent (if necessary) and to keep the fibers for later observation. Several different methods of collection and storage of the fibers were examined: storage of the fibers wound onto copper wire frames, storage of fibers on both hydrophobic and hydrophilic glass substrates, direct storage of the fiber in the coagulation bath solvent, and storage of the fibers while freely-hanging. While copper wire frames were found to be easy to work with and additional flexibility from being able to fabricate shapes, the wire frames ended up being unsuitable. During the drying process, the fibers often broke from and collapsed on the wire frames, a consequence both of the wetting of the polymer solution to the copper substrates and the tension induced by the wire frame once the polymer is dried. An example of a representative wire frame on which PB fibers were collected is shown in Figure 42, though the problems with breaking were seen, regardless of the wire frame geometry and how much slack was introduced in the fibers before storage.



*Figure 42. A wire frame onto which polybutadiene fibers spun from *n*-hexane were collected and stored overnight. The pink circles indicate points at which the fiber was originally fixed to the frame; as can be seen, out of the seven small segments of fiber, only two remained, with the rest lost due to breakage.*

Among the storage methods explored, we found the most effective methods, with a maximum of intact fibers, for the pure polymer fibers to be either storage on glass slides treated with a hydrophobic silane (DMOAP), directly storing the fiber in an ethanol bath, or storing the fibers freely hanging with an absolute minimum of tension. Long-term storage of the fibers on hydrophilic surfaces led to fiber collapse, where the fibers were unable to be readily removed, confirming the observations made by Kim et al [30] and Kye et al [31]. This is in part due to the wetting of the solvent-swelled polymer to the glass if the fibers were collected while the fiber was still "wet" with solvent, which is normally the case with fibers directly collected from the spinneret.

### **4.3 Wet Spinning of Pure Polymer Fibers**

Prior to incorporating a core into the polymer fiber, we first need to be able to consistently spin a fiber out of a pure polymer. This section presents the results of wet spinning pure polymer fibers without cores, using PI and PB, both elastomeric polymers [93,213], and PVA, a popular fiber to electrospin [190,214–216] which is considerably more brittle and inelastic than PI and PB. Spinning of PI fibers is emphasized here instead of PB due to the higher molecular weight of PI, which, in turn, facilitates the spinning process through the greater number of entanglements, though similar results for the pure polymer fibers have also been obtained with the use of PB dopes of similar concentrations and in the same solvents.

#### **4.3.1 Spinning of Polyisoprene Fibers**

From an elastomer dope, we can spin fibers containing just polyisoprene. To do so, we first need to identify a solvent to dissolve the elastomers into and a solvent for the coagulation bath appropriate for extracting the dope solvent. As described in Section 4.2.2, we prepared 14% w/w polymer in *n*-hexane or 12.5% w/w polymer in

toluene and allowed it to stir overnight, the result being a highly viscous gel-like fluid. The coagulation bath used was the standard ethanol coagulation bath outlined in Section 4.2.1 (7% w/w LiBr or CaCl<sub>2</sub> and 10% w/w PVP in 99% ethanol).

First, the spinneret device was flushed with isopropanol and water to clean the device and remove any residues. Spinneret devices are generally not reusable after experiments due to the adhesion of polymer residues, particularly at the polymer injection port, so a fresh device is prepared and used each time. Both the spinning dope and the coagulation bath were loaded into borosilicate glass syringes<sup>b</sup> (ILS) and allowed to stand for at least 20 min to allow removal of any visible gas bubbles. The filled syringes were then loaded into the syringe pump units and connected to the spinneret device before beginning the flowing process. The coagulation bath is pumped through the system for at least five to ten minutes, flushing the system and ensuring a stable flow of the bath. This is then followed by the pumping of polymer dope into the spinneret, continuously ensuring that stable conditions for flow are present at the spinneret junction.

Fibers of just the elastomer are readily obtainable within the length of the spinneret, using a flow rate ratio of 3 : 1 to 5 : 1 of coagulation bath to dope. The development of fibers within the spinneret is visible in the form of a thin, opaque, spiraling thread that, once it exits the spinneret, can be readily collected, either in an ethanol bath, on a collector (such as tweezers), or on hydrophobized glass slides. Images of the spinning process, both as seen at the spinneret junction under the microscope and macroscopically, can be seen in Figure 43.

---

<sup>b</sup>Plastic syringes should be avoided when using any organic solvents, especially toluene or *n*-hexane, since organic solvents can quickly destroy the plastic.

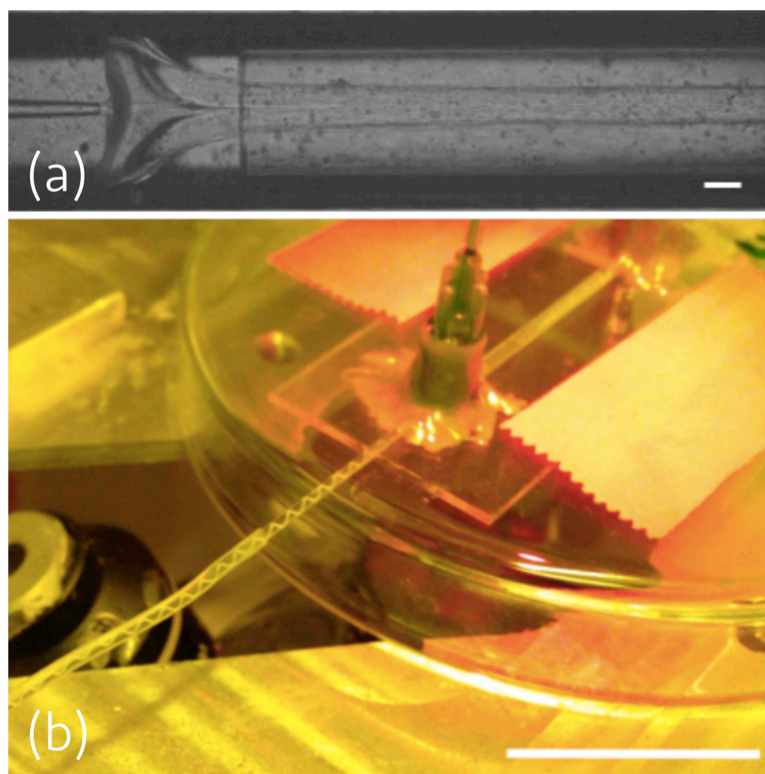


*Figure 43. Spinning process of pure polyisoprene fibers, viewed both (a) microscopically, at the spinneret junction; and (b) macroscopically, as the fiber begins to exit the spinneret device. Flow rates are 2.0 mL/h coagulation bath and 0.55 mL/h polymer dope. Scale bars are 0.2 mm in (a) and 25 mm in (b). The spiraling thread of polymer is as a result of a mismatch between flow velocity of the coagulation bath and the polymer, where the polymer fiber is produced more quickly than the coagulation bath pushes it out. Reproduced from Honaker et al (2019) with permission from the Royal Society of Chemistry [48].*

It is possible to spin using more disparate flow rates, including as high as 20 : 1 of bath to dope, particularly with PI. Higher ratios of bath to polymer dope flow lead to a much thinner jet, which also decrease the diameter of the resultant fiber. Thinner fibers, however, are considerably harder to handle and more prone to breakage, whereas flow rate ratios of 3 : 1 to 5 : 1 allowed us to produce fibers that were easily manipulable.

The PI fibers themselves, when viewed between crossed polarizers, were not immediately birefringent when removed from the spinneret, but very gentle stretching (strain of 2% to 5%) induced birefringence corresponding to lower orders of the Michel-Lévy birefringence chart [95]. The development of birefringence comes from the alignment of polymer chains during flow [217]. Once the polymer fibers are stretched, this strengthens the orientational order in the polymer chains and consequently produces birefringence, much like we see in well-aligned liquid crystal phases. The birefringence we see upon spinning pure PI samples is consistent with previous observations of the birefringence character of rubbers [94]. A sample fiber is presented in Figure 44.

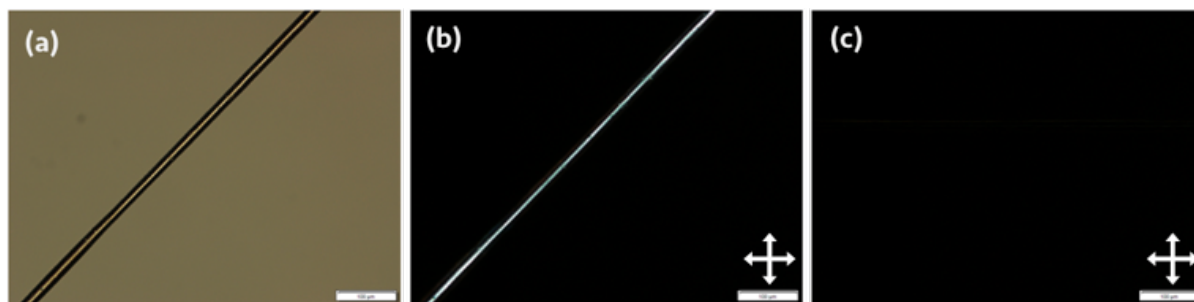


Figure 44. A PI fiber spun from 14% w/w PI in *n*-hexane dope, as viewed (a) without crossed polarizers; (b) with crossed polarizers; and (c) with crossed polarizers, but upon 45° rotation of the fiber, showing extinction of birefringence due to the polymer chains being oriented along one of the polarizer axes. Scale bars 100  $\mu\text{m}$ ; fiber diameter is  $\sim 30 \mu\text{m}$ . Fiber has been slightly stretched after production for mounting on the observation stage. Flow rates for fiber production were 1.25 mL/h bath and 0.30 mL/h polymer dope. Reproduced from Honaker et al (2019) with permission from the Royal Society of Chemistry [48].

Using the micrographs in Figure 44(a) and (b), along with the Michel-Lévy birefringence chart [92,95], we can determine the birefringence of the polymer. To do so, we first need the sample thickness, for which we can use the fiber diameter (estimated visually in Figure 44(a) to be  $\sim 30 \mu\text{m}$ ). We then assign the color we see the appropriate color hex code and use this hex code to finally match the fiber color to the coordinates on the Michel-Lévy chart, which, in turn, corresponds to the birefringence value. The process of this is shown in Figure 45.

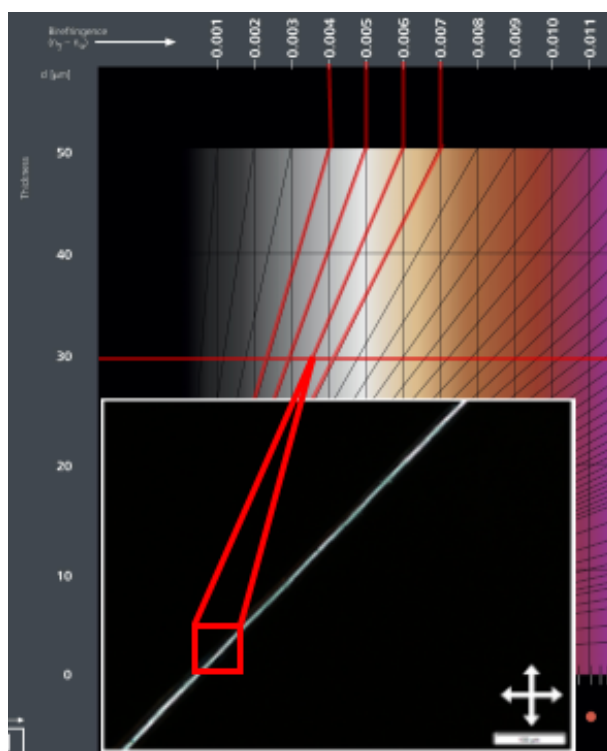


Figure 45. Birefringence of a PI fiber and the correlation of the birefringent color to the numerical value. Using the thickness of the fiber ( $\sim 30 \mu\text{m}$ ), we determine the coordinates that correspond to the color observed (red guide lines are included as a visual aid), using the area indicated in red as a representative sample, which then gives us a value for the birefringence. Chart adapted from an image by Carl Zeiss GmbH (<https://www.flickr.com/photos/zeissmicro/21257606712/>) and used under a Creative Commons License.

By using the process described in Figure 45, we estimate the birefringence as  $\sim 0.006$  [95], which is quite low when compared to typical liquid crystal birefringences. The PI fibers, when collected directly from the spinneret, normally had diameters of  $70\text{--}100 \mu\text{m}$  and could be readily thinned by stretching to  $20\text{--}40 \mu\text{m}$  without breaking, achieving a maximum strain of up to and exceeding 1000% in some cases.

Due to the absence of induced chemical cross-linking in the PI fibers, however, the stretched fibers did not restore their original shape upon release of tension as a result of stress relaxation. Lack of cross-linking would mean that, due to reptation relaxation, the polymer within the fibers will eventually flow and the fiber shape would be lost. Assuming that the polymers are completely uncrosslinked, however, is likely not the case: because we have a polymer below its melting point, the presence of crystallites, or small ordered domains, cannot be entirely ruled out. These crystallites can act as physical crosslinks, provided that the polymer does not melt, which helps to maintain the shape of the fibers we produce. Additionally, polydienes, such as PI and PB, are quite sensitive to oxygen and light and can easily cross-link in the presence of the same [109,218,219]. Relaxation time, however, scales significantly with the molecular weight of the polymer [106], so the very high molecular weights of the polymers used suggest that, over the time of the



experiments and storage of the fibers, the fiber shape will remain intact and can even be reinforced with a slight degree of cross-linking, either chemical or physical. This can be seen in Figure 46, where a sample of polybutadiene, stored over six months, still has largely retained its shape.



*Figure 46. A sample of polybutadiene kept at  $\sim 5^{\circ}\text{C}$  for a period of six months. While there appears to be some flow of the polymer, as represented by the flattening of the sample against the walls of the container, the polymer largely retained its original shape. Similar behavior can be seen with polyisoprene kept under identical conditions.*

We were able to keep even 20-40  $\mu\text{m}$  fibers intact over long-term storage, ranging from days to weeks for some samples, further confirming that the polymer does not flow over the observational time scales.

#### **4.3.2 Spinning of Pure PVA Fibers**

The wet spinning of fibers of PVA can be achieved through the use of aforementioned polymer dope (15%, 20%, or 25% w/w in water). While many traditional methods for wet spinning PVA fibers use super-saturated aqueous salt solutions as coagulation baths [201], we found that highly concentrated salt solutions led to the spinneret jamming and clogging: this is most likely a consequence of the salt solution drying the polymer dope immediately when the two solutions come into contact with each other in the spinneret<sup>c</sup>. In contrast, the use of a low-concentrated salt solution (1% or 2%) as the coagulation bath did not extract solvent from the jet quickly enough to obtain a fiber. Another limiting factor is that we were unable to prepare the coagulation bath with both PVP and a salt in water, the result being a gelatinous, inhomogeneous mess with a very clear phase separation between polymer and solvent in the preparation vial. One coagulation bath we found that did work for the PVA solutions we spun from was identical to the

---

<sup>c</sup>Because of how the spinneret is designed, where the bath and polymer dope come in contact with each other during jet production, the clogging occurs when this interface between bath and dope is created. As presented in the conclusions in this chapter, a different spinneret geometry which would minimize the contact between the liquid phases can mitigate this issue.

one that ended up being used for the PI and PB fibers: 7%-15% w/w lithium bromide or calcium chloride and 10% w/w PVP in 99% ethanol.

The procedure went as described for the elastomer fibers, with a flow of the coagulation bath first being stabilized before introducing the PVA dope. While the white spiraling thread that we saw when spinning PI fibers (in Figure 43(b)) is not present, long, continuous fibers are still obtainable within the length of the device and can be readily drawn from the spinneret. While fibers are somewhat flexible when wet, once dried, they become stiff and brittle, breaking under very low strains. Micrographs of a representative fiber are shown in Figure 47, both with and without crossed polarizers. The very weak birefringence observed in Figure 47(c) upon rotating the fiber between crossed polarizers suggests that there is some, but minimal, alignment of the PVA chains as a consequence of the flow alignment during the spinning process, but the birefringent color is faint and not easily perceptible. The observed birefringent color is markedly weaker than that seen in Figure 44, which comes from the reduced degree of polymer alignment.

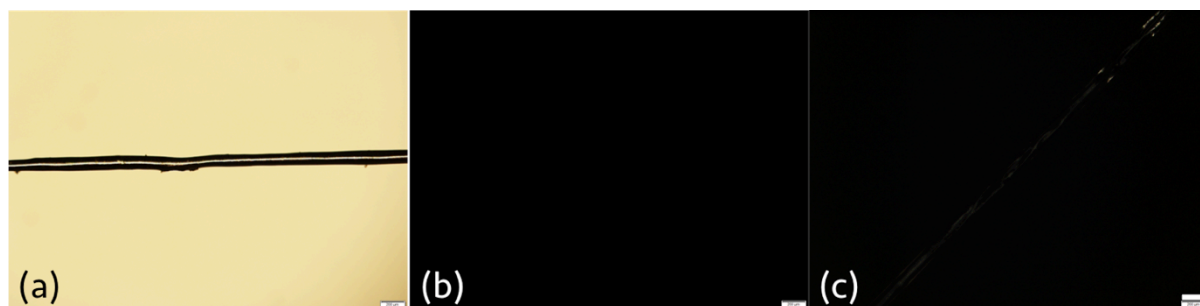


*Figure 47. A PVA fiber spun from 20% w/w PVA (aq) dope, as viewed (a) without crossed polarizers; (b) with crossed polarizers; and (c) with crossed polarizers, but upon 45° rotation of the fiber. Very faint color due to birefringence can be observed in (c), suggesting that the polymer chains have become slightly aligned during the fiber production process, though the intensity of the transmitted light is low and barely perceptible to the unaided eye. Scale bars 200  $\mu\text{m}$ ; fiber diameter is  $\sim 100 \mu\text{m}$ .*

We are additionally able to obtain very thin samples of PVA fibers, as presented in Figure 48. Predictably, due to the low thickness combined with the lack of stretching, no birefringence is observed.



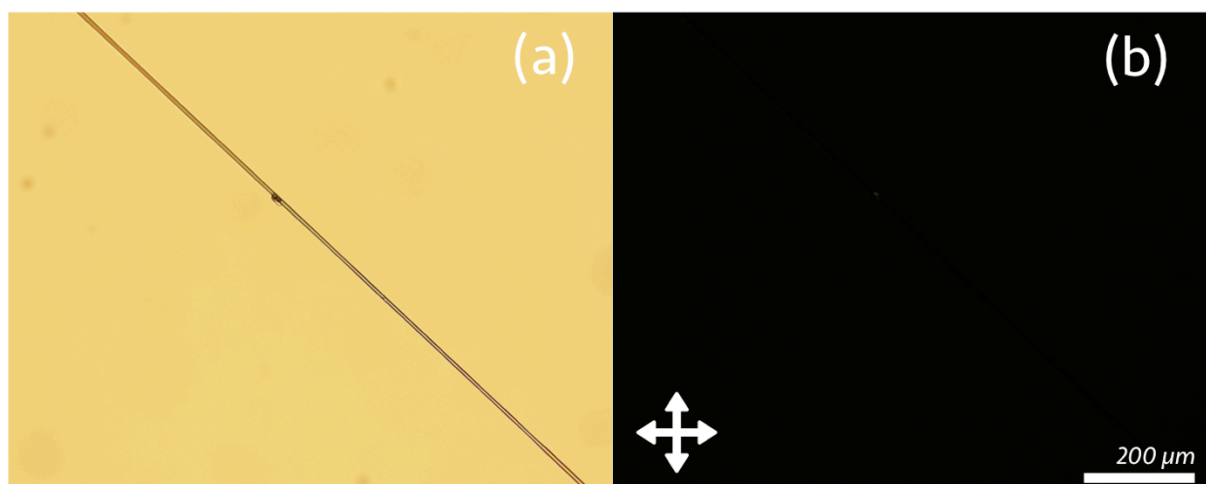


Figure 48. A PVA fiber spun from 25% w/w PVA (aq) dope, as viewed (a) without crossed polarizers; (b) with crossed polarizers and with the fiber oriented  $45^\circ$  with respect to the polarizer axis. No birefringent color is seen in (b), which suggests that the chains were not stretched sufficiently during the spinning process to align the polymer chains, leading to a lack of optical anisotropy. Scale bar  $200\ \mu\text{m}$ ; fiber diameter is  $\sim 10\ \mu\text{m}$ .

Despite their fragility under strain, the fibers themselves are robust under storage, with some samples lasting several months. The longevity of these fibers is a consequence of the higher glass transition temperature, being well above the temperature of the storage conditions ( $T_g \sim 85^\circ\text{C}$ ), meaning that the fibers remain stable and do not flow. The fibers obtained are normally of diameter  $\sim 100\text{--}200\ \mu\text{m}$ , with some thinner samples obtainable, though the thinner fibers have to be obtained during the spinning process and not by stretching during post-processing (such as is the case with the polyisoprene), since the resultant polymer is below the glass transition temperature. Similarly to the PI fibers, long samples of PVA could be spun readily (upwards of 30 cm), with the best results from using the combination of a higher concentration of PVA (25% w/w) in the dope and a coagulation bath with a high salt content (here, 15% w/w  $\text{CaCl}_2$ ) to accelerate the coagulation process.

#### 4.4 Wet Spinning of Fibers with a Liquid Crystal Core

Incorporating liquid crystals into the cores of fibers is of interest in its own right, since liquid crystals in textiles have numerous potential applications [4,7,189]. We can also use the development of a technique for wet spinning with a liquid crystal to provide us with valuable insight and knowledge about the fiber spinning process when a core is involved. This is with the aim of developing a more universalized protocol that can be generalized for any fiber spinning with a heterocore, including potentially liquid metals.

In this section, I present the spinning of fibers with liquid crystal cores: first, with an achiral nematic liquid crystal, and then with a cholesteric liquid crystal. The primary goal of this is to establish the conditions for coaxial wet spinning which can then be applied generally, with modifications as appropriate for the needs of both

the polymer and heterocores used, to simultaneous spinning with a wide variety of heterocores.

#### 4.4.1 Achiral Nematic Liquid Crystal Core Elastomer Fibers

One of the first and obvious interests is to spin fibers with liquid crystal cores. Polymer fibers filled with liquid crystal cores have been achieved through electrospinning [29,31,32,189,220], though most commonly by using a glassy polymer such as PVA or PVP as the sheath and with varying degrees of difficulty.

Using the same protocol that was used to spin the pure PI and PB fibers, a core of a liquid crystal can be simultaneously introduced into the spinneret through the third channel. The choice of liquid crystal requires attention: since most liquid crystals are miscible with the polymer dope solvents (such as toluene and hexane), while some degree of miscibility helps to reduce the interfacial tension and ensure good jetting [35,49], using a liquid crystal that is highly miscible with the dope solvent can lead to the core integrity being quickly lost. Likewise, if the liquid crystal is not miscible at all with the polymer dope solvent, this will lead to ready jet break-up. Micrographs of a successful jetting co-flow are shown in Figure 49, showing the flows both without polarizers and between crossed polarizers.

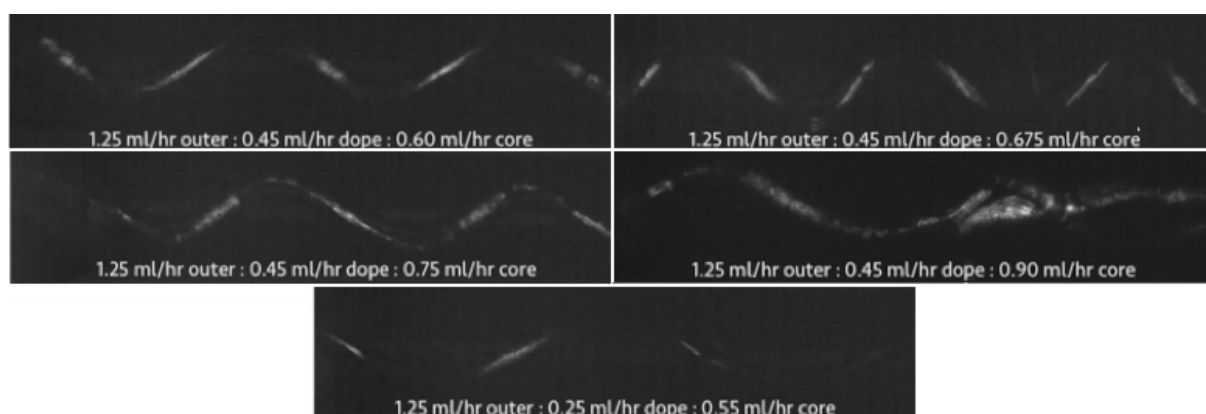


Figure 49. Jetting of a core of RO-TN 651 within a sheath of 12.5% PI in *n*-hexane and a coagulation bath of 7% LiBr and 10% PVP in ethanol, as viewed between (a) parallel polarizers and (b) crossed polarizers. The birefringent jet in (b) comes from the aligned jet of the RO-TN, while the darkening at the right-hand side of (a) arises from the onset of coagulation of the polymer sheath. Scale bar 200  $\mu\text{m}$ . Flow rates are 1.25 mL/h bath, 0.45 mL/h polymer dope, and 0.60 mL/h liquid crystal. Reproduced from Honaker et al (2019) with permission from the Royal Society of Chemistry [48].

In this work, we initially used the pure liquid crystal 5CB (Xinhua Yantai), the nematic liquid crystal mixture E55 (British Drug House, UK; mixed with a small amount of CB15), and the RO-TN class nematic liquid crystal mixtures (primarily RO-TN 615 and RO-TN 651, F. Hoffmann-La Roche, Basel, Switzerland). Ultimately, for the work presented in this chapter, the mixtures were chosen for use as opposed to pure 5CB. The reduced solubility of these liquid crystal mixtures in ethanol, in

addition to their extended nematic temperature range compared to 5CB, is why we chose them as core materials<sup>d</sup>.

Much like the ratio of flow rates between the coagulation bath and the polymer dope, the ratio between the liquid crystal and polymer dope flow is essential to obtain good fiber filling: if the flow rate of the dope is too high relative to the flow rate of the core, the core will pinch off and become discontinuous; if the flow rate of the core is too high, on the other hand, the liquid crystal jet was observed to break through the sheath, leading to a loss of material and negative impact on core continuity. We found that a good flow rate ratio of liquid crystal to polymer dope was between 4 : 3 and 5 : 3, where jet contiguity was maintained throughout the flowing process and reflected in the final fibers. The contiguity of the liquid crystal core jet can be verified by observing the co-flowing system between crossed polarizers in the collection capillary, as seen in Figure 50: because of the birefringence of the aligned liquid crystal, seeing a continuous line of birefringence, broken only at the crests and troughs of the spiraling jet (due to the alignment of the liquid crystal director along either the polarizer or the analyzer; in this case, the polarizer axis), suggests that the core of liquid crystal is continuous.



*Figure 50. Micrographs taken during the spinning process of a core of RO-TN 615 flowing within a polyisoprene sheath (14% w/w in n-hexane), as viewed between crossed linear polarizers, at different flow rate combinations. The zigzagging character reflects the fact that we are observing the projection into the image plane of an overall helicoidal fiber shape, as observable in Figure 43(b), that spontaneously forms downstream from the spinneret.*

The fibers we obtained showed birefringence, but markedly different from the birefringence seen in Figure 44 for the pure polymer fibers. As can be seen in Figure 51 for a thinner sample (fiber diameter of  $\sim 30\ \mu\text{m}$ ) and Figure 52 for a thicker sample (fiber diameter of  $\sim 80\ \mu\text{m}$ ), the colors present correspond to a much higher degree of optical retardation [95], clearly confirming the presence of liquid crystal.

<sup>d</sup>E55 and RO-TN mixtures, similar to the Galinstan manufactured by Geratherm GmbH, are proprietary liquid crystal blends whose precise compositions are unknown.

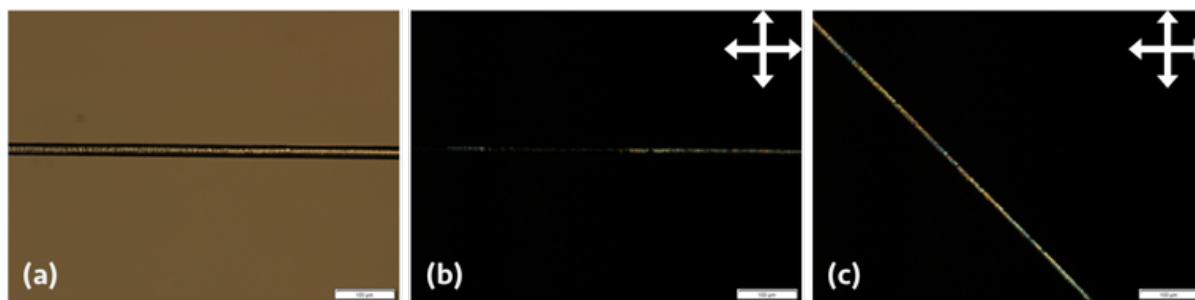


Figure 51. A PI fiber spun from a 14% w/w PI in *n*-hexane dope with a core consisting of the liquid crystal mixture RO-TN 615. Scale bars indicate 100  $\mu\text{m}$  with an approximate fiber diameter of  $\sim 30\text{ }\mu\text{m}$ , of which 10-15  $\mu\text{m}$  is the core. (a) A fiber viewed under a single polarizer. (b) The same fiber in (a) viewed between crossed polarizers; arrows indicate the direction of the linear polarizers. (c) As (b), but upon 45° clockwise rotation, showing birefringence that differs from (b) in being of higher order [95]. Reproduced from Honaker et al (2019) with permission from the Royal Society of Chemistry [48].

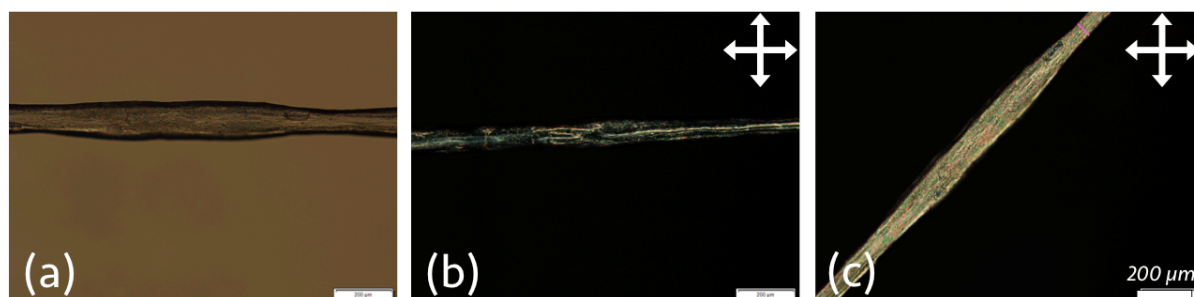
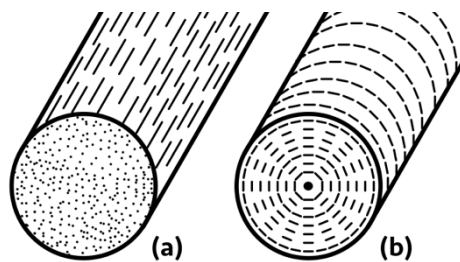


Figure 52. A PI fiber spun from a 14% w/w PI in *n*-hexane dope with a core consisting of the liquid crystal mixture RO-TN 615. Scale bars indicate 100  $\mu\text{m}$  with an approximate fiber diameter of  $\sim 80\text{ }\mu\text{m}$ , of which of which  $\sim 50\text{ }\mu\text{m}$  is the core. (a) A fiber viewed under a single polarizer. (b) The same fiber in (a) viewed between crossed polarizers; arrows indicate the direction of the linear polarizers. (c) As (b), but upon 45° clockwise rotation. The thicker fiber has a liquid crystal core that overall is less well aligned in the bulk, which explains the lack of complete extinction in birefringence upon rotation. Reproduced from Honaker et al (2019) with permission from the Royal Society of Chemistry [48].

The color from the thinner sample becomes almost completely extinguished upon rotation to an angle at which the fiber is aligned along either the polarizer or analyzer direction. The thicker sample color does become extinguished, but to a lesser degree than the thinner fiber. The polymer is a planar aligning substrate, but degenerate on its own; however, we can see that the liquid crystal is well-aligned, especially in thinner samples. To explain this, we consider the two extremes of planar liquid crystal alignment, as shown in Figure 53.



*Figure 53. Two configurations of planar alignment of a liquid crystal confined within a core, corresponding to (a) where the director field lies along the fiber long axis and (b) where the director field is orthogonal to the fiber long axis. No defects or elastic deformation are necessary for the configuration in (a), whereas a defect and its corresponding bend deformation are necessary to achieve the director configuration in (b), resulting in (a) being more favorable.*

From an energy minimization standpoint, the equilibrium configuration of the liquid crystal is where the liquid crystal director field lies along the fiber long axis, as shown in Figure 53(a), as this avoids the presence of a defect and elastic deformation. This arrangement is further facilitated by the flow-induced alignment created from the flow of the liquid crystal during the fiber production process, which provides an initial alignment of the liquid crystal along the long fiber axis [52,69,221], and from the small degree of polymer chain alignment during the flow itself without stretching. Since the liquid crystal is already in a minimized energy state, it is not favorable for it to adopt another configuration.

The resulting planar alignment is especially pronounced in the immediate vicinity of the polymer-liquid crystal interface, but becomes lost towards the interior of the fiber where the aligning effect from the polymer does not persist [222,223], likely within the first few microns of the fiber core. In the case of the thinner fibers, the anchoring can persist well through the thickness of the fiber (as seen in Figure 51), but the thicker fibers are a case where such anchoring and alignment becomes more readily lost within the fiber bulk (Figure 52). Because the liquid crystal lacks a crystalline lattice structure and is subject to molecular fluctuations within the sample, the fluctuations become more significant within the bulk and the aligning effect from the polymer sheath becomes weakened within the core.

#### **4.4.2 Cholesteric Liquid Crystal Core Elastomer Fibers**

Cholesteric liquid crystals are notable for showing strongly reflected colors, so another application of the incorporation of liquid crystals into the fibers is to create fibers with structural color. One of the advantages of structural color as opposed to the use of a dye is that it does not photobleach over time [224], thus maintaining the color during long periods provided the material structure itself remains intact. Another utility is that the color reflected from a cholesteric is tunable with temperature, allowing for its use as a thermal sensor.

Cholesteric mixtures to be used as core phases were prepared by mixing 25% w/w *R*-2-octyl 4-[4-(hexyloxy)benzoyloxy] benzoate (ZLI-3786/S-811, Yilin) with the host liquid crystal, either an RO-TN mixture (RO-TN 615 or RO-TN 651) or E55,



producing a liquid crystal mixture that reflects in the red region of the UV-Visible spectrum upon illumination with normally-incident light, but with a green reflection upon oblique illumination. (Such a mixture with the reflected color dependence on illumination angle is shown in Figure 7.) To ensure homogeneity and that the dopant was well incorporated into the liquid crystal, we briefly heated the mixture to the isotropic phase before cooling back into the cholesteric phase. The same flow rate ratios for the cholesteric-filled fibers were used as for the achiral nematic-filled fibers (usually a ratio of 3.5 : 1.0 : 1.5 for the coagulation bath, polymer dope, and liquid crystal, respectively). Flow rate ratios like this allowed for the production of long samples of cholesteric-filled fibers, a sample of which is presented in Figure 54.



*Figure 54. A long (~20 cm) sample of a PI fiber filled with a mixture of 25% w/w ZLI-3786 in RO-TN 651, viewed under ambient room lighting. A green reflected color is visible throughout the sample, indicating the presence of liquid crystal in the fiber core. Reproduced from Honaker et al (2019) with permission from the Royal Society of Chemistry [48].*

A remarkable feature of the cholesteric-filled fibers provided by the cholesteric liquid crystal core is that they display an angle-dependent Bragg reflection: while the cholesteric liquid crystal has a helical pitch such that a flat sample sandwiched between two planar-aligning substrates reflects in the red region of the visible light spectrum with normally-incident light, the light reflected from the fiber is of a much different color, most commonly green to the naked eye. The color of the fibers in transmission mode is red, the complementary color to the green reflection observed. Macroscopically, the fibers show a vivid green color when viewed under room lighting, as seen in Figure 54, but the observed color can be markedly different upon changing the angle of illumination of the fiber. An example of this is shown in Figure 55, where, when viewed with the polarizing optical microscope, the observed reflected color goes from more yellow-green with normally incident light to blue as the angle of illumination approaches 90°.

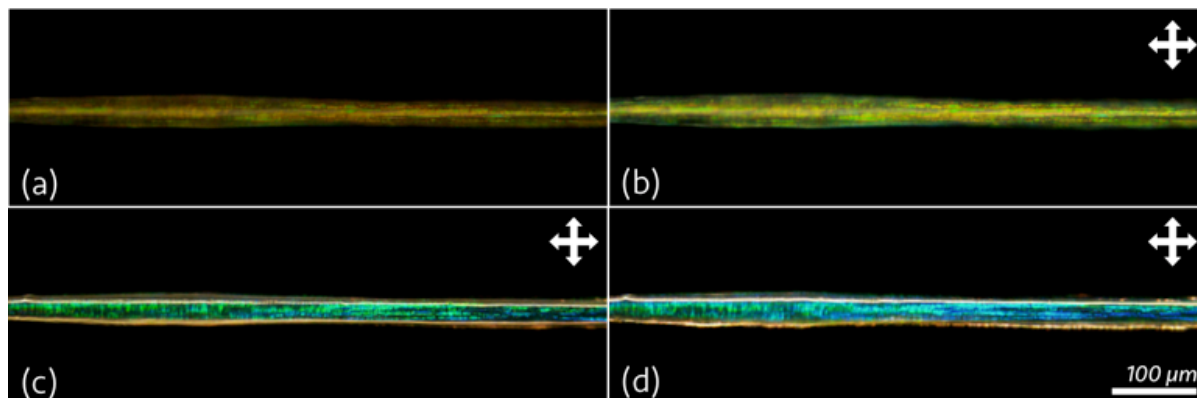


Figure 55. A PI fiber filled with a mixture of 25% w/w ZLI-3786 in RO-TN 615. Scale bars indicate 100  $\mu\text{m}$ . Viewed in reflective mode (a) without crossed polarizers and between crossed polarizers (b) with normally incident illumination; (c) with obliquely incident illumination from  $\sim 45^\circ$ ; (d) with obliquely incident illumination from  $\sim 60^\circ$ .

The angle dependence of the reflected color from the liquid crystal is due to Bragg reflection, likely from two different sources: reflection from an aligned "shell" of liquid crystal very close to the polymer-liquid crystal interface and from a multidomain "powder" within the fiber core.<sup>e</sup> During the jetting process, the liquid crystal is aligned by the flow [201] to orient with the director along the flow direction, consequently with the helical axes normal to the fiber interface and similarly to the case of the achiral nematic-filled fibers. Once the flow ceases, since other defect configurations would be energetically costly to adopt, the liquid crystal within the fiber maintains this structure near the interface, but with internal fluctuations from the liquid causing the loss of order away from the interface. A proposed structure for the orientation of the core in the fiber geometry is presented in Figure 56.

<sup>e</sup>While spectral measurements of the colors reflected from the fibers were not performed in this work, the use of spectral measurements, in particular UV-Vis spectroscopy, would give us insights into how well-aligned the liquid crystal is within the fibers. If the fiber cores are well-aligned, the spectra would show clear peaks at given reflected wavelengths, while broad spectra would be more indicative of a non-uniform alignment.

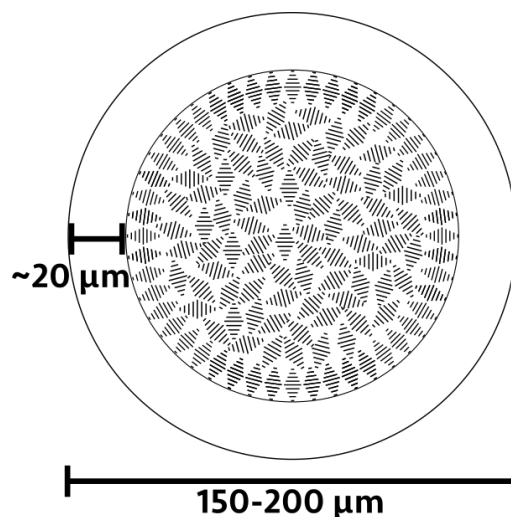


Figure 56. An idealized schematic of the proposed liquid crystal structure of a spun PI fiber filled with a cholesteric, using a typical unstretched fiber. Very close to the border between the liquid crystal core and the polymer sheath, a well-aligned cholesteric structure is predicted. This, however, quite rapidly decays in the interior of the fiber core. The schematic represents the projection of a director structure in the fiber cross-section, but there would additionally be variation along the fiber axis (orthogonal to the plane of the page). Adapted and reproduced from Honaker et al (2019) with permission from the Royal Society of Chemistry [48].

Fibers filled with such a cholesteric additionally display a thermochromic response, with the color reflected from the fiber blueshifting upon fiber heating and redshifting upon cooling. This corresponds to the tightening and loosening of the cholesteric helix due to heating and cooling, leading to a change in the pitch and the colors that are consequently reflected. An example of such a response can be seen in Figure 57.

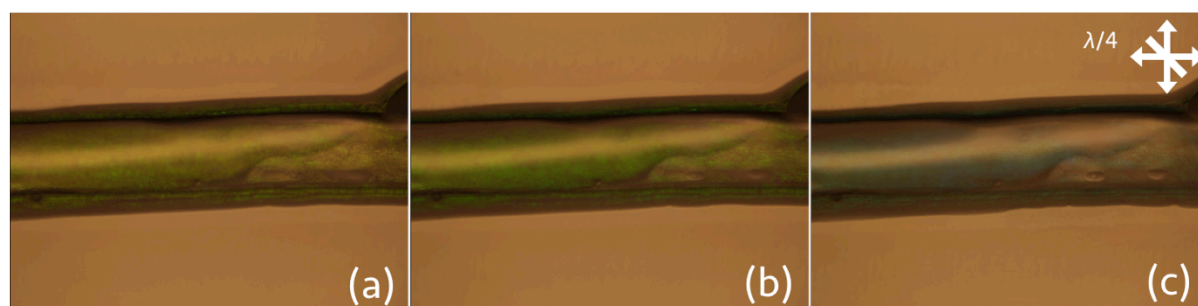


Figure 57. A PI fiber filled with a mixture of 25% w/w ZLI-3786 in RO-TN 615, mounted on a glass slide and viewed in reflection mode between crossed polarizers with an inserted quarter wave plate. The fiber begins in (a) at room temperature ( $\sim 20^\circ\text{C}$ ) before being heated to  $\sim 35^\circ\text{C}$  in (b) and  $\sim 50^\circ\text{C}$  in (c). The heating from (a) to (c) corresponds to the reflected color shifting from yellow-green in (a) to greener in (b) and eventually to blue in (c). Similar behaviors are observed in the freely-hanging fibers. Reproduced from Honaker et al (2019) with permission from the Royal Society of Chemistry [48].



In contrast to the pure polyisoprene fibers, the fibers filled with a liquid crystal were not as stable, especially when stored for long periods of time, and could not endure as much strain before failure. The most likely cause of this is a combination of the very thin sheath (estimated at 15-30  $\mu\text{m}$  from the co-flow images and the micrographs) and the swelling of the polymer by the liquid crystal; while, as mentioned earlier, polyisoprene and polybutadiene are subject to flow, the high molecular weights of the polymers, combined with the "short" experimental times we work with, means that any effects from flow of the unstressed polymer are negligible in comparison to the polymer-liquid crystal interaction.

For a typical synthetic liquid crystal (eg. 5CB), we can calculate its Hansen solubility parameters using methods presented by Fedors [134], Araya et al [135], and Hansen [138], as described in Chapter 2.6. These parameters, for 5CB, were found to be  $\delta_D = 19.3 \text{ MPa}^{1/2}$ ,  $\delta_P = 8.3 \text{ MPa}^{1/2}$ , and  $\delta_H = 3.0 \text{ MPa}^{1/2}$ <sup>f</sup>. We can then compare this to typical reported parameters for PI ( $\delta_D = 16.9 \text{ MPa}^{1/2}$ ,  $\delta_P = 1.1 \text{ MPa}^{1/2}$ ,  $\delta_H = -0.4 \text{ MPa}^{1/2}$ , and  $R_o = 9.6 \text{ MPa}^{1/2}$  [137,138]) by using equation (2.11) to obtain  $R_a$ , then comparing the ratio of  $R_a$  to  $R_o$ :

$$\begin{aligned} R_a^2 &= 4 \cdot (19.3 - 16.9)^2 + (8.3 - 1.1)^2 + (3.0 + 0.4)^2 \\ R_a^2 &= 23.4 + 53.3 + 11.6 = 88.3 \text{ MPa} \\ R_a &= 9.4 \text{ MPa}^{1/2} \end{aligned}$$

As  $R_a < R_o$ , this satisfies the condition for solubility of the polyisoprene in the liquid crystal. Backed up by observations, we can conclude that the liquid crystal swells the polymer to some degree, acting as a plasticizer that negatively affects the sheath integrity. This is, naturally, a major issue for the eventual use of these fibers in application, since they degrade quite rapidly (often within one to two weeks, likely due to the presence of liquid crystal preventing crystallization of the PI, thus removing the possibility of any physical crosslinks). One possible means to mitigate this miscibility after fiber production would be through chemical cross-linking of the fibers immediately after production.

While it is conceivable that fibers of a sufficiently thin diameter are usable for tensile sensors [189], the fibers we produce are not thin enough to be useful for such an application. The principle of such a fiber sensor would be similar to the principle of the Grandjean-Cano cell for measuring cholesteric pitch [225]. As only half-integer multiples of pitch are admitted in a cell consisting of two substrates with identical planar anchoring conditions, by decreasing the fiber thickness, the effective pitch decreases since the number of pitch units remains constant, thus blueshifting the reflected light. (The inverse is the case for making the sample thicker, where the effective pitch is also distorted from equilibrium due to conservation of the pitch number, but results in a redshift instead.) This decrease in thickness, however, frustrates the pitch and produces an elastic energy deformation.

---

<sup>f</sup>While RO-TN and E55 mixtures are not chemically or physically equivalent to 5CB, for the purpose of these calculations, I chose 5CB as a representative nematic liquid crystal for these calculations. This is additionally motivated by the fact that 5CB is the primary component of a commonly-used mixture, E7, originally developed by BDH [242] (who also produced E55).

Because the interior of the fiber core is liquid and free to move, however, when the thickness of the sample approaches another half-integer multiple of the pitch, it becomes more energetically favorable for the liquid crystal to "snap" back to a configuration with the cholesteric adopting a configuration with a half-integer multiple of the equilibrium pitch. This process is illustrated in Figure 58.

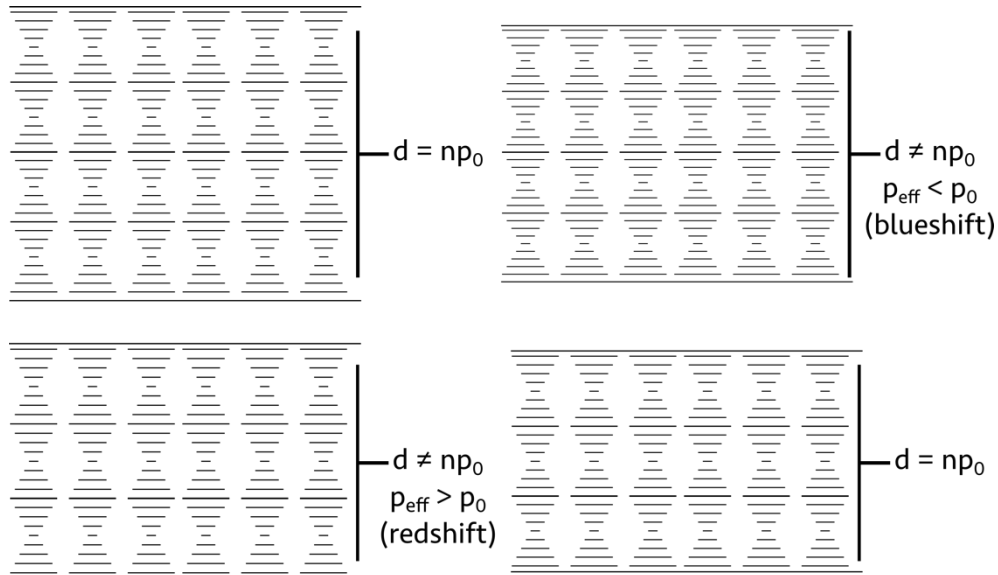


*Figure 58. Schematic representation of the pitch within a confined cholesteric between two parallel glass substrates with a sample thickness  $d$ . We assume identical planar alignment conditions on both substrates. The preferred configuration of the liquid crystal is with half-integer multiples of the equilibrium pitch ( $d = p_0 | 2n \in \mathbb{Z}^+$ ) in the cell: either increasing or decreasing the sample thickness will increase or decrease the effective pitch, and thus shift the reflected color. If the thickness of the sample approaches another half-integer multiple of the equilibrium pitch, however, the liquid crystal will adopt such a configuration.*

Due to symmetry considerations, a cylindrical geometry requires instead that full integer multiples of pitch be accommodated inside the fiber [189] since there needs to be a defect at the center from which the helix radiates outward. The effect, however, is similar, where, because of the constraints imposed by the boundary conditions, by decreasing the sample thickness, we will see a similar "snapping" effect. Therefore, in principle, we should be able to see a color change if the fiber thickness were much closer to the order of the cholesteric pitch, as small changes in the fiber diameter will increase and decrease the effective pitch of the liquid crystal.<sup>§</sup>

<sup>§</sup>Because the core is liquid, when the core is thinned, the material can "snap" to readopt the equilibrium pitch. To show this, we consider a well-aligned cholesteric liquid crystal with an equilibrium pitch of 600 nm (red reflecting), with five pitch steps confined within a fiber (producing a core diameter of 3.0  $\mu\text{m}$ ). To keep the five pitch steps while getting a green-reflecting cholesteric (pitch step of 500 nm), we would need to compress the core to a diameter of 2.5  $\mu\text{m}$ , but this is near the next integer multiple of the equilibrium pitch (2.4  $\mu\text{m}$ ), meaning that the liquid crystal would become more likely to show reflect red. Only by either freezing in the pitch, which would require

On the other hand, a color change can be observed upon stretching a typical filled fiber, as shown in Figure 59, but this shift is subtle and rapidly relaxes away.

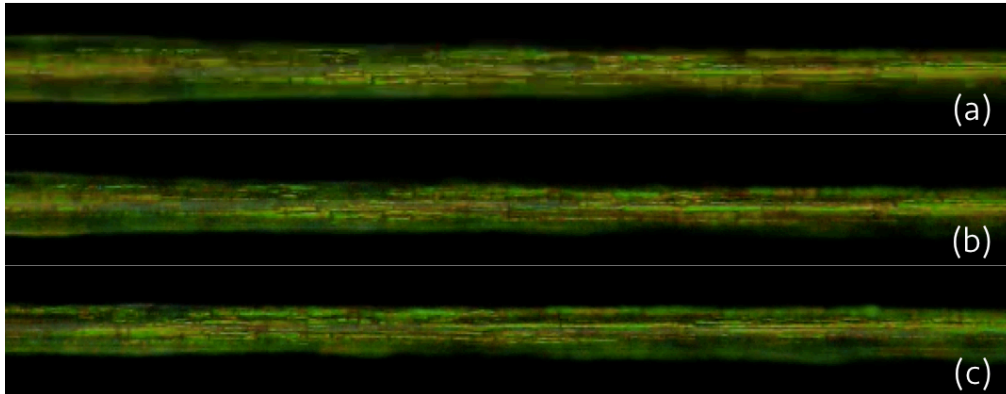


Figure 59. A PI fiber filled with 25% w/w ZLI-3786 in RO-TN 615 mixture, as viewed in reflection mode between crossed polarizers. The difference between (a), (b), and (c) is stretching the fiber to thin it progressively, with (c) being the most stretched; the stretching induces a color change that is somewhat more obvious between (a) and (c), but is still quite subtle and does not remain. Reproduced from Honaker et al (2019) with permission from the Royal Society of Chemistry [48].

At a first glance, the response upon stretching is more characteristic of the response of the fiber upon heating and cooling, similar to that presented in Figure 57, which suggests that there could be stretching-induced heating of the liquid crystal very close to the polymer-liquid crystal interface. To investigate whether this is the source, we can calculate the heating induced by stretching, assuming an instantaneous deformation before the onset of stress relaxation and dissipation of the applied energy.

For a polymer composed of  $N$  units of length  $b$  (often called the *Kuhn length* [98]), with an end-to-end distance  $R$ , as described in chapter 2, upon stretching, we apply work to the fiber due to the polymer coil behaving like a spring with spring constant  $k = \frac{3k_B T}{Nb^2}$  [98]. Therefore, knowing that the restoring force from Hooke's Law is:

$$\vec{F} = -k\vec{x} \quad (4.1)$$

the work performed between the states is:

$$W = \int_{R_i}^{R_f} \vec{F} \cdot d\vec{r} = -\frac{3k_B T}{2Nb^2} (x^2) \Big|_{R_1}^{R_2} = -\frac{3k_B T}{2Nb^2} (R_2^2 - R_1^2) \quad (4.2)$$

Therefore, the work put into the system is the same as the heat lost to the LC core, assuming that all of the input energy is dissipated as heat rather than being converted into internal energy.

Considering the physical parameters of the polyisoprene used in these experiments ( $b \sim 9 \cdot 10^{-10} \text{ m}$  [106],  $M_w \sim 10^3 \frac{\text{kg}}{\text{mol}}$ ,  $N = \frac{M_w}{M_{\text{monomer}}} = \frac{10^6 \text{ g/mol}}{68 \text{ g/mol}} \sim 1.5 \cdot 10^4$ ),

polymerizing the core material, or by having a core with diameter comparable to that of the helical pitch would it be possible to readily see the color change upon stretching.

and taking  $R_1$  as the average length of the polymer ( $R_1 = \sqrt{N} \cdot b = 1.1 \cdot 10^{-7} \text{m}$ ), and assuming a strain to  $R_2 = 2 \cdot R_1$ , by using room temperature for  $T$ , we then get the heat lost per molecule as:

$$\begin{aligned} [q_{pol}] = W &= -\frac{3(1.4 \cdot 10^{-23} \text{ J/K})(290 \text{ K})}{2(1.5 \cdot 10^4)(9 \cdot 10^{-10} \text{ m})^2} (3 \cdot (1.1 \cdot 10^{-7} \text{ m})^2) \\ &= -\frac{(1.2 \cdot 10^{-20} \text{ J})}{(3 \cdot 10^4)8.1 \cdot 10^{-19} \text{ m}^2} (3.6 \cdot 10^{-14}) \text{ m}^2 \\ &= -\frac{(1.2 \cdot 10^{-20} \text{ J})}{2.4 \cdot 10^{-14}} (8.7 \cdot 10^{-15}) = -6.0 \cdot 10^{-21} \text{ J} \end{aligned} \quad (4.3)$$

This is then multiplied by Avogadro's number to get the heat loss per mole:

$$-6.0 \cdot 10^{-21} \cdot 6.0 \cdot 10^{23} = -3.6 \cdot 10^3 \frac{\text{J}}{\text{mol}}$$

Dividing by the polymer molar mass, this then gives  $q = -3.6 \cdot 10^{-3} \frac{\text{J}}{\text{g}}$  as the heat loss per unit mass.

We consider a fiber of length  $R_1 = 2 \cdot 10^{-3} \text{m}$  and thickness  $d = 2.5 \cdot 10^{-4} \text{m}$ , with a core thickness of  $d_{core} = 2 \cdot 10^{-4} \text{m}$ . The corresponding volume of the polymer portion of segment (assuming a conservation of volume throughout the sample) is then

$$V = \pi[(1.25 \cdot 10^{-4} \text{m})^2 - (10^{-4} \text{m})^2] \cdot 2 \cdot 10^{-3} \text{m} = 3.5 \cdot 10^{-11} \text{m}^3$$

Using a density of polyisoprene as  $9 \cdot 10^5 \frac{\text{g}}{\text{m}^3}$  [106], the mass of polyisoprene in the system is then  $3.2 \cdot 10^{-5} \text{g}$ , which corresponds to a heat loss of  $1.2 \cdot 10^{-7} \text{J}$  to be transferred to the LC.

For the mass of the liquid crystal, assuming a density similar to that of 5CB (as well as a similar heat capacity), we first calculate the mass of the LC:

$$m = \rho V = 10^3 \frac{\text{kg}}{\text{m}^3} \cdot \pi(7.5 \cdot 10^{-5} \text{m})^2 \cdot 2 \cdot 10^{-3} \text{m} = 3.5 \cdot 10^{-5} \text{g}$$

With a heat capacity of  $\lambda = 1.9 \frac{\text{J}}{\text{g} \cdot \text{K}}$  [226], the mass-adjusted heat capacity becomes  $\lambda = 6.7 \cdot 10^{-5} \frac{\text{J}}{\text{K}}$ . Knowing the heat loss from the polymer entropy and assuming uniform heating of the LC core, this then becomes:

$$\Delta T = \frac{q}{\lambda} = \frac{9.1 \cdot 10^{-6} \text{ J}}{6.7 \cdot 10^{-5} \text{ J/K}} = 0.0018 \text{ K}$$

The assumption of simultaneous uniform heating of the liquid crystal, however, is likely not the case here. If we assume uniform heating, this temperature change is not enough to induce a perceptible color change in the bulk liquid crystal mixture. However, the outermost shell of the liquid crystal core closest to the interface between polymer and liquid crystal, from which Bragg reflection from an aligned sample occurs, can very rapidly be heated by this temperature change. If the stretching thus occurs very quickly, this may be sufficient to produce a very fast, short-lived temperature increase before the heat uniformly distributes throughout the liquid crystal and viscous response to deformation causes the elastic energy to be dissipated, but this response is minor and barely perceptible, especially to the unaided eye, and the corresponding response time should be on the order of milliseconds [227]. A more likely source could be that, because the liquid crystal core becomes better aligned due to flow induced by stretching, the reflected color

becomes more uniform, which corresponds to a green reflection, but more investigation and characterization would be needed to answer the question of the source of the color shift.

#### **4.5 PVA Fibers with Cholesteric Liquid Crystal Cores**

We additionally investigated the spinning of PVA fibers containing a liquid crystal core. This was done to see if we are able to spin a core-sheath fiber from liquids with a much higher interfacial tension between them. While the interfacial tension between hexane and a liquid crystal is likely quite low because of miscibility between the two materials, probably on the order of  $10^{-7}$  mN/m [49], we found the interfacial tension between a PVA solution and a liquid crystal to be on the order of that between a liquid crystal and water ( $10^{-2}$  mN/m).

We spun the PVA fibers from 20% w/w aqueous dope while co-flowing a core of E55 mixed with ZLI-3786. The PVA fibers spun with the cholesteric mixture as a core did not show any core incorporation, either to the naked eye or with POM, whereas the PI fibers did. The likely reason for this is the (comparatively) very high interfacial tension between the PVA solution and the liquid crystal due to the absence of miscibility (four to five orders of magnitude higher). To introduce some miscibility between the liquid crystal and the polymer sheath, however, we mixed ethanol into the liquid crystal: since the liquid crystal is not miscible in water or PVA, we introduced ethanol to create some miscibility with the sheath solvent (here, water). By adding 5% w/w anhydrous ethanol into the liquid crystal mixture, producing an optically-transparent isotropic phase, and spinning the core from this, however, we do observe eventual incorporation of the cholesteric in the fiber, although with considerable beading both in the jetting and in the fibers produced. Images of the jetting process and the instability that developed at low flow rates of core can be seen in Figure 60: in (a), we can see that the jet begins to break apart very soon after the production from the spinneret. While increasing the inner flow rate upwards does help to avoid jet break-up near the spinneret, it is quite clear that instability begins to develop in the form of undulations in the jet of liquid crystal, especially when compared to the case depicted in Figure 49 showing a co-flowing system where the core and sheath phases have some miscibility with each other.

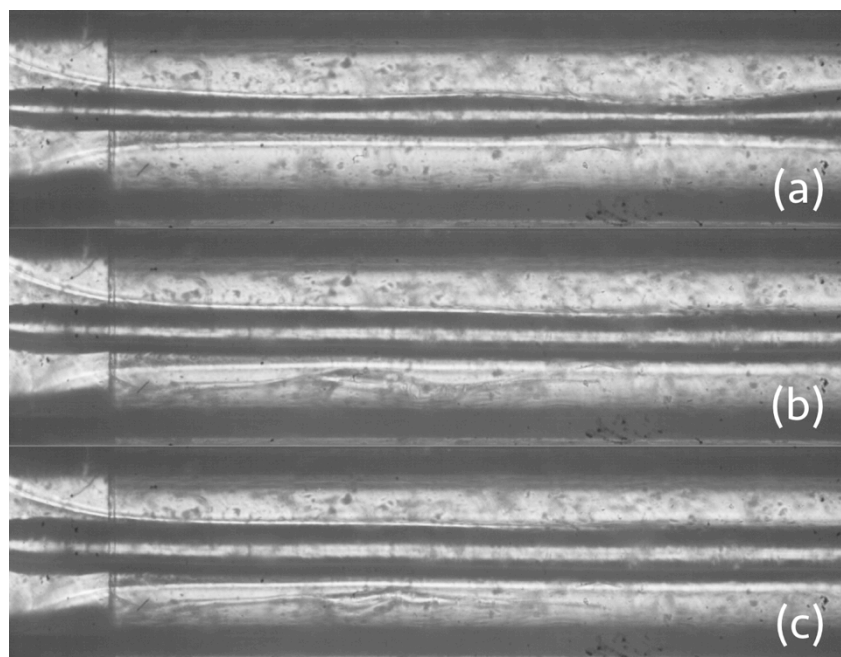


Figure 60. Jetting observed in a tri-flowing system consisting of an outer bath phase of 8%  $\text{CaCl}_2$  and 10% PVP in anhydrous ethanol, an aqueous polymer dope prepared with 20% PVA as a middle phase, and a core of 25% ZLI-3786 in E55 mixed with 5% w/w anhydrous ethanol. Flow rates are 1.05 mL/h for the bath and 0.35 mL/h polymer dope in all images. Core flow rates are (a) 0.5 mL/h; (b) 1.0 mL/h; and (c) 2.0 mL/h. While not as apparent in (c) as in (a) and (b), undulations in the core that are hallmarks of the development of instability can be observed.

Considerable beading was present in the morphology of both core and sheath, with the fiber showing a "bead-on-a-chain" structure, both macroscopically and microscopically: liquid crystal was visibly incorporated into the core in places, but not as a single, contiguous strand. Since PVA does not exhibit Bragg reflection, the colors we see in Figure 61 result solely from the liquid crystal and not from the polymer sheath.

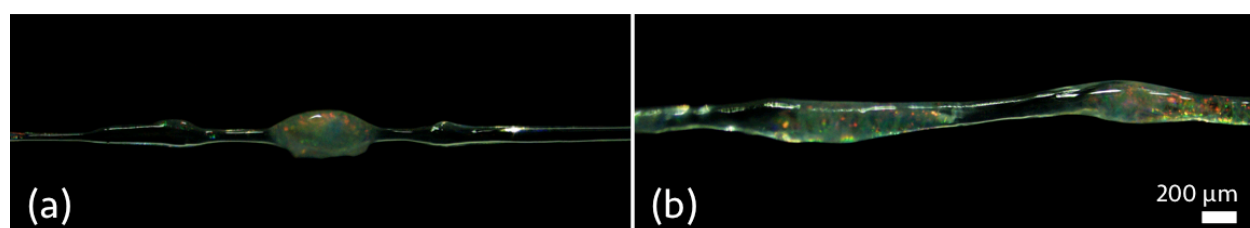


Figure 61. Beading shown in a fiber spun from 20% PVA (aq) with a core of 25% ZLI-3786 in RO-TN 615, as viewed in reflection mode between crossed polarizers, shown in two different sections of fiber. Flow rates were 1.05 mL/h bath, 0.35 mL/h polymer dope, and 8.0 mL/h liquid crystal. Scale bar as shown. The colored reflection arises from the presence of liquid crystal material.

This result is similar to the irregularly-filled fibers obtained by Reyes et al [4] when electrospinning PVP with a 5CB core. Reyes et al reported that the reason for the

discontinuous cores in their PVP fibers spun from ethanol was the swelling of the PVP sheath by water, particularly due to PVP's highly hygroscopic nature and the additional infiltration of ethanol from the fiber dope into the liquid crystal core [4,188]. As seen with the beading of liquid crystal in PVA fibers, though, the beading of the liquid crystal within the core could also likely be a result of an increased interfacial tension between the polymer and liquid crystal due to a lack of miscibility. PVP and 5CB are both soluble in ethanol, but 5CB is not a solvent for PVP<sup>h</sup>, thus producing a considerable interfacial tension between the two materials in the absence of ethanol [172].

Remarkably, though, unlike with the polyisoprene, the PVA did not show swelling and residues after storage. To explain this, we can look at the theoretical miscibility by using the Hansen parameters and solubility radius for PVA (reported as  $\delta_D = 17.0 \text{ MPa}^{1/2}$ ,  $\delta_P = 9.0 \text{ MPa}^{1/2}$ ,  $\delta_H = 18.0 \text{ MPa}^{1/2}$ , and  $R_o = 4.0 \text{ MPa}^{1/2}$  [137,138]) in eq. (2.11):

$$\begin{aligned} R_a^2 &= 4 \cdot (19.3 - 17.0)^2 + (8.3 - 9.0)^2 + (3.0 - 18.0)^2 \\ R_a^2 &= 21.2 + 0.5 + 225 = 246.7 \text{ MPa} \\ R_a &= 15.7 \text{ MPa}^{1/2} \end{aligned}$$

Since  $R_a \gg R_o$ , the miscibility condition is very clearly not met, which means that the liquid crystal cannot readily swell the PVA. This is an asset, since the final fibers will not degrade with time due to swelling from the liquid crystal; on the other hand, the lack of miscibility with the PVA drives the interfacial tension upwards, at least by three orders of magnitude [49,172], which makes achieving core continuity difficult. At the same time, however, adding ethanol to the liquid crystal core creates its own set of issues, with the phase behavior of a liquid crystal-ethanol mixture showing complicated behavior [188], and considering that PVA is not significantly soluble in ethanol, its extraction from the core can be difficult.

#### 4.6 Numerical Analysis of the Spinning Parameters

The necessity of the degree of miscibility between the core and sheath (where we have a lack of core continuity) can also be modeled numerically. For liquid crystals, the interfacial tensions between aqueous phases and polymer phases are somewhat moderate (in chapter 3, the interfacial tension between a dilute solution of PVA and the common liquid crystal 5CB was found to be on the order of 30 mN/m).

To see how the theoretical predictions stand up to what we observe during jetting, we consider in a typical microfluidic set-up used to produce fibers by using a coaxial

---

<sup>h</sup>To show this, we can quantify the relative energy distance of PVP to 5CB, using  $\delta_D = 21.4 \text{ MPa}^{1/2}$ ,  $\delta_P = 11.6 \text{ MPa}^{1/2}$ ,  $\delta_H = 21.6 \text{ MPa}^{1/2}$ , and  $R_o = 17.3 \text{ MPa}^{1/2}$  [138]. Inserting these values into equation (2.11), we get  $R_a = 19.4 \text{ MPa}^{1/2}$ .  $R_a > R_o$ , which does not satisfy the condition for miscibility. If the solubility parameters are similar, though, as is the case here, then polymer swelling can instead occur [138]. Work performed by collaborators at the Technische Hochschule Bonn-Rhein-Sieg, Mr. Lukas Pschyklenk and Dr. Peter-Michael Kaul, suggests that 5CB can swell PVP, though to a lesser degree than PI or PB.

jet of a liquid crystal (ex. 5CB) inside a polymer solution (a jet with diameter of 100  $\mu\text{m}$  and with a viscosity of  $\sim 30 \text{ mPa}\cdot\text{s}$  [228], flowing at a rate of 1 mL/h inside a polymer flow, such as a 15% PVA in water solution of 1 mL/h<sup>i</sup>), we can first estimate the Reynolds number:

$$Re = \frac{\rho v l}{\eta} = \frac{\left(1010 \frac{\text{kg}}{\text{m}^3}\right) \left(5.7 \cdot 10^{-3} \frac{\text{m}}{\text{s}}\right) (10^{-4} \text{m})}{0.03 \text{ Pa} \cdot \text{s}} = 0.12 \quad (4.4)$$

This is a low Reynolds number case, meaning that the controlling inner flow parameter should be the capillary number, which determines how strongly the viscous forces in the inner flow will dominate the interfacial tension forces within the jet:

$$Ca_{in} = \frac{\eta_{LC} v_{in}}{\gamma} = \frac{(0.03 \text{ Pa} \cdot \text{s}) \left(5.7 \cdot 10^{-3} \frac{\text{m}}{\text{s}}\right)}{0.03 \frac{\text{N}}{\text{m}}} = 5.7 \cdot 10^{-3} \quad (4.5)$$

This does not satisfy the condition necessary in Castro-Hernandez et al, so the capillary number of the outer flow, which quantifies how the viscous forces in the *outer* flow (here, the polymer solution) will damp the propagation of instability, is then considered<sup>j</sup>. Assuming a viscosity of 10 Pa·s for the outer phase, which is typical for concentrated solutions of either PVA [104] or PI, and that the capillary in which the flow occurs has a diameter of 700  $\mu\text{m}$  (typical for our microfluidics set-ups):

$$Ca_{out} = \frac{\eta_{PVA} v_{out}}{\gamma} = \frac{(10 \text{ Pa} \cdot \text{s}) \left(7.3 \cdot 10^{-4} \frac{\text{m}}{\text{s}}\right)}{0.03 \frac{\text{N}}{\text{m}}} = 0.25 \quad (4.6a)$$

The outer phase capillary number condition is largely met, meaning that jetting should result. On the other hand, the transition to Weber number-driven flow should take place for a flow rate eight times larger (8 mL/h), for which the Reynolds number is approximately one. By inputting these numbers into the Weber number equation:

$$We_{in} = \frac{\left(1010 \frac{\text{kg}}{\text{m}^3}\right) \left(4.6 \cdot 10^{-2} \frac{\text{m}}{\text{s}}\right)^2 (10^{-4} \text{m})}{0.03 \frac{\text{N}}{\text{m}}} = 0.007 \quad (4.6b)$$

This additionally fails to satisfy the stability condition. We did see such a behavior in the case of jetting a cholesteric liquid crystal mixture in a co-flow with an extremely viscous PVA solution, as shown in Figure 60, where, for very low flow rates, we saw

---

<sup>i</sup>We estimate the flow speed by dividing flow rate by cross-section area; for the polymer solution, this becomes  $v = \frac{Q}{\pi(r_{capillary}^2 - r_{jet}^2)}$ .

<sup>j</sup>As described in Section 2.7, the capillary number equation is used twice, both in (4.5) and (4.6a), but the different uses of the capillary number here actually have two physically different meanings. In the case of the outer phase capillary number, equation (4.6a) quantifies how the viscous forces of the outer phase will prevent the development of instability at the interface. The inner phase capillary number in (4.5) instead looks at how the viscous forces of the inner phase will impede the development of jet instability.



that the jet broke very quickly, resulting in inhomogeneous fiber filling in the final product.

Predicting the flow stability of the liquids used in the successful wet spinning of liquid crystal-filled fibers, however, requires a different consideration of the interfacial tension: when spinning an elastomer fiber containing a liquid crystal core, for example, the standard solvent used is hexane, which is extremely miscible with most liquid crystals. Lacaze et al report that, for two miscible phases, a transient interfacial tension between the two materials does exist, but on the order of  $10^{-8}$ – $10^{-7}$  N/m<sup>k</sup> and that such an interfacial tension quickly decays until the phases fully mix [49]. Thus, by using an estimate of the interfacial tension to be on the order of  $10^{-7}$  N/m, for example, we then transform equation (4.9b) into:

$$Ca_{in} = \frac{(0.03 \text{ Pa} \cdot \text{s})(5.7 \cdot 10^{-3} \text{ m/s})}{10^{-7} \text{ N/m}} = 1710 \quad (4.7)$$

which is extremely high and very easily satisfies the jetting condition predicted by both Castro-Hernández et al [36] and Utada et al [37], showing that the transformation from dripping to jetting conditions can be achieved simply by tuning the miscibility of the core and sheath phases. Thus, from this flow-rate analysis, we can see that the presence of miscibility transforms what would be a non-jetting case into a jetting case: with a very low interfacial tension, this allows the body and viscous forces to dominate, resulting in continuous jetting without breaking. This is noticeable in the cases of the liquid crystal jetting in polymer flows, where we observe clear and continuous jetting in presence of an organic solvent miscible with the liquid crystal (such as toluene and hexane). The major difference between the two situations (with good jetting and without good jetting) is, indeed, the miscibility between sheath and core, which has a corresponding effect on the interfacial tension and the flow stability numbers.

## 4.7 Conclusions

In this chapter, a wet-spinning approach for producing fibers has been developed and used to spin fibers both of pure polymers, such as PVA and PI, and fibers containing liquid crystal cores on a laboratory scale. To my knowledge, this is the first report of wet spinning elastomer sheath-liquid crystal core fibers, with previous results of incorporating liquid crystals into fibers being achieved either by phase separation spinning or electrospinning. The set-up used here is amenable to upscaling for potential industrial applications, a distinct advantage over electrospinning processes.

The pure polymer fibers obtained are robust and long-lived, capable of maintaining their shape and physical properties even upon long-term storage (on the order of weeks for PI and months for PVA) though the fibers filled with liquid crystals are not yet usable in applications. The miscibility issues, both with the

---

<sup>k</sup>Unfortunately, as demonstrated with the CNC dispersions, such a magnitude of interfacial tension is not yet measurable with our system for interfacial tensiometry as presented in Chapter 3.

liquid crystal being a solvent for the polyisoprene and not for PVA, lead to very different outcomes, neither of which is desirable. Both filled and unfilled polyisoprene fibers are stretchable, with maximum deformations exceeding 500% strain, and the fibers filled with a cholesteric show color changes upon heating and cooling.

This work has additionally confirmed that the miscibility between core and sheath plays a role in ensuring core contiguity, in particular during the spinning of PVA fibers with liquid crystal cores. By introducing a small degree of miscibility to the liquid crystal core, we go from a situation where no liquid crystal survives in the core in the final product to a situation where the liquid crystal is incorporated, though as a beaded and discontinuous core. This work is additionally being continued in the ESMP group within the framework of the Ph.D. thesis of Mr. Shameek Vats, more from the electrospinning side, in examining the effects of core continuity when spinning fibers of 5CB with a sheath of poly(acrylic acid): since this polymer is soluble in both ethanol and water, while 5CB is soluble only in ethanol, this allows the systematic study of systems of varying degrees of miscibility.

To improve the fibers obtained and enable their use in future applications, the following are proposed:

- The spinning of both PVA and PI fibers was performed without chemical cross-linking, neither during the spinning process nor afterwards. To improve the durability of the fibers and to reduce the likelihood of the liquid crystal leaching out, chemical cross-linking is necessary, most likely through photocrosslinking [109]. While other techniques for cross-linking, such as cold vulcanization, exist, these require materials and set-ups (such as sulfurous compounds [110]) that are far from suitable for the laboratory setting.
- The present work shows considerable limitations in terms of the minimum size of fiber achievable. While fibers of diameters as low as 10  $\mu\text{m}$  of polymer alone and 40  $\mu\text{m}$  when filled with liquid crystal are obtainable, their fragility means that cross-linking *in situ* would likely be necessary to achieve even thinner fibers that are robust and capable of being handled and stored.
- Exploration of different polymers as sheaths, such as polysiloxanes (like PDMS), is another direction. Since polysiloxanes are less soluble in liquid crystals compared to the polydienes studied here, they could be a good choice in ensuring that the core does not leach from the liquid crystal. At the same time, though, having miscibility between the core and sheath improves the outcomes of the continuous fiber, thus improving the longevity of the fibers and allowing for their use in applications.
- Additional work has been done on the production of liquid crystal elastomers, which show actuation from light, heat, or another stimulus that can manifest itself in the form of a shape deformation or a color change [7,27,220]. The wet spinning system presented here is a promising method to incorporate these materials into a fiber, especially with a polymer sheath (such as an elastomer) to help protect the fiber and improve its durability. This would require optimization of timing and the protocol for spinning, in particular to ensure that the elastomer would remain intact during the fiber production process. This could be achieved

either by *in situ* polymerization, such as by photopolymerization or a chemical reaction which could to suppress flow instability and ensure a continuous fiber, or by the simply adapting the protocol presented here for nematic-filled fibers before polymerization in post-processing.

- As stated earlier, there are issues when trying to wet-spin with certain systems, as the spinneret device can easily clog as a result of the coagulation process. To overcome this, alternate spinneret geometries can be employed, such as one proposed in Figure 62, to minimize the interface between the coagulation bath and the sheath material, but fabricating such a spinneret is technically much more challenging than the simpler spinnerets we use, as several nested capillaries would need to be employed.

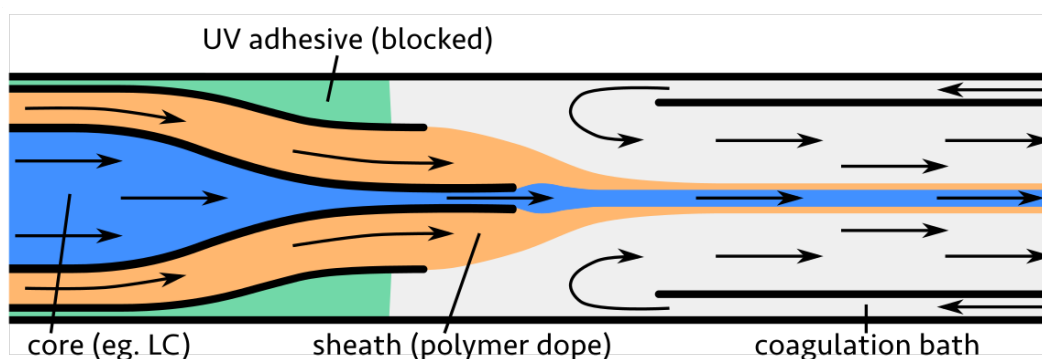


Figure 62. Alternate proposed spinneret geometry to minimize clogging issues. This would use two nested, tapered capillaries, much like an electrospinning spinneret.

The lessons learned and knowledge gained in producing core-sheath fibers here will be further expounded on in Chapter 5, in which the spinning of fibers with liquid metal cores is presented. This is a considerably more challenging system, not least because of the combination of the high interfacial tension of the liquid metal with its low viscosity, but the wet-spinning approach developed here will greatly help in achieving our aim.



## **CHAPTER 5**

# **LIQUID METAL JETTING IN CO-FLOWING SYSTEMS: TOWARDS PRODUCING CORE-SHEATH FIBERS WITH LIQUID METAL CORES**

As detailed in the introduction, the dynamics of flowing systems are a delicate interplay between both material properties (such as density, viscosity, and miscibility) and flow parameters, and this is particularly the case when one of the components is a liquid metal. In order to successfully produce fibers incorporating a heterocore, the ability to characterize and determine the flow behavior within a co-flowing system is a necessary step towards the production of fibers with a continuous core.

This chapter presents the characterization of the flow of galinstan and work towards encapsulating galinstan as a continuous core within a polymer fiber. We first comment on the flow parameters relevant to jetting of galinstan from a more theoretical standpoint. We then discuss the co-flows of galinstan in various fluids (the viscous acrylate monomer PETA; glycerol; and solutions of both PVA and PI in their respective solvents), both in two-flow systems, with the galinstan flowing within a single co-flowing liquid, and in three-flow systems, akin to what would be used for producing the desired core-sheath fibers.

I would like to thank the research group of Prof. Michael D. Dickey at North Carolina State University (Raleigh, NC), with whom I spent a week learning about gallium alloy usage, handling, and manipulation, essential to the performance of the experiments detailed in this chapter. I additionally would like to thank Dr. V.S.R. Jampani for his help in performing the initial experiments with galinstan jetting for fiber production.

### **5.1 Motivation and Background: Co-Flowing of Galinstan**

The work presented in this chapter, and in fact the main reason for developing the project underlying the thesis, was initially inspired by a paper in 2011 by Dong et al, which showed electrospinning of liquid metal-core coaxial fibers [34]. These fibers were spun with a galinstan core, which served as the cathode for the composite light-emitting fibers, with an electroluminescent polymer sheath prepared from a mixture of poly(ethylene oxide) and a ruthenium complex. A final coating of indium tin oxide around this sheath served as the anode. Electrospinning a fiber with a conductive core is a tantalizing prospect, with applications for miniaturized electronics for wearable technology.

Reproducing these results, however, has proven elusive. In 2013, attempts of the Soft Nano- and Microstructures group at Seoul National University in South Korea (the predecessor of the ESMP group) to electrospin fibers containing a simple polymer sheath, such as PVP, with a galinstan core were unsuccessful, though the atmospheric conditions and consistent high humidity also played a role in many of the electrospinning issues [28]. This was followed up with experiments to see the co-flowing of galinstan and whether successful jetting of the galinstan jet could be obtained, over what length, and how. As presented in Figure 63, jetting was obtainable in a co-flowing set-up using an outer phase consisting of an aqueous 6% w/w PVA ( $M_w = 145\text{-}168\text{ kDa}$ , 87-89% hydrolyzed) solution.

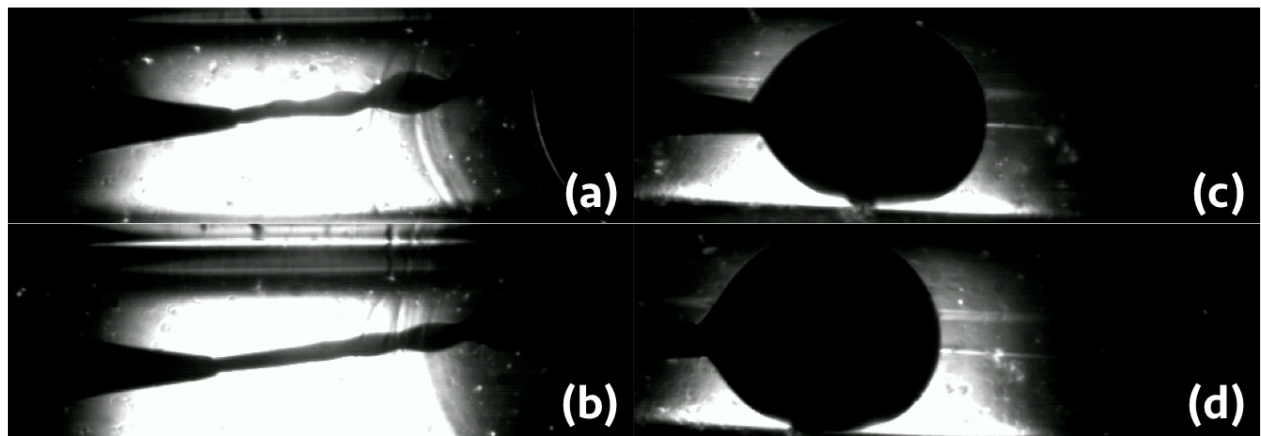


*Figure 63. Jetting of galinstan in a viscous medium, with pressure readings of (a) 100 mbar bath and 500 mbar galinstan; (b) 300 mbar bath and 500 mbar galinstan; (c) 652 mbar bath and 300 mbar galinstan; and (d) 652 mbar bath and 500 mbar galinstan. Images courtesy of Julia Martius, YooMee Kye, JungHyun Noh, and Jan Lagerwall.*

With the recoverable information about flow parameters in the system, we can observe that there is a threshold of inner flow rate above which galinstan jets, as predicted by both Castro-Hernández et al [36] and Utada et al [37], but that the flow rate of the outer phase can additionally serve to destabilize the jet, possibly by the presence of slip between the galinstan and the outer phase at high outer phase flow rates. There are several possible explanations for the jet becoming unstable in Figure 63(d), one being that the outer phase shows a considerable shear thinning with high flow rates, the development of Rayleigh instability then becomes no longer viscously dampened and is allowed to develop. However, an equally-important takeaway is that the images show that a galinstan jet can be stabilized, even if for a short while, during the flowing process, which is a first step towards incorporating galinstan into a fiber with a continuous core.

In general, directly electrospinning conductive materials is challenging and not common, with most production of electrospun conductive fibers coming from first spinning a "carrier" fiber or substrate, then depositing or coating the obtained fibers with a conductive material [229,230] rather than directly electrospinning the conductive polymer. Alternative methods have additionally incorporated conductive components, either nanoparticles or polymers, to create a composite, though these

additionally show challenges in obtaining an ideal final structure [230]. Combined with the difficulties in causing a liquid metal to jet in a co-flow, it is unclear that electrospinning will be consistently successful in obtaining fibers with the liquid metal.

However, as detailed in Chapter 4, we are able to produce core-sheath fibers through a wet spinning process. This avoids many of the issues in the electrospinning process while additionally giving us a view of the spinning process under the microscope, allowing us to see the jetting at each step and determine more easily where issues arise. The first goal in this work was to attempt to replicate/reproduce the jetting of galinstan in a co-flowing set-up, using a viscous material as the outermost phase and to see the presence or absence of jetting as a function of the flow stability predictors (in particular, Weber and capillary numbers of the inner and outer flows). Once jetting parameters are known, we can then proceed towards fiber production with galinstan cores, using the wet spinning technique developed in Chapter 4 to achieve this aim.

## 5.2 Theoretical Framework

Compared to liquid crystals or other fluids, liquid metals have a completely different set of physical properties that makes their incorporation into a jet quite difficult. Liquid metals have the combination of high densities [26,111], low viscosities, and extremely high interfacial tensions [26,44,231]. The flow stability predictors, Capillary number (in low Reynolds number co-flows [35,36]) and Weber number (for higher Reynolds number situations [36,37]), are both sensitive to the interfacial tension between the two phases, which can be considerable in the case of galinstan [26,154]. In this section, the relevant flow parameters that can be used to predict the behavior of the galinstan jet, with respect to our system, will be reviewed.

### 5.2.1 Recap: Numerically Predicting Flow and Jetting Stability

In Chapter 4, we presented the spinning of polymer fibers incorporating liquid crystal cores. Liquid metals, such as galinstan, are very different in behavior from liquid crystals in behavior. Galinstan, for example, has considerably higher density (approximately 6.4 g/mL [26]) and interfacial tensions (normally on the order of 500 mN/m [154]), but an extremely low viscosity (2.4 mPa·s [26]). Substituting these values into the definition of Reynolds number, using exactly the same parameters otherwise (flow rates and orifice diameters) that were used to describe the system in section 4.5, gives:

$$Re = \frac{(6400 \frac{\text{kg}}{\text{m}^3})(5.7 \cdot 10^{-3} \text{m/s})(10^{-4} \text{m})}{0.0024 \text{ Pa} \cdot \text{s}} = 1.5 \quad (5.1)$$

This is a sufficiently high Reynolds number case, which requires an analysis of the Weber number of the inner flow.

$$We = \frac{(6400 \frac{\text{kg}}{\text{m}^3})(5.7 \cdot 10^{-3} \text{m/s})^2 (10^{-4} \text{m})}{0.5 \frac{\text{N}}{\text{m}}} = 4.2 \cdot 10^{-5} \quad (5.2)$$

This Weber number is well below the threshold above which jetting is predicted, and the capillary number does not help much either (being on the order of 0.02). It can fairly readily be seen that, on the scale of the microfluidics experiment, several parameters need to be scaled upwards to satisfy the Weber number condition. Material parameters such as the density and the viscosity of the liquid metal are largely invariable, and, while it is possible to tune the interfacial tension of the metal by using an electric field [171], Khan et al found that this can only be reduced to an interfacial tension of 100 mN/m. This is still significantly higher than that between a liquid crystal and an aqueous solution of any kind [44,45], including in the case where we spun PVA fibers with beaded liquid crystal cores (and still higher than that between water and air [232]).

Therefore, the only parameters that can readily be adjusted in these experiments with respect to the jet itself are the flow speeds, which are related to the flow rate, and the jet diameter (or characteristic length scale), though these normally vary hand-in-hand with each other. In order to get a Weber number of at least unity with the jet diameter and other material parameters as described, which should result in jetting, we would need flow rates of at least 154 mL/h. Alternately, to increase the Weber number, one can decrease the jet diameter: while decreasing the jet diameter will also decrease the characteristic length scale, it will also increase the flow speed (due to a decrease in surface area). As the Weber number scales linearly with characteristic length but quadratically with flow speed, going for thinner jets will help to produce jetting solely from the Weber number characteristic.

Another property that makes liquid metal work less straightforward, on the other hand, is the oxidation of the gallium component of galinstan, as outlined in section 2.2, which forms a solid oxide. This is a property that can also be tuned to obtain stable jetting, but it is not entirely straightforward and adds additional considerations to the system, as detailed in the next section.

### 5.2.2 Oxidation of Galinstan and the Péclet Number

During the experiments in chapter 3, successful interfacial tension measurements were achieved by using an environment where the oxide skin either did not form or was quickly etched away. On the other hand, the formation of the oxide here can help to stabilize the jet during the formation process, as this would create a solid-liquid interface (gallium oxide-polymer dope) as opposed to a liquid-liquid (polymer dope-galinstan) interface. Galinstan can flow freely within the gallium oxide layer [233], so this would allow us to have a fiber with a flexible, liquid core while still being stabilized. The formation of gallium oxide requires a more neutral pH environment (pH 3-10) and the presence of dissolved oxygen in the solvent, which is more likely the case when PVA solutions are used.

In microfluidics flow regimes, as outlined in Section 2.8, laminar flow is present rather than turbulent flow due to the low Reynolds number [132], meaning that



oxygenation of the galinstan occurs from diffusion of oxygen to the interface between the two materials (here, the polymer dope and the liquid metal). To see whether diffusion plays a significant role in oxidizing the liquid metal sheath, we can look at the Péclet number of the polymer flow, such as in the case of 15% w/w PVA in water. The diffusivity of oxygen in such a PVA solution was estimated to be  $\sim 10^{-9} \text{ m}^2/\text{s}$  [234] (or, alternately,  $10^{-5} \text{ cm}^2/\text{s}$  in CGS units): we can thus estimate the Péclet number, assuming a dope flow rate of 0.35 mL/h (typical for the wet-spinning experiments in Chapter 4), a total jet diameter of 170  $\mu\text{m}$  with a core diameter of 90  $\mu\text{m}$ , and the characteristic length as the width of the PVA portion of the jet (80  $\mu\text{m}$ ), as follows:

$$\begin{aligned}
 Pe = \frac{Q/A}{D/L} &= \frac{(3.5 \cdot 10^{-7} \text{ m}^3/\text{h})/(\pi[(85 \cdot 10^{-6} \text{ m})^2 - (45 \cdot 10^{-6})^2])}{(10^{-9} \text{ m}^2/\text{s})/(80 \cdot 10^{-6} \text{ m})} \\
 &= \frac{(9.7 \cdot 10^{-11} \text{ m}^3/\text{s})}{(1.3 \cdot 10^{-5} \text{ m/s}) \cdot (1.6 \cdot 10^{-8} \text{ m}^2)} \\
 &= \frac{(9.7 \cdot 10^{-11} \text{ m}^3/\text{s})}{(2.1 \cdot 10^{-13} \text{ m}^3/\text{s})} = 460
 \end{aligned} \tag{5.3}$$

The high Péclet number suggests that the diffusion of the oxygen through the polymer flow is minimal, with most of the oxygen transport instead being the result of flow parallel to the galinstan stream [132]. Under most circumstances, this means that we cannot expect the galinstan to readily oxidize while under co-flow. Oxidation requires adsorption of oxygen at the interface [235], and the adsorption of a material to the system in a co-flow such as this, where laminar flow as opposed to turbulent mixing is dominant, means that it is unlikely to happen, especially with the very high flow rates at which the galinstan is flowed<sup>a</sup>. This suggests that we should primarily aim to stabilize the galinstan jet by tuning the flow parameters alone. It is conceivable that the formation of the gallium oxide skin could further help to stabilize the jet, but it cannot achieve this aim alone.

### 5.3 Experimental Set-Ups for Co-Flowing and Jetting

The first aim is to see here under what circumstances the liquid metal we have will jet in our microfluidic set-up. When the conditions for a stabilized liquid metal flow are determined, we can then attempt to incorporate this into a fiber, using either a wet-spinning technique or another means of polymerization, such as photopolymerization.

Since we aim to produce fibers, we performed the co-flowing of galinstan in another fluid in geometric conditions very similar to those under which the galinstan would be flowed during the fiber spinning process, where the polymer sheath flows parallel to the galinstan. The microfluidic device, therefore, needs to

---

<sup>a</sup>This can also be seen in a simple experiment, where galinstan is loaded into a syringe and then expelled: even in air, the galinstan stream remains a jet and maintains its lustrous silver color. Only once stationary or close to stationary will gallium (III) oxide form. In the case of interfacial tensiometry, droplet generation of galinstan in non-degassed media was achievable, but, once stationary for measurements, oxidation occurred.

mimic these conditions. We employed three microfluidic set-ups in all: one dedicated to just the co-flow of galinstan in a viscous medium ("two-flow") and two set-ups for the conditions under which fiber spinning would be performed ("three-flow").

### 5.3.1 Two-Flow: Materials and Configuration

For the study of the galinstan co-flow in a two-flow configuration, we used a microfluidic set-up similar to the first-generation tensiometer presented in Chapter 3 was employed to observe the co-flows of liquid crystals and liquid metals. The device had two inlets (one for the galinstan and the other for the co-flowing material) and a single outlet that would eject directly into either air or a collection bath. This spinneret device configuration is shown in Figure 64.

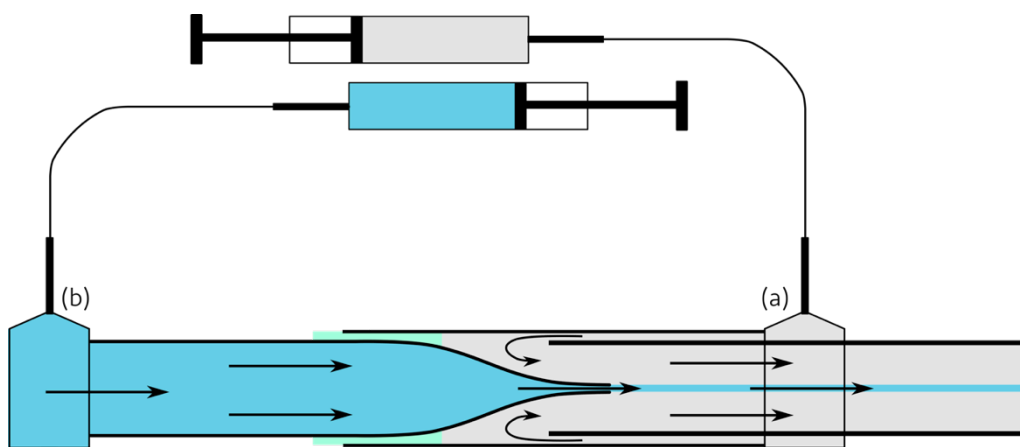


Figure 64. Co-flowing device used to observe the flow behavior of galinstan in contact with another solution. The bath phase is introduced through (a), while the galinstan is introduced through (b). UV-reactive epoxy (indicated in green) is used to seal the device.

In the two-flow geometry, galinstan was used as received as the inner fluid. For the outer fluid, we chose two materials: a 20% w/w SBS solution, from which we originally intended to spin fibers, prepared in toluene and a 15% w/w PVA solution in water. We estimate the viscosities of these solution to be on the order of 1.7 Pa·s for the SBS solution (determined experimentally by rheology) and 10 Pa·s [104] for the 15% w/w PVA solution. Each of these solutions was degassed at room temperature under vacuum before loading into syringes, as we sought to observe the co-flow in these systems without the influence of oxidation and to avoid any air bubbles that would destabilize an otherwise uniform flow. The syringes were allowed to stand for several hours to remove any gas bubbles before beginning the co-flowing process.

When loading galinstan into a syringe, we first filled the syringe with a small amount of 0.1-1.0 M NaOH (aq) solution, as shown in Figure 65. This was done to ensure a smooth, continuous flow of the galinstan into the spinneret, as NaOH will rapidly remove the oxide skin from the interface (more than an acid would). This solution was expelled from the syringe before the start of the experiment and fiber production, with only the galinstan remaining in the syringe.

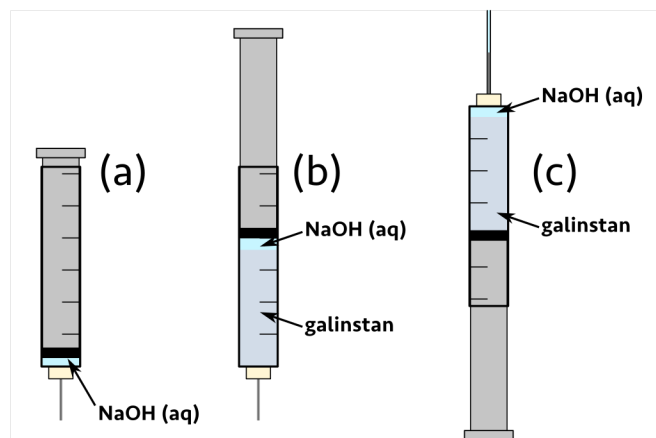


Figure 65. Filling procedure for loading the syringes with galinstan. (a) The syringe is first filled with a small quantity ( $< 0.5$  mL) of NaOH (aq) solution. (b) Galinstan is then drawn into the syringe to the desired fill level. (c) Once the syringe is connected to the tubing that will then feed into the spinneret, the syringe is inverted and the NaOH solution gently flushed out, leaving behind only galinstan in the syringe to flow into the device.

### 5.3.2 Three Flow Set-Ups for Jetting towards Fiber Production

For the conditions similar to fiber spinning, we used the same spinneret devices as used in Chapter 4 for the spinning of core-sheath fibers with liquid crystal cores. These are depicted in both Figure 38, with a tapered collection capillary, and Figure 40, with an untapered collector. Both of these set ups are meant for use with three flows (bath, polymer dope, and core). As described in Chapter 4, however, the tapered collector can create a condition where flow velocity drops sharply from the orifice, which destabilized the polymer flow and could lead to snaking: we stuck, therefore, with using untapered collection capillaries. These capillaries could be treated with silane or used untreated.

We used several combinations of fluids for the dope-bath systems. In the first combination, the organic tetraacrylate monomer PETA (Sigma Aldrich, 99%, viscosity  $\sim 1.3$  Pa·s) was used without further purification. For the bath phase to stabilize the flow, we note that PETA does not coagulate in a wet-spinning process, but instead photopolymerizes in the presence of UV light and a photoinitiator, which means no salt is necessary. We prepared a bath phase of 7.5% w/w PVP in a mixture of 75% v/v ethanol with the balance as water.

For mimicking the wet-spinning process, we used the same combinations of bath and dope that were used to spin PVA fibers in Chapter 4. We prepared aqueous PVA solutions of varying concentrations (15-25% w/w), using the same ethanol coagulation bath (7-15% w/w  $\text{CaCl}_2$  and 10% w/w PVP in 99% ethanol) to obtain fibers. We estimate the viscosity of these spinning dopes to be on the order of 10 Pa·s for 15% w/w PVA and as high as 20 Pa·s for 25% w/w PVA. [104]

To see if we could induce a small degree of miscibility/solubility between the galinstan core (from the gallium oxide skin) and the polymer dope, we attempted to prepare solutions of PVA prepared under acidic and basic conditions (either using

1.0 M HCl (aq) or 1.0 M NaOH (aq) as the solvent), but this was not successful. The acidic and basic conditions each coagulated the polymer out of solution, resulting in either an inhomogeneous mixture with visible polymer globules or clear phase separation of the polymer out of solution.

## 5.4 Experimental Results

The two groups of experiments, while similar, yielded two different sets of data. First, we present the results on the state diagram of jetting galinstan in the two-flow geometry in order to construct a state diagram of liquid metal jetting behavior. The behavior we see is somewhat as expected and in concordance with theory, as galinstan itself is a Newtonian liquid, but there were complications that arose from the widening of the galinstan jet during the laminar flow, resulting in an otherwise stable jet losing stability.

Secondly, we show the outcome of jetting in three-flow set-ups with a view to obtain fibers along with a sample of an obtained galinstan fiber. This fiber is not yet ideal, as it does not have a continuous core, but being able to encapsulate the galinstan in a PVA sheath is a promising first step. We found that the best jetting conditions, where the inner galinstan jet was smooth, aimed to maximize both the galinstan Weber number while still having high capillary numbers for the bath and dope flows.

### 5.4.1 Two-Flows and the Galinstan Flow State Diagram

For a two-phase system, consisting of a bath phase into which galinstan is jetted, we can construct a state diagram, plotting the Weber number of the galinstan flow with the capillary number of the outer flow that represents the transition from a dripping regime to the onset of a jetting regime. Both Utada et al [37] and Castro-Hernández et al [35,36] found that the transition will occur, as stated earlier, when either the inner flow Weber number or outer flow capillary number approaches unity. As shown in Figure 66, the state diagram we have largely confirms these observations, where we see the onset of jetting especially with a high Weber number of the inner flow, both by using a 20% w/w SBS solution in toluene (viscosity experimentally determined to be  $\sim 1.7$  Pa·s) and in the 15% w/w PVA aqueous solution used in spinning (viscosity determined by literature to be  $\sim 10$  Pa·s [104]). In contrast, higher capillary number flows themselves did not stabilize the jet, but, in borderline cases between jetting and dripping, higher capillary numbers did stabilize the flow into jetting when the Weber number alone did not suffice.

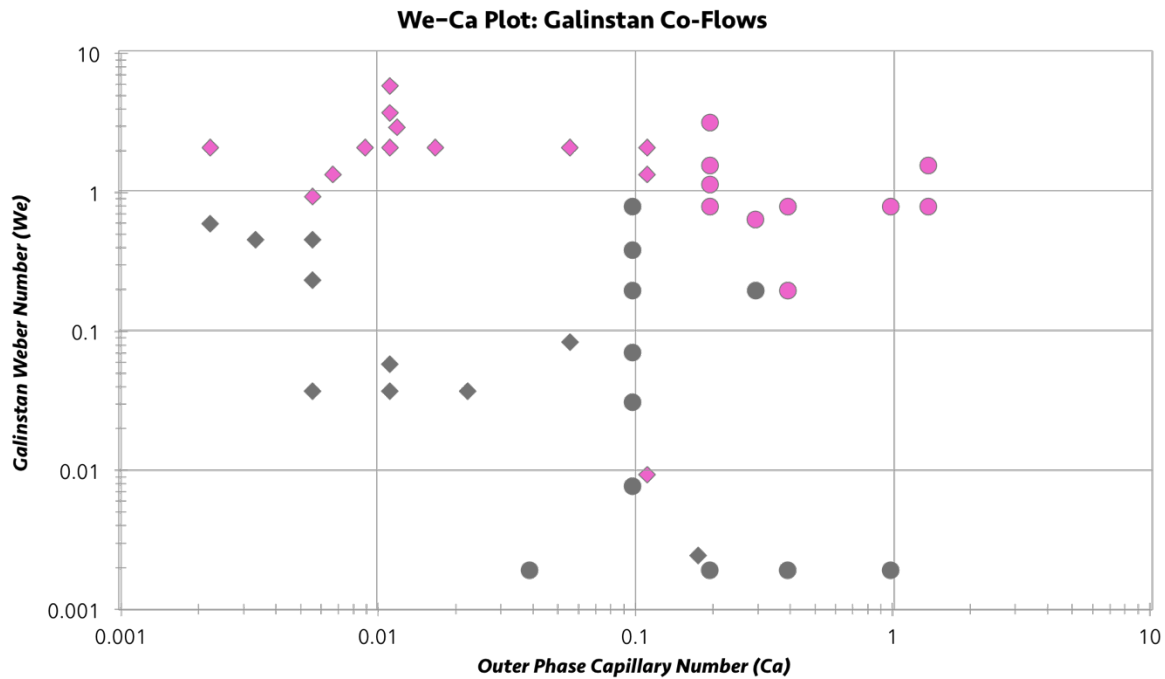


Figure 66. State diagram constructed from a two-flow system of galinstan in a polymer solution. Circles represent points obtained from the co-flow in SBS solution, while diamonds are data points from the co-flow in PVA solution. Data points marked with pink are where jetting was observed, while gray points indicate where jetting was not visible.

This state diagram, however, does not paint a complete picture of the jetting behavior. The high interfacial tension of galinstan [44] means that the jet, even once formed, will very quickly begin to break into droplets, and even two cases that are indicated as jetting cases will provide different outcomes. Taking, for example, three cases under which jetting is predicted by the state diagram in Figure 66 (and where, in fact, jetting is observed), we can see in Figure 67 that the flows are quite different.

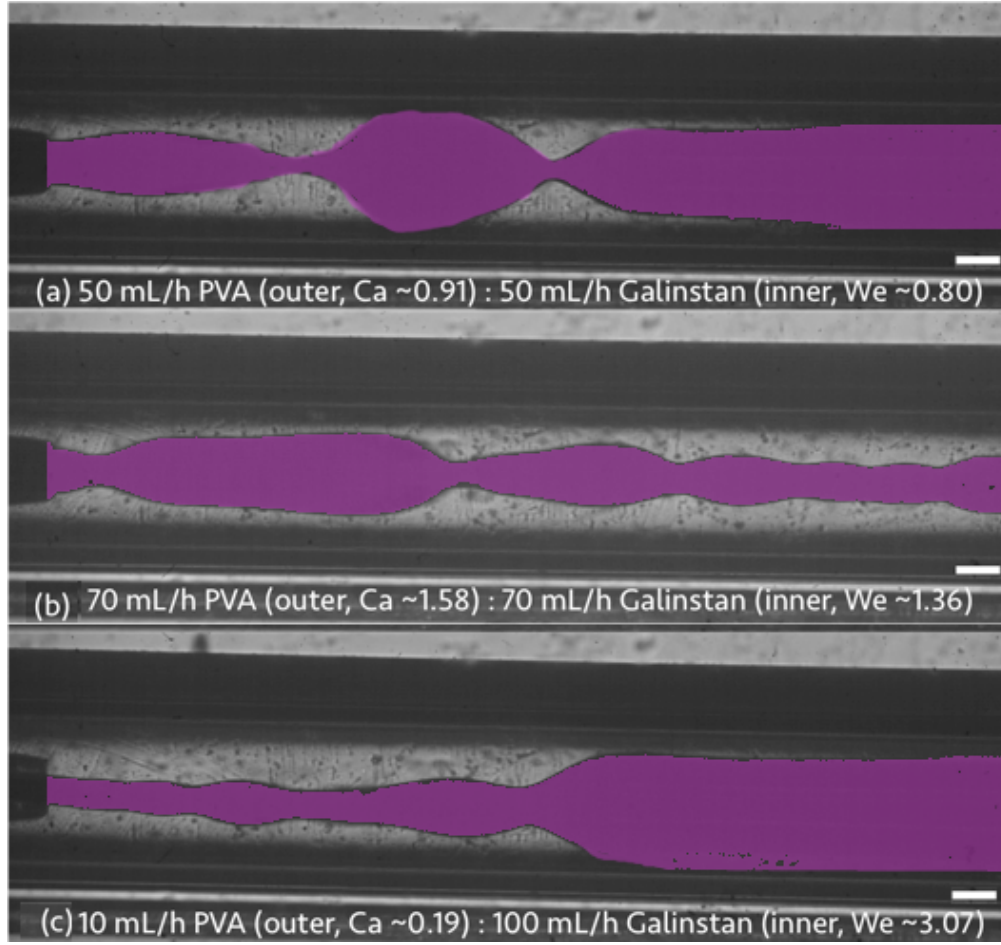


Figure 67. Two-flow jetting of galinstan in 15% w/w PVA solution with different flow rate combinations and corresponding different combinations of outer phase capillary number and inner phase Weber number. Scale bar 200  $\mu\text{m}$ . Image retouched to add false color (pink) to better indicate the contours of the jets. (a) Jetting with flow rates of 50 mL/h PVA solution and 50 mL/h galinstan, corresponding to  $v_{\text{PVA}} = 0.039 \text{ m/s}$ ,  $Ca_{\text{PVA}} \sim 0.91$ ,  $v_{\text{Galinstan}} = 0.51 \text{ m/s}$ , and  $We_{\text{Galinstan}} \sim 0.80$ . (b) Jetting with flow rates of 70 mL/h PVA solution and 70 mL/h galinstan, corresponding to  $v_{\text{PVA}} = 0.054 \text{ m/s}$ ,  $Ca_{\text{PVA}} \sim 1.58$ ,  $v_{\text{Galinstan}} = 0.054 \text{ m/s}$ , and  $We_{\text{Galinstan}} \sim 1.36$ . (c) Jetting with flow rates of 10 mL/h PVA solution and 100 mL/h galinstan, corresponding to  $v_{\text{PVA}} = 0.0078 \text{ m/s}$ ,  $Ca_{\text{PVA}} \sim 0.19$ ,  $v_{\text{Galinstan}} = 1.02 \text{ m/s}$ , and  $We_{\text{Galinstan}} \sim 3.07$ . Micrographs are from a top-down view.

We see in Figure 67 that jetting is visible in all three cases, but the development of instability near the jet is minimized in (b), which corresponds to a low capillary number and a high Weber number. One discrepancy may be that the capillary numbers calculated in Figure 66 and Figure 67 assume a constant viscosity for the PVA solution under flow, but polymer solutions show anisotropic shear-dependent viscosities that, in the case of directions normal to the flow direction, may actually be higher than in the equilibrium un-sheared state [236]. Since the oscillations that lead to jet breakup are normal to the flow direction, with a higher viscosity in that direction, this will serve to reduce the propagation of the waves that will break the jet apart. This viscosity anisotropy, however, is not readily measured with standard rheometers and requires further investigation [237]; until the degree of viscosity

anisotropy of the polymer flows is better known, however, it is probably better to work with Weber number-driven flows. Additionally, as will be covered in Section 5.4.2, the galinstan jet actually widens during the flow, leading to a corresponding loss of Weber number due to a constant volumetric flow rate. This then leads to a loss of the stability condition for the galinstan jet, which becomes more noticeable when the inner phase Weber number starts with a value closer to unity.

#### 5.4.2 Three-Flow Results for Jetting of Galinstan in PETA

One of the first experiments for the jetting of galinstan was with the viscous tetraacrylate monomer pentaerythritol tetraacrylate (PETA), used with the idea to photopolymerize the sheath in order to form a rigid thermoplastic sheath. The idea is that we can perform an *in situ* photopolymerization of the tri-flow before galinstan break-up to create a solid fiber. While the presence of dissolved oxygen in the flow should not lead to oxidation due to the high Péclet number, we saw experimentally in Chapter 3 that, when measuring the interfacial tension of liquid metal droplets in PETA, oxidation was not observed over the experimental timescale: oxidation of galinstan normally is a rapid process, so seeing that the material remained liquid means that there should not be oxidation during the flow and jetting process.

Initially, experiments were performed using devices that are typically used for shell and droplet generation [24,169,238], the idea being to replicate the flow-focusing geometry but to extend the flow to a jetting condition rather than breaking off the jet into droplets. If sufficiently equipped, the jet can then be stabilized by photo-crosslinking the PETA, thus producing a stabilized galinstan jet. An example of such jetting is shown in Figure 68.

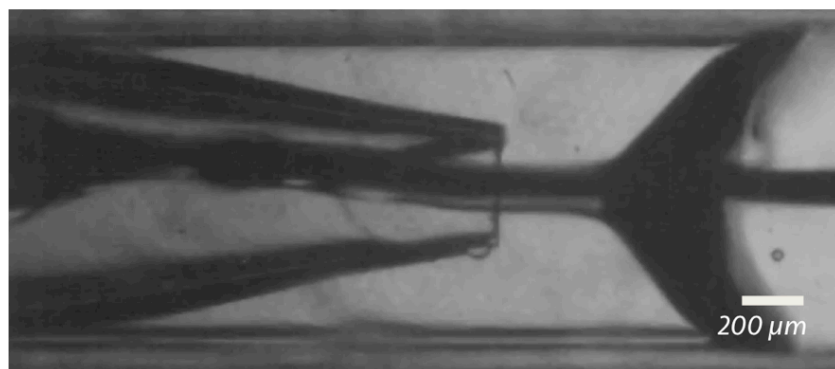


Figure 68. Jetting of galinstan in a flow of degassed PETA (sheath) and 7.5% w/w PVP in 25% v/v ethanol in water (outer). Flow rates are 25 mL/h galinstan, ~3.0 mL/h bath, and ~1.0 mL/h PETA. Micrograph is from a top-down view.

Notably, considerable jet instability is seen to quickly develop here, within the first few millimeters of jet flow, as the liquid metal begins to bead. In looking carefully at the jet, however, one can see two notable characteristics of the flow: first, the liquid metal jet appears to widen as it progresses through the channel. Similar behavior is seen in the co-flow images in Figure 63(a) and (b), where, before the onset of beading, the jet becomes wider. The widening appears somewhat similar to the die swelling that is seen in polymer solutions or phases extruded from a nozzle, though



a perhaps better analogy is to the spreading of the jet as can be seen in co-flows in microfluidic geometries where the jet will widen within the channel as it flows [132], which is additionally sometimes seen in laminar flows in microfluidic geometries [239]. The reason for this widening is probably a kinetic energy transfer from the galinstan jet, which is travelling much faster than the outer phase. As the galinstan jet slows down, we still need to meet the condition of a constant volumetric flow rate (as galinstan is an incompressible fluid). To do so, we thus need to increase the cross-section area of galinstan. The main outcome of this is that the Weber number that would predict a stable flow decreases quite quickly: as a recap, if the flow stability number is less than unity, the condition for stable flow is lost, absent a sufficiently high capillary number. In Figure 69, we link the position in the channel to an estimated Weber number at that point. Within the first few millimeters of the channel, the stable flow condition is still met, but it rapidly becomes lost. We can additionally see that the initial onset of beading due to Rayleigh instability occurs at 150 px within the channel (the second mark from the left in the image), which neatly corresponds to the point when  $We \leq 1$ .

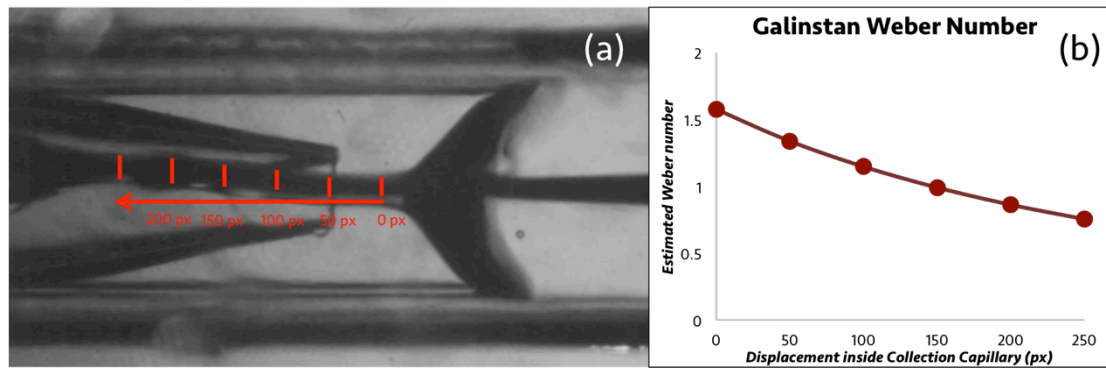


Figure 69. (a) Galinstan flow in PETA (middle) and PVP in 25% ethanol (outer), as in Figure 68, accompanied by (b) the estimated Weber number at different points in the channel indicated, beginning at the edge of the collection capillary and proceeding inwards (as indicated in (a)).

The decrease in flow velocity quickly outpaces the increase in characteristic length due to the quadratic scaling of velocity in the Weber number (and especially in comparison to the increase in the characteristic length scale, which is only linear), meaning that the condition for galinstan jetting then becomes lost.

A high capillary number of the outer phase, in particular the polymer sheath phase, would also theoretically slow down jet break up and increase the length scale over which a continuous jet is observed, but is not practical in the scales of the experiment. To get a capillary number on the order of unity, for example, by using PETA as the sheath phase (with a viscosity of 1.3 Pa·s), assuming a total jet width of 150  $\mu\text{m}$  of which galinstan comprises 100  $\mu\text{m}$ :

$$Ca = 1 = \frac{\eta v}{\gamma} = \frac{(1.3 \text{ Pa} \cdot \text{s})v}{0.5 \text{ N/m}}$$

$$v = \frac{\gamma}{\eta} = 0.38 \frac{\text{m}}{\text{s}}$$



$$Q = vA = 0.38 \frac{\text{m}}{\text{s}} \cdot \pi[(0.75 \cdot 10^{-4} \text{ m})^2 - (0.5 \cdot 10^{-4} \text{ m})^2]$$

$$Q = 3.7 \cdot 10^{-9} \frac{\text{m}^3}{\text{s}} = 1.3 \cdot 10^{-5} \frac{\text{m}^3}{\text{h}} = 13 \frac{\text{mL}}{\text{h}} \quad (5.4)$$

This flow rate is quite low, particularly with respect to the flow rates of the galinstan with which jetting is achievable, but it is still quite high to the polymer dope flow rates presented in Chapter 4 with which fibers were obtained. The equal issue is the pressure required to get this flow rate of polymer dope, for which we can use the Hagen-Poiseuille equation (equation (3.6)) to determine. In this, we assume a tubing length of 30 cm with a diameter of 800  $\mu\text{m}$ , with all other parameters as given above:

$$\Delta P = \frac{8\eta L Q}{\pi R^4} = \frac{8(1.3 \text{ Pa} \cdot \text{s})(0.3 \text{ m}) \left(3.7 \cdot 10^{-9} \frac{\text{m}^3}{\text{s}}\right)}{\pi(4 \cdot 10^{-4} \text{ m})^4}$$

$$= \frac{1.2 \cdot 10^{-4} \text{ Pa} \cdot \text{m}^4}{8.0 \cdot 10^{-14} \text{ m}^4} = 1.5 \cdot 10^9 \text{ Pa} = 15000 \text{ bar}$$

Pressures like this are not achievable with the equipment we have or that is commonly available from syringe pump equipment (the MFCS device we have can only achieve a maximum pressure of 1 bar; the syringe pump can only achieve 3 bar). While the pressure required for the flow can be decreased by either decreasing the tubing length and/or increasing the tubing radius, there is a practical limit to what tubing is available.

Because of the comparatively low viscosity of PETA, which led to considerable beading, we instead switched to a wet-spinning approach, where we are able to use polymer solutions with considerably higher viscosities and be able to solidify the fiber without UV light. Setting up the galinstan-PETA system to quickly photopolymerize the sheath before the onset of beading requires specialized equipment and is not straightforward, so we aimed to work with a system that is less taxing on set-up considerations and with which we have had experience previously.

### 5.4.3 Three-Flow Results for the Jetting of Galinstan in Polymer Solutions

Since the wet spinning of polymer fibers containing liquid crystal cores is achievable, as presented in Chapter 4, we additionally looked into the wet spinning of galinstan in similar systems with a view to obtaining fibers. Jetting was obtainable within the spinneret device when spinning both in PI in toluene and in PVA in water, much like with the PETA flow. Because of the considerable interfacial tension, though, very high galinstan flow rates were necessary in order to observe significant jetting without breaking. In both Figure 70 and Figure 71, for flows of galinstan in a sheath of PVA solutions of different concentrations, we see that prolonged jetting that does not break apart into beading requires galinstan flow rates of upwards of 65 mL/h<sup>b</sup>.

---

<sup>b</sup>While the jetting in Figure 70(d) is sustained over a longer distance than that in Figure 71(e), the two experiments were performed using different spinneret devices: the initial jet in Figure 70 is much narrower due to a narrower orifice, which corresponds to a higher initial flow speed despite the same flow rate.

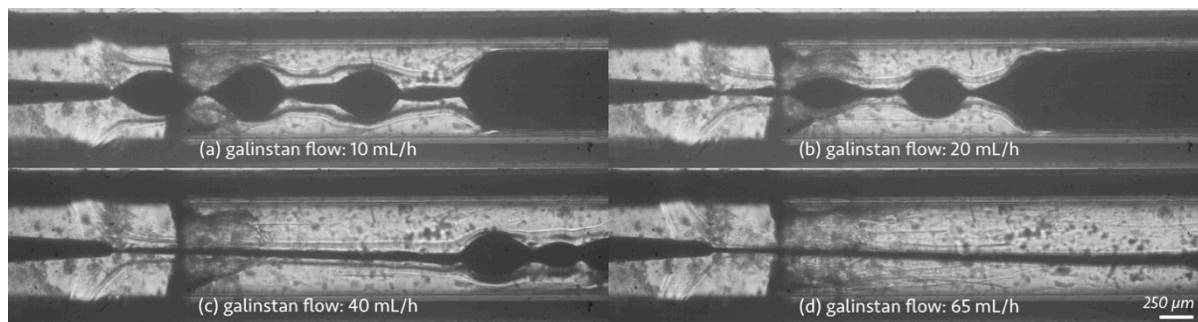


Figure 70. Jetting of galinstan in a co-flow of 20% w/w PVA (aq) (middle) as a dope and 15% w/w  $\text{CaCl}_2$  and 10% w/w PVP in ethanol (outer) as the bath. Flow rates are 1.25 mL/h ethanol bath and 0.40 mL/h dope in all images. Scale bar 250  $\mu\text{m}$ . Galinstan flows are (a) 10 mL/h; (b) 20 mL/h; (c) 40 mL/h; and (d) 65 mL/h.

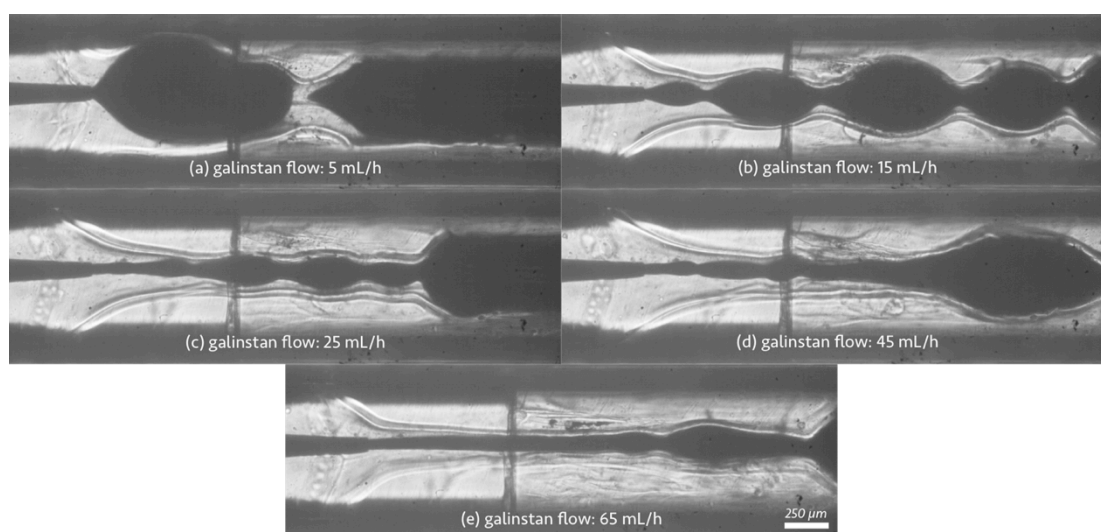


Figure 71. Jetting of galinstan in a co-flow of 25% w/w PVA (aq) (middle) as a dope and 15% w/w  $\text{CaCl}_2$  and 10% w/w PVP in ethanol (outer) as the bath. Flow rates are 1.05 mL/h ethanol bath and 0.35 mL/h dope in all images. Scale bar 250  $\mu\text{m}$ . Galinstan flows are (a) 5 mL/h; (b) 15 mL/h; (c) 25 mL/h; (d) 45 mL/h; and (e) 65 mL/h. All micrographs are from a top-down view.

However, even at very high flow rates of galinstan, as seen in Figure 71(e) in particular, the jetting quickly was lost and resulted in beading and the jet breaking apart. If we consider the volumetric flow rate as constant, this means the galinstan flow velocity decreases over the length of the channel, as shown in Figure 72. The decrease in flow velocity quickly outpaces the increase in characteristic length, meaning that the condition for galinstan jetting is no longer satisfied within the first few millimeters of the injection capillary.

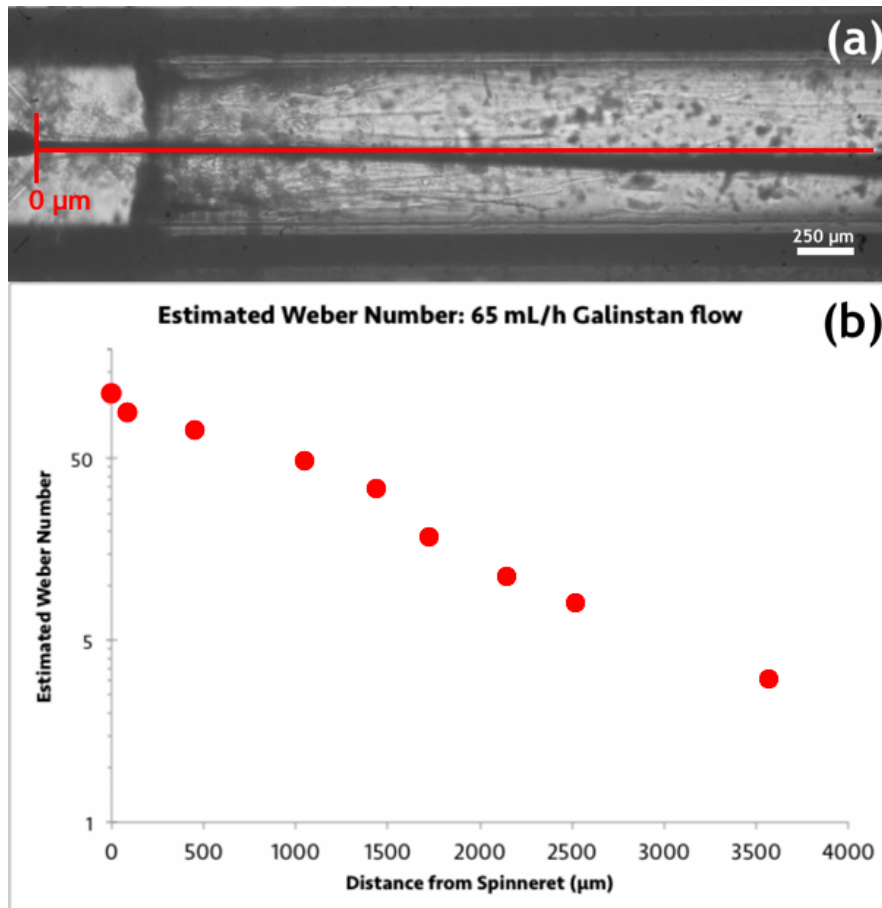


Figure 72. (a) A still frame of the galinstan jetting seen in Figure 70(d) with (b) the corresponding estimated Weber numbers relative to the position from the spinneret. Scale bar in (a) 250  $\mu\text{m}$ .

The theoretical threshold flow rate for galinstan jetting is dependent on the achievable Weber number in the geometry. In practice, with the spinneret devices we use, the minimum galinstan flow rate needed to obtain jetting is about 20-25 mL/h, as our initial jet diameters normally run from 70  $\mu\text{m}$  to 100  $\mu\text{m}$ . The effect on diameter on the minimum flow rate for jetting is shown in Figure 73, where the threshold increases quadratically and substantially with the increase in jet diameter. As the jet additionally widens during the flow, we can also see that the flow rate threshold also no longer remains met once breaking begins.

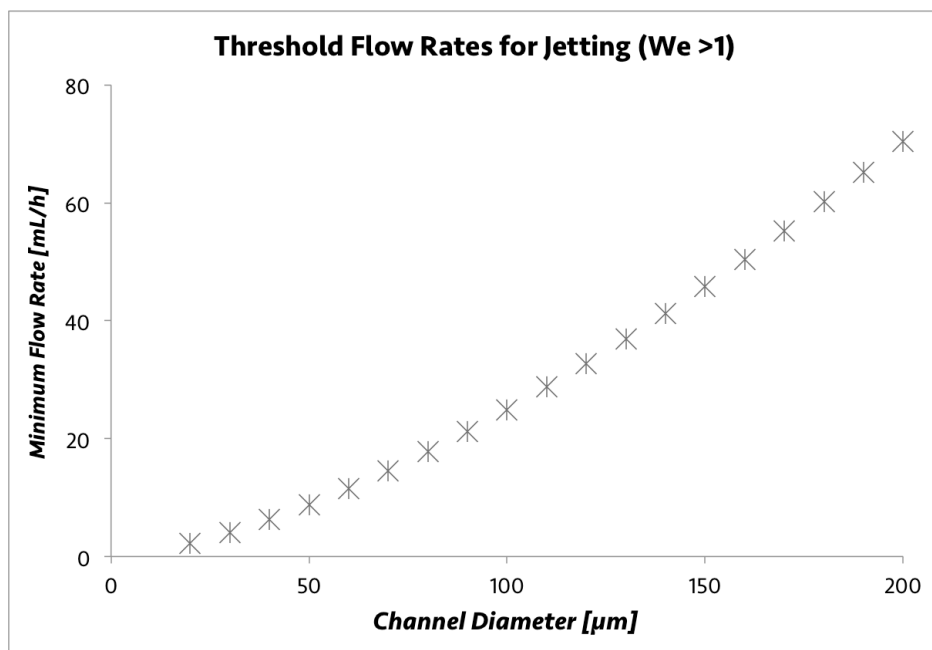
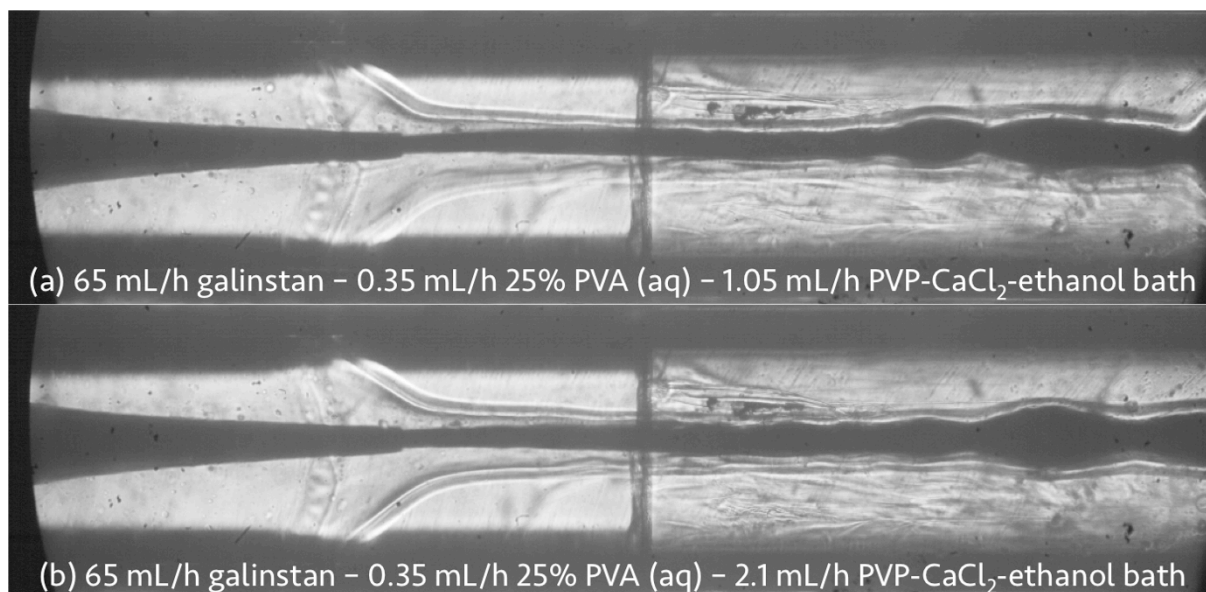


Figure 73. Calculated threshold flow rates for galinstan jetting as a function of initial jet diameter. The threshold varies from ~9 mL/h for a diameter of 50  $\mu\text{m}$  to up to ~25 mL/h for 100  $\mu\text{m}$  and even up to 70 mL/h for diameters of 200  $\mu\text{m}$ .

Since the capillary number of the outer phase is an additional predictor of flow stability, we additionally examined if increasing the flow rates of the outer phases, in this case both the coagulation bath and the dope flow, had any effect on helping to reduce the beading and breaking observed during the flow. First, using the example illustrated in Figure 71(e), we doubled the outer bath flow rate, keeping the other two flows (galinstan and PVA dope) constant, results of which are shown in Figure 74.



*Figure 74. Jetting of galinstan in a co-flow of 25% w/w PVA (aq) (middle) as a dope and 15% w/w CaCl<sub>2</sub> and 10% w/w PVP in ethanol (outer) as the bath. Flow rates are 65 mL/h galinstan and 0.35 mL/h dope in all images. Bath flow rates are (a) 1.05 mL/h and (b) 2.10 mL/h. Micrographs are from a top-down view.*

There did appear to be a difference in jet stability by increasing the outer bath flow rate. Such an increase would double the capillary number of the outer phase. On the other hand, the system is not a simple two-flow system with a single interface, but a three-flow system with two separate interfaces (bath–dope and galinstan–dope). The polymer dope flows in all the jetting cases, both in Chapter 4 and this chapter, are all quite thin with respect to the total diameter of the jet, but the galinstan–dope interface is still present. We additionally explored the effects of increasing both the bath flow rate and the dope flow rates to see if this had an effect on smoothing the jet and suppressing the onset of beading, the results of which are shown in Figure 75.

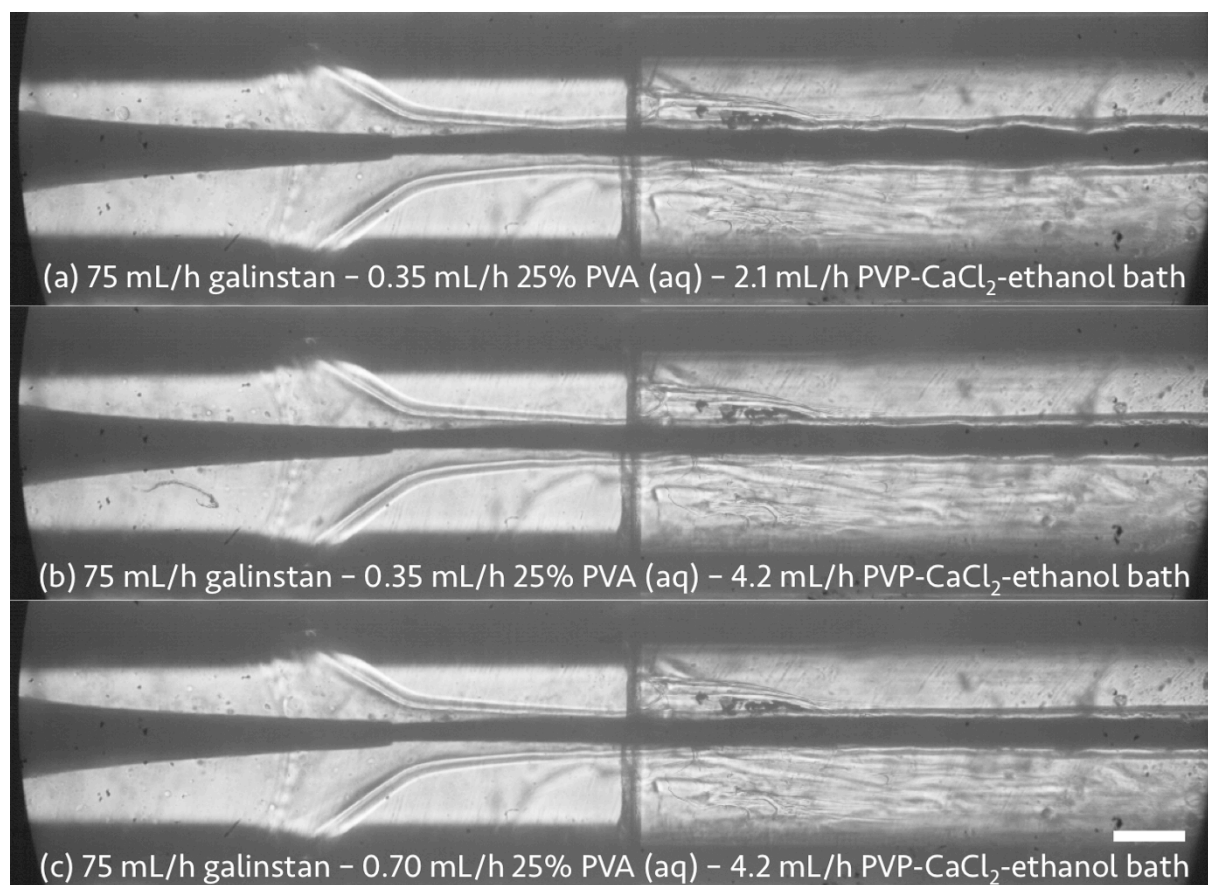


*Figure 75. Jetting of galinstan in a co-flow of 25% w/w PVA (aq) (middle) as a dope and 15% w/w CaCl<sub>2</sub> and 10% w/w PVP in ethanol (outer) as the bath. Flow rates are 75 mL/h galinstan in all images. Scale bar 250  $\mu$ m. Dope and bath flow rates are (a) 0.35 mL/h dope and 2.1 mL/h bath; (b) 0.35 mL/h dope and 4.2 mL/h bath; (c) 0.70 mL/h. Micrographs are from a top-down view.*

Between the jetting seen in Figure 75(a) and (b), there appears to be an improvement in the jet smoothness by increasing the bath flow rate. Increasing the bath flow could have an effect on helping to stretch and align the sheath flow, which may suppress the onset of beading by reducing the number of "seeding" points from which instability could develop. A similar result is noted by increasing the sheath flow rate from (b) to (c), but because of the high flow rate of the bath that stabilizes the flow between (a) and (b), only subtle changes in core continuity between (b) and (c) are noticeable, though the jet in (c) is smoother.

Regardless of the flow rate combinations used, though, when fibers were obtainable, the core continuity was still lacking. A sample of a coaxial fiber, macroscopically and microscopically, is shown in Figure 76: by using PVA as the sheath phase, we are able to encapsulate the galinstan into the polymer, and the presence of the polymer sheath is clearly noticeable, but, as seen especially in (a) and (b), no continuous core is observed, and instead the fibers are beaded.

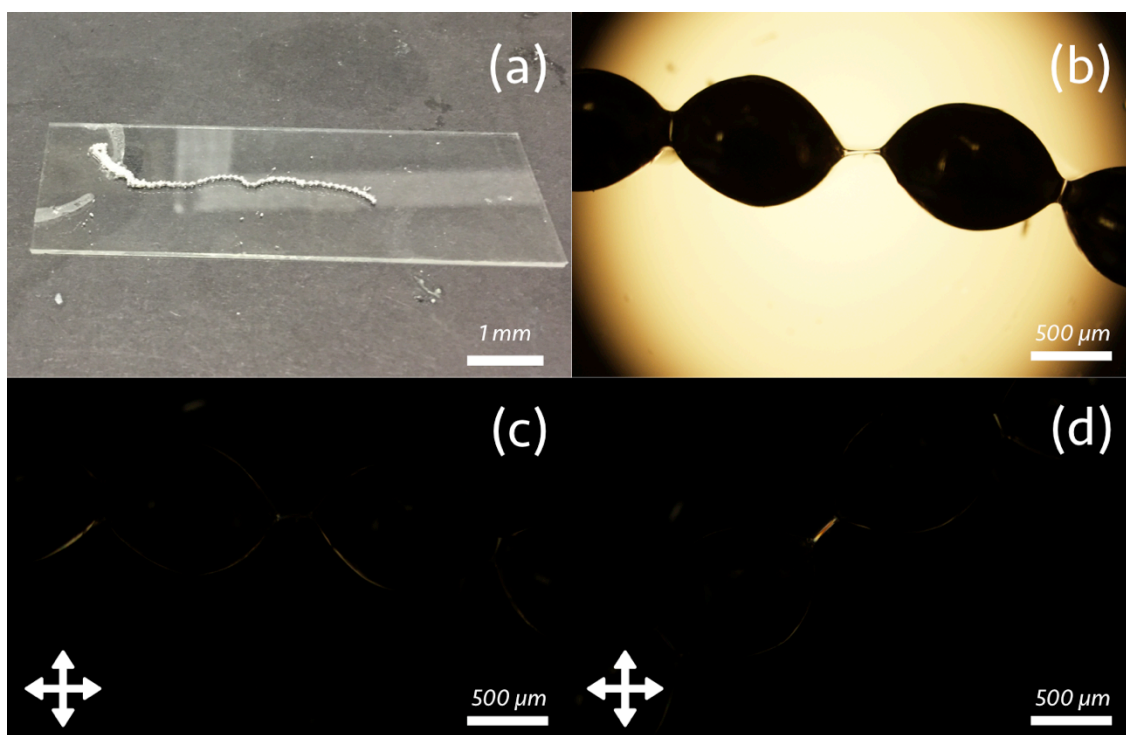


Figure 76. Sample of a PVA fiber spun from 20% w/w PVA dope with galinstan as the core. (a) A macroscopic view of the fiber, showing a "bead on a chain" texture. (b-d) Transmission mode micrographs of the fiber, as viewed (b) without crossed polarizers; (c) between crossed polarizers; and (d) between crossed polarizers and rotated clockwise by 45°. The birefringence visible in (c) and (d) comes from the PVA encapsulating the liquid metal.

## 5.5 Conclusions

The jetting of liquid metals in a co-flowing set-up was achievable, and we were able to get liquid metals inside the polymer fibers using wet spinning though we were not able to obtain the desired fibers with a continuous core and a polymer sheath. The high interfacial tension of the liquid metal quickly breaks the jet apart, similar to the case we saw with liquid crystal-filled PVA fibers.

During the wet spinning of fibers in Chapter 4, we postulated that the ideal situation was a relatively low polymer dope flow rate with a high bath flow rate to extract the solvent from the dope more quickly. This also appears to be a sound strategy for spinning liquid metal-filled fibers, though coagulation of the jet would need to happen on much shorter time scales than we have previously achieved to work around the jet break-up during fiber production. This can be done by adjusting the concentrations of the polymer within the dope and the salt in the coagulation bath, though this has practical issues in terms of the maximum achievable salt concentration in the coagulation bath and the maximum polymer dope concentration. More viscous polymer solutions are also considerably harder to flow with the equipment we have, necessitating syringe pumps and syringes capable of withstanding much higher pressures. Other polymer dope and bath combinations can also be examined.

From both a theoretical standpoint, considering the laminar flow profile and the diffusivity of oxygen in the polymer dope, and from the experiments performed in this chapter, reliance on the oxidation of the galinstan during the spinning does not seem to be the ideal way to stabilize the galinstan jet. The formation of gallium (III) oxide in post processing, naturally, would be useful to stabilize the fiber and make it easier to work with, but oxidation of the skin during production is problematic to achieve and to tune without a complete understanding of the chemical processes behind the flow. Further work can explore the *in situ* oxidation of the galinstan jet, but we believe that the most successful outcomes will focus on both maintaining the jet continuity and extracting the polymer dope solvent as quickly as possible. Some of the directions we can imagine future work exploring include the following:

- We could use an electric field-assisted jetting process, where we use an applied electric field in conjunction with adjusting ion concentrations in the polymer dope to reduce the galinstan interfacial tension [115]. While removing the electric field will reset the interfacial tension to its higher value, if, during fiber post processing, we can oxidize the galinstan at the polymer-galinstan interface, this would potentially give us a fiber with a continuous liquid metal core that remains intact due to both the solid nature of the gallium oxide skin and the lower interfacial tension between gallium oxide and the interior galinstan.
- Rather than a physical osmotic process of solvent extraction, an *in situ* polymerization reaction could also serve to stabilize the galinstan core, similar to the approach of Takeuchi et al for producing water droplets encapsulated by a nylon shell [240]. Such would need to be carefully tuned so that the polymerization reaction occurs rapidly enough for the sheath to solidify before break-up, but to avoid spinneret clogging. Depending on the polymer used, one could also include functionality, such as actuation from a liquid crystalline elastomer, into the polymer sheath [27,179].

There still remains much work to be done with incorporating liquid metals into fibers, but this opens up many opportunities for research and to be able to attack problems in both fundamental physics and applications. We think that wet spinning-based approaches are the most promising in terms of outcomes, but, again, these require further work to produce a tangible, final product.



## CHAPTER 6

### CONCLUSIONS AND OUTLOOK

The world of soft matter research is characterized by both interdisciplinarity and interconnectedness, as reflected in the concepts and work presented in this thesis. The originally envisaged goal, to encapsulate a liquid metal into a fiber, led us on a journey through interfacial tensiometry and microfluidics to polymers, liquid crystals (as an intermediate step towards the final product), and eventually liquid metals. But, as with most journeys, the path to the final destination has been just as rewarding as the destination, and, even though the main aim was not fully achieved, we have laid a strong groundwork towards accomplishing this.

In the course of this thesis, I first used glass capillary-based microfluidics and the principle of micropipette aspiration of living cells to construct an interfacial tensiometer and subsequently a protocol for measuring the interfacial tensions between immiscible fluids [44]. This is achieved by first generating a droplet of fluid, then aspirating it (preferably) into a constriction produced in the collection capillary. This technique uses only experimentally obtained data, the pressure needed to aspirate a droplet and the radii of curvature before and after the aspiration, without relying on sometimes imprecise literature values for parameters (such as density and viscosity). Where they exist, the results obtained by our technique show good agreement with literature data, and we were additionally able to obtain data on the interfacial tensions of the common liquid crystal 5CB that are somewhat lacking in literature. While we were able to use the technique to measure dynamic interfacial tension, such measurements are difficult to achieve due to the time between droplet generation and its subsequent measurement. We also were unable to measure the extremely low interfacial tension between the two phases of a cellulose nanocrystal suspension, in part due to the emulsification between the anisotropic and isotropic phases, but designing new tensiometer geometries to account for phenomena like this (such as a vertical set-up) is a way forward towards a more universal technique. The ultimate implementation of automation is another step that can be taken to turn this tensiometer into a more powerful, user-friendly instrument that can be easily implemented in the laboratory setting.

Using the know-how about device making developed in the work described in Chapter 3 plus some of the interfacial tension data acquired in the same, we then proceeded towards fiber production using wet spinning. I was able to develop both a microfluidic spinneret device and technique for small-scale wet spinning of pure polymer fibers on a laboratory setting, using both PVA and elastomers, and produce fibers from the same. These fibers are not as thin as those achievable by

electrospinning or other methods, but we can draw long, continuous samples of fibers that can be dried before processing and, in the case of the elastomer, we can stretch the fibers manually to readily achieve diameters of as low as 20-40  $\mu\text{m}$ . More notably, we can incorporate both an achiral nematic and a cholesteric liquid crystal as a continuous core into the elastomer fibers, creating a functionalized fiber. We can already use these cholesteric liquid crystal-filled fibers for thermal sensing, as they show a blueshift in the reflected color upon heating (and a redshift upon cooling).

By using the example of a PVA fiber spun with the cholesteric liquid crystal mixture, I also show that the miscibility between core and sheath plays a role in fiber core contiguity: since miscibility decreases the interfacial tension between two phases, which thus improves the jetting, having at least some degree of miscibility between the core and sheath phases will greatly improve the outcome of core continuity. On the other hand, the miscibility between core and sheath in the liquid crystal-filled elastomer fibers is detrimental to their longevity and durability, as the core can leach into the sheath and act as a plasticizer; additionally, the rubber fibers we have are liquids, not solids, though the flow times of these rubbers is considerable.

From the standpoint of improving the durability of our fibers, cross-linking of the polymer, either during or immediately after fiber production, appears to be the most immediately interesting. By cross-linking the elastomer, for example, we hope to achieve a more durable rubber, capable of reversibly undergoing stretching with the liquid crystal core intact and not swelling the polymer. We also need to work more towards incorporating a continuous liquid crystal core in the PVA fibers; to do so, we can explore different PVA dope solvents or add more ethanol to the liquid crystal to increase its miscibility with the PVA during spinning.

As for galinstan-filled fibers, we are not yet able to achieve the aim of a continuous core of liquid metal, but we can at least encapsulate the liquid metal in an otherwise continuous polymer sheath, showing a "bead on a chain" morphology of the core. Jetting experiments show that very high flow rates of galinstan are necessary to obtain a continuous core. While high polymer dope flow rates also can have a stabilizing effect due to the anisotropic viscosity of the sheared flow (with a higher viscosity in the direction in which Rayleigh instability waves will propagate), further research is needed into both how anisotropic the viscosity under shear actually is and if this is significant enough to play a role in jet stabilization. As it stands now, the ideal situation for liquid metal jetting focuses on maintaining Weber number stability, with both high flow rates and a narrow initial jet of galinstan. The effect of the oxidation of galinstan on the stabilization of the jet will additionally be examined: while a Péclet number analysis suggests that, on the scales of the experiments, galinstan oxidation will be minimal if at all present, with sufficient dissolved oxygen concentration, it may be possible to induce such an oxidation, which would serve to stabilize the jet and allow for a continuous fiber.

In short, the directions in which we can proceed for experiments are diverse and numerous, both from the laboratory standpoint and, resources permitting, at an industrial scale. With a bit more optimization of the materials and spinning

conditions, I think the wet spinning approach presented here will prove to be a powerful technique to produce both liquid crystal- and liquid metal-filled fibers on an industrial level; additionally, the interfacial tensiometry technique can prove itself to be powerful, versatile, and close to universal.



## REFERENCES

- [1] M. Schadt, *Mol. Cryst. Liq. Cryst.* **647**, 253 (2017).
- [2] R. Eelkema and B. L. Feringa, *Org. Biomol. Chem.* **4**, 3729 (2006).
- [3] J. L. West, J. Wang, and A. Jákli, *Adv. Sci. Technol.* **100**, 43 (2017).
- [4] C. G. Reyes, A. Sharma, and J. P. F. Lagerwall, *Liq. Cryst.* **43**, 1986 (2016).
- [5] L. N. Tan and N. L. Abbott, *J. Colloid Interface Sci.* **449**, 452 (2015).
- [6] J. Wang, A. I. Jákli, and J. L. West, *ChemPhysChem a Eur. J. Chem. Phys. Phys. Chem.* **17**, 3080 (2016).
- [7] M. Urbanski, C. G. Reyes, J. Noh, A. Sharma, Y. Geng, V. S. R. Jampani, and J. P. F. Lagerwall, *J. Phys. Condens. Matter* **28**, 1 (2017).
- [8] N. Popov, L. W. Honaker, M. Popova, N. Usol'tseva, E. K. Mann, A. Jákli, P. Popov, and P. Popov, *MDPI Mater.* **11**, 14 (2018).
- [9] P. Popov, L. W. Honaker, E. E. Kooijman, E. K. Mann, and A. I. Jákli, *Sens. Biosensing Res.* **8**, 31 (2016).
- [10] P. Popov, E. K. Mann, and A. Jakli, *Biophys. J.* **106**, 415a (2014).
- [11] J. T. Hunter and N. L. Abbott, *ACS Appl. Mater. Interfaces* **6**, 2362 (2014).
- [12] M. D. Dickey, R. C. Chiechi, R. J. Larsen, E. A. Weiss, D. A. Weitz, and G. M. Whitesides, *Adv. Funct. Mater.* **18**, 1097 (2008).
- [13] B. L. Cumby, G. J. Hayes, M. D. Dickey, R. S. Justice, C. E. Tabor, and J. C. Heikenfeld, *Appl. Phys. Lett.* **101**, (2012).
- [14] C. Ladd, J. So, J. Muth, and M. D. Dickey, *Adv. Mater.* (2013).
- [15] V. Bharambe, D. P. Parekh, C. Ladd, K. Moussa, M. D. Dickey, and J. J. Adams, *Addit. Manuf.* **18**, 221 (2017).
- [16] G. Speckbrock, S. Kamitz, M. Alt, and H. Schmitt, 6,019,509 (2000).
- [17] V. K. Gupta, J. J. Skaife, T. B. Dubrovsky, and N. L. Abbott, *Science* **279**, 2077 (1998).
- [18] R. J. Carlton, J. T. Hunter, D. S. Miller, R. Abbasi, P. C. Mushenheim, L. N. Tan, and N. L. Abbott, *Liq. Cryst. Rev.* **1**, 29 (2013).
- [19] S.-R. Kim and N. L. Abbott, *Adv. Mater.* **13**, 1445 (2001).

- [20] J. H. Park, T.-K. Truong, M. A. Rahman, M. Urbanski, H. Agha, D. Suh, and G. Scalia, *Phys. Status Solidi B Basic Res.* **1800689**, 1 (2019).
- [21] P. Popov, L. W. Honaker, M. Mirheydari, E. K. Mann, and A. Jákli, *Sci. Rep.* **7**, (2017).
- [22] A. Sharma and J. P. F. Lagerwall, *Liq. Cryst.* **45**, 2319 (2018).
- [23] H.-G. Lee, S. Munir, and S.-Y. Park, *ACS Appl. Mater. Interfaces* **8**, 26407 (2016).
- [24] J. Noh, K. Reguengo De Sousa, and J. P. F. Lagerwall, *Soft Matter* **12**, 367 (2015).
- [25] Y. Geng, J.-H. Jang, K.-G. Noh, J. Noh, J. P. F. Lagerwall, and S.-Y. Park, *Adv. Opt. Mater.* **6**, 1700923 (2018).
- [26] T. Liu, P. Sen, and C. J. Kim, *J. Microelectromechanical Syst.* **21**, 443 (2012).
- [27] A. Sharma and J. P. F. Lagerwall, *MDPI Mater.* **11**, 1 (2018).
- [28] C. G. Reyes, *Confined in a Fiber: Realizing Flexible Gas Sensors by Electrospinning Liquid Crystals*, University of Luxembourg, 2019.
- [29] D. K. Kim, M. Hwang, and J. P. F. Lagerwall, *J. Polym. Sci. Part B Polym. Phys.* **51**, 855 (2013).
- [30] D. K. Kim and J. P. F. Lagerwall, *ACS Appl. Mater. Interfaces* **6**, 16441 (2014).
- [31] Y. Kye, C. Kim, and J. Lagerwall, *J. Mater. Chem. C* **3**, 8979 (2015).
- [32] Y. Kye, *Multi-Core Liquid Crystal-Polymer Composite Fibers Produced by Electrospinning*, Seoul National University, 2015.
- [33] J. Xue, T. Wu, Y. Dai, and Y. Xia, *Chem. Rev.* **119**, 5298 (2018).
- [34] H. Yang, C. R. Lightner, and L. Dong, *ACS Nano* **6**, 622 (2011).
- [35] E. Castro-Hernández, J. Guerrero, A. Fernandez-Nieves, and J. M. Gordillo, in *Soft Mater. Gener. Phys. Prop. Fundam. Appl.*, edited by A. Fernandez-Nieves (John Wiley & Sons, 2016), p. 30.
- [36] E. Castro-Hernández, V. Gundabala, A. Fernandez-Nieves, and J. M. Gordillo, *New J. Phys.* **11**, (2009).
- [37] A. S. Utada, A. Fernandez-Nieves, H. A. Stone, and D. A. Weitz, *Phys. Rev. Lett.* **99**, 1 (2007).
- [38] N.-T. Nguyen, S. Lassemone, F. A. Chollet, and C. Yang, *IEEE Proc. Nanobiotechnology* **153**, 102 (2006).
- [39] Q. Brosseau, J. Vrignon, and J.-C. Baret, *Soft Matter* **10**, 3066 (2014).
- [40] K. Harth and R. Stannarius, *Phys. Chem. Chem. Phys.* **15**, 7204 (2013).
- [41] K. Harth, L. M. Shepherd, J. Honaker, and R. Stannarius, *Phys. Chem. Chem. Phys.* **17**, 26198 (2015).

- [42] J. F. Boyce, S. Schürch, Y. Rotenberg, and A. W. Neumann, *Colloids and Surfaces* **9**, 307 (1984).
- [43] O. I. del Río and A. W. Neumann, *J. Colloid Interface Sci.* **196**, 136 (1997).
- [44] L. W. Honaker, J. P. F. Lagerwall, and V. S. R. Jampani, *Langmuir* **34**, 2403 (2018).
- [45] J. E. Proust, E. Perez, and L. Ter-Minassian-Saraga, *Colloid Polym. Sci. Kolloid-Zeitschrift Zeitschrift Für Polym.* **256**, 666 (1978).
- [46] J. W. Kim, H. Kim, M. Lee, and J. J. Magda, *Langmuir* **20**, 8110 (2004).
- [47] L. M. Tarakhan, *Ukr. J. Phys.* **51**, 22 (2006).
- [48] L. W. Honaker, S. Vats, M. Anyfantakis, and J. P. F. Lagerwall, *J. Mater. Chem. C* **7**, 11588 (2019).
- [49] L. Lacaze, P. Guenoun, D. Beysens, M. Delsanti, P. Petitjeans, and P. Kurowski, *Phys. Rev. E* **82**, 1 (2010).
- [50] Y. Geng, J. Noh, I. Drevenšek-Olenik, R. Rupp, G. Lenzini, and J. P. F. Lagerwall, *Sci. Rep.* **6**, 1 (2016).
- [51] J. V. Selinger, *Introduction to the Theory of Soft Matter: From Ideal Gases to Liquid Crystals*, 1st editio (Springer International Publishing Switzerland, 2016).
- [52] A. Jákli and A. Saupe, *One- and Two-Dimensional Fluids: Properties of Smectic, Lamellar and Columnar Liquid Crystals*, 1st Editio (CRC Press, Boca Raton, Florida, 2006).
- [53] P. Pálffy-Muhoray, *Phys. Today* **60**, 54 (2007).
- [54] H. Nemati, *Color Tuning in Polymer-Stabilized Liquid Crystals*, Kent State University, 2015.
- [55] P. Popov, E. K. Mann, and A. Jakli, *J. Mater. Chem. B* **5**, 5061 (2017).
- [56] N. Popov, A. Smirnova, N. Usol'tseva, and P. Popov, *Liq. Cryst. Their Appl.* **17**, 34 (2017).
- [57] J. M. Brake and N. L. Abbott, *Langmuir* **23**, 8497 (2007).
- [58] L. N. Tan, R. J. Carlton, K. Cleaver, and N. L. Abbott, *Mol. Cryst. Liq. Cryst.* **1406**, 37 (2014).
- [59] Z. S. Davidson, *Assembly, Elasticity, and Structure of Lyotropic Chromonic Liquid Crystals and Disordered Colloids*, University of Pennsylvania, 2017.
- [60] Z. S. Davidson, Y. Huang, A. Gross, A. Martinez, T. Still, C. Zhou, P. J. Collings, R. D. Kamien, and A. G. Yodh, *Nat. Commun.* **8**, 1 (2017).
- [61] S. Zhou, *Liq. Cryst. Today* **27**, 91 (2018).
- [62] T. M. Drwenski, *Colloidal Liquid Crystals: Phase Behavior, Sedimentation, and Percolation of Rods, Boomerangs, and Cuboids*, University of Utrecht, 2018.

- [63] W. Chen and D. G. Gray, *Langmuir* **18**, 633 (2002).
- [64] M. J. Stephen and J. P. Straley, *Physics of Liquid Crystals* (1974).
- [65] F. Berride, E. Troche, G. Feio, E. Cabrita, T. Sierra, A. Navarro Vazquez, and M. Cid, *Soft Matter* (2017).
- [66] W. Iglesias, N. L. Abbott, E. K. Mann, and A. Jákli, *ACS Appl. Mater. Interfaces* **4**, 6884–6890 (2012).
- [67] A. Jákli, O. D. Lavrentovich, and J. V. Selinger, *Rev. Mod. Phys.* **90**, 45004 (2018).
- [68] J. Stelzer, R. Berardi, and C. Zannoni, *Chem. Phys. Lett.* **299**, 9 (1999).
- [69] A. I. Jákli, 196 (2012).
- [70] M.-J. Lee, Y.-C. Sung, Y.-C. Hsiao, and W. Lee, *Proc. SPIE* **9940**, 12 (2016).
- [71] W. D. St. John, W. J. Fritz, Z. J. Lu, and D.-K. Yang, *Phys. Rev. E* **51**, 1191 (1995).
- [72] V. S. R. Jampani, R. H. Volpe, K. Reguengo de Sousa, J. Ferreira Machado, C. M. Yakacki, and J. P. F. Lagerwall, *Sci. Adv.* **5**, 1 (2019).
- [73] D. Mistry, S. D. Connell, S. L. Mickthwaite, P. B. Morgan, J. H. Clamp, and H. F. Gleeson, *Nat. Commun.* **9**, 1 (2018).
- [74] J. M. Brake, M. K. Daschner, Y.-Y. Luk, and N. L. Abbott, **302**, 2094 (2003).
- [75] P. Popov, L. W. Honaker, E. E. Kooijman, E. K. Mann, and A. I. Jákli, *Sens. Bio-Sensing Res.* **8**, 31 (2016).
- [76] P. Popov, *Liquid Crystal Interfaces: Experiments, Simulations and Biosensors*, Kent State University, 2015.
- [77] M. A. Rahman, H. Agha, T.-K. Truong, J. H. Park, D. Suh, and G. Scalia, *J. Mol. Liq.* **267**, 363 (2018).
- [78] F. C. Frank, *Discuss. Faraday Soc.* **25**, 19 (1958).
- [79] T. J. Sluckin, D. A. Dunmur, and H. Stegemeyer, *Crystals That Flow: Classic Papers from the History of Liquid Crystals* (CRC Press, 2004).
- [80] S. Chandrasekhar and G. S. Ranganath, *Adv. Phys.* **35**, 507 (1986).
- [81] A. V. Zakharov, M. N. Tsvetkova, and V. G. Korsakov, *Phys. Solid State* **44**, 1795 (2002).
- [82] A. A. Joshi, J. K. Whitmer, O. Guzmán, N. L. Abbott, and J. J. de Pablo, *Soft Matter* **10**, 882 (2014).
- [83] M. Kleman and O. D. Lavrentovich, *Philos. Mag.* **86**, 4117 (2006).
- [84] H.-L. Liang, E. Enz, G. Scalia, and J. P. F. Lagerwall, *Mol. Cryst. Liq. Cryst.* **549**, 69 (2011).
- [85] H. Agha, J. B. Fleury, and Y. Galerne, *Eur. Phys. J. E* **35**, 1 (2012).



- [86] E. Bukusoglu, J. A. Martinez-Gonzalez, X. Wang, Y. Zhou, J. J. de Pablo, and N. L. Abbott, *Soft Matter* (2017).
- [87] O. D. Lavrentovich, *Liq. Cryst.* **24**, 117 (1998).
- [88] H. Koo, *J. Korean Phys. Soc.* **32**, 48 (1998).
- [89] M. Mięslowicz, *Nature* **158**, 27 (1946).
- [90] J. Li, S. Gauza, and S.-T. Wu, *J. Appl. Phys.* **96**, 19 (2004).
- [91] U. Mur, S. Čopar, G. Posnjak, I. Mušević, and M. Ravnik, *Liq. Cryst.* **8292**, (2016).
- [92] A. Michel-Lévy, *Les Minéraux des roches* (Baudry et Cie, Paris, France, 1888).
- [93] H. Okamoto, T. Inoue, and K. Osaki, *J. Polym. Sci. Part B Polym. Phys.* **33**, 417 (1995).
- [94] D. W. Saunders, *Nature* **165**, 360 (1950).
- [95] B. E. Sørensen, *Eur. J. Mineral.* **25**, 5 (2013).
- [96] J. E. Bigelow and R. A. Kashnow, *Appl. Opt.* **16**, 2090 (1977).
- [97] C. Bayon, G. Agez, and M. Mitov, *Lab Chip* **14**, 2063 (2014).
- [98] A. Y. Grosberg and A. R. Khokhlov, *Giant Molecules: Here, There, Everywhere*, Second ed. (World Scientific, Singapore, 1997).
- [99] T. C. B. McLeish, *Adv. Phys.* **51**, 1379 (2002).
- [100] T. Lister, *Classic Chemistry Demonstrations* (London, 1993).
- [101] P. Sakellariou, *Polymer* **33**, 1339 (1992).
- [102] J. K. Nielsen, H. K. Rasmussen, O. Hassager, and G. H. McKinley, *J. Rheol. (N. Y. N. Y.)* **50**, 453 (2006).
- [103] G. H. McKinley and T. Sridhar, *Annu. Rev. Fluid Mech.* **34**, 375 (2002).
- [104] Y. Ōyanagi and M. Matsumoto, *J. Colloid Sci.* **17**, 426 (1962).
- [105] Chemical Retrieval on the Web, *Polym. Database Online* (2015).
- [106] Chemical Retrieval on the Web, *Polym. Database Online* (2017).
- [107] Chemical Retrieval on the Web, *Polym. Database Online* (2016).
- [108] B. Oktay, N. Kayaman-Apohan, and S. Erdem-Kuruca, *IOP Conf. Ser. Mater. Sci. Eng.* **64**, 6 (2014).
- [109] M. I. Avadanei, *J. Macromol. Sci. Part B Phys.* **51**, 313 (2012).
- [110] M. Akiba and A. S. Hashim, *Prog. Polym. Sci.* **22**, 475 (1997).
- [111] M. D. Dickey, *ACS Appl. Mater. Interfaces* **6**, 18369 (2014).
- [112] R. A. Bilodeau, D. Y. Zemlyanov, and R. K. Kramer, *Adv. Mater. Interfaces* **1** (2017).

- [113] K. Doudrick, S. Liu, E. M. Mutunga, K. L. Klein, V. Damle, K. K. Varanasi, and K. Rykaczewski, *Langmuir* **30**, 6867 (2014).
- [114] P. Sipos, T. Megyes, and O. Berkesi, *J. Solution Chem.* **37**, 1411 (2008).
- [115] M. R. Khan, C. B. Eaker, E. F. Bowden, and M. D. Dickey, *Proc. Natl. Acad. Sci.* **111**, 14047 (2014).
- [116] M. Kernaghan, *Phys. Rev.* **37**, 990 (1931).
- [117] Y. Lin, C. Ladd, S. Wang, A. Martin, J. Genzer, S. A. Khan, and M. D. Dickey, *Extrem. Mech. Lett.* **7**, 55 (2016).
- [118] M. Frenzel, C. Mikolajczak, M. A. Reuter, and J. Gutzmer, *Resour. Policy* **52**, 327 (2017).
- [119] R. M. Hochmuth, *J. Biomech.* **33**, 15 (2000).
- [120] J.-L. Salager, *Surfactants in Aqueous Solutions*, 1st ed. (Escuela de Ingenieria Quimica, Universidad de los Andes, Mérida, Venezuela, 1993).
- [121] D. Needham, K. Kinoshita, and A. Utoft, *MDPI Micromachines* **10**, 1 (2019).
- [122] J. N. Israelachvili, D. J. Mitchell, and B. W. Ninham, *J. Chem. Soc. Faraday Trans. 2 Mol. Chem. Phys.* **72**, 1525 (1976).
- [123] Y. P. Patil and S. Jadhav, *Chem. Phys. Lipids* **177**, 8 (2014).
- [124] A. Bąk and W. Podgórska, *Colloids Surfaces A Physicochem. Eng. Asp.* **504**, 414 (2016).
- [125] B. V. Zhmud, F. Tiberg, and J. Kizling, *Langmuir* **16**, 2557 (2000).
- [126] C. Barnaba, M. A. García-Alvarado, J. M. Tejero-Andrade, and I. G. Medina-Meza, *Rev. Mex. Ing. Qum.* **12**, 283 (2013).
- [127] J. W. Strutt III, *Proc. London Math. Soc.* **10**, 4 (1878).
- [128] G. Mason, *J. Colloid Interface Sci.* **32**, 172 (1970).
- [129] A. Sauret and H. C. Shum, *Int. J. Nonlinear Sci. Numer. Simul.* **13**, 351 (2012).
- [130] Y. Ren, Z. Liu, and H. C. Shum, *Lab Chip* **15**, 121 (2015).
- [131] K. Avila, A. De Lozar, M. Avila, B. Hof, D. Moxey, and D. Barkley, *Science* **333**, 192 (2011).
- [132] T. M. Squires and S. R. Quake, *Rev. Mod. Phys.* **77**, 977 (2005).
- [133] J. H. Hildebrand, *J. Am. Chem. Soc.* **5**, 1452 (1916).
- [134] R. F. Fedors, *Polym. Eng. Sci.* **14**, 147 (1974).
- [135] K. Araya and K. Iwasaki, *Mol. Cryst. Liq. Cryst.* **392**, 49 (2003).
- [136] Sigma-Aldrich, *Polym. Prod. from Aldrich* 46 (1999).
- [137] C. M. Hansen, *The Three Dimensional Solubility Parameter and Solvent Diffusion Coefficient*, Technical University of Denmark, 1967.

- [138] C. M. Hansen, *Hansen Solubility Parameters: A User's Handbook*, 2nd Ed. (CRC Press, Boca Raton, Florida, 2000).
- [139] A. F. M. Barton, *Chem. Rev.* **75**, 731 (1975).
- [140] A. Hasan, M. Nurunnabi, M. Morshed, A. Paul, A. Polini, T. Kuila, M. Al Hariri, Y. Lee, and A. A. Jaffa, *Biomed Res. Int.* **2014**, 1 (2014).
- [141] E. K. Sackmann, A. L. Fulton, and D. J. Beebe, *Nature* **507**, 181 (2014).
- [142] Y. Xia and G. M. Whitesides, *Annu. Rev. Mater. Sci.* **28**, 153 (1998).
- [143] N. Chronis, G. Liu, K.-H. Jeong, and L. Lee, *Opt. Express* **11**, 2370 (2003).
- [144] H. Gu, M. H. G. Duits, and F. Mugele, *Colloids Surfaces A Physicochem. Eng. Asp.* **389**, 38 (2011).
- [145] P. Bao, D. A. Paterson, P. L. Harrison, K. Miller, S. Peyman, J. C. Jones, J. Sandoe, S. D. Evans, R. J. Bushby, and H. F. Gleeson, *Lab Chip* **19**, 1082 (2019).
- [146] R. K. Shah, H. C. Shum, A. C. Rowat, D. Lee, J. J. Agresti, A. S. Utada, L. Chu, J. Kim, A. Fernandez-Nieves, C. J. Martinez, and D. A. Weitz, *Mater. Today* **11**, 18 (2008).
- [147] G. T. Vladislavljević, H. Shahmohamadi, D. B. Das, E. E. Ekanem, Z. Tauanov, and L. Sharma, *J. Colloid Interface Sci.* **418**, 163 (2014).
- [148] J. S. Mellors, V. Gorbounov, R. S. Ramsey, and J. M. Ramsey, *Anal. Chem.* **80**, 6881 (2008).
- [149] J. Derganc, B. Božič, S. Svetina, and B. Žekš, *Biophys. J.* **79**, 153 (2000).
- [150] S. Lee, D. H. Kim, and D. Needham, *Langmuir* **17**, 5544 (2001).
- [151] S. Lee, D. H. Kim, and D. Needham, *Langmuir* **17**, 5537 (2001).
- [152] L. M. Lee and A. P. Liu, *J. Nanotechnol. Eng. Med.* **5**, 040902 (2014).
- [153] Y.-C. Fung, *Biomechanics: Mechanical Properties of Living Tissue*, 2nd ed. (Springer New York, New York, 1993).
- [154] L. W. Honaker, J. P. F. Lagerwall, and V. S. R. Jampani, *Langmuir* **34**, 2403 (2018).
- [155] M. Hashimoto, P. Garstecki, H. A. Stone, and G. M. Whitesides, *Soft Matter* **4**, 1403 (2008).
- [156] K. K. Mohan, *The Pendant Drop Method for Measuring Interfacial Tension* (n.d.).
- [157] S. M. I. Saad, Z. Policova, and A. W. Neumann, *Colloids Surfaces A Physicochem. Eng. Asp.* **384**, 442 (2011).
- [158] F. Peters and D. Arabali, *Colloids Surfaces A Physicochem. Eng. Asp.* **426**, 1 (2013).
- [159] M. G. J. Gannon and T. E. Faber, *Philos. Mag. A* **37**, 117 (1978).
- [160] G. A. Oweimreen, A. K. Shihab, K. Halhouli, and S. F. Sikander, *Mol. Cryst. Liq.*

- Cryst. **138**, 327 (1986).
- [161] M. Tintaru, R. Moldovan, T. Beica, and S. Frunza, *Liq. Cryst.* **28**, 37 (2001).
  - [162] P. Popov, L. W. Honaker, M. Mirheydari, E. K. Mann, and A. Jákli, *Sci. Rep.* **7**, 1 (2017).
  - [163] P. Lecomte du Noüy, *J. Gen. Physiol.* **625** (1925).
  - [164] K. Kinoshita, E. Parra, and D. Needham, *J. Colloid Interface Sci.* (2016).
  - [165] S. D. Hudson, J. T. Cabral, W. J. Goodrum, K. L. Beers, and E. J. Amis, *Appl. Phys. Lett.* **87**, 20899 (2005).
  - [166] J. T. Cabral and S. D. Hudson, *Lab Chip* **6**, 427 (2006).
  - [167] D. Molino, S. Quignard, C. Gruget, F. Pincet, Y. Chen, M. Piel, and J. Fattaccioli, *Sci. Rep.* **6**, 29113 (2016).
  - [168] Q. Brosseau, *Dynamics of Soft Interfaces in Droplet-Based Microfluidics*, Georg-August-Universität Göttingen, 2014.
  - [169] J. Noh, B. Henx, and J. P. F. Lagerwall, *Adv. Mater.* **28**, 10170 (2016).
  - [170] V. S. R. Jampani, *Surface Coupling Agent (DMOAP) for Colloidal Liquid Crystal Studies* (Ljubljana, Slovenia, 2010).
  - [171] M. R. Khan, C. Trlica, J. So, M. Valeri, and M. D. Dickey, *Appl. Mater. Interfaces* (2014).
  - [172] A. Schanen, *Microfluidics for Measuring the Interfacial Tension of Liquid Crystals*, University of Luxembourg, 2019.
  - [173] J. H. Xu, S. W. Li, W. J. Lan, and G. S. Luo, *Langmuir* **24**, 11287 (2008).
  - [174] C. Vautier-Giongo and B. L. Bales, *J. Phys. Chem. B* **107**, 5398 (2003).
  - [175] A. J. Prosser and E. I. Franses, *Colloids Surfaces A Physicochem. Eng. Asp.* **178**, 1 (2001).
  - [176] J. Guo, S. Hong, H. Yoon, G. Babakhanova, O. D. Lavrentovich, and J. Song, *Adv. Sci.* **1900785** (2019).
  - [177] G. M. Koenig, I.-H. Lin, and N. L. Abbott, *Proc. Natl. Acad. Sci.* **107**, 3998 (2010).
  - [178] P. Popov, E. K. Mann, and A. Jákli, *Phys. Rev. Appl.* **1**, 034003 (2014).
  - [179] V. S. R. Jampani, D. J. Mulder, K. Reguengo de Sousa, A.-H. Gélébart, J. P. F. Lagerwall, and A. P. H. J. Schenning, *Adv. Funct. Mater.* **28**, 1 (2018).
  - [180] P. Popov, D. J. Lacks, A. Jákli, and E. K. Mann, *J. Chem. Phys.* **141**, 054901 (2014).
  - [181] W. G. Iglesias, N. L. Abbott, E. K. Mann, and A. Jákli, *ACS Appl. Mater. Interfaces* **4**, (2012).
  - [182] J. Zhang and Y. Meng, *Tribol. Lett.* **56**, 543 (2014).

- [183] B. Gol, F. J. Tovar-Lopez, M. E. Kurdzinski, S.-Y. Tang, P. Petersen, A. Mitchell, and K. Khoshmanesh, *Lab Chip* **15**, 2476 (2015).
- [184] C. Schütz, *Fabrication of Nanocellulose-Based Materials*, Stockholm University, 2015.
- [185] C. Honorato-Rios, C. Lehr, C. Schütz, R. Sanctuary, M. A. Osipov, J. Baller, and J. P. F. Lagerwall, *NPG Asia Mater.* **10**, 455 (2018).
- [186] N. A. Lockwood and N. L. Abbott, *Curr. Opin. Colloid Interface Sci.* **10**, 111 (2005).
- [187] N. Popov, A. Smirnova, P. Popov, and N. Usol'tseva, *Liq. Cryst. Their Appl.* **17**, 34 (2017).
- [188] C. G. Reyes, J. Baller, T. Araki, and J. P. F. Lagerwall, *Soft Matter* **1** (2019).
- [189] E. Enz and J. Lagerwall, *J. Mater. Chem.* **20**, 6866 (2010).
- [190] M. O. Pehlivaner Kara and M. W. Frey, *J. Appl. Polym. Sci.* **40305**, 1 (2014).
- [191] M. Bognitzki, W. Czado, T. Frese, A. Schaper, M. Hellwig, M. Steinhart, A. Greiner, and J. H. Wendorff, *Adv. Mater.* **4095**, 70 (2001).
- [192] A. Rawal and S. Mukhopadhyay, in *Adv. Filam. Yarn Spinn. Text. Polym.* (Woodhead Publishing Limited, 2014), pp. 75–99.
- [193] Y. Guan, D. M. Agra-Kooijman, S. Fu, A. Jákli, and J. L. West, *Adv. Mater.* **1902168**, 1902168 (2019).
- [194] C. J. Kuo and W. L. Lan, in *Adv. Filam. Yarn Spinn. Text. Polym.* (Woodhead Publishing Limited, 2014), pp. 100–112.
- [195] J.-D. Lin, C.-P. Chen, L.-J. Chen, Y.-C. Chuang, S.-Y. Huang, and C.-R. Lee, *Opt. Express* **24**, 3112 (2016).
- [196] S. Ribeiro, P. Costa, C. Ribeiro, V. Sencadas, G. Botelho, and S. Lanceros-Méndez, *Compos. Part B Eng.* **67**, 30 (2014).
- [197] D. Puppi and F. Chiellini, *Polym. Int.* **66**, 1690 (2017).
- [198] M. Vehviläinen, T. Kamppuri, M. Rom, J. Janicki, D. Ciechańska, S. Grönqvist, M. Siika-Aho, K. E. Christoffersson, and P. Nousiainen, *Cellulose* **15**, 671 (2008).
- [199] B. Ozipek and H. Karakas, in *Adv. Filam. Yarn Spinn. Text. Polym.* (Woodhead Publishing Limited, 2014), pp. 174–186.
- [200] T. A. Hancock, J. E. Spruiell, and J. L. White, *J. Appl. Polym. Sci.* **21**, 1227 (1977).
- [201] B. Vigolo, A. Pénicaud, C. Coulon, C. Sauder, R. Pailler, C. Journet, P. Bernier, and P. Poulin, *Science* **290**, 1331 (2000).
- [202] J. Yuan, W. Neri, C. Zakri, P. Merzeau, K. Kratz, A. Lendlein, and P. Poulin, *Science* **158**, 155 (2019).

- [203] J.-S. Noh, MDPI Polym. **8**, 1 (2016).
- [204] J. Zhang, S. Seyedin, S. Qin, P. A. Lynch, Z. Wang, W. Yang, X. Wang, and J. M. Razal, J. Mater. Chem. A (2019).
- [205] E. Cuttaz, J. Goding, C. Vallejo-Giraldo, U. Aregueta-Robles, N. Lovell, D. Ghezzi, and R. A. Green, Biomater. Sci. (2019).
- [206] P. Zhou, C. Lu, J. Shi, K. Li, F. He, S. Zhang, and Y. Li, J. Macromol. Sci. Part B Phys. **50**, 1215 (2011).
- [207] S. Montesanto, G. A. Mannella, F. C. Pavia, V. La Carrubba, and V. Brucato, J. Appl. Polym. Sci. **42151**, 1 (2015).
- [208] J.-M. Hung, US. Pat. 4 602 083 (1986).
- [209] C. Jumeaux, R. Chapman, R. Chandrawati, and M. M. Stevens, Polym. Chem. **6**, 4116 (2015).
- [210] H. Du, R. Wickramasinghe, and X. Qian, J. Phys. Chem. B **114**, 16594 (2010).
- [211] T. Driessen, R. Jeurissen, H. Wijshoff, F. Toschi, D. Lohse, T. Driessen, R. Jeurissen, H. Wijshoff, and F. Toschi, Phys. Fluids **25**, 1 (2013).
- [212] D. T. Papageorgiou, Phys. Fluids **7**, 1529 (1995).
- [213] M. Tian, Q. Hu, H. Wu, L. Zhang, H. Fong, and L. Zhang, Mater. Lett. **65**, 3076 (2011).
- [214] P. Supaphol and S. Chuangchote, J. Appl. Polym. Sci. **108**, 969 (2010).
- [215] M. Xiao, J. Chery, and M. W. Frey, ACS Appl. Nano Mater. **1**, 722 (2018).
- [216] A. K. Sonker, K. Rathore, R. K. Nagarale, and V. Verma, J. Polym. Environ. **1** (2017).
- [217] S. Trabelsi, P.-A. Albouy, and J. Rault, Rubber Chem. Technol. **77**, 303 (2011).
- [218] A. Bogris, J. Wang, M. Anyfantakis, B. Loppinet, S. L. Craig, H. J. Butt, and G. Fytas, J. Phys. Chem. B **122**, 6995 (2018).
- [219] C. Adam, J. Lacoste, and J. Lemaire, Polym. Degrad. Stab. **32**, 51 (1991).
- [220] E. Enz, Electrospun Polymer - Liquid Crystal Composite Fibres, Martin Luther University Halle-Wittenberg, 2013.
- [221] W. W. Beens and W. H. De Jeu, J. Chem. Phys. **82**, 3841 (1985).
- [222] M. Nikkhou, *Liquid Crystal in Confined Environment* (Ljubljana, Slovenia, 2011).
- [223] H. Yokoyama, Mol. Cryst. Liq. Cryst. **165**, 265 (1988).
- [224] S. S. Lee, H. J. Seo, Y. H. Kim, and S. Kim, Adv. Mater. **1606894**, 1 (2017).
- [225] T.-T. Tang, H.-Y. Wu, C.-J. Lin, and R.-P. Pan, Mol. Cryst. Liq. Cryst. **478**, 143/[899] (2007).
- [226] G. S. Iannacchione and D. Finotello, Phys. Rev. E **50**, 4780 (1994).

- [227] P. T. Ireland and T. V. Jones, *J. Phys. E.* **20**, 1195 (1987).
- [228] P. K. Rai, M. M. Denn, and C. Maldarelli, *Langmuir* **19**, 7370 (2003).
- [229] F. Boubée de Gramont, *Electrospinning of Conducting Polymer Fibers for Stretchable Electronics*, University of Montréal, 2017.
- [230] E. Llorens, E. Armelin, M. del M. Pérez-Madrigal, L. J. del Valle, C. Alemán, and J. Puiggalí, *MDPI Polym.* **5**, 1115 (2013).
- [231] J. Thelen, M. D. Dickey, and T. Ward, *Lab Chip* **12**, 3961 (2012).
- [232] K. J. Mysels, *Langmuir* **2**, 423 (1986).
- [233] L. Majidi, D. Gritsenko, and J. Xu, *Front. Mech. Eng.* **3**, 1 (2017).
- [234] P. Marek, J. J. Velasco-Veléz, T. Doll, and G. Sadowski, *J. Sensors Sens. Syst.* **3**, 291 (2014).
- [235] T. Daeneke, K. Khoshmanesh, N. Mahmood, I. A. de Castro, D. Esrafilzadeh, S. J. Barrow, M. D. Dickey, and K. Kalantar-Zadeh, *Chem. Soc. Rev.* **47**, 4073 (2018).
- [236] B. B. Boika, N. I. Insarova, and A. S. Lugina, *Mekhanika Polim.* **1**, 13 (1965).
- [237] V. S. Volkov, *Polym. Sci. Ser. A* **56**, 712 (2014).
- [238] J. Noh, *Tuning Self-Assembly in Liquid Crystal Shells: From Interfacial- to Polymer-Stabilization*, University of Luxembourg, 2018.
- [239] E. P. Symons and T. L. Labus, *Experimental Investigation of an Axisymmetric Fully Developed Laminar Free Jet* (1971).
- [240] S. Takeuchi, P. Garstecki, D. B. Weibel, and G. M. Whitesides, *Adv. Mater.* **17**, 1067 (2005).
- [241] I. Teraka, *Polymer Solutions: An Introduction to Physical Properties* (John Wiley & Sons, New York, 2002).
- [242] J. Cooper, *Compositional Analysis of Merck E7 Liquid Crystal Intermediates Using UltraPerformance Convergence Chromatography (UPC 2) with PDA Detection* (Milford, Massachusetts, USA, 2013).





## ACKNOWLEDGEMENTS

When I started my Ph.D. journey seven years ago, I think it's safe to say that I had no idea what lay in store for me: I thought I was going to stay in the U.S., do some good research there, and end up maybe vacationing in Europe or travelling here for a conference or two. A trip to Korea and a move to Luxembourg later, it's needless to say that this has been a fun and rewarding experience beyond my wildest dreams.

First and foremost, I want to thank Jan Lagerwall, my supervisor, for allowing me to be a part of his group for the past four years (and for the professional relationship for the past six years!). It's been a rewarding time, academically, professionally, and personally, and I feel like I've grown a lot in these years. Being able to work in your group has also helped me to achieve so much, from the places I've been able to travel as a part of my work (like to Russia and Japan!) to the research I've been able to accomplish. The fact that you've been so encouraging and supportive of (most of) my crazy ideas really is something I never thought I would have in a research group.

Of course, behind every researcher is a lot of behind-the-scenes help. First, I would like to mention both Anshul Sharma, one of my candidacy preparation tutors in Kent and who I've known the longest during my Ph.D. journey (seven years!), and JungHyun Noh, who I had the pleasure of working with both during my visit to Korea and during three years here in the Grand Duchy. While the life and journey of a researcher involves a lot of coming and going, having two coworkers and friends who've been with me for a large part of it have made it so much more rewarding. I'm indebted in particular to Paula Souza for her help during the process of me applying for the grant to come to Luxembourg (and the associated paperwork with moving here); Vanessa Schmidt for helping me to navigate the sometimes-crazy paperwork labyrinth; Dr. Uli Siegel, Nicolas Tournier, and Robbie Wagener for helping me with constructing set-ups; and Alex Ewen for being so willing to print off posters and other material on short notice. I'm equally thankful for my coworkers for their support, both academically and professionally. I'm especially grateful to my travel companions (Shameek Vats, Meenu, Ashik Rahman, and Rijeesh Kizhakidathazhath) for travelling with me to interesting and fun conferences in several different countries. Apart from that, I also want to thank Christina Schütz, Oliver Willekens, Manos Anyfantakis, Martin Urbanski, Anna Urbanski, V.S.R. Jampani, Catherine Reyes, Hakam Agha, Mouna Jemli, Claudius Lehr, Nicolò Maccaferri, Ivan Titov, Philipp Bender, Artem Malyeyev, Daniel Siopa, Thibaut Gallet, and Jonathan Rommelfangen for making both research and life at the University so much more fun. I would also like to thank the other research groups at Campus Limpertsberg for

various lively conversations and banter, and additionally Verena Görtz, Jörg Baller, and Rudolf Zentel for their feedback during my mock defense.

The work during my studies has spanned across three continents, so it's definitely worth mentioning a number of other people, especially from my time at Kent State. I particularly want to thank Antal ("Tony") Jáklí for funding my stay in South Korea that led to me ending up in Luxembourg; Elizabeth Mann for her support of my research during my stay in Kent and for being a part of my Ph.D. here in Luxembourg; lots of the academic staff at the LCI (Peter Pálffy-Muhoray, Deng-Ke Yang, Qi-Huo Wei, Chanjoong Kim, Robin Selinger, and Jonathan Selinger, to name a few); Mary Ann Kopcak for helping to navigate the sometimes formidable mountain of paperwork at Kent State; and my fellow students and researchers from my time there (especially, but not limited to, Hamed Shahsavan, Piotr Popov, Mirek Salamończyk, Roberta Rarumy, Muhammad Salili, Tianyi Guo, Oliver da Silva-Kress, Joe Angelo, Leah Bergquist, Sahil Gandhi, Afsoon Jamali, Kai-Han Chang, Youssef Golestani, Colin McGinty, Ali Moheghi, Sajedah Afghah, Hossein Nemati, Mona Mirheydari, Young-Ki Kim, Chenhui Peng, Jinghua Jiang, Taras Turiv, and Nick Diorio).

Even with all my moving, one constant has been my friends outside of research, who've both made me feel welcome wherever I've ended up and been a refuge from the craziness in research. In particular, I especially want to give a shout out to Max Frantz, Steve Brück, Bob Wintersdorff, Christoph Sourcin, Zach Grieves, Tuan Dinh, Fabian Bernstein, Dennis Brunner, Tamás Repa, Gilles Zanen, Fabio Nogueira, Sergi Pérez Casas, Jeff Jonas, and Cyril Foissy (in Luxembourg and the environs); Mike and Aubrey Klements, Herbie Wilson, Mitch Harmon, Andy Parina, Vincent Font, Carl McCormick, and Mark Brewster (in Ohio); and Myriam and Philippe Herzog, Sebastian Culpó, and Christine Lecart (from my time in central France). (I especially want to thank Myriam for proofreading and correcting the abstract in French!)

There are countless other people I can thank, but there are a few in particular I really would like to mention: David A. Young, Linda Clemente, and Dominique A. Poncelet, my French professors, for really getting me interested in French and Francophone culture; Mas Iimura, Colleen Byron, Joe Scanlon, and Mary Williams-Norton for giving me a solid foundation of chemistry and physics (and actually making me like both!); Patricia Beck, my high school chemistry and physics teacher, for getting me started on this crazy journey and really igniting my desire to do science; Cara Jesse and N. René Corders, two key figures who, during my high school time, really encouraged me to push further and harder despite inertia and opposition from the machinery at the school otherwise; and Regine Pöflinger, my elementary school German teacher who sparked in me a love and fascination with this part of Europe.

Last, but not least of all, I want to extend my gratitude to my family for being there throughout my journey, but especially to my brother, James, and mother, Colette, for their support of my many crazy decisions, regardless of where they ended up taking me, and for sparking in me a love of travel that ended up taking me back to (near) where I grew up to finish my doctorate.